

**CONCRETE-FILLED FIBRE-REINFORCED
POLYMER TUBES FOR AXIAL AND FLEXURAL
STRUCTURAL MEMBERS**

By

AMIR Z. FAM

A Dissertation
Submitted to the Faculty of Graduate Studies
In Partial Fulfilment of the Requirements for the Degree of

DOCTOR OF PHILOSOPHY

Structural Engineering Division
Department of Civil and Geological Engineering
The University of Manitoba
Winnipeg, Manitoba

© July 2000



National Library
of Canada

Acquisitions and
Bibliographic Services

395 Wellington Street
Ottawa ON K1A 0N4
Canada

Bibliothèque nationale
du Canada

Acquisitions et
services bibliographiques

395, rue Wellington
Ottawa ON K1A 0N4
Canada

Your file Votre référence

Our file Notre référence

The author has granted a non-exclusive licence allowing the National Library of Canada to reproduce, loan, distribute or sell copies of this thesis in microform, paper or electronic formats.

The author retains ownership of the copyright in this thesis. Neither the thesis nor substantial extracts from it may be printed or otherwise reproduced without the author's permission.

L'auteur a accordé une licence non exclusive permettant à la Bibliothèque nationale du Canada de reproduire, prêter, distribuer ou vendre des copies de cette thèse sous la forme de microfiche/film, de reproduction sur papier ou sur format électronique.

L'auteur conserve la propriété du droit d'auteur qui protège cette thèse. Ni la thèse ni des extraits substantiels de celle-ci ne doivent être imprimés ou autrement reproduits sans son autorisation.

0-612-53056-6

Canada

**THE UNIVERSITY OF MANITOBA
FACULTY OF GRADUATE STUDIES

COPYRIGHT PERMISSION PAGE**

**Concrete-Filled Fibre-Reinforced Polymer Tubes for Axial
and Flexural Structural Members**

BY

Amir Z. Fam

A Thesis/Practicum submitted to the Faculty of Graduate Studies of The University

of Manitoba in partial fulfillment of the requirements of the degree

of

Doctor of Philosophy

AMIR Z. FAM © 2000

Permission has been granted to the Library of The University of Manitoba to lend or sell copies of this thesis/practicum, to the National Library of Canada to microfilm this thesis/practicum and to lend or sell copies of the film, and to Dissertations Abstracts International to publish an abstract of this thesis/practicum.

The author reserves other publication rights, and neither this thesis/practicum nor extensive extracts from it may be printed or otherwise reproduced without the author's written permission.

ACKNOWLEDGEMENT

Words cannot express the authors sincere gratitude and appreciation to his supervisor Dr. Sami H. Rizkalla for his guidance, inspiration, and encouragement throughout this research program.

The author wishes to thank Dr. N. Rajapakse and Dr. M. Singh for serving on his Ph.D. committee. Thanks are extended to Dr. I. Harik from the University of Kentucky for reviewing this thesis as the external examiner. The support provided by the Network of Centres of Excellence on the Intelligent Sensing for Innovative Structures (ISIS Canada) is greatly acknowledged.

The author also expresses his thanks to Mr. M. McVey of the W. R. McQuade Structures Laboratory at the University of Manitoba for his assistance during fabrication and testing of the specimens. Special thanks are extended to Mr. B. Flisak, Mr. M. Dawood, and Mr. G. Horeczy for their assistance during the experimental phase of this study. The support provided by Mr. R. Greene, president of Lancaster Composite, is greatly appreciated.

The love, support and patience of my family Zakaria, Marcelle, and Maged cannot be praised enough; to them this thesis is dedicated.

ABSTRACT

The use of fibre reinforced polymers, FRP, in new structures is still limited to few demonstration projects. Innovative hybrid systems such as the concrete-filled FRP tubes are effective in facing the great demand for piling, poles, highway overhead sign structures and bridge components. The new products have to withstand aggressive corrosive environments such as the splash zone in case of marine piles. The concrete-filled glass fibre reinforced polymer, GFRP; cylindrical tube system utilizes the best characteristics of the individual materials. The FRP tube provides lightweight permanent formwork as well as non-corrosive reinforcement for the concrete, which simplify construction and reduce erection time. The round tube also confines the concrete in compression and increases its strength and ductility, while the concrete core supports the tube and prevents premature local buckling failure. Research work related to the flexural behaviour of concrete-filled FRP tubes and their behaviour under axial compression loading conditions is, however, very limited to date.

A two-phase experimental program was conducted at the University of Manitoba to examine the flexural behaviour of concrete-filled GFRP tubes and their behaviour under axial compression loads as short columns. Phase-I included eighteen simple beam tests conducted under four-point bending. The beams ranged from 1.07 to 10.4 meters in span and from 89 to 942 mm in diameter. The specimens included hollow and concrete-filled GFRP and steel tubes. Different cross-section configurations including totally and

partially-filled GFRP tubes with central voids were considered. GFRP tubes of different laminate structures including filament-wound and pultruded tubes were included. Also GFRP tubes with different diameter-to-thickness ratios were also considered. Phase-II included twelve stub tests under axial compression. The stubs ranged from 100 to 219 mm in diameter. Different cross-section configurations including totally-and partially-filled GFRP tubes were considered. The partially filled GFRP tubes included different inner-to-outer diameter ratios. Different laminate structures included filament-wound and pultruded GFRP tubes. A concrete-filled steel tube was also tested for comparison.

The thesis also presents two theoretical equilibrium/strain compatibility models, proposed to predict the behaviour of concrete-filled FRP tubes under axial compression as well as in flexure. The first model is a confinement model intended to predict the full stress-strain response of concrete confined by FRP shells, which is subjected to a variable confining pressure and also accounts for the concrete nonlinearity. The model can predict the behaviour of totally and partially filled FRP tubes, and also accounts for axially loaded concrete core only or axially loaded core and tube. The second model is capable of predicting the full load-deformation response of concrete-filled FRP tubes in flexure using a layer-by-layer approach. The model accounts for the linear FRP material, the concrete nonlinearity in compression and the tension stiffening effect. The predictions using the theoretical models showed excellent agreement with the experimental results. The models were used in parametric studies to investigate the effect of wall thickness and laminate architecture of the tube and the inner void size. The effect of concrete filling on flexural behaviour of high and low stiffness tubes is also studied.

TABLE OF CONTENTS

ACKNOWLEDGEMENT	ii
ABSTRACT	iii
TABLE OF CONTENTS	v
LIST OF TABLES	xii
LIST OF FIGURES	xiii
NOTATION	xxiii

Chapter 1: Introduction

1.1 General	1
1.2 Objectives	3
1.3 Scope and Contents	4

Chapter 2: Hybrid FRP/Concrete Structural Members - Background and Review

2.1 Introduction	8
2.2 Fibre Reinforced Polymer (FRP) Laminates	9
2.2.1 Fabrication Process	10
2.2.2 Mechanics of Composite Laminates	12
2.2.2.1 Elastic behaviour of unidirectional lamina	12
2.2.2.2 Elastic behaviour of multidirectional laminates	14

2.2.2.3	Strength of unidirectional lamina	16
2.2.2.4	Strength of multidirectional laminates	18
2.3	Background of Concrete-Filled Steel Tubular Members	20
2.4	Concrete-Filled FRP Tubes as Axial Compression Members	24
2.4.1	Comparison Between Steel and FRP-Confined Concrete	26
2.4.2	Effect of Geometry and Configuration of the Cross-section.....	28
2.4.3	Length Effects	31
2.4.4	Bond Effects	32
2.4.5	Analytical Modelling of FRP-Confined Concrete.....	34
2.5	Concrete-Filled FRP Tubes as Beams and Beam-Columns	36
2.5.1	Concrete-Filled FRP Tubes for Bridges.....	37
2.5.2	Concrete-Filled FRP Tubes for Piles	41
2.6	Prestressed Concrete-Filled FRP Tubes	42
2.7	Splices and Joints in Concrete-Filled FRP Tubes	44
2.8	Other Forms of Hybrid FRP/Concrete Sections	46

Chapter 3: The Experimental Program

3.1	Introduction	65
3.2	Materials used to fabricate the Specimens.....	66
3.2.1	Tubes	66
3.2.1.1	Mechanical properties of the tubes	67
3.2.2	Concrete.....	69
3.3	Experimental Phase I - Beam Tests	70

3.3.1	Test Specimens.....	70
3.3.2	Fabrication of the Beams.....	71
3.3.3	Instrumentation.....	73
3.3.4	Test Setup.....	74
3.4	Experimental Phase II - Stub Tests.....	75
3.4.1	Test Specimens.....	75
3.4.2	Fabrication of Stubs.....	76
3.4.3	Instrumentation.....	77
3.4.4	Test Setup.....	77

Chapter 4: Results of the Experimental Program and Discussion

4.1	Introduction.....	94
4.2	Phase I - Beam Tests.....	94
4.2.1	Effect of Concrete Filling.....	95
4.2.1.1	Flexural behaviour.....	95
4.2.1.2	Failure modes.....	97
4.2.2	Effect of Cross-section Configuration.....	97
4.2.2.1	Flexural behaviour.....	97
4.2.2.2	Failure modes.....	99
4.2.3	Effect of Laminate Structure of the Shell.....	99
4.2.3.1	Flexural behaviour.....	99
4.2.3.2	Failure modes.....	102

4.2.4	Reinforcement Ratio and Size Effects	103
4.2.4.1	Flexural behaviour.....	103
4.2.4.2	Failure modes	107
4.2.5	The Reinforcement Index	108
4.2.6	Cracking Strength of the Beams.....	111
4.3	Phase II – Stub Tests	112
4.3.1	Confinement Effect on Concrete	113
4.3.1.1	Behaviour under axial load	113
4.3.1.2	Failure modes.....	114
4.3.2	Effect of Material Type of the Confining Shell.....	115
4.3.2.1	Behaviour under axial load	115
4.3.2.2	Failure modes.....	116
4.3.3	Effect of Laminate Structure of the Shell	116
4.3.3.1	Behaviour under axial load	116
4.3.3.2	Failure modes.....	117
4.3.4	Effect of Cross-section Configuration and Interface Condition	117
4.3.4.1	Behaviour under axial load	117
4.3.4.2	Failure modes.....	119
4.3.5	Effect of Void Size	119
4.3.5.1	Behaviour under axial load	119
4.3.5.2	Failure modes.....	121
4.3.6	Effect of Stiffness of the Shell in the Hoop Direction	121
4.3.7	Effect of Loading the Shell in the Axial Direction	122
4.3.8	Strain Behaviour of the FRP Tube.....	123

4.4	Concrete Expansion during Curing	124
-----	--	-----

Chapter 5: Analytical Modelling

5.1	Introduction	159
5.2	Variable Confinement Model for Axially Loaded Concrete Confined by FRP Shells	160
5.2.1	Significance of the Model	162
5.2.2	Constant Confinement Model by Mander (1988)	162
5.2.3	Variable Confining Pressure	164
5.2.3.1	Radial displacements of the individual components	165
5.2.3.2	Radial displacement compatibility	166
5.2.4	Material Parameters	168
5.2.4.1	Variable secant modulus of concrete	168
5.2.4.2	Variable Poisson's ratio of concrete	169
5.2.5	Applying the Model using Step-by-step Approach	171
5.2.6	Failure Criteria	173
5.2.7	Comments on the Model	175
5.2.8	Verification of the Model	176
5.2.8.1	Present study	177
5.2.8.2	Tests by Kawashima et al (1997)	178
5.2.8.3	Tests by Nanni and Bradford (1995)	178
5.2.8.4	Tests by Picher and Labossiere (1996)	179
5.2.8.5	Tests by Mirmiran and Shahawy (1997)	180

5.2.9	Parametric Study using the Confinement Model	180
5.2.9.1	Effect of shell thickness	181
5.2.9.2	Effect of fibre-orientation and loading condition	182
5.2.9.3	Effect of void size	183
5.3	Analytical Modelling of Flexural Behaviour of Concrete-Filled FRP Tubes	183
5.3.1	Strain Compatibility/Equilibrium Model	184
5.3.1.1	Geometry of the problem	184
5.3.1.2	Stress distribution and material constitutive relationships	186
5.3.1.3	Internal forces and moments	188
5.3.1.4	Procedure of analysis	190
5.3.1.5	Cracking moment	192
5.3.1.6	Load-deflection calculations.....	192
5.3.2	Confinement of Concrete in the Compression Zone.....	193
5.3.3	Verification of the Model.....	195
5.3.3.1	Beam 4.....	195
5.3.3.2	Beam 10.....	197
5.3.3.3	Beams 11, 12 (a, b) and 13 (a, b)	197
5.3.4	Significance of Concrete Filling	198
5.3.5	Optimization of Void Size in Flexural Members	200
5.3.6	Parametric Study using the Proposed Model for Flexural Analysis.....	201
5.3.6.1	Effect of laminate structure	202
5.3.6.2	Effect of the reinforcement ratio	203

5.3.6.3	Effect of concrete strength	204
5.3.6.4	Concrete contribution in cases of low and high stiffness Tubes.....	205

Chapter 6: Summary and Conclusions

6.1	Summary	243
6.2	Conclusions	245
6.2.1	Flexural Members.....	245
6.2.2	Axial Compression Members.....	249
6.3	Recommendations for Future Work	252
REFERENCES		254

LIST OF TABLES

Chapter 3

3.1	Dimensions and details of the tubes used to fabricate the beams and the stubs	79
3.2	Mechanical properties of the tubes used to fabricate the beams and the stubs.....	80
3.3	Summary of experimental Phase I. test beams	81
3.4	Summary of experimental Phase II. test stubs	82

Chapter 4

4.1	Details of the beams used to study the effect of reinforcement index on ultimate moment, curvature, and neutral axis depth	127
4.2	Details of the beams used to compare the cracking strength to different codes..	128
4.3	Details of the stubs used to study the effect of stiffness of the shell on the confinement effectiveness.....	129
4.4	Details of the stubs tested by Mirmiran and Shahawy (1997) and used in this study to examine the effect of loading the shell in the axial direction	129

LIST OF FIGURES

Chapter 1

1.1	Different configurations of FRP tubes totally and partially filled with concrete	6
1.2	Different structural applications of concrete-filled FRP tubes	6
1.3	Concrete-filled FRP tubes as flexural members	7
1.4	Concrete-filled FRP tubes as axial compression members.....	7

Chapter 2

2.1	Unidirectional lamina (a) and Multidirectional laminate (b).....	53
2.2	Schematic of the filament-winding process.....	53
2.3	Multidirectional laminate with coordinate notation of individual plies (a) and stress resultants acting on a general shell element (b)	54
2.4	Failure envelope of E-glass/epoxy lamina with different levels of shear stress using Tsai-Wu criterion [Daniel and Ishai 1994]	54
2.5	Normalized stress-strain curves of concrete-filled GFRP circular and square tubes [Mirmiran et al 1998].....	55
2.6	Stress-strain response of GFRP-confined concrete versus steel-confined concrete [Samaan et al 1998]	55
2.7	Volumetric strain response of GFRP-confined concrete versus steel-confined concrete [Samaan et al 1998].....	56

2.8	Dilation curves of GFRP-confined concrete versus steel-confined concrete [Samaan et al 1998]	56
2.9	Concrete-filled carbon shell column systems [Seible 1996].....	57
2.10	Carbon shell space truss bridge systems [Seible 1996]	58
2.11	Details of connections in space truss carbon shell bridge systems [Seible 1996].....	58
2.12	Carbon shell girder-type bridge system [Seible et al 1997].....	59
2.13	Carbon shell girder bending tests [Karbhari et al 1998].....	59
2.14	Proposed systems for pedestrian bridge superstructures utilizing the carbon shell concept [Seible 1998]	60
2.15	Connection details of concrete-filled carbon shell system [Seible et al 1998]	61
2.16	Load-deflection behaviour of under and over-reinforced concrete-filled GFRP box sections [Fardis and Khalili 1981]	61
2.17	Hybrid concrete/GFRP/CFRP rectangular section [Triantafillou and Meier 1992].....	62
2.18	Load-deflection behaviour of hybrid beam and the GFRP box section [Triantafillou 1995].....	62
2.19	Modified hybrid concrete/GFRP/CFRP rectangular section [Canning et al 1999]	62
2.20	Different configurations proposed for stronger web for the hybrid rectangular section. (a) Intermediate flange. (b) Diamond-shape stiffener. (c) Full diaphragm. (d) Web diaphragm. (e) Cellular web. (f) Foam sandwich. (g) Corrugated web. [Canning et al 1999].....	63

2.21	Pultruded FRP panel [Hall and Mottram 1998].....	64
2.22	Hybrid rectangular beam cross-section [Hall and Mottram 1998]	64
2.23	Moment-deflection behaviour of hybrid beams 1 and 2 [Hall and Mottram 1998]	64

Chapter 3

3.1	Tension Coupons used to determine the mechanical properties of the tubes in axial direction.....	83
3.2	GFRP rings used to determine the mechanical properties in the circumferential direction using the split-disk test	84
3.3	Stress-strain curve of GFRP tube 8 under axial tension	85
3.4	Stress-strain curves of concrete under axial compression	85
3.5	GFRP and steel tubes before casting (See Table 3.1 for identification numbers)	86
3.6	Casting setup of beams 1b, 4, 5, 6, and 7 at the structures laboratory.....	87
3.7	Casting setup of beams 10, 11, 12, and 13 at a precast plant	88
3.8	Instrumentation of test beams	89
3.9	Schematic of test setup for beams.....	90
3.10	Test setup of small and medium size beams, beams 8 and 4	90
3.11	Test setup of large beams, beams 11 and 13	91
3.12	Cutting the stubs from the ends of tested beams using a diamond saw	92
3.13	Different stubs used in experimental Phase II	92
3.14	Test setup and instrumentation of stubs tested under axial compression	93

Chapter 4

4.1	Load-deflection behaviour of hollow and concrete-filled steel tubes.....	130
4.2	Load-deflection behaviour of hollow and concrete-filled GFRP tubes	130
4.3	Load-axial strain behaviour of hollow and concrete-filled steel tubes	131
4.4	Load-axial strain behaviour of hollow and concrete-filled GFRP tubes	131
4.5	Load-lateral strain behaviour at compression side of hollow and concrete-filled tubes	132
4.6	Variation of neutral axis depth with the moment for hollow and concrete-filled GFRP and steel tubes	132
4.7	Failure mode of hollow steel tube, beam 1a	133
4.8	Failure mode of concrete-filled steel tube, beam 1b	133
4.9	Failure modes of hollow GFRP tubes, beams 2a and 3a	134
4.10	Failure modes of concrete-filled GFRP tubes, beams 2b and 3b.....	134
4.11	Load-deflection behaviour of totally and partially filled GFRP tubes	135
4.12	Load-axial strain behaviour of totally and partially filled GFRP tubes.....	135
4.13	Variation of neutral axis depth with the moment for totally and partially filled GFRP tubes	136
4.14	Failure mode of beams 4, 5, 6, and 7	136
4.15	Load-deflection behaviour of beams 8 and 9 with different laminate structures	137
4.16	Load-axial strain behaviour of beams 8 and 9	137
4.17	Variation of neutral axis depth with the moment in beams 8 and 9	138
4.18	Failure modes of beams 8 and 9	138

4.19	Load-deflection behaviour of beams 10 and 11 with different laminate structures	139
4.20	Load-axial strain behaviour of beams 10 and 11	139
4.21	Variation of neutral axis depth with the moment in beams 10 and 11	140
4.22	Load-slip behaviour of beams 10 and 11	140
4.23	Failure modes of beams 10 and 11	141
4.24	Load-deflection behaviour of beams 12 (a, b)	141
4.25	Load-axial strain behaviour of beams 12 (a, b)	142
4.26	Variation of the neutral axis depth in beams 12 (a, b)	142
4.27	Load-deflection behaviour of beams 13a and b	143
4.28	Load-axial strain behaviour of beams 13 (a, b)	143
4.29	Variation of the neutral axis depth in beams 13 (a, b)	144
4.30	Load-deflection behaviour of beams 11, 12a, and 13a	144
4.31	Normalized moment-curvature response of beams 11, 12a, and 13a	145
4.32	Failure mode of beams 12 (a, b)	145
4.33	Failure mode of beams 13 (a, b)	146
4.34	Variation of the normalized ultimate moment with the reinforcement index.....	147
4.35	Variation of the normalized ultimate curvature with the reinforcement index....	147
4.36	Variation of the normalized neutral axis depth with the reinforcement index	148
4.37	Concrete cracking strength factor of beams versus different codes	148
4.38	Confinement effect on axial load-strain behaviour of stub 11.....	149
4.39	Failure modes of plain concrete, hollow GFRP tube, and concrete-filled GFRP tube.....	149

4.40	Load-strain behaviour of GFRP-confined concrete, stub 1, and steel-confined concrete, stub 7	150
4.41	Failure modes of GFRP-confined concrete, stub 1, and steel confined concrete, stub 7	150
4.42	Load-strain behaviour of concrete confined using filament-wound GFRP tube, stub 11, and pultruded GFRP tube, stub 12	151
4.43	Failure modes of concrete confined using filament-wound GFRP tube, stub 11, and pultruded GFRP, stub 12.....	151
4.44	Load-strain behaviour of stubs 1 to 6 with different cross-section configurations and different interface conditions	152
4.45	Load-lateral strain behaviour of the inner and outer shells of stubs 5 and 6	152
4.46	Failure modes of stubs 1 to 6 with different cross-section configurations	153
4.47	Load-strain behaviour of stubs 8, 9, and 10 with different void sizes	153
4.48	Effect of void size on stress-strain behaviour of concrete confined by GFRP shells	154
4.49	Variation of confined strength ratio with the inner-to-outer diameter ratio	154
4.50	Failure modes of stubs 8, 9, and 10 with different void sizes.....	155
4.51	Equilibrium of internal pressure and the hoop tensile stress	155
4.52	Effect of stiffness of the shell on confinement effectiveness	155
4.53	Variation of lateral strains at different axial strain levels	156
4.54	Development of hoop strains over time due to expansion of concrete in stubs 1, 3, 5, and 7.....	157

4.55	Development of hoop strains over time due to expansion of concrete in stubs 8, 9, and 10.....	157
4.56	Variation of pressure due to expansion of concrete with stiffness of the shell....	158
4.57	Effect of the void size on the pressure due to expansion of concrete	158

Chapter 5

5.1	Constant confinement model by Mander (1988)	206
5.2	Solid cylinder and thin shell under different stresses	206
5.3	Variable material parameters for concrete	207
5.4	Average axial-lateral strain behaviour under different confinement pressures [Gardner 1969].....	208
5.5	Variation of constant "C" at different confinement ratios	208
5.6	Flowchart of the proposed incremental variable confinement model.....	209
5.7	Effect of the axial loading conditions on the strength of FRP shell	210
5.8	Schematic stress-strain behaviour of FRP and steel confined concrete.....	211
5.9	Schematic of Poisson's ratio variation over the history of loading	211
5.10	Bi-axial strength failure envelope and stress path of tubes 5 and 6.....	212
5.11	Experimental versus analytical stress-strain response of stubs tested in this study	213
5.12	Experimental versus analytical stress-strain response [Kawashima et al 1997]..	214
5.13	Experimental versus analytical stress-strain response [Nanni and Bradford 1995]	214

5.14	Experimental versus analytical stress-strain response [Picher and Labossiere 1996]	215
5.15	Experimental versus analytical stress-strain response [Mirmiran and Shahawy 1997]	215
5.16	Effect of the thickness of GFRP shell on the behaviour of the confined concrete	216
5.17	Effect of fibre orientation within the shell on the behaviour of confined concrete under two different loading conditions	217
5.18	Effect of the void size in the concrete core on the confinement level	218
5.19	Concrete-filled FRP tube subjected to pure bending	219
5.20	Geometry of the problem	219
5.21	Stress and strain distributions along the depth of the section	220
5.22	Constitutive relationships for the concrete core and FRP shell	220
5.23	Flowchart of the analytical model used to predict the moment-curvature response of concrete-filled FRP tubes	221
5.24	Constructing the load-deflection diagram using the moment-curvature response of the section and the moment-area method.....	222
5.25	Confinement effect of concrete in the compression zone	222
5.26	Comparison between axial-lateral strain behaviour in beams and stubs	223
5.27	Predicted versus experimental moment-curvature behaviour of beam 4.....	224
5.28	Predicted versus experimental load-deflection behaviour of beam 4	224
5.29	Predicted versus experimental moment-strain behaviour of beam 4	225
5.30	Predicted versus experimental variation of the neutral axis depth of beam 4	225

5.31	Effect of bond factor α_1 on tension stiffening level.....	226
5.32	Predicted versus experimental moment-curvature behaviour of beam 10.....	226
5.33	Predicted versus experimental load-deflection behaviour of beam 10	227
5.34	Predicted versus experimental moment-strain behaviour of beam 10	227
5.35	Predicted versus experimental variation of the neutral axis depth for beam 10.....	228
5.36	Predicted versus experimental moment-curvature behaviour of beam 11	228
5.37	Predicted versus experimental load-deflection behaviour of beam 11	229
5.38	Predicted versus experimental moment-strain behaviour of beam 11	229
5.39	Predicted versus experimental variation of the neutral axis depth for beam 11	230
5.40	Predicted versus experimental moment-curvature behaviour of beam 12.....	230
5.41	Predicted versus experimental load-deflection behaviour of beam 12.....	231
5.42	Predicted versus experimental moment-strain behaviour of beam 12.....	231
5.43	Predicted versus experimental variation of the neutral axis depth for beam 12.....	232
5.44	Predicted versus experimental moment-curvature behaviour of beam 13.....	232
5.45	Predicted versus experimental load-deflection behaviour of beam 13	233
5.46	Predicted versus experimental moment-strain behaviour of beam 13	233
5.47	Predicted versus experimental variation of the neutral axis depth for beam 13.....	234
5.48	Predicted versus experimental moment-curvature response of beams 2 (a and b)	234

5.49	Moment-curvature response of hollow and concrete-filled tubes for beams 4, 10, 11, 12 and 13.....	235
5.50	Optimization of void size in flexural members for minimizing the self-weight used in the parametric study.....	236
5.51	Stress-strain curves of the concrete used in the parametric study.....	236
5.52	Stress-strain curves of the [0/90] laminates used in the parametric study	237
5.53	Effect of laminate structure of the tube on the moment-curvature response	237
5.54	Effect of laminate structure of the tube on the moment-strain behaviour	238
5.55	Effect of laminate structure of the tube on the variation of neutral axis depth....	238
5.56	Effect of wall thickness of the tube on moment-curvature response	239
5.57	Effect of wall thickness of the tube on moment-strain behaviour	239
5.58	Effect of wall thickness of the tube on variation of the neutral axis depth.....	240
5.59	Effect of concrete strength on the moment-curvature response.....	240
5.60	Effect of concrete strength on moment-strain behaviour	241
5.61	Effect of concrete strength on variation of the neutral axis depth	241
5.62	Variation of the flexural strength with the reinforcement index.....	242
5.63	Effect of concrete filling on flexural behaviour of tubes with high and low stiffness	242

NOTATION

a_{ij}	=	Element of the laminate compliance matrix relating the in-plane strains to in-plane loads
A	=	Constant in a second order polynomial relating axial and lateral strains of concrete
$A_c(i)$	=	Net area of concrete within a general strip i of a cross-section of a concrete-filled FRP tube
A_f	=	Cross-sectional area of the FRP tube
$A_f(i)$	=	Area of the part of the FRP tube within a general strip i of the cross-section of a concrete-filled FRP tube
A_{ij}	=	Element of the laminate stiffness matrix relating the in-plane loads to in-plane strains (membrane coefficient)
b_{ij}	=	Element of the laminate compliance matrix relating the in-plane strains to moments
B	=	Constant in a second order polynomial relating axial and lateral strains of concrete
$B(i)$	=	Half of the width of a general strip i in the cross-section of concrete-filled FRP tube
B_{ij}	=	Element of the laminate stiffness matrix relating the in-plane loads to curvatures and the moments to in-plane strains (coupling coefficient)
c	=	Neutral axis depth in a concrete-filled tube subjected to bending, measured from the outer surface of the tube in the compression side
c_{ij}	=	Element of the laminate compliance matrix relating the curvatures to in-plane loads
C	=	Constant in a linear relationship relating Poisson's ratio of concrete to the axial strain level

$C'CC$	=	Compressive stress resultant in concrete in the compression zone of a concrete-filled FRP tube under bending
$CC(i)$	=	Compression force in concrete in a general strip i in a concrete-filled FRP tube under bending
CFF	=	Compressive stress resultant in FRP tube in the compression zone of a concrete-filled FRP tube under bending
$CF(i)$	=	Compression force in FRP within a general strip i in a concrete-filled FRP tube under bending
d	=	Corner radius of a square or rectangular FRP jacket
d_{ij}	=	Element of the laminate compliance matrix relating the curvatures to moments
D	=	Average diameter of the hollow tube
D_i	=	Diameter of the central void inside the concrete core of a concrete-filled tube
D_{ij}	=	Element of the laminate stiffness matrix relating the moments to curvatures (bending coefficient)
D_o	=	Outer diameter of the hollow tube
$D_{\alpha\alpha}$	=	Circumferential bending stiffness of the FRP tube
E	=	Modulus of elasticity
E_c	=	Elastic modulus of concrete
$E_{c,i}$	=	Secant modulus of concrete at a general point i on the stress-strain curve
$E_{c,0}$	=	Initial tangential elastic modulus of concrete at zero stress
$E_{f,c}$	=	Effective elastic modulus of FRP tube under compression in the axial direction
$E_{f,t}$	=	Effective elastic modulus of FRP tube under tension in the axial direction
$E_{f(axial)}$	=	Effective elastic modulus of FRP tube in the axial direction
$E_{f(hoop)}$	=	Effective elastic modulus of the FRP tube in the hoop direction
E_f	=	Effective elastic modulus of cylindrical FRP jacket in the hoop direction

E_m	=	Young's modulus of the matrix
E_{c}	=	Effective elastic modulus of cylindrical FRP shell in the hoop direction
E_{sec}	=	Secant modulus of concrete at peak strength
E_x	=	Effective elastic modulus of a laminate in direction of reference axis x, which refers to the circumferential direction in case of cylindrical tubes
E_y	=	Effective elastic modulus of a laminate in direction of reference axis y, which refers to the axial direction in case of cylindrical tubes
E_1	=	Young's modulus of a lamina in the axial direction, parallel to the fibres
E_{1f}	=	Young's modulus of fibres the axial direction
E_2	=	Young's modulus of a lamina in the transverse direction, perpendicular to the fibres
E_{2f}	=	Young's modulus of fibres the transverse direction
$f_c(i)$	=	Axial stress level in concrete at a general strip i in a concrete-filled FRP tube under bending
f'_c	=	Unconfined concrete compressive strength
f_{cc}	=	Axial stress level in confined concrete at a general stage of loading
f'_{cc}	=	Peak compressive strength of confined concrete
$f'_{cc(\text{vanded})}$	=	Compressive strength of confined concrete in case of partially-filled FRP tubes
$f'_{cc(\text{total})}$	=	Compressive strength of confined concrete in case of totally-filled FRP tubes
f_{cr}	=	Cracking strength of concrete in tension
f'_{cu}	=	Compressive strength of confined concrete at ultimate
$f_f(i)$	=	Axial stress level in the FRP tube at a general strip i in a concrete-filled FRP tube under bending
f_i	=	Coefficient of Tsai-Wu failure criteria (Used in Chapter 2)
f_i	=	Stress level at a general point i on a stress-strain curve (Used in Chapter 5)

f_{ii}	=	Coefficients of Tsai-Wu failure criteria
f_t	=	Hoop tensile strength of FRP cylindrical jacket
f_r	=	Confinement pressure
f_u	=	Ultimate tensile strength of FRP tube in the axial direction
$f_{u(ten)}$	=	Ultimate tensile strength of FRP tube
$f_{u(comp)}$	=	Ultimate compressive strength of FRP tube
f_y	=	Yielding strength of steel
F_{1c}	=	Longitudinal compressive strength of a lamina
F_{1t}	=	Longitudinal tensile strength of a lamina
F_{12}	=	In-plane shear strength of a lamina
F_{2c}	=	Transverse compressive strength of a lamina
F_{2t}	=	Transverse tensile strength of a lamina
G_m	=	Shear modulus of matrix
G_{12}	=	Shear modulus of a lamina
G_{12f}	=	Shear modulus of fibres
h	=	Thickness of a laminate
$h(i)$	=	Depth of the centroid of a general strip i within the cross-section of concrete-filled tube, measured from the upper mid-thickness level of the tube in the compression side
h_i	=	Thickness of strip within the circular cross-section of concrete-filled tube
h_k	=	The z coordinate of the upper surface of layer k in a laminate
h_{k-1}	=	The z coordinate of the lower surface of layer k in a laminate
H	=	Constant in a linear relationship relating Poisson's ratio of concrete to the axial strain level
I	=	Moment of inertia
I_c	=	Moment of inertia of the concrete core in a circular tube
I_f	=	Moment of inertia of the hollow FRP tube

I_t	=	Transformed moment of inertia of a section
i	=	Identification number of a strip within the cross-section of a concrete-filled FRP tube
k	=	A general layer (ply) within a laminate located at a distance z from the reference plane at mid-thickness of the laminate
k_{ACI}	=	A factor in concrete cracking strength equation based on the ACI code
k_{CEB}	=	A factor in concrete cracking strength equation based on the CEB-FIP code
k_{mean}	=	A factor in concrete cracking strength equation based on the average of experimental results
L	=	Length of a column
$L(i)$	=	Length of the part of the perimeter of the tube in one side within a strip i in a cross-section of a concrete-filled FRP
M	=	Bending moment
M_r	=	Cracking moment of a beam
M_{crit}	=	Critical buckling bending moment of hollow cylindrical tube
M_u	=	Ultimate moment capacity of a beam
MCC	=	Internal moment of the concrete compressive stress resultant in a concrete-filled FRP tube under bending
MCF	=	Internal moment of the compressive stress resultant of the FRP tube in a concrete-filled FRP tube under bending
MTC	=	Internal moment of the concrete tensile stress resultant in a concrete-filled FRP tube under bending
MTF	=	Internal moment of the tensile stress resultant of the FRP tube in a concrete-filled FRP tube under bending
\overline{M}	=	Normalized ultimate moment capacity of a beam
n	=	Number of plies (layers) within a laminate (Used in Chapter 2)
n	=	Number of strips within a the cross-section of concrete-filled FRP tube (Used in Chapter 2)

N	=	In-plane force acting on a laminate
P	=	Load acting on a beam
P_c	=	The axial load sharing of concrete in a concrete-filled tube under compression load
P_f	=	The axial load sharing of the FRP tube in a concrete-filled FRP tube under compression load
P_T	=	Total axial load acting on a concrete-filled tube under axial compression
Q	=	Symbol of the stiffness matrix of FRP laminate
R	=	Average radius of FRP tube
R_c	=	Radius of the central void inside the concrete core of a concrete-filled tube
R_m	=	Average radius of the FRP tube in a concrete-filled FRP tube system with a central void
S_f	=	Safety factor in Tsai-Wu failure criteria of a FRP lamina
t	=	Structural wall thickness of FRP tube
t_c	=	Structural thickness of FRP confining jacket
T	=	Symbol of the transformation matrix relating stresses or strains in local lamina axis (1, 2) to those with respect to the reference laminate axis (x, y) (Used in Chapter 2)
T	=	Hoop tensile force in the FRP tube per unit length (Used in Chapter 4)
TCC	=	Tensile stress resultant in concrete in the tension zone of a concrete-filled FRP tube under bending
$TC(i)$	=	Tension force in concrete in a general strip i in a concrete-filled FRP tube under bending
TFF	=	Tensile stress resultant in the FRP tube in the tension zone of a concrete-filled FRP tube under bending
$TF(i)$	=	Tension force in the FRP tube in a general strip i in a concrete-filled FRP tube under bending
u_r	=	Radial displacement at the interface between the concrete core and the confining jacket

V_f	=	Fibre volume fraction in FRP lamina
V_m	=	Matrix volume fraction in FRP lamina
y	=	Deflection of flexural member
$y(i)$	=	Distance between the neutral axis and a general strip i in the cross-section of a concrete-filled FRP tube under bending
z	=	Distance between a general layer (ply) k and the mid-thickness plane of a composite laminate
Z	=	Neutral axis depth at ultimate of a concrete-filled FRP tube under bending
Z	=	Neutral axis depth at ultimate of a concrete-filled FRP tube under bending provided no slip occurs
Z'	=	Distance between the top surface at maximum compression of concrete-filled FRP tube under bending and the zero stress level of FRP tube at failure. Note that $Z'=Z$ if no slip occurs and $Z'>Z$ if slip takes place
\bar{Z}	=	Normalized neutral axis depth
α_1	=	Factor accounting for the bond characteristics of the reinforcement
α_2	=	Factor accounting for the nature of loading (short term, sustained)
γ_0	=	In-plane shear strain in a FRP lamina
$\varepsilon(i)$	=	Normal strain at a general strip i within the cross-section of concrete-filled FRP tube under bending
ε_a	=	Axial strain in a concrete cylinder under axial compression
ε_h	=	Maximum tensile strain at the bottom fibres of the FRP tube in a concrete-filled FRP tube under bending
ε_{hu}	=	Ultimate axial tensile strain of the FRP tube
ε_c	=	Axial strain level corresponding to a general stress level f_c in axially loaded unconfined concrete
ε'_c	=	Axial strain level corresponding to the peak unconfined strength f'_c in axially loaded unconfined concrete
ε_{cc}	=	Axial strain level corresponding to a general stress level f_{cc} in axially

		loaded confined concrete
ε_{cc}^*	=	Axial strain level corresponding to the peak confined strength f_{cc}^* in axially loaded confined concrete
ε_{cr}	=	Cracking strain of concrete in tension
ε_{cu}	=	Ultimate axial compressive strain of confined concrete
ε_i	=	Strain level corresponding to a general stress level at point i on a stress-strain curve
ε_l	=	Lateral strain in a concrete cylinder under axial compression
ε_r	=	Radial strain in a concrete cylinder under axial compression
ε_t	=	Maximum compressive strain at the top fibres of the FRP tube in a concrete-filled FRP tube under bending
ε_m	=	Ultimate axial compressive strain of the FRP tube
ε_v	=	Volumetric strain of a concrete cylinder under axial compression
ε''	=	In-plane strains in a lamina at the level of the reference plane located at the mid-thickness
ε_τ	=	Hoop tensile strain in FRP tube
ε_ν	=	Axial compressive strain in FRP tube
$\varepsilon_{(axial)}$	=	Axial compressive strain in FRP cylindrical tube
$\varepsilon_{(hoop)}$	=	Hoop tensile strain in FRP cylindrical tube
ε_1	=	In-plane normal strain in a lamina in the direction of the fibres
ε_2	=	In-plane normal strain in a lamina perpendicular to the fibres
θ	=	Angle between the reference axis "x" of a laminate and the local axis "1" of an individual lamina, measured positive in counter-clockwise direction
κ	=	Curvature of a FRP lamina
μ_{max}	=	Maximum dilation ratio of FRP-confined concrete
μ_u	=	Ultimate dilation ratio of FRP-confined concrete
ρ	=	Reinforcement ratio

σ_R	=	Confinement pressure acting on a concrete cylinder in the radial direction
$\sigma_{R_{max}}$	=	Confinement pressure acting on a concrete cylinder in the radial direction at ultimate
σ_{Ro}	=	Sustained radial pressure developed by expansion of concrete inside a FRP tube
$\sigma_{Ro(solid)}$	=	Sustained radial pressure developed by expansion of concrete inside a FRP tube totally filled with concrete
$\sigma_{Ro(vanded)}$	=	Sustained radial pressure developed by expansion of concrete inside a FRP tube partially filled with concrete
σ_c	=	Tensile stress level in the hoop direction in a confining FRP jacket
$\sigma_{c,u}$	=	Ultimate tensile strength in the hoop direction in a FRP jacket
σ_r	=	Tensile stress level in the hoop direction in a confining FRP jacket
$(\sigma_r)_u$	=	Ultimate tensile strength in the hoop direction of a confining FRP jacket
σ_x	=	Compressive stress level in the axial direction in a confining FRP jacket
$(\sigma_x)_u$	=	Ultimate compressive strength in the axial direction of a confining FRP jacket
σ_1	=	In-plane normal stress in a lamina in the direction of the fibres
σ_2	=	In-plane normal stress in a lamina perpendicular to the fibres
τ_6	=	In-plane shear stress in a FRP lamina
ν	=	Poisson's ratio of a FRP jacket, used to estimate the hoop strain due to axial loading
ν_c	=	Poisson's ratio of concrete
ν_{c0}	=	Initial Poisson's ratio of concrete
ν_m	=	Poisson's ratio of matrix
ν_s	=	Poisson's ratio of the confining jacket, used to estimate the hoop strain due to axial loading
ν_{σ}	=	Effective Poisson's ratio of a FRP laminate, used to estimate the strain in y

		direction due to loading in x direction
ν_{1x}	=	Effective Poisson's ratio of a FRP lamina. used to estimate the strain in x direction due to loading in y direction
ν_{12}	=	Major Poisson's ratio of a FRP lamina. used to estimate the lateral strain due to loading in the axial direction. parallel to the fibres
ν_{12f}	=	Poisson's ratio of fibres
$\phi(i)$	=	Angle in radians between the vertical centre line and the radius reaching to the mid-length of the arc $L(i)$ in the cross-section of a concrete-filled FRP tube
$\phi_1(i)$	=	Angle in radians between the vertical centre line and the radius reaching to the beginning of the arc $L(i)$ in the cross-section of a concrete-filled FRP tube
$\phi_2(i)$	=	Angle in radians between the vertical centre line and the radius reaching to the end of the arc $L(i)$ in the cross-section of a concrete-filled FRP tube
ψ	=	Curvature of a section of a beam under bending
$\bar{\psi}$	=	Normalized curvature of a beam under bending at ultimate
ω	=	Reinforcement index

Chapter 1

Introduction

1.1 General

There is a great demand for piling, poles, highway overhead sign structures and bridges to be made of materials that are more durable in comparison to traditional construction materials and systems. The new products have to withstand aggressive corrosive environments, such as the splash zone in case of marine piles, where they would be alternately submerged and exposed [Stapleman 1997]. Similarly, highway overhead sign structures, poles, and bridge columns have to retain their integrity in cold regions where salt is used for de-icing the roads. One promising innovative structural system is concrete-filled fibre reinforced polymer, FRP, cylindrical tubes. The proposed system consists of FRP round tube totally or partially-filled with concrete as shown in Fig. 1.1. The void inside the concrete core, which is intended to reduce the self-weight of the member, could be maintained by a non-structural tube such as a cardboard tube, or by an additional FRP tube to enhance the strength and stiffness. The inner FRP tube could also be concentric in an axisymmetric pattern, which is suited for applications involving loads applied from various directions such as wind pressure, or could be eccentric to provide more reinforcement in the tension side and more concrete in the compression side in beam applications.

The proposed system provides many unique advantages. The FRP tube acts as a stay-in-place structural formwork to contain the fresh concrete, which saves the cost of formworks used in cast-in-place or precast industries. At the same time, the FRP shell acts as a non-corrosive reinforcement for the concrete for flexure and shear, utilizing the multi-direction fibre orientation in the tube, which saves the time and cost of assembling the longitudinal rebars together with the stirrups in conventional fabrication methods. More importantly, the FRP tube provides confinement to the concrete in compression, which significantly improves the strength and ductility of the member. The contained concrete is protected from severe environmental effects and deterioration resulting from freeze-thaw cycles. This system also provides the designers with several flexible parameters, which can be controlled to achieve optimum design for each individual application including type of fibres, orientation of the fibres, number of layers in the composite shell, and the concrete wall thickness. Literature indicated that hollow FRP round tubes fail prematurely in local buckling before the full strength of the material is utilized [Ibrahim 2000]. Therefore, it is strongly believed that the concrete filling, in addition to its contribution to the strength of the section, would provide support for the shell to allow for the development of the full strength of FRP, even for small wall thicknesses.

Fig. 1.2 shows the different potential applications of concrete-filled FRP tubes including marine piles, overhead sign structures, poles and posts [Lancaster Composite Inc.- Composite Post 40], bridge columns and piers, girders, large pipes and tunnels.

1.2 Objectives

The main objective of this study is to examine the structural behaviour of concrete-filled glass fibre reinforced polymer, GFRP, tubes in flexure as beams and under axial compression loads as short columns. The various aspects considered in the study are:

1. Evaluation of the load-deformation response of concrete-filled FRP tubes in bending, shown in Fig. 1.3, in terms of stiffness and strength.
2. Evaluation of the stress-strain response of confined concrete using FRP tubes as compared to that of unconfined concrete as shown in Fig. 1.4.
3. Analytical modelling of axially loaded concrete columns confined by FRP shells.
4. Analytical modelling of concrete-filled FRP tubes as flexural members.
5. Examining the different potential failure modes of both beams and columns.
6. Examining the effects of the following parameters on the behaviour:
 - Effect of concrete filling of tubes as compared to hollow tubes for beams.
 - Different materials including concrete-filled FRP and steel tubes for beams and columns.
 - Different configurations including totally and partially filled tubes for beams and columns.
 - Effect of void size inside the concrete core in columns.
 - Effect of laminate structure of the GFRP tubes in beams and columns
 - Effect of FRP tube/concrete core interface condition in columns
 - Size Effect and reinforcement ratio in beams.
 - Effect of stiffness of the tube on beam and column behaviour

1.3 Scope and Contents

The scope of the study consists of an experimental investigation, and analytical modelling. The experimental program is designed to provide better understanding of the behaviour of concrete-filled FRP tubes in bending and under axial loads, as well as to examine the effects of different parameters. The experimental results of this study, as well as other studies, are used to examine the proposed analytical models. The analytical models are also used in parametric studies to examine larger sets of parameters.

The experimental program includes two phases. The first phase, Phase I, is focussed on the flexural behaviour of concrete-filled FRP tubes. This was achieved by testing the tubes in a simple beam configuration subjected to four-point bending. The study included eighteen beams ranging from 1.07 to 10.4 meters in span and from 89 to 942 mm in diameter. The second phase, Phase II, is designed to evaluate the behaviour of concrete-filled FRP tubes subjected to axial loads as short columns. A total of twelve stubs were included in this phase.

The analytical study is focused on the development of two analytical models. The first model is a variable confinement model capable of predicting the full response of round concrete axial members confined by FRP shells, accounting for the variable confining pressure induced by the FRP shell as well as the material non-linearity of concrete. The second model is a strain compatibility model capable of predicting the full response of concrete-filled FRP tubes subjected to bending using a layer-by-layer approach and also

accounts for the linear FRP material properties as well as the concrete non-linearity. The models are verified by the experimental results and extended to two parametric studies.

The following is a brief description of the contents of this thesis:

Chapter 2: presents literature review related to hybrid FRP/concrete systems in general with more emphasis on concrete-filled FRP tubes. The background of concrete-filled steel tubes is given. The characteristics, properties, and analysis methods of FRP laminates are briefly discussed.

Chapter 3: Describes the experimental program conducted at the University of Manitoba including Phase I for beam tests and Phase II for short column tests.

Chapter 4: Presents the results of the experimental program including the effects of different parameters as well as the failure modes. Discussion of the observed behaviour is also provided.

Chapter 5: Presents the proposed analytical models for predicting the responses of concrete-filled FRP tubes under axial compression and under bending. The models are examined using experimental results. This chapter also presents the parametric studies.

Chapter 6: Provides summary and conclusions of the study. Recommendations for future work are also given in this chapter.

References.

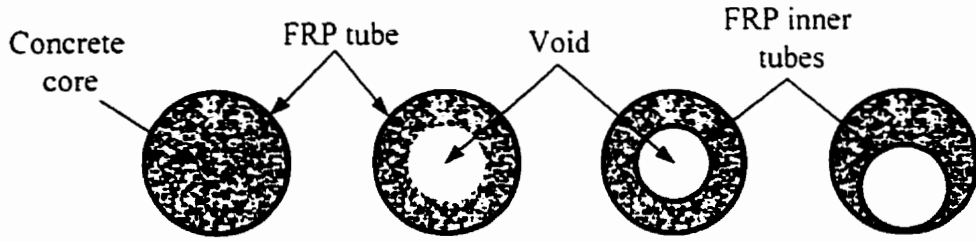


Fig. 1.1 Different configurations of FRP tubes totally and partially filled with concrete

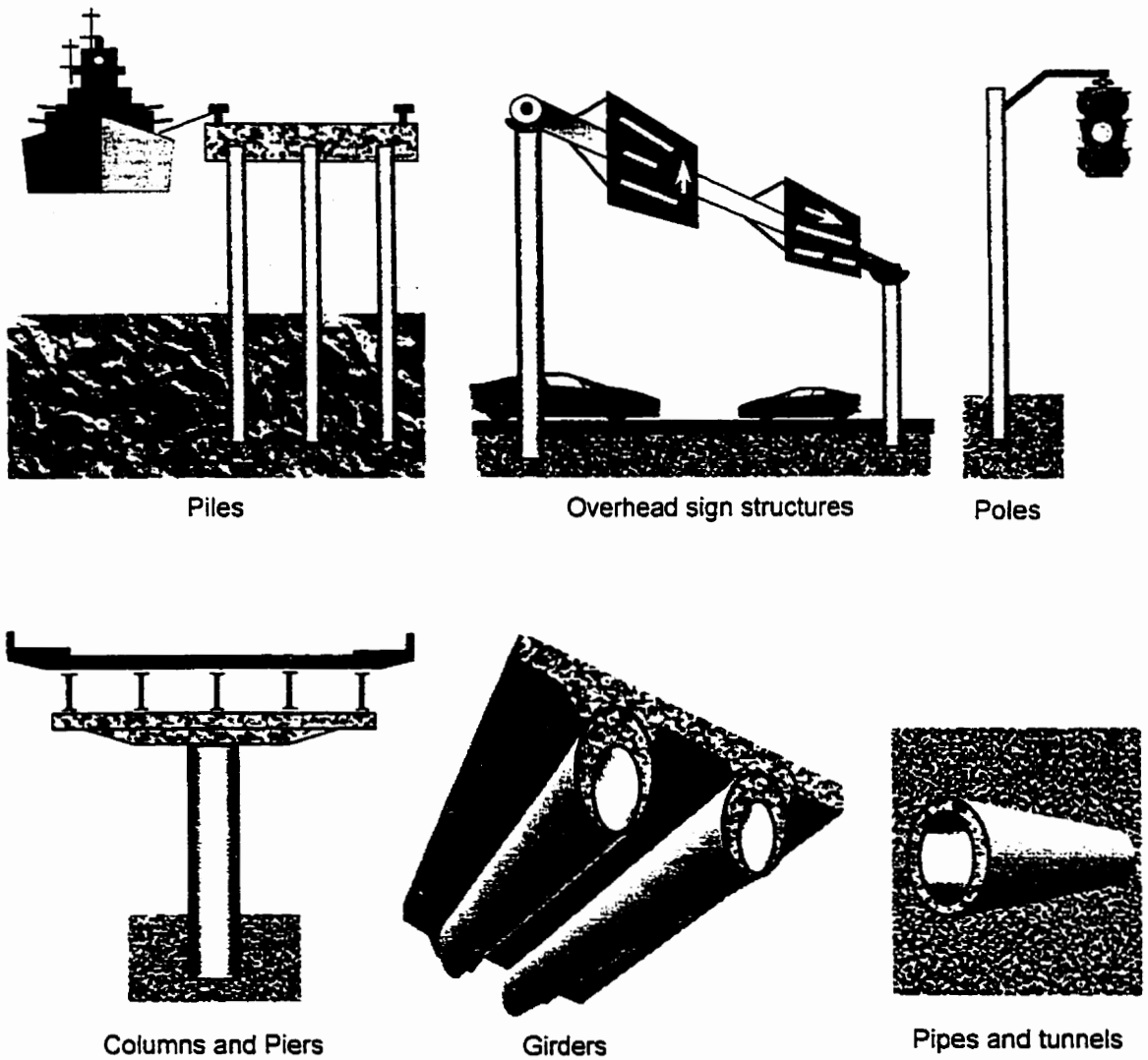


Fig. 1.2 Different structural applications of concrete-filled FRP tubes

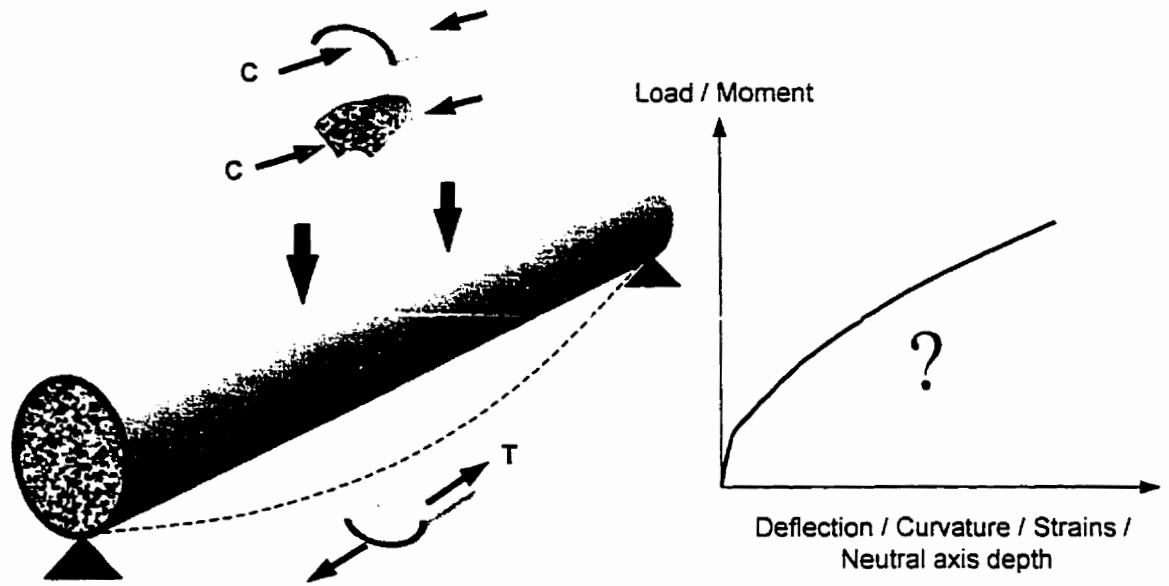


Fig. 1.3 Concrete-filled FRP tubes as flexural members

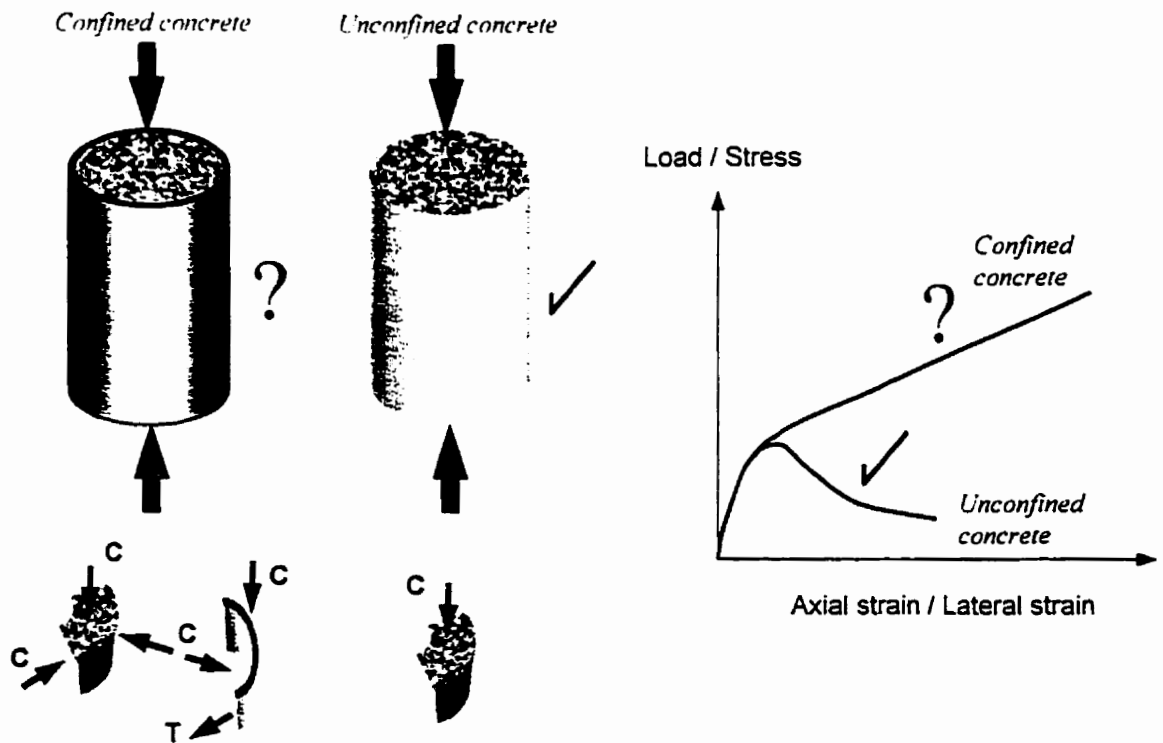


Fig. 1.4 Concrete-filled FRP tubes as axial compression members

Chapter 2

Hybrid FRP/Concrete Structural Members - Background and Review

2.1 Introduction

Fibre reinforced polymers, FRPs, have been widely used in recent years for strengthening and repair of existing structures such as seismic retrofit and service load strengthening. Their use to date in new structural systems is limited to few projects [Fam et al 1997]. In most cases FRPs are used in the form of a structural component replacement such as FRP tendons or rebars for steel ones, or FRP I-beam for steel I-beam, which might not necessarily be cost effective. The advantages of FRPs for civil engineering applications such as the lightweight and high strength can be utilized in various hybrid FRP/concrete new structural systems such as the concrete-filled FRP round tubes or other hybrid systems. The concrete-filled FRP tube system utilizes the best characteristics of the individual materials. The concrete core support the FRP tube and prevents premature local buckling failure experienced in hollow tubes [Ibrahim 2000], while the tube confines the concrete and increases its strength and ductility. The concrete-filled tube system also simplifies construction procedures, and reduces erection time. The concept of Concrete-filled FRP tubes was developed for two different purposes. The development of non-corrosive piles for marine environments is to replace the reinforced, prestressed, and concrete-filled steel tube piles [Lancaster Composite, INC.-Marine

Piling]. [Mirmiran and Shahawy 1996]. and [Parvathaneni et al 1996]. The concrete filling also significantly enhances the ductility of the tubes. therefore. they can be used as bridge columns and piers in seismic zones [Seible 1996] and [Seible et al 1998].

This chapter summarizes the developments of different hybrid FRP/concrete structural systems with more emphasis on the concrete-filled FRP round tubes in particular. A brief discussion about concrete-filled steel tubes is introduced since it has been developed and used for some time and research findings in this area are useful. FRP composite laminates used to fabricate FRP tubes. which forms the backbone of the concrete-filled tubular members. are also discussed including manufacturing process and mechanics. The tubes act as the reinforcement of the member and the formwork at the same time.

2.2 Fibre Reinforced Polymer (FRP) Laminates

Fibre reinforced polymers, FRP. refer to composite materials consisting of two phases including a dispersed phase, reinforcement, and a continuous phase. matrix. The dispersed phase is usually continuous-fibre reinforcement. which is the load-carrying element of the composite material, which controls the stiffness and strength. The matrix phase provides protection and support for the sensitive fibres as well as local stress transfer from one fibre to another. The continuous fibres can be all parallel (unidirectional continuous fibre composites), can be oriented at right angle to each other (cross ply or woven fabric continuous fibre composites), or can be oriented along several directions (multi-directional continuous fibre composites). Polymer matrix composites include thermoset (epoxy, polyimide, polyester) or thermoplastic (poly-ether-ether-

ketone, polysulfone) resins reinforced with glass (GFRP), carbon (CFRP), aramid (AFRP), or boron fibres (BFRP) [Daniel and Ishai 1994].

A lamina or a ply is a plane or curved layer of unidirectional fibres or woven fabric in a matrix. The lamina is considered an orthotropic material with principal material axes (1, 2, and 3) as shown in Fig. 2.1a. A laminate is made up of two or more unidirectional laminae or plies stacked together at various orientations. Since the principal material axes differ from one ply to another, it is more convenient to analyze laminates using a common fixed system of coordinates (x , y , and z) as shown in Fig. 2.1b. The orientation of a given ply is given by the angle between x -axis and principal axis-1 of the ply, measured positive in a counter clockwise direction. The configuration of the laminate indicating its ply composition and exact location or sequence of various plies is called stacking sequence. A laminate is symmetric when for each layer on one side of the middle surface there is a corresponding layer at an equal distance from that reference plane on the other side with identical thickness, orientation and properties. In addition, a laminate is called balanced when it consists of pairs of layers with identical thickness and elastic properties but have $+\theta$ and $-\theta$ orientations with respect to the laminate reference axes [Daniel and Ishai 1994].

2.2.1 Fabrication Process

A variety of fabrication methods suitable for different applications are available. They include autoclave molding, filament winding, pultrusion, and resin transfer molding. Filament winding technique, however, is the most common process used to produce

hollow tubular sections. Filament winding was invented in 1946 and incorporated into missile applications in the 1950s [Daniel and Ishai 1994]. The technique is generally used to produce hollow symmetrical products such as pipes, tanks, rocket motors, or any element not containing concave geometry. A mandrel of the required shape is rotated on its axis, and wound with a continuous filament of reinforcement, which is passed through a resin bath immediately before contact with the laminate as shown in Fig. 2.2. When fully wound with resin-wetted reinforcement, the lay-up is cured, on or off the mandrel. The reinforcement in many cases consists of a band of several rovings. The band may be positioned perpendicular to the axis of the mandrel (circumferential winding) or inclined at an angle relative to the axis (helical winding). The process is capable of great flexibility in type, mix, density, and direction of winding and normally high fibre volume (60-75%) are obtained. Winding can be done with dry fibres which are impregnated with resin during the winding process (wet winding), or with fibres encapsulated in a semi-hardened resin (prepreg winding). In some cases the part is wound dry and then the entire part is impregnated under pressure. Filament winders are typically computer-controlled and application software allows the process and winding patterns to be simulated first before winding [Carrino et al 1998]. Winder sizes range from small tabletop machines to giants capable of winding parts of up to 9 meters diameter and 46 meter length. The mandrel is essentially light but stiff to avoid sagging, with dimensional accuracy and smooth surface to facilitate extraction of the wound parts [Murphy 1998].

2.2.2 Mechanics of Composite Laminates

The following sections summarize the constitutive relationships governing the analysis of composite laminates and relating the different stress and strain components through the material constants. Also the failure criteria governing the laminate strength is introduced [Daniel and Ishai 1994].

2.2.2.1 Elastic behaviour of unidirectional lamina

A thin unidirectional lamina is assumed to be under a state of plane stress. The in-plane stresses and strains along the principal material axes are related as follows:

$$\begin{bmatrix} \sigma_1 \\ \sigma_2 \\ \tau_{12} \end{bmatrix} = \begin{bmatrix} \frac{E_1}{1-\nu_{12}^2 E_2/E_1} & \frac{\nu_{12} E_2}{1-\nu_{12}^2 E_2/E_1} & 0 \\ \frac{\nu_{12} E_2}{1-\nu_{12}^2 E_2/E_1} & \frac{E_2}{1-\nu_{12}^2 E_2/E_1} & 0 \\ 0 & 0 & G_{12} \end{bmatrix} \begin{bmatrix} \varepsilon_1 \\ \varepsilon_2 \\ \gamma_{12} \end{bmatrix}$$

Or in brief,
$$[\sigma]_{1,2} = [Q]_{1,2} [\varepsilon]_{1,2} \quad (2.1)$$

Where $[Q]_{1,2}$ is the stiffness matrix with respect to the lamina local axis in terms of the engineering constants. E_1 and E_2 are the Young's moduli in direction of the fibres and in the transverse direction respectively. G_{12} and ν_{12} are the shear modulus and the major Poisson's ratio respectively. The lamina engineering constants are given in terms of the fibres and matrix properties using the rule of mixture as follows:

$$\begin{aligned} E_1 &= V_f E_{1f} + V_m E_m & \frac{1}{E_2} &= \frac{V_f}{E_{2f}} + \frac{V_m}{E_m} \\ \frac{1}{G_{12}} &= \frac{V_f}{G_{12f}} + \frac{V_m}{G_m} & \nu_{12} &= V_f \nu_{12f} + V_m \nu_m \end{aligned} \quad (2.2)$$

Where $E_{1,}$ and $E_{2,}$ are the axial and transverse elastic moduli of the fibres. E_m is the elastic modulus of the matrix. $G_{12,}$ and G_m are the shear moduli of the fibres and matrix respectively. $\nu_{12,}$ and ν_m are the Poisson's ratios of fibres and matrix respectively. V_f and V_m are the fibre and matrix volume fractions respectively.

Normally the lamina principal axes (1, 2) do not coincide with the loading axes (x, y) as shown in Fig. 2.1b. Therefore, the strain and stress components referred to the (1, 2) axes can be expressed in terms of those referred to the (x, y) axes through the transformation matrix $[T]$ as follows:

$$[\sigma]_{1,2} = [T][\sigma]_{x,y} \quad (2.3)$$

$$[\varepsilon]_{1,2} = [T][\varepsilon]_{x,y} \quad (2.4)$$

$$[T] = \begin{bmatrix} \cos^2 \theta & \sin^2 \theta & 2 \cos \theta \sin \theta \\ \sin^2 \theta & \cos^2 \theta & -2 \cos \theta \sin \theta \\ -\cos \theta \sin \theta & \cos \theta \sin \theta & \cos^2 \theta - \sin^2 \theta \end{bmatrix} \quad (2.5)$$

Where θ is the angle between the reference axis x and the local axis 1, measured positive in counter-clockwise direction.

The stresses and strains with respect to the reference axis (x, y) are related as follows:

$$[\sigma]_{x,y} = [Q]_{x,y} [\varepsilon]_{x,y} \quad (2.6)$$

Where $[Q]_{x,y}$ is the transformed stiffness matrix of the lamina, which is given as follows:

$$[Q]_{x,y} = [T^{-1}] [Q]_{1,2} [T] \quad (2.7)$$

From which, the transformed engineering constants can be obtained as a function of the basic engineering constants of the lamina and the angle between the principal and reference axes l and x .

2.2.2.2 Elastic behaviour of multidirectional laminates

The overall behaviour of a multidirectional laminate is a function of the properties and stacking sequence of the individual layers. From Equation 2.6, the stress-strain relationship of a single layer, k , is given as follows:

$$[\sigma]_{x,y}^k = [Q]_{x,y}^k [\varepsilon]_{x,y}^k \quad (2.8)$$

The strains $[\varepsilon]_{x,y}^k$ at any layer within the thickness are related to the strain at the reference plane (x - y) which is located at mid-thickness, $[\varepsilon^0]_{x,y}$, as follows:

$$[\varepsilon]_{x,y}^k = [\varepsilon^0]_{x,y} + z[\kappa]_{x,y} \quad (2.9)$$

Where z is the distance from the reference plane to the layer k , and $[\kappa]_{x,y}$ is the curvature vector of the laminate. From Equations 2.8 and 2.9:

$$[\sigma]_{x,y}^k = [Q]_{x,y}^k [\varepsilon^0]_{x,y} + z [Q]_{x,y}^k [\kappa]_{x,y} \quad (2.10)$$

For an n -ply laminate, shown in Fig. 2.3a, the total force and moment resultants are obtained by summing the stress integrals, shown in Fig. 2.3b over the thickness as follows:

$$\begin{aligned} [N]_{x,y} &= \sum_{k=1}^n \int_{h_{k-1}}^{h_k} [\sigma]_{x,y}^k dz = \left[\sum_{k=1}^n [Q]_{x,y}^k \int_{h_{k-1}}^{h_k} dz \right] [\varepsilon^0]_{x,y} + \left[\sum_{k=1}^n [Q]_{x,y}^k \int_{h_{k-1}}^{h_k} z dz \right] [\kappa]_{x,y} \\ &= [A]_{x,y} [\varepsilon^0]_{x,y} + [B]_{x,y} [\kappa]_{x,y} \end{aligned} \quad (2.11)$$

$$\begin{aligned}
[M]_{x,y} &= \sum_{k=1}^n \int_{h_{k-1}}^{h_k} [\sigma]_{x,y}^k z dz = \left[\sum_{k=1}^n [Q]_{x,y}^k \int_{h_{k-1}}^{h_k} z dz \right] [\varepsilon'']_{x,y} + \left[\sum_{k=1}^n [Q]_{x,y}^k \int_{h_{k-1}}^{h_k} z^2 dz \right] [\kappa]_{x,y} \\
&= [B]_{x,y} [\varepsilon'']_{x,y} + [D]_{x,y} [\kappa]_{x,y}
\end{aligned} \quad (2.12)$$

From Equation 2.11 and 2.12, forces and moments are related to strains and curvatures through the stiffness matrix as follows:

$$\begin{bmatrix} N_x \\ N_y \\ N_s \\ M_x \\ M_y \\ M_s \end{bmatrix} = \begin{bmatrix} A_{xx} & A_{xy} & A_{xs} & B_{cx} & B_{cy} & B_{cs} \\ A_{yx} & A_{yy} & A_{ys} & B_{yx} & B_{yy} & B_{ys} \\ A_{sx} & A_{sy} & A_{ss} & B_{sx} & B_{sy} & B_{ss} \\ B_{cx} & B_{cy} & B_{cs} & D_{cx} & D_{cy} & D_{cs} \\ B_{yx} & B_{yy} & B_{ys} & D_{yx} & D_{yy} & D_{ys} \\ B_{sx} & B_{sy} & B_{ss} & D_{sx} & D_{sy} & D_{ss} \end{bmatrix} \begin{bmatrix} \varepsilon_x'' \\ \varepsilon_y'' \\ \gamma_s'' \\ \kappa_x \\ \kappa_y \\ \kappa_s \end{bmatrix} \quad (2.13)$$

Where A_{ij} , B_{ij} , and D_{ij} correspond to membrane, coupling and bending stiffness coefficients and are defined as follows:

$$A_{ij} = \sum_{k=1}^n Q_{ij}^k (h_k - h_{k-1}) \quad B_{ij} = \frac{1}{2} \sum_{k=1}^n Q_{ij}^k (h_k^2 - h_{k-1}^2) \quad D_{ij} = \frac{1}{3} \sum_{k=1}^n Q_{ij}^k (h_k^3 - h_{k-1}^3) \quad (2.14)$$

With $i, j = x, y, s$. h_k and h_{k-1} are the z coordinate of the upper and lower surface of layer k . For symmetric laminates $B_{ij} = 0$, therefore there is no coupling between the in plane loading and curvatures or between the moments and in-plane strains.

Equation 2.13 can be inverted to establish a relationship between strains and stresses as follows:

$$\begin{bmatrix} \varepsilon_x'' \\ \varepsilon_y'' \\ \gamma_{xy}'' \\ \kappa_x \\ \kappa_y \\ \kappa_z \end{bmatrix} = \begin{bmatrix} a_{xx} & a_{yy} & a_{xy} & b_{xx} & b_{yy} & b_{xy} \\ a_{yx} & a_{xx} & a_{xy} & b_{yx} & b_{xx} & b_{xy} \\ a_{xx} & a_{yy} & a_{xy} & b_{xx} & b_{yy} & b_{xy} \\ c_{xx} & c_{yy} & c_{xy} & d_{xx} & d_{yy} & d_{xy} \\ c_{yx} & c_{yy} & c_{xy} & d_{yx} & d_{yy} & d_{xy} \\ c_{xx} & c_{yy} & c_{xy} & d_{xx} & d_{yy} & d_{xy} \end{bmatrix} \begin{bmatrix} N_x \\ N_y \\ N_{xy} \\ M_x \\ M_y \\ M_z \end{bmatrix} \quad (2.15)$$

It is, however, convenient to use the effective laminate engineering constants in theoretical analysis including the elastic moduli in x and y directions, E_x and E_y , as well as the Poisson's ratio ν_{xy} , based on Equation 2.15 as follows:

$$E_x = \frac{1}{h a_{xx}} \quad E_y = \frac{1}{h a_{yy}} \quad \nu_{xy} = -\frac{a_{yx}}{a_{xx}} \quad (2.16)$$

Where h is the thickness of the laminate.

2.2.2.3 Strength of unidirectional laminae

Failure mechanisms and processes vary with type of loading and are intimately related to the properties of the constituents, which are the fibres, matrix, and the interface. Under longitudinal tension, the phase with the lower ultimate strain, whether the fibres or the matrix, will fail first. Under longitudinal compression, failure is assumed to be associated with microbuckling or kinking of the fibres within the matrix. The most critical loading of a unidirectional composite is transverse tensile loading as it results in high stress and strain concentrations at the interface, which usually governs the strength. Under transverse compression, stress concentration at the interface may cause compressive failure in the matrix and/or fibre crushing, matrix shear failure and/or debonding, leading to an overall shear failure. Under in-plane shear, high shear stress

concentration develops at the fibre-matrix interface, which causes shear failure in the matrix and/or fibre-matrix debonding. A lamina, therefore, may be characterized by five strength parameters F_{1t} , F_{1c} , F_{2t} , F_{2c} , and F_{12} , which are the longitudinal tensile and compressive strengths, the transverse tensile and compressive strengths, and the in-plane shear strength respectively. Different failure theories have been developed. The Tsai-Wu failure criterion [Daniel and Ishai 1994] is widely used because it accounts for the interaction between different stress components. Tsai and Wu proposed a tensor polynomial theory by assuming the existence of a failure surface in the stress space. The reduced form of the Tsai-Wu criterion is:

$$f_1\sigma_1 + f_2\sigma_2 + f_{11}\sigma_1^2 + f_{22}\sigma_2^2 + f_{66}\tau_6^2 + 2f_{12}\sigma_1\sigma_2 = 1 \quad (2.17)$$

Where σ_1 , σ_2 , and τ_6 are the applied in-plane normal and shear stresses. The coefficient f_i and f_{ij} are defined in terms of the strength parameters as follows:

$$\begin{aligned} f_1 &= \frac{1}{F_{1t}} - \frac{1}{F_{1c}} & f_2 &= \frac{1}{F_{2t}} - \frac{1}{F_{2c}} & f_{66} &= \frac{1}{F_{12}^2} \\ f_{11} &= \frac{1}{F_{1t}F_{1c}} & f_{22} &= \frac{1}{F_{2t}F_{2c}} & f_{12} &= -\frac{1}{2}(f_{11}f_{22})^{1/2} \end{aligned} \quad (2.18)$$

The failure envelope described by Equation 2.17 is a closed surface in the σ_1 , σ_2 , τ_6 space. Fig. 2.4 illustrates the failure envelopes for different constant values of shear stress τ_6 . The theory is used to determine the safety factor S_f for a given state of stress (σ_1 , σ_2 , and τ_6). The safety factor is a multiplier that is applied to all stress components to produce a failure state as follows:

$$f_1S_f\sigma_1 + f_2S_f\sigma_2 + f_{11}S_f^2\sigma_1^2 + f_{22}S_f^2\sigma_2^2 + f_{66}S_f^2\tau_6^2 + 2f_{12}S_f^2\sigma_1\sigma_2 = 1 \quad (2.19)$$

The safety factor can be determined by solving the following quadratic:

$$aS_1^2 + bS_1 - 1 = 0 \quad (2.20)$$

Where: $a = f_{11}\sigma_1^2 + f_{22}\sigma_2^2 + f_{66}\tau_6^2 + 2f_{12}\sigma_1\sigma_2$ and $b = f_1\sigma_1 + f_2\sigma_2$

The transformed lamina strength in x-direction is calculated by introducing a unit applied normal stress in the x direction, $\sigma_x = 1.0$ and all other stresses are set to zero. Then the roots of the quadratic equation will give both, the tensile and compressive strength components in x-direction. Same procedure can be repeated for the normal strength in y-direction as well as the shear strength.

2.2.2.4 Strength of multidirectional laminates

The laminate strength is a function of many factors including the strength parameters of the laminae, stiffness, stacking sequence, orientations of laminae, and fabrication process, which affect the residual stresses. Three different types of failure can be defined. In the initial or first-ply failure (FPF), the laminate is considered failed when the first layer fails. In the ultimate laminate failure (ULF), the laminate is considered failed when the maximum load level is reached or exceeded, following multi-layer failure. In the interlaminar failure, failure is a result of separation between layers even when the layers themselves remain intact. The first two definitions represent two levels in the failure process, the initial and the ultimate, which are analogous to the yield and ultimate stress criteria in steel. The following discussion is focussed on the first two types of failure.

Given a multidirectional laminate under a general loading condition $[N, M]_{x,y}$, the following procedure is followed to compute the safety factor and strength components using the FPF and Tsai-Wu criterion:

1. The stiffness matrix of each layer k , $[Q]_{1,2}$ given in is obtained using Equation 2.1
2. The transformed stiffness matrix of each layer k , $[Q]_{x,y}$ is obtained using Equation 2.7
3. The stiffness sub-matrices $[A]$, $[B]$, and $[D]$ are calculated from Equations 2.14
4. The global compliance sub-matrices $[a]$, $[b]$, $[c]$, and $[d]$, given in Equation 2.15 are obtained from the inverse of the global stiffness matrix in Equation 2.13
5. Given the state of loading $[N, M]_{x,y}$, the reference plane strains $[\varepsilon^0]_{x,y}$ and curvatures $[\kappa]_{x,y}$ are obtained using Equation 2.15
6. The strains referred to (x, y) axis, $[\varepsilon]_{x,y}$ are calculated for any layer k using Equation 2.9, then transformed to the layer principal axes $(1, 2)$, $[\varepsilon]_{1,2}$ using Equation 2.4
7. For each layer k the stresses, $[\sigma]_{1,2}$ are calculated as follows using Equation 2.1
8. In the FPF approach, the Tsai-Wu criterion (Equations 2.19 and 2.20) is applied to each layer, and the laminae safety factors are obtained.
9. The minimum safety factor of all laminae is considered as the laminate safety factor.
10. The laminate strength components are obtained by applying unit stress in the respective direction of each component.

It should be noted that the layer that fails first in a laminate depends on the state of stress. Whereas the failure envelope for any given layer is a continuous surface, the failure surface for a laminate based on FPF is discontinuous, consisting of portions of envelopes of individual layers.

In most cases failure in a multidirectional laminate is initiated in the layers with the highest stress normal to the fibres. Failure initiation takes the form of distributed micro cracks, which merge into macro cracks extending across the thickness of the layer,

constituting the state of FPF. The failure process continues up to ULF level, which could occur at a much higher load than FPF. The ultimate strength of a laminate is determined through the following steps:

1. The load required to produce FPF is determined from the lamina stresses
2. The failed lamina or laminae are replaced with laminae of reduced stiffnesses or the affected stiffnesses could be discounted completely. New laminate stiffnesses $[A]$, $[B]$, and $[D]$ are then calculated
3. Lamina stresses are recalculated and checked against the selected failure criterion to ensure that the undamaged laminae do not fail immediately under their increased share of stress following the FPF
4. The load is increased until the next ply fails and steps 1, 2, and 3 are repeated
5. When the remaining undamaged laminae, at any stage of progressive ply failures, cannot sustain the stresses, ultimate failure of the laminate occurs

2.3 Background of Concrete-Filled Steel Tubular Members

The first recorded use of concrete-filled tubes as columns was by Sewell in 1901 [Gardner, and Jacobson 1967]. Sewell's motives were to use the concrete only to resist internal rusting of steel box columns. However, after some of these columns had been accidentally overloaded, Sewell concluded that the stiffness had been increased by at least 25 percent compared to that of hollow sections. It has also been shown that the steel tube acts as permanent formwork, and provides well-distributed reinforcement located at the most efficient position [Furlong 1967, Gardner and Jacobson 1967, Prion and Boehme 1994, and Kilpatrick and Rangan 1997]. The concrete core forces the local

buckling of the steel tube into a higher order mode, by buckling outwards rather than inwards, resulting in a higher critical buckling load. This can be utilized in using thinner walls, which can reach the yielding strength before local buckling [Lu and Kennedy 1992 and Wei et al 1995]. The steel tube confines the concrete laterally, which provides a tri-axial state of stress for concrete under compression. This allows the concrete to sustain higher stresses and strains and to have large capacity for plastic flow, which improves the ductility. Filling the tube with concrete increases the ultimate bending strength by about 10-30 percent and also increases the initial flexural stiffness and ductility [Lu and Kennedy 1992] with insignificant increase in cost, and without any increase in size. Moreover, circular sections provide uniform flexural strength and stiffness in all directions. Due to the large shear capacity of concrete-filled steel tubular members, they predominantly fail in flexure in a ductile manner [Tomii and Sakino 1979]. The system is suited for pre-cast industry, where close-shop control of concrete casting permits use of high strength concrete, or expansive cement, which enhances the level of confinement and provides chemically prestressed elements [Furlong 1967 and Bertero and Moustafa 1970]. A number of disadvantages, however, have been pointed out including the low fire resistance, corrosion of steel tubes, and high cost of floor-to-column connections.

Concrete-filled steel tubes have been utilized in columns supporting platforms in offshore structures, columns supporting roofs of storage tanks, bridge piers, piles, and in general as columns in structures located in earthquake zones due to their superior ductility [Kilpatrick and Rangan 1997]. Recently, a 60 m span space-truss pedestrian bridge was constructed in Quebec, Canada, utilizing High-performance Reactive Powder Concrete, RPC, with steel fibres, confined and pressed in steel tubes which were used as the

diagonal members of the trussed bridge. The compressive strength of the confined and pressed RPC reached 375 MPa [Dallaire et al 1998]. Palbol et al (1998) reported about a unique hybrid pipes consisting of hollow concrete core encased inside steel tube, which is circumferentially prestressed using steel wire and later covered by mortar. In 1987, Narayanan et al proposed an innovative double-skin composite construction for submerged tube tunnels, where concrete is sandwiched between two tubular steel sections.

In 1967, Furlong showed that when a concrete-filled circular steel tube is loaded in compression, where the load is applied to both steel and concrete, at axial strain levels less than 0.001, the steel tube has no confining effect since Poisson's ratio of concrete, 0.15~0.25, is lower than that of steel, 0.283, which rather tends to separate. As loading increases, lateral expansion of unconfined concrete approaches that of steel as micro cracking of the concrete increases and Poisson's ratio reaches up to 0.6. Consequently, a radial pressure develops at the steel-concrete interface, thereby, restraining the concrete core and setting up hoop tension in the tube. Normally, after the unconfined cylinder strength is attained, concrete would tend to spall and disintegrate in the absence of the confining jacket. However, if the jacket buckles before strains are large enough to develop the unconfined cylinder strength, the full strength of concrete cannot be utilized. It was reported that concrete begins to increase in volume at a strain level of about 0.002 [Knowles and Park 1969] and confinement is activated at stress level of 95 percent of the concrete strength [Prion and Boehme 1994]. At this stage, the concrete is stressed tri-axially and the tube bi-axially. The interaction between the tube and the core results in a

synergistic effect where the capacity of the composite column exceeds the sum of the individual strengths of steel and concrete [Kilpatrick and Rangan 1997]. Prion and Boehme (1994) reported that the confining level is higher if the axial load is applied to the concrete only as the steel shell will not expand laterally and keep in contact with concrete. However, in practice, bond stresses and friction cause longitudinal strain in steel, which also reduces the yield strength in both directions.

Different researchers have concluded that the confinement effectiveness is reduced much by using rectangular or square tubes, by using high strength concrete, by increasing the slenderness of columns or under pure bending [Furlong 1967, Kennedy and MacGregor 1984, Schneider 1998, Kilpatrick and Rangan 1997, Knowles and Park 1969, Prion and Boehme 1994, Barber et al 1987, and Lu and Kennedy 1992].

Kennedy and MacGregor (1984) have studied the load transfer mechanism and bond effects. Prion and Boehme studied the effect of cyclic loading in 1994. Long term effects such as creep and shrinkage have been studied by Kilpatrick and Rangan in 1997. Chemical and mechanical prestressing have also been studied by Bertero and Moustafa in 1970. The concept of tube-in-tube with concrete filling in between was demonstrated by Wei et al in 1995. Design guidelines of concrete-filled steel tubular sections are given in Clause 18 of the *CAN/CSA-S16.1-94*.

2.4 Concrete-Filled FRP Tubes as Axial Compression Members

With the development of different FRP manufacturing technologies such as the filament winding techniques, tubular FRP sections of various shapes and laminate structures became available for the construction industry. FRP jackets, other than being much lighter than steel jackets and non-corrosive, provide other advantages from the structural point of view. Its low modulus of elasticity forces concrete to take most of the axial load, therefore, allowing the shell to be utilized more in the hoop direction rather than failing prematurely by outward local buckling in the axial direction. Unlike steel jackets, the FRP expansion in the hoop direction due to axial load is less than that of concrete at the early stage of loading for most laminates. This results in eliminating any separation or delay of the confinement process. Also the orthotropic laminate structure of FRP shells allows uncoupling of the two fibre orientations for design optimization as reported by Shahawy and Mirmiran (1998).

Attempts to confine concrete with non-metallic shells started in the late 1970s. In 1978, Kurt suggested using commercially available plastic pipes (PVC or ABS) filled with concrete. The goal of the study was to evaluate the increase in strength of short columns and the influence of slenderness ratio on the ultimate strength. The improvement in strength was quantified in terms of the confined compressive strength with respect to the ultimate confining pressure of the plastic pipe. The average ratio was 3.25. For a slenderness ratio less than 20, failure of such columns was by 45 degrees shear, in both the plastic pipe and the concrete core. This failure mode resulted from the combination of

vertical compression and hoop tension in the pipe. Because the plastic materials were neither very strong nor very stiff, the increase in strength due to confinement was small.

Fardis and Khalili (1981) reported about concrete encased in fibreglass-reinforced plastic, which is believed to be one of the earliest attempts to utilize structural composites for confinement. They pointed out that the role of hoop fibres is to confine the concrete, whereas that of axial fibres is to take any tension caused by bending and to improve buckling resistance by increasing the flexural rigidity. They also pointed out that the hoop stiffness of the FRP tube controls lateral strains and micro cracking in the concrete core and that the failure of the system is governed by failure of the shell in the hoop direction. Although the authors wrapped the cylinders with GFRP cloth impregnated with resin, they proposed using filament wound tubes to achieve about 80 percent fibre volume fraction, rather than 50 percent, in the composite shell. The study concluded that confinement using FRP jackets resulted in a very high increase in strength and ductility. A 1.9 mm thick GFRP jacket increased both the strength and ductility of the 102 mm diameter concrete cylinder by 5 and 8.5 times respectively.

In 1997, Mirmiran and Shahawy reported the results of twenty-four 152.5x305 mm concrete-filled GFRP round tubes and 6 plain concrete specimens. The unconfined concrete strength was 30 MPa. Six, ten and fourteen layers-GFRP tubes were used. The wall thicknesses were 1.3, 2.1 and 3.0 mm. The shells were filament-wound angle plies of polyester resin and unidirectional E-glass fibres at ± 15 degrees hoop winding angle. The jacket hoop strengths ranged from 524 to 641 MPa respectively, and the elastic

moduli from 37.2 to 40.7 GPa respectively. To prevent interaction between the jacket and the concrete in the axial direction, a 5 mm thick groove was cut through the thickness of the shell on both ends of each tube at about 19 mm from the edge. Both axial and transverse strains were measured during axial loading. Fig. 2.5 shows the normalized stress-strain curves of the confined concrete with different jacket thicknesses. The behaviour indicates significant improvement in strength and ductility. The response consists of three distinct regions. In the first region, behaviour is similar to plain concrete, since lateral expansion of the core is insignificant. With the increase of micro cracks, a transition zone is observed where the tube exerts a lateral pressure on the core to counteract the stiffness degradation of concrete. Finally, a third region is recognized, where the tube is fully activated and the stiffness is stabilized around a constant rate. The slope in this region is mainly dependent on the stiffness of the tube while the ultimate peak strength is dependent on the hoop strength of the shell.

Kanathrana and Lu (1998) showed that when FRP pultruded tubes are used as concrete-filled specimens under compression, the tubes would split immediately once the concrete starts to excessively increase in volume at the unconfined concrete strength level. This is attributed to the lack of stiffness in the hoop direction. They also pointed out the advantages of filament-wound tubes in this regard.

2.4.1 Comparison between Steel and FRP-Confined Concrete

The stress-strain behaviour of concrete-filled GFRP tubes is compared to that of concrete-filled steel tubes in Fig. 2.6 [Samaan et al 1998]. Because of its high modulus,

the steel jacket starts to confine the concrete at low load levels if only loaded in the hoop direction, as only a small lateral strain in concrete is needed to develop significant hoop stresses and result in a noticeable confining pressure. On the other hand, GFRP-confined concrete is insensitive to small lateral expansion, therefore, it behaves very similar to unconfined plain concrete up to the unconfined strength, mainly due to the low hoop modulus of GFRP jackets. As the unconfined strength is approached, major micro cracking develops and high lateral expansion occurs resulting in activation of the FRP jacket, which induces variable confining pressure, continuously increasing due to the linear FRP characteristics. Once the jacket reaches the hoop strength, it ruptures and the concrete fails. This is totally different from the behaviour of the steel jacket, which induces a constant confining pressure, independent of the lateral expansion of concrete, once the steel yields at low strain level [Mirmiran 1995]. Another way of comparing steel-confined concrete to FRP-confined concrete is to examine the volumetric strain as well as the dilation behaviour as shown in Fig. 2.7 and Fig. 2.8 [Samaan et al 1998]. The volumetric strain ε_v is defined as:

$$\varepsilon_v = \varepsilon_a + \varepsilon_l + \varepsilon_r = \varepsilon_a + 2\varepsilon_l \quad (2.21)$$

Where ε_a , ε_l , and ε_r are the axial, hoop and radial strains. For plain concrete, as observed in Fig. 2.7, the volumetric strain reflects compaction and volume reduction at the beginning due to bond cracks closure. Poisson's ratio at this stage is constant, 0.15 to 0.2 for most cases as shown in Fig. 2.8. At about $0.5 f'_c$, Poisson's ratio increases due to lateral expansion resulting from initiation of micro cracking till it reaches 0.5 at about $0.9 f'_c$. At this point the concrete reaches its minimum possible bulk, and starts to increase in volume rapidly and Poisson's ratio can reach more than 0.7 [Avram et al

1981]. For steel-confined concrete, the steel shell effectively confines the concrete and controls the dilation as long as it is elastic. Once it is yielded, concrete dilation becomes unstable as shown in Fig. 2.8. The dilation rate of FRP-confined concrete, on the other hand, displays a different response. Despite some volume expansion beyond the critical stress level, the linearly increasing hoop stress of FRP reduces the expansion according to the stiffness of the FRP tube and reverses its direction as shown in Fig. 2.7 and Fig. 2.8. The dilation ratio, μ , represents the rate of change of lateral strain with respect to axial strain. Fig. 2.8 shows that all three curves start at dilation ratio equal to the Poisson's ratio of concrete. The dilation response of FRP-confined concrete, even though it behaves similar to unconfined concrete at the beginning, it reaches a peak value of μ_{max} , after which, it decreases and finally stabilizes at a value of μ_u . Both μ_{max} and μ_u depend on the stiffness of the FRP jacket as shown by Mirmiran and Shahawy (1997) in Equations 2.22 and 2.23.

$$\mu_{max} = -0.7611 \ln\left(\frac{2E_j t_j}{f'_c(D-t_j)}\right) + 4.0167 \quad (2.22)$$

$$\mu_u = -0.1375 \ln\left(\frac{2E_j t_j}{f'_c(D-t_j)}\right) + 0.8646 \quad (2.23)$$

Where E_j and t_j are the hoop modulus and thickness of the jacket. D is the average diameter of the tube.

2.4.2 Effect of Geometry and Configuration of the Cross-section

Mirmiran et al. (1998) reported about testing of twelve 152.5x152.5x305 mm concrete-filled GFRP tubes with square cross section including round corners of 6.35 mm radius.

The tubes were filament-wound E-glass with polyester resin wound at ± 75 degrees with respect to the vertical axis. Three different wall thicknesses were considered including 1.45, 2.21, 2.97 mm, using 6, 10, and 14 plies. The unconfined concrete strength was 40 MPa. Only the concrete core was loaded in axial compression to allow the shell to be fully utilized in the hoop direction. Fig. 2.5 shows the normalized stress-strain response of the square specimens, compared to the 152.5 mm diameter circular specimens with similar jackets, but using 30 MPa concrete. Unlike the circular sections, the ultimate strength of square sections is lower than their peak strength and stabilizes at about 70 percent of the peak strength, regardless of the tube thickness. The circular specimens failed by rupture of fibres near mid-height in the hoop direction whereas, in square tubes, significant load drop occurs after the peak strength is reached accompanied by noise. The specimen eventually fails due to stress concentration at the corners. The authors concluded that square sections are less effective than their circular counterparts.

Rochette (1996) conducted a similar study using 33 specimens including circular, square, and rectangular cross sections, different fibres including carbon and aramid, different corner radius, different concrete strengths, 29 to 44 MPa, and different number of plies, 2 to 5 plies for carbon and 3 to 12 plies for aramid. Rochette concluded that the corner radius of the tube affects its confinement effectiveness. Using this data, Mirmiran et al (1998) introduced a modified confinement ratio MCR defined as follows:

$$MCR = \left(\frac{2d}{D-t_f} \right) \frac{f_r}{f'_c} \quad (2.24)$$

Where d is the corner radius. D is the average diameter of the tube and f_r is the confinement pressure given by:

$$f_r = \frac{2 f_t t_t}{D - t_t} \quad (2.25)$$

Where f_t is the hoop strength of the tube. f_r / f'_c is the confinement ratio for circular sections. The ratio of ultimate strength to peak strength of the confined concrete, f'_{cu} / f'_c was correlated to MCR for the specimens tested by Rochette (1996) as well as the square specimens tested by Mirmiran et al. (1998) as follows:

$$\frac{f'_{cu}}{f'_c} = 0.169 \ln MCR + 1.32 \quad \text{for } MCR < 0.15 \quad (2.26)$$

The MCR dictates whether or not a post peak descending part will be present in the response curve. The correlation indicated that for MCR less than 15 percent, the jacket is not very effective in confining the concrete core. There may be additional ductility due to crack opening containment, but no strength enhancement should be expected.

In 1996, Picher and Labossiere reported the results of CFRP-confined 152x152x500 mm square columns, and 152x203x500 mm rectangular columns. The specimens included a 5 mm, 25 mm, 38 mm, and 75 mm radius at the corners. Although, the columns were wrapped with CFRP sheets rather than being cast in pre-fabricated tubes, they showed a similar behaviour to that reported by Mirmiran et (1998). In all cases, confinement improved the ductility. For the most effective configurations, square specimens strength was increased by up to 20 percent. The behaviour showed an initial slope following the unconfined concrete up to the unconfined strength, and then shows a plastic zone with

large ductility. Failure occurs when the sheets fail at or near the corners due to stress concentration. The study concluded that for square columns, the number of layers has no influence on the initial slope, but it shifts the inflexion point to a higher stress level. However, the over all gain is little compared to circular columns. Also increasing the corner radius causes the behaviour of square columns to become gradually similar to that of circular cylinders.

2.4.3 Length Effects

Kurt (1978) examined the length effect on concrete-filled plastic (PVC and ABS) tubes under compression. Although, the tubes were not FRP but rather plastics, it is considered analogous to a case of low modulus composites. Kurt showed that slenderness effect becomes important when the slenderness ratio is greater than 20.

Mirmiran et al (1998) tested 24 concrete-filled 152.5 mm diameter cylindrical tubes with three GFRP tube thicknesses of 1.45, 2.21, and 2.97 mm and four different lengths, L , including 305, 457, 610 and 762 mm to provide (L/D) ratios of 2:1 to 5:1. The unconfined concrete strength was 44.8 MPa. Although some local buckling was observed, shear failure was noted as the primary mode of failure for the tubes. No overall buckling, as a result of slenderness, was noticeable since the length effects were insignificant within the range of (L/D) ratios studied, however, the ultimate strength was some what affected by the length. The strengths and strains at ultimate were normalized with respect to those of the 2:1 specimens and given in terms of (L/D) ratio in the following equations:

$$f'_{cu} = f'_{cu,21} \left[0.0288 \left(\frac{L}{D} \right)^2 - 0.263 \left(\frac{L}{D} \right) + 1.418 \right] \quad (2.27)$$

$$\varepsilon_{cu} = \varepsilon_{cu,21} \left[0.0529 \left(\frac{L}{D} \right)^2 - 0.5214 \left(\frac{L}{D} \right) + 1.8506 \right] \quad (2.28)$$

It should be noted, however, that the range of lengths considered in this study is not sufficient and that for longer columns significant effect could be expected.

2.4.4 Bond Effects

Bond between the FRP jacket and the concrete core can be achieved by using an adhesive, a series of mechanical shear connectors as in concrete filled tubes with internal ribs, or by using an expansive agent in the concrete to produce higher friction with the shell. The interface bond affects the state of stresses in the shell, and may also affect the capacity of the column. In 1998, Mirmiran et al reported about the behaviour of FRP-confined concrete cylinders, both bonded and unbonded. The bonded specimens were made by wrapping fabric around the cylinders with the fibres oriented in the hoop direction. Prior to placing the first ply, the concrete surface was saturated with resin. The unbonded specimens were made by casting concrete into a pre-fabricated tube with the same thickness and laminate structure as the jacket used for the bonded specimens. Later, the unbonded tubes were grooved circumferentially at the top and bottom to prevent contact with concrete in the axial direction. Failure generally occurred by rupture of fibres in the hoop direction for all specimens. The jacket was removed from two of the tested tubes, which were not taken to failure, to examine the bond and the concrete core. The unbonded tube separated with ease, showing no sign of distress and no attachment to

the core. In the bonded specimens, once the jacket was cut, its stresses were suddenly released, causing the concrete core to crack circumferentially, and leaving the exterior portion of the core attached to the jacket. The measured stress-strain behaviour showed insignificant difference between the behaviour of bonded and unbonded specimens. This finding is not justified unless the shell in the unbonded specimens must have contributed somehow in the axial direction, perhaps through friction, otherwise it should have shown significantly higher strength if it was only utilized in the hoop direction compared to the bonded ones.

In the same study, they also reported about bond using shear connector ribs in the inner surface of the tube. 178x178x305 mm tubes were made using a special collapsible mandrel. The internal ribs in axial and lateral directions were made using special polyester paste consisting of polyester resin, 1 percent by volume chopped glass fibres, and 1.5 percent catalyst. The longitudinal and transverse ribs were 42 mm and 19 mm wide respectively, and 6.4 mm thick. The tubes consisted of 15 plies of ± 75 degrees E-glass/polyester. The tubes were filled with 18.6 MPa concrete and tested in compression. The behaviour of those tubes was compared to a similar square tube with no ribs as well as a circular tube with the same shell thickness. Although the square tube with the ribs did not achieve the same effectiveness of circular tubes, it showed significant improvement of strength and ductility compared to the square specimen without ribs. The ribs helped improve the load-carrying capacity by distributing the confining pressure more effectively around the circumference of the tube, thus minimizing the stress concentrations at the corners. The longitudinal ribs act as stringers and help the tube

resist axial and lateral loads. They also divide the shell into small panels, thus increasing the buckling and compressive resistance. The horizontal ribs help maintain the cross-sectional shape of the skin, provide end restrains for the longitudinal ribs, and finally acts with the shell in resisting hoop stresses. This study concluded that, whereas adhesive bond does not affect the load-carrying capacity of FRP-confined concrete, mechanical bond significantly improves the performance of the section.

2.4.5 Analytical Modelling of FRP-Confined Concrete

Different analytical models have been developed to predict the stress-strain behaviour of FRP-confined concrete. A major challenge is related to the variable confining pressure induced by the FRP jacket, which is the main difference between FRP and steel-confined concrete. In 1997, Parent and Labossiere proposed a modified Mander's theory [Mander et al 1988], which is capable of predicting the full response of axially loaded concrete member under a constant confining pressure such as a yielded steel jacket. An energy balance method has been proposed to calculate the axial strain at failure. The additional strain energy, which is stored in confined concrete, is provided by the energy built up in the shell. In other words, the difference in area under the confined and unconfined stress-strain curves integrated with the area of the concrete is set equal to the area under the FRP stress-strain curve integrated with the area of the shell. From this equation the ultimate axial strain is obtained. An iterative procedure is used. The method was applied by Becque (2000) to concrete-filled GFRP tubes and highly underestimated the failure strain as it resulted in a 0.0124 ultimate axial strain rather than 0.043. It was also confirmed by Samaan et al (1998) that the energy balance method fails to predict the

behaviour because it neglects the lateral strain energy stored in concrete, which accounts for about 80 percent of the total energy.

In 1998, Samaan et al proposed a fully empirical model based on testing concrete cylinders confined with GFRP shells of different thicknesses. The model assumes a bi-linear stress-strain response of confined concrete, defined by four parameters including the first and second slope, the intercept of the second slope with the vertical axis and the ultimate strength. The model, however, only allows for strain hardening behaviour for the second slope of the bi-linear response although tests have shown that, under low confinement pressure, the strength reaches a peak value than shows plastic or softening behaviour. Also the model does not allow for partially filled tubes with central voids, neither allows for the case of axially loaded tubes. Two different equations were given by the authors for each of the ultimate confined strength and the dilation ratio at ultimate in two different papers [Mirmiran and Shahawy 1997] and [Samaan et al 1998]. No justification was given for the difference in the equations describing the same variables.

In 1999, Spoelstra and Monti proposed a modified Mander's model. The model utilizes an empirical equation relating the lateral strain in concrete to the intensity of internal cracking, which allows for a variable strain related to the axial stress level. An iterative procedure is used. Failure is indicated when the lateral strain reaches the failure strain of the jacket.

In 2000, Becque proposed a confinement model based on strain compatibility and the octahedral stress and strain theory. The model accounts for totally and partially filled FRP tubes including voided concrete core as well as the tube-in-tube configuration. It also accounts for axially loaded FRP tubes. However, the model capability is limited to high confinement levels producing a strain-hardening behaviour and fails to predict post-peak plastic or softening behaviour.

2.5 Concrete-Filled FRP Tubes as Beams and Beam-Columns

Concrete-filled FRP tubular sections have great potential for beam and beam-column applications. Although the benefits of concrete confinement are less in presence of bending as compared to axially loaded members, other advantages such as utilization of the FRP shells as stay-in-place form work, ease of fabrication and speed of erection still makes this system attractive.

In 1995, Descovic et al reported that GFRP thin-walled box sections are efficient for beams, however, they suffer from some disadvantages. The compressive flange is considerably weaker than the tensile flange, because GFRP has a compressive strength about half its tensile strength and because of local buckling phenomena. Failure is usually catastrophic without warning, mainly due to the linear elastic behaviour of composite materials. Also the design is usually governed by stiffness because of the relatively low Young's modulus of GFRP, resulting in a need for excessive use of composite material to satisfy certain displacement requirements. In view of this they

proposed combining GFRP box sections with other materials such as concrete which is superior in compression and possibly CFRP which is superior in tension.

2.5.1 Concrete-Filled FRP Tubes for Bridges

In 1996, Seible introduced the concrete-filled carbon shell concept for new bridge systems, in which, a filament-wound CFRP shell is filled with light weight concrete and used as a girder or a column. The shell is envisioned to replace the reinforcing steel and formwork, provide better seismic response, more durability, and greater speed of erection. Two different criterion were adopted for bridge columns as shown in Fig. 2.9, the ductile design concept with steel starter bars at foundation level, and the strength design concept with the shell extended into foundation, in which, the response is essentially elastic. In the first system, it was verified that short development lengths of the bars are required due to the high confinement. In the second system, behaviour was linear elastic up to failure, which occurred at only 52 percent of the column capacity due to stress concentration at the footing level. The observed excellent response of those columns led to the development of complete bridge systems. Fig. 2.10a shows the dual tied arch bridge, which is proposed to cover a 61 m span. The arch is comprised of concrete-filled CFRP segments, the tie girder consists of post-tensioned concrete-filled CFRP tube, and the cross-beams are CFRP tubes placed in a link-and-log system over the beams with only the joints are concrete-filled. Fig. 2.10b shows an alternative system utilizing a carbon shell space truss with post-tensioned truss members and connections as shown in Fig. 2.11.

In 1997, Seible et al. also proposed using the carbon shell system for short and medium span girder-bridges as shown in Fig. 2.12. Conventional reinforced concrete or new FRP decks are connected to the girders through rebars or special FRP dowel connections [Zhao et al 1997]. The CFRP shells are round or square filament-wound with hoop (90 degrees) and longitudinal (± 10 degrees) fibres. A special mandrel is used to produce helical ribs on the inside of the shell for better bond with concrete. The typical span-to-depth ratio in this system is 17 to 20 including the 150 mm deck, and higher ratios can be achieved with post-tensioning or continuous girder action [Seible 1996]. Preliminary characterization studies [Seible et al 1997 and Burgueno et al 1998] have shown that the design is stiffness driven with the material strength not fully utilized, and an optimal diameter-to-thickness ratio can be found to satisfy a span length requirement. Also different lamination architectures of the tube can modify the performance of the complete system. A series of four beam tests using 4-point loads were performed on concrete-filled CFRP tubes including both, circular sections, and square sections with corner radius equals to 1/3 the depth. The tubes had wall thicknesses of 2.3 and 4.6 mm and inner diameter (or depth in case of the square section) of 152 mm. The laminate structure consisted of 80 and 20 percent fibres in both, the longitudinal and hoop directions respectively. 44.8 MPa lightweight concrete was used. The test span was 1.83 m and the shear span was 0.71 m. The capacity of the square shell was 25 percent higher than that of the circular one, while the stiffness was 50 percent higher. It should be noted however that a square section has a larger concrete and CFRP cross sectional areas compared to a round section of the same size. The beam with the thicker wall failed in compression. Full scale testing [Karbahri et al. 1998] was also conducted on the carbon shell system.

A non-destructive 4-point bending test over a 7.9 m span was performed on a 343 mm diameter non-grouted carbon shell with 10 mm wall thickness to establish the stiffness of hollow shells and the limits of local instabilities. A similar test was conducted on a tube grouted with 20.7 MPa concrete and compression failure occurred in the shell at a 0.55 percent compressive strain. Behaviour was linear till failure. The experimental work was also extended to full-scale beam-slab assemblies. Two test units were considered. The first consists of a single beam-slab assembly as shown in Fig. 2.13, with the shell affixed to normal weight concrete slab, while the second unit is composed of three girders spaced at 2.3 m with a 181 mm integral E-glass advanced composite deck system. In both tests, 2 # 6 steel bars spaced at 610 mm were used as shear connectors. The first unit was cyclically loaded for 1000 cycles, at a load level chosen to match the shear demand on the dowels at service load level. Subsequently the unit was cycled up to three times the service load with no significant stiffness degradation. At 3.3 times the service load, degradation was gradually observed as the beam-slab interface slipped. In the second unit, the girders were connected to reinforced concrete end diaphragms, supported over six load cells, located under the girders. Four loads were applied on top of the deck system. Only initial stiffness characterization tests were performed at this point. The stiffness and moment capacity of the beam-slab unit were increased compared to the single girder. Also the strains along the compression side were reduced, therefore, the compression failure mode of the single girder is not expected unless the system becomes uncoupled.

The carbon shell system was also proposed by Seible (1998) for pedestrian bridges. The Scripps Crossing bridge at LaJolla, California was used to demonstrate the new concepts. The adopted design solution consists of a cable-stayed 42.3 m long bridge with a single eccentric 18.3 m long pylon and a slender super structure. Fig. 2.14a shows the conventional design of the super structure. Subsequent to the completion of the bridge, alternative designs were developed. The cross-sectional geometry of the conventional design was almost preserved by utilizing the carbon shell system for the exterior girders with a GFRP bridge deck spanning between the longitudinal girders as shown in Fig. 2.14b, or concrete deck as shown in Fig. 2.14c. Cable stays can be anchored to the carbon shell girders. While the stiffness of all three super structures is almost identical, weight savings of the FRP superstructure with GFRP deck resulted in factors of 2 to 3 compared to the concrete super structure. For a single cable plane and wider cable spacing, the use of a central larger carbon shell and precast concrete deck was also investigated as shown in Fig. 2.14d. Although the study demonstrated the advantages of weight reduction using FRP (ratio of dead-to-live loads of 1.0 compared to 2.3 for conventional design), it also pointed out that other design aspects such as the aerodynamic stability and vibrations under live load become more critical and need to be addressed. The study also concluded that it is difficult for the FRP bridge design system to compete with conventional designs, however, hybrid solutions, which utilize conventional concrete decks with carbon shell girders, provide cost competitive solutions.

2.5.2 Concrete-Filled FRP Tubes for Piles

In 1999, Mirmiran and Shahawy reported about the behaviour of a 348 mm diameter over-reinforced, and a 369 mm diameter under-reinforced concrete-filled FRP tubes. The motivation was to develop a new piling system for the Florida DOT, which has sponsored a detailed study since 1994. Because of the corrosion problems associated with reinforced and prestressed concrete piles, the Florida DOT requires a minimum of 0.0155 m² section when the pile is driven in water including salt or high chloride contents and wet/dry cycles, regardless of the load level. It is believed that the FRP tubes protect the concrete core and alleviates the problems of moisture intrusion and permeability of concrete. The wall thickness of the FRP tubes were 14 mm and 6.6 mm for the over and under-reinforced concrete-filled FRP tubes respectively, which results in 18.24 and 7.51 percent reinforcement ratios, respectively. Since the strengths of the tubes were different, the researchers proposed a reinforcement index, which is the reinforcement ratio multiplied by the ratio of the tensile strength of the tube in the axial direction, to the concrete compressive strength. The reinforcement index of the over and under-reinforced sections were 3.39 and 0.19, respectively. The tubes were tested under increasing bending and fixed axial loads ranging from zero to 2792 kN. The moment-curvature response was bi-linear for the two types of specimens, with the transition point between the two slopes corresponding to major cracking of concrete. While the first slope is approximately the same for both types, the second slope is considerably larger for the over-reinforced specimen. The ultimate deflections of the over-reinforced specimens were about 0.5 to 0.75 those of the under-reinforced specimens, where as their strengths were 1.25 to 4 times higher. The effect of secondary moments was less for the over-

reinforced sections. Shahawy and Mirmiran (1998) reported more details about one of the under reinforced beam-column tests. The GFRP tube was filament wound using E-glass fibres at ± 45 degrees and epoxy resin, and had axial tensile and compressive strengths of 105 and 230 MPa, respectively. The tube was filled with 21 MPa concrete and tested over a 2.6 m span. The specimen was first loaded with a 1779 kN axial load, then bending was applied using four-point loads. The test was stopped at 89 mm deflection. Upon unloading, over 50 percent of deflection was recovered and no cracking was observed during loading or unloading. The specimen was then loaded and unloaded twice in pure bending until failure occurred at 200 kN.m bending and deflection of about 1/20 of the span length. Tension failure was marked by fracture of the bottom fibres. No slippage was observed. The secondary moments were significant, mainly because of the low stiffness of the tubes. Based on this study, Mirmiran et al (2000), concluded that bond failure is not an issue in beam-columns, therefore off-the-shelf products can be used, however, shear transfer mechanism is needed for beams. They also recommended the over-reinforced section design due to the higher failure load, lower deformation, and more ductility. The study showed that, the 348 mm concrete-filled tube is comparable to 584 mm diameter prestressed round pile including 20-1862 MPa strands, whereas the 369 mm diameter concrete-filled tube was comparable to a 460 mm square section with eight strands.

2.6 Prestressed Concrete-Filled FRP Tubes

Parvathaneni et al (1996) proposed using concrete-filled filament wound GFRP tubes made out of E-glass and vinyl ester resin and prestressed in the axial direction to produce

alternative piles of 318 mm diameter. The goal was to replace the traditional steel tubes been used as piles in the Cedar shore resort marina at Chamberlain in South Dakota. because of the corrosion problems. Due to the confinement effects, the authors reported that the ultimate strength of concrete would increase 6 to 8 times the unconfined strength, depending on the tube thickness, diameter, filament architecture, Poisson's ratio, and the unconfined strength. As the piles are subjected to bending and tensile stresses, it was decided to take advantage of the high confined strength by prestressing the concrete to a high compressive stress in order to reduce the tensile stresses and the term "super prestressing" was adopted for prestressing the confined concrete. Two methods were used to produce the 6.35 mm thick GFRP tubes using filament winding, one with a stay-in mandrel of plastic tubing, and the other with a removable aluminium tube mandrel, which proved to be more effective in confinement. The 13.72 m long tube was fabricated as 3 separate segments, which were spliced later using short steel tubes. Three 35 mm diameter Dywidag bars were stressed inside the tubes, a 35 MPa concrete was cast and cured, and finally the bars were distressed, producing a 31 MPa compressive stress in concrete. The conventional method of driving the pile was used, using diesel hammer. Driving went smoothly without damage and the maximum recorded dynamic strain in the concrete was 1360 micro strains in compression, and no tension stresses were induced. The 13.72 m pile was driven 7.62 m into the river bed and was tested under a lateral load of 8.9 kN. The lateral deflection was 34 mm.

2.7 Splices and Joints in Concrete-Filled FRP Tubes

Different types of connections and joints include splices within the member itself to overcome the problem of limited lengths that can be manufactured. In 1996, Parvathaneni and Iyer produced a 13.72 m pile using concrete-filled GFRP tubes. Three 4.57 m long filament-wound tubes were spliced using short steel tubing, 0.6 m long, which matched with the inside of the GFRP tubes. Concrete was then cast into the spliced tube.

There are also ductile connections within the hybrid member intended to provide plastic failure. The concrete-filled carbon shell bridge columns, shown in Fig. 2.9a, can be connected to the foundation through short steel starter bars to produce more ductility as compared to carbon shells fixed into the foundation, which gives higher strength but less ductility [Seible et al. 1998]. For girder type bridges, it is proposed that the mid-span section and the sections over the columns could be designed for full strength, whereas plastic hinges can be designed some distance away from the self-weight inflection points. Under overloads, an increase in moment will result in a hinge formation and a ductile system response. Since cracking may be concentrated in the joint and ordinary steel reinforcement could corrode, it is desired to develop a pseudo-ductile system with FRP-rebars as connectors. Since FRP does not experience yielding like steel, ductility can only be achieved by other mechanisms such as slippage between the concrete and the rebars. However, the achieved ductility is only in one direction and the deformation and damage can not be reversed, thus cyclic ductility demand for earthquake regions can not be satisfied. The anchorage lengths of the FRP connectors are chosen such that slippage

occurs before they rupture [Wernli and Seible 1998]. Special preparation is first done to the ends of the bars including sand blasting followed by coating with epoxy and dipping in sand. In addition, the rods at the ends can also have longitudinal cuts and splayed apart. The concept is investigated on a full-scale concrete-filled CFRP tube of 362 mm diameter. The spliced tube has a total length of 6.71 m with a 25 mm gap at the connection. The bending capacity of the tube is 1100 kN.m and the connection has a maximum capacity of 60 percent of the tube. 40 CFRP rods, 1.1 m long, were used at the connection and were arranged evenly in a circle. At both ends, the rods had at least 400 mm of length sanded, cut, and splayed with eight 200 mm long legs. Numerical analysis accounting for the bond-slip behaviour of the rods showed a ductile behaviour. The initial stiffness of the moment-deflection response is slightly less than that of the tube and gradually decreases till the first rods start to slip entirely at a moment of about 450 kN.m resulting in the expected ductile response. It was also proposed that any slip should be avoided during design service loads, and the mechanism should only act as a last redistribution of loads before failure.

There are also connections between the hybrid element and other structural components such as deck slabs or columns. Fig. 2.15 shows connections between carbon shell girder and GFRP deck as well as two carbon shell girders over a carbon shell column [Seible et al 1998]. Zhao et al in 1997 showed that the dowel-type joint between carbon shell and composite deck using polymer concrete anchorage for the dowel in the deck has demonstrated higher shear transfer capacity than that between the carbon shell and

ordinary reinforced concrete slabs, shown in Fig. 2.14c and Fig. 2.14d. Other types of connections in truss-type bridges are shown in Fig. 2.11.

2.8 Other Forms of Hybrid FRP/Concrete Sections

One of the earliest attempts to produce hybrid FRP/concrete beam elements was done by Fardis and Khalili in 1981. They simply proposed casting concrete into FRP boxes. They also pointed out the mechanical role of FRP and concrete as follows: 1. FRP carries the tensile forces in the tension zone. 2. It provides partial confinement of concrete in the compression zone, enhancing strength and ductility. 3. It carries part of the shear force in the beam through the two sides. 4. The concrete core provides compressive strength and rigidity and prevents local buckling of the FRP casing. They also pointed out that adhesion between the concrete and FRP is not necessary provided that the FRP box is closed at the two ends and the unidirectional fibres at the bottom have adequate end anchorage, otherwise mechanical interlock can be introduced. Five FRP-encased concrete beams were constructed using 0, 5, or 10 layers of unidirectional GFRP reinforcement at the bottom. A 76x152x1220 mm wooden mold was used to build the three-sided GFRP boxes using hand lay up. Concrete was then cast after curing of the box and after 28 days, the top and two sides were covered with two layers of epoxy wetted GFRP cloth. The beam without any unidirectional axial tension fibres, was considered under reinforced and failed by fracture of the GFRP cloth in tension. All other beams were over reinforced and experienced ductile behaviour with concrete failing in compression. Later, removal of the GFRP casing revealed that concrete was severely cracked in tension and shear and crushed at the top, however the FRP on the three sides

was still intact and provided confinement. As a result, unloading after failure led to almost total recovery of the deflection. Fig. 2.16 shows the load-deflection response of the under reinforced beam compared to that of the over reinforced beam with 10 unidirectional GFRP layers. The strength of all the beams tested was greater than that of typical conventional reinforced concrete beams of the same dimensions and ranging from over-reinforced to overly under-reinforced. This study proved that FRP-encased concrete beams are superior to reinforced concrete beams on a strength/material cost basis.

Triantafillou and Meier (1992), Deskovic et al. (1995), and Triantafillou (1995) presented an innovative hybrid box section suited for simply supported spans. The new system combines composite materials with low-cost construction material, concrete, to result in new concepts for the design of lightweight, corrosion immune and yet inexpensive beams with excellent damping and fatigue properties. A schematic illustration of the hybrid section is given in Fig. 2.17. The section consists of GFRP pultruded box section with an upper layer of concrete in the compression side and a thin layer of CFRP in the tension side. The idea was initiated by considering the thin-walled GFRP pultruded box sections, which are considered to be efficient and widely used in structural applications, yet they suffer from some disadvantages. The compressive flange is considerably weaker than the tensile flange, because GFRP has compressive strength about half its tensile strength and because of local buckling phenomena. Failure is usually catastrophic without warning because of the linear nature of the material. Finally, the relatively low stiffness of GFRP results in excessive use of composite materials to satisfy certain displacement requirements. In view of this, the new design is driven by the following considerations.

The compressive stresses in the section should be carried by material with the highest compressive strength and stiffness-to-cost ratio, and therefore the GFRP flange could be eliminated and substituted by a layer of concrete. Another composite material with a failure strain less than that of GFRP could be added to the section's tension zone, so that it will be the first element to fail, thus giving warning of an imminent collapse (pseudo-ductility). It should preferably also possess a high stiffness to increase the section rigidity. A thin layer of externally epoxy-bonded CFRP appears to be the best candidate material for this purpose as it will also enhance the member's creep and fatigue behaviour. Because the proposed design involves casting of concrete, part of the GFRP box section is extended to act as formwork for the wet concrete and to transfer the GFRP-concrete interface shear stresses. A good bond between the concrete and GFRP can be achieved by either using epoxy adhesive or providing mechanical deformations to the top GFRP surface.

A preliminary experimental program using small-scale specimens revealed that the desired failure sequence could hardly be achieved using standard pultruded GFRP profiles. Therefore, it was decided to fabricate the GFRP box sections using the filament winding technique. Three 180x300x3200 mm filament-wound GFRP box sections were fabricated. The webs included GFRP plates with fibres wound at ± 45 degrees, sandwiched between layers with fibres at ± 45 degrees to add shear strength. The average web, and flange thicknesses were 3.2 and 5.3 mm respectively. Prior to attaching the concrete or the CFRP layers, the beams were loaded elastically in three-point bending over 3 m span to establish their stiffness characteristics. A 53 mm thick concrete layer

was then cast on top of the GFRP flange and bonded using epoxy adhesive in beam 1. steel shear connectors in beam 2 and beam 3 in order to enhance the shear transfer between the concrete and upper flange. Two pultruded CFRP straps, 1 mm thick and 10 mm wide were attached to the bottom flanges, near the corners, using adhesive. The beams were then re-loaded to failure. Beam 1 failed by CFRP fracture, followed by GFRP-concrete interface debonding. Beams 2 and 3 failed in a pseudo-ductile mode, where the CFRP fractured, followed by crushing of concrete at higher load level. Fig. 2.18 shows the load-deflection behaviour of the hybrid beam compared to a GFRP box beam, loaded to failure. The gradual failure, which starts by fracture of CFRP accompanied by the sudden drop of load and reduced stiffness, provides adequate warning before the complete failure. This pseudo-ductility is a major part of the innovation in this new system.

In 1999, Canning et al proposed a similar, but improved, hybrid system consisting of concrete section in the compressive region, GFRP composite sandwich foam core web section, and a GFRP tension flange interleaved with high strength unidirectional carbon fibre tape as shown in Fig. 2.19. The beam was designed such that the neutral axis is situated at the bottom of the concrete to eliminate tensile stresses from concrete. Indents were placed in the vertical faces of the shuttering to enhance the bond with concrete. At early stages of the program, it was realized that buckling of the webs would be one of the critical modes of failure, therefore, an optimization study was performed to compare different configurations as shown in Fig. 2.20. Although the web diaphragm model was found to be the optimum solution, the sandwich foam core was selected for its ease of

fabrication. Fig. 2.19 shows the details of the 1.5 m long beam used in the investigation. The sandwiched web below the neutral axis consists of inner and outer faces of 3 and 7 layers bi-directional GFRP fibres at ± 45 degrees respectively. A 12 mm thick rigid foam core was placed in between. The GFRP face materials of the web was extended to the compression zone to form the permanent shuttering for the concrete. The bottom flange of the beam was fabricated by wrapping ± 45 degrees GFRP prepreg around unidirectional CFRP layers. A 1.5 m span was used to test the beam under four-point bending. The beam was designed to fail in compression. During testing, bond between the concrete and the vertical GFRP shuttering was failed but concrete continued to be held in position by the mechanical shear connectors in the vertical walls and a 1–2 mm slip occurred. Failure occurred when the concrete crushed in compression and as a result of the impact, the webs failed by buckling in shear. The study concluded that the hybrid beam had a similar ultimate bending capacity, half the flexural rigidity, and a weight reduction of about 75 percent compared to a singly reinforced concrete beam of the same dimensions with a 2 percent reinforcement ratio. The production time of 24 hours, including the vacuum process, is similar to that of reinforced concrete beams. Up to 42 percent of the ultimate load, both adhesion and shear keys allowed full composite action, after that, the adhesion bond failed and the shear key permitted high percentage of composite action with some slippage. No buckling of the sandwich webs was observed.

In 1998, Hall and Mottram presented a novel hybrid section combining GFRP “off-the-shelf” pultruded sections, commercially available as floor panels, with concrete. The GFRP sections act as tensile reinforcement and permanent formwork at the same time.

Fig. 2.21 shows a section of the GFRP reinforcing system having two T-up-stands and a continuous base. The whole floor panel is 500 mm wide and composed of polyester resin matrix reinforced with E-glass fibres including unidirectional (UD) roving and continuous filament mat (CFM). The elastic modulus of both, the web and flange is 30 GPa, while that of the base is 12 GPa. The elastic modulus of the whole section was determined using a compression test and found to be 20.7 GPa. The position of the centroid axis of the panels was estimated through small scale bending tests on the panels and was determined to be 17 mm from the lower surface of the base. As the panels have smooth surface, the study included push-out bond tests of concrete cast around the panels as received, and concrete cast around the panels after coating with epoxy mortar. The contact length was 100 mm. The ultimate bond strength from those tests was 5.2 and 3.3 MPa for the bonded and unbonded cases respectively. The unbonded specimen failed at the smooth interface, while the bonded one, concrete failed in the form of cone-shaped plug. A total of 12 beams were tested in four-point bending over a 2 m span. The constant moment length was 0.8 m. Five different reinforcement arrangements were considered as shown in Fig. 2.22 including both, bonded and unbonded conditions, normal and lightweight concrete, as well as steel fibres in the mix. The moment-deflection response of beams 1 and 2 is given in Fig. 2.23. The study concluded that: 1. Plain reinforcement bond strength is similar to that quoted elsewhere for plain FRP rebars. 2. Conventional theoretical assumptions about reinforced concrete are still valid. 3. Beams behaved in a linear elastic manner for loading up to serviceability and continued to deform in a nonlinear manner to ultimate failure. 4. Failure was often by concrete in shear, no shear reinforcement was present, and the beams were over

reinforced in flexure. 5. To provide adequate bond, it will be necessary for plain reinforcement to be bonded to concrete by an adhesive such as epoxy.

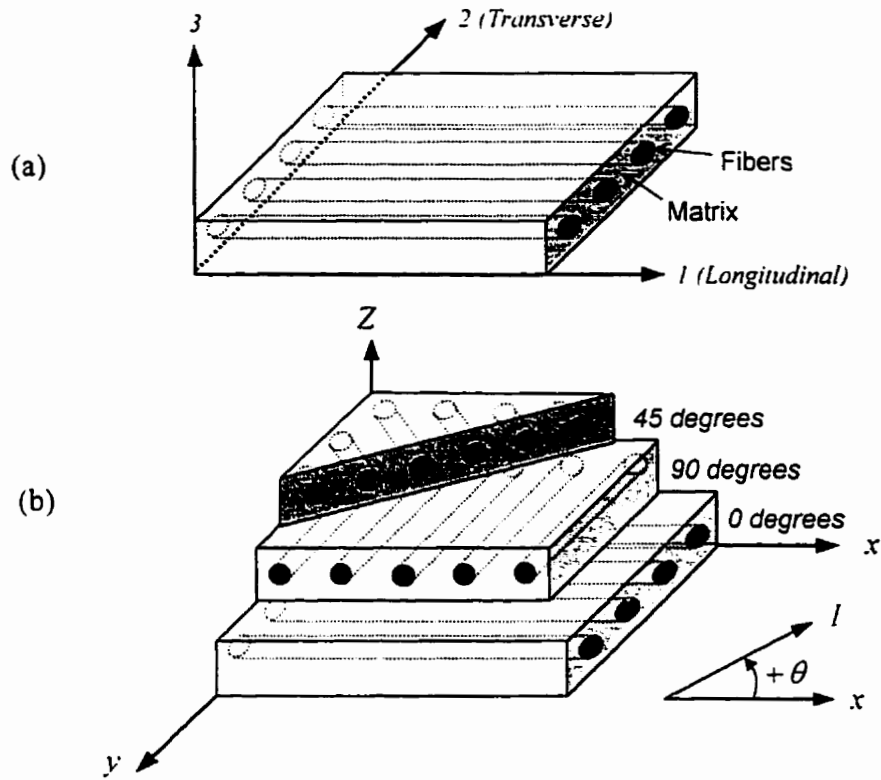


Fig. 2.1 Unidirectional lamina (a) and multidirectional laminate (b)

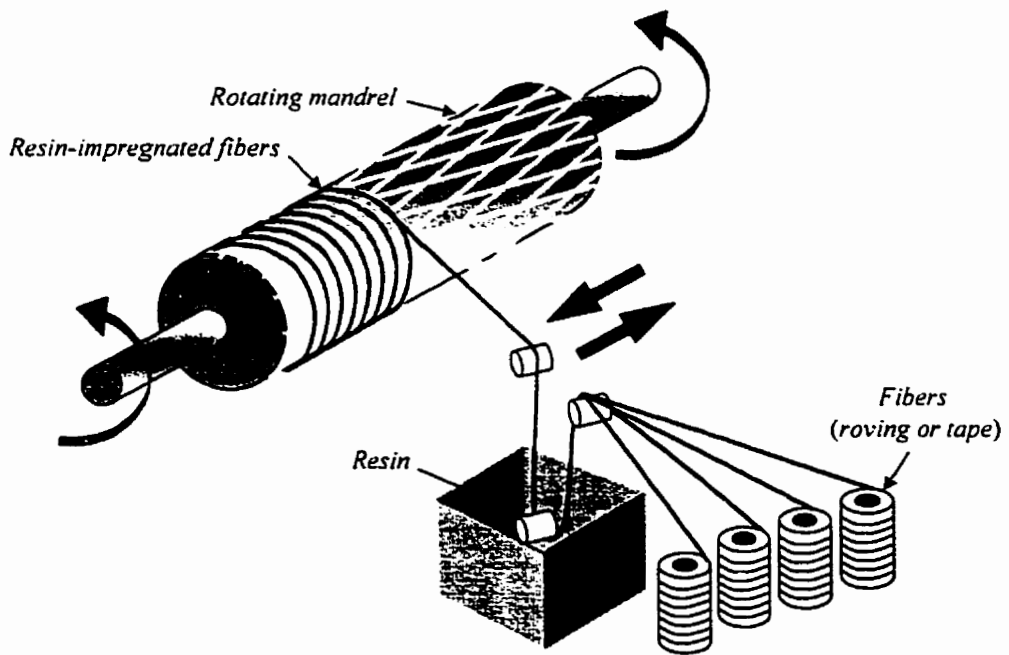


Fig. 2.2 Schematic of the filament-winding process

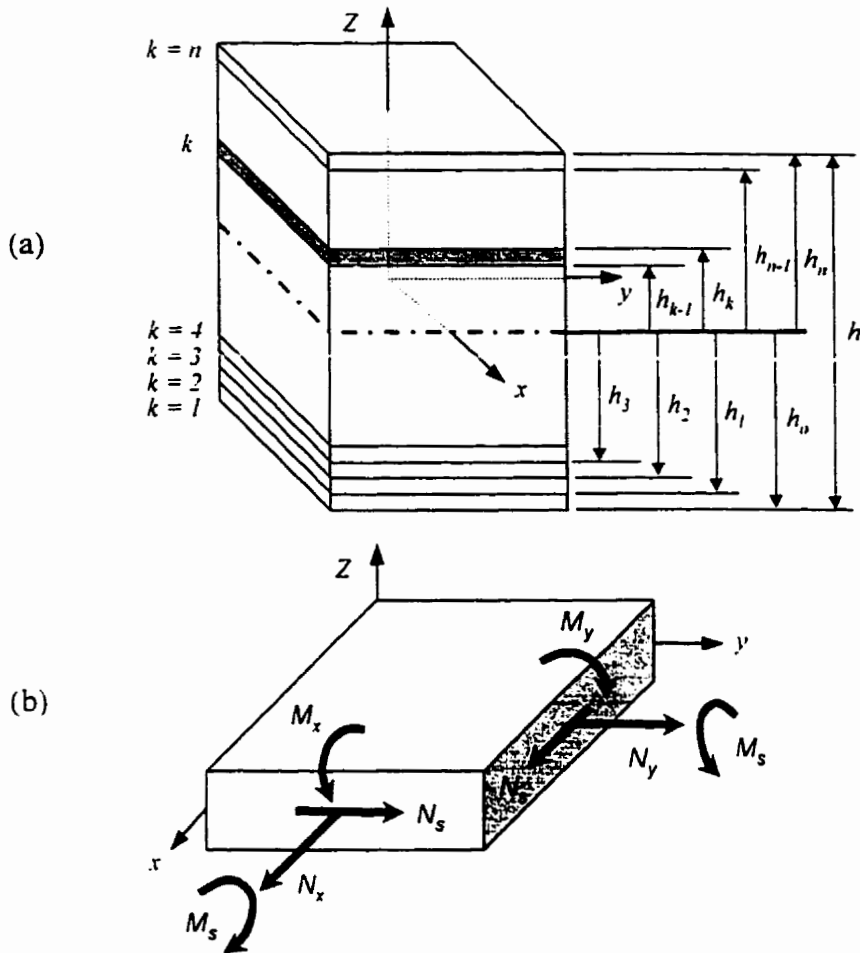


Fig. 2.3 Multidirectional laminate with coordinate notation of individual plies (a) and stress resultants acting on a general shell element (b)

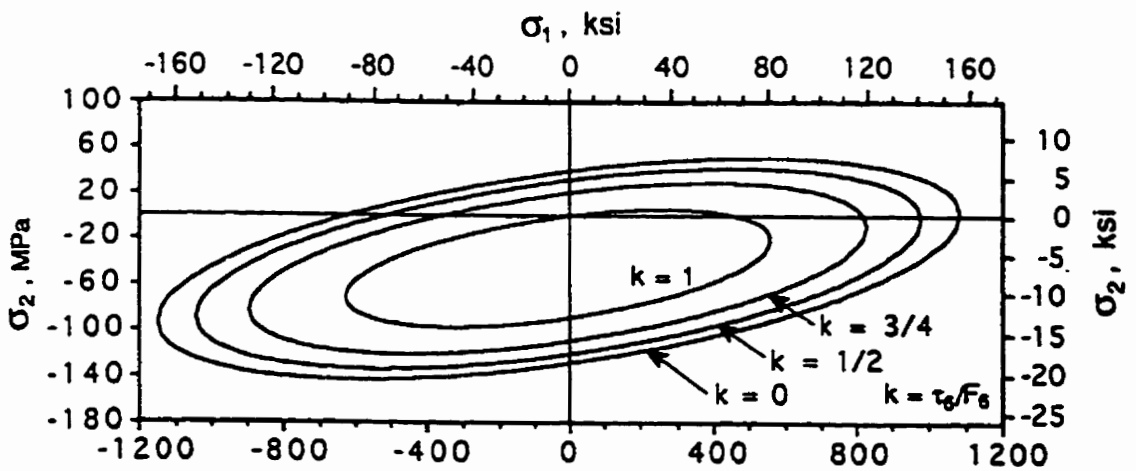


Fig. 2.4 Failure envelope of E-glass/epoxy lamina with different levels of shear stress using Tsai-Wu criterion [Daniel and Ishaï 1994]

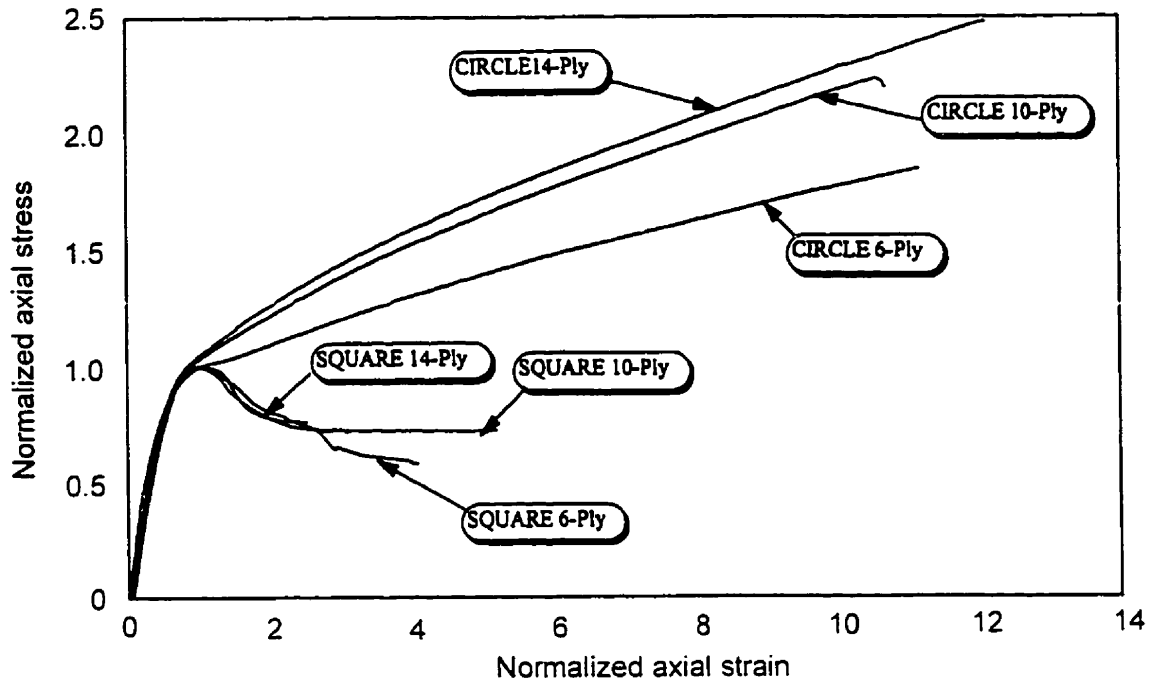


Fig. 2.5 Normalized stress-strain curves of concrete-filled GFRP circular and square tubes [Mirmiran et al 1998]

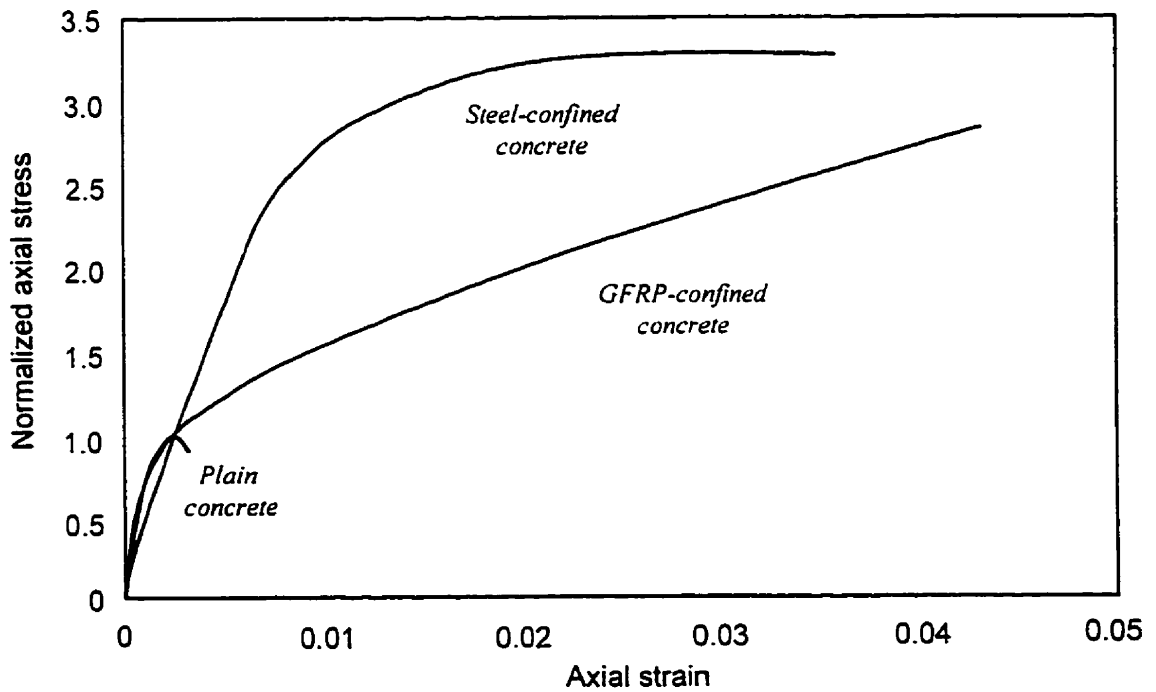


Fig. 2.6 Stress-strain response of GFRP-confined concrete versus steel-confined concrete [Samaan et al 1998]

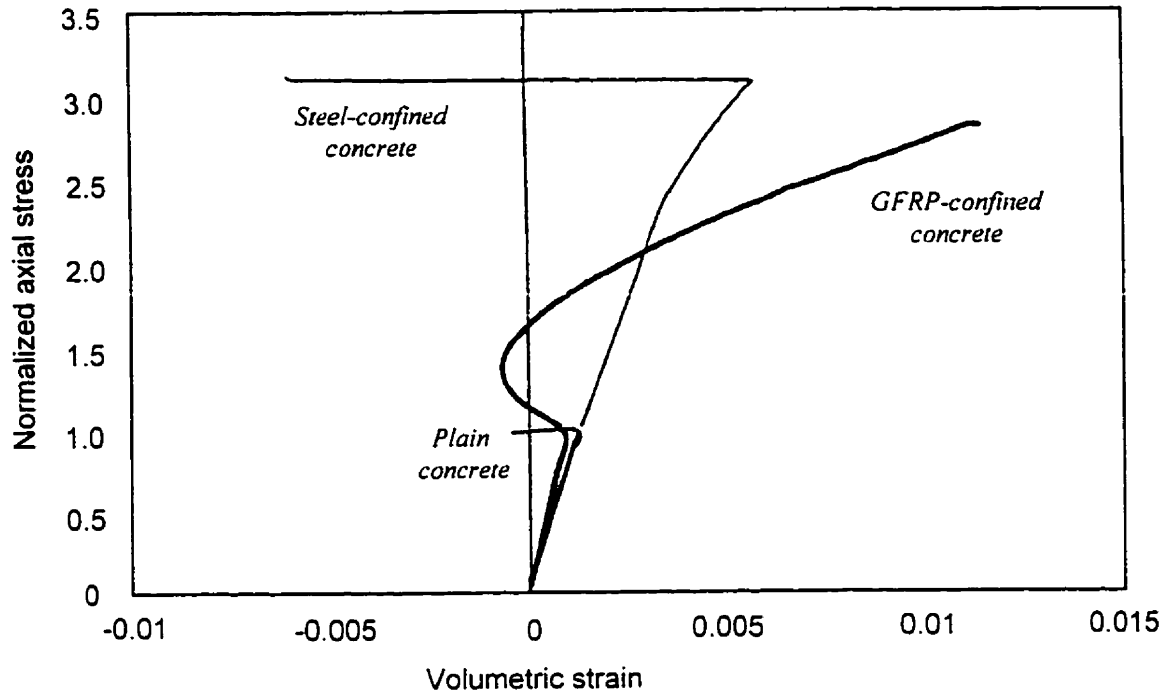


Fig. 2.7 Volumetric strain response of GFRP-confined concrete versus steel-confined concrete [Samaan et al 1998]

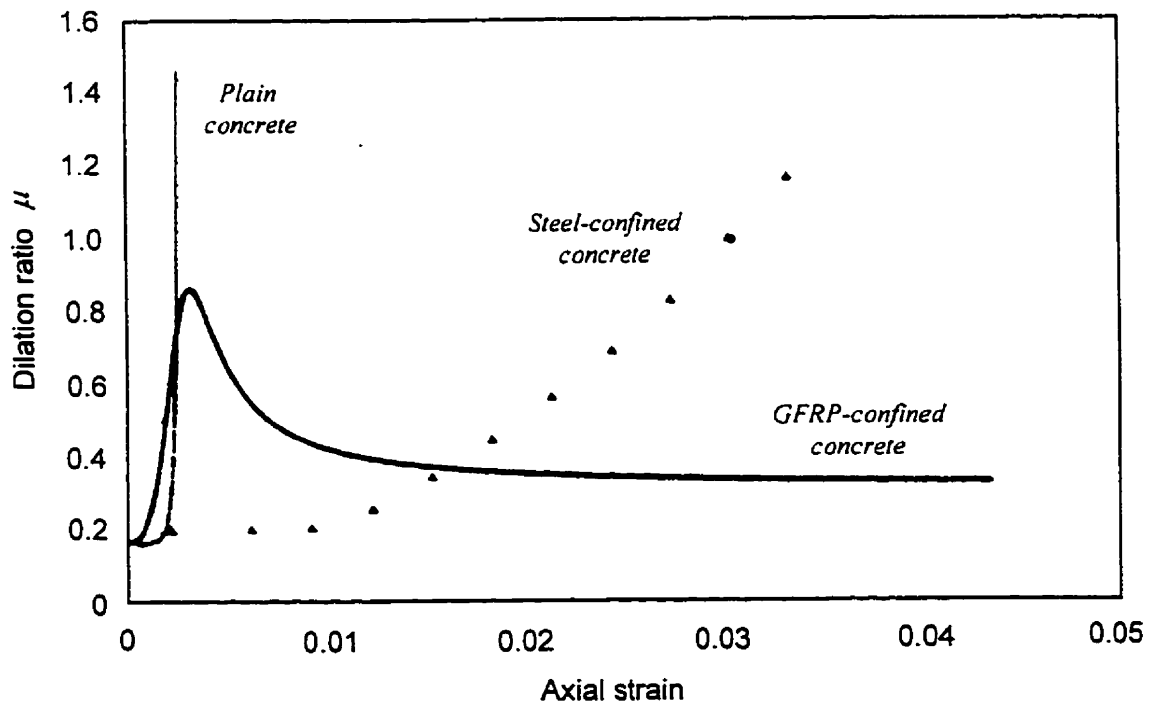


Fig. 2.8 Dilation curves of GFRP-confined concrete versus steel-confined concrete [Samaan et al 1998]

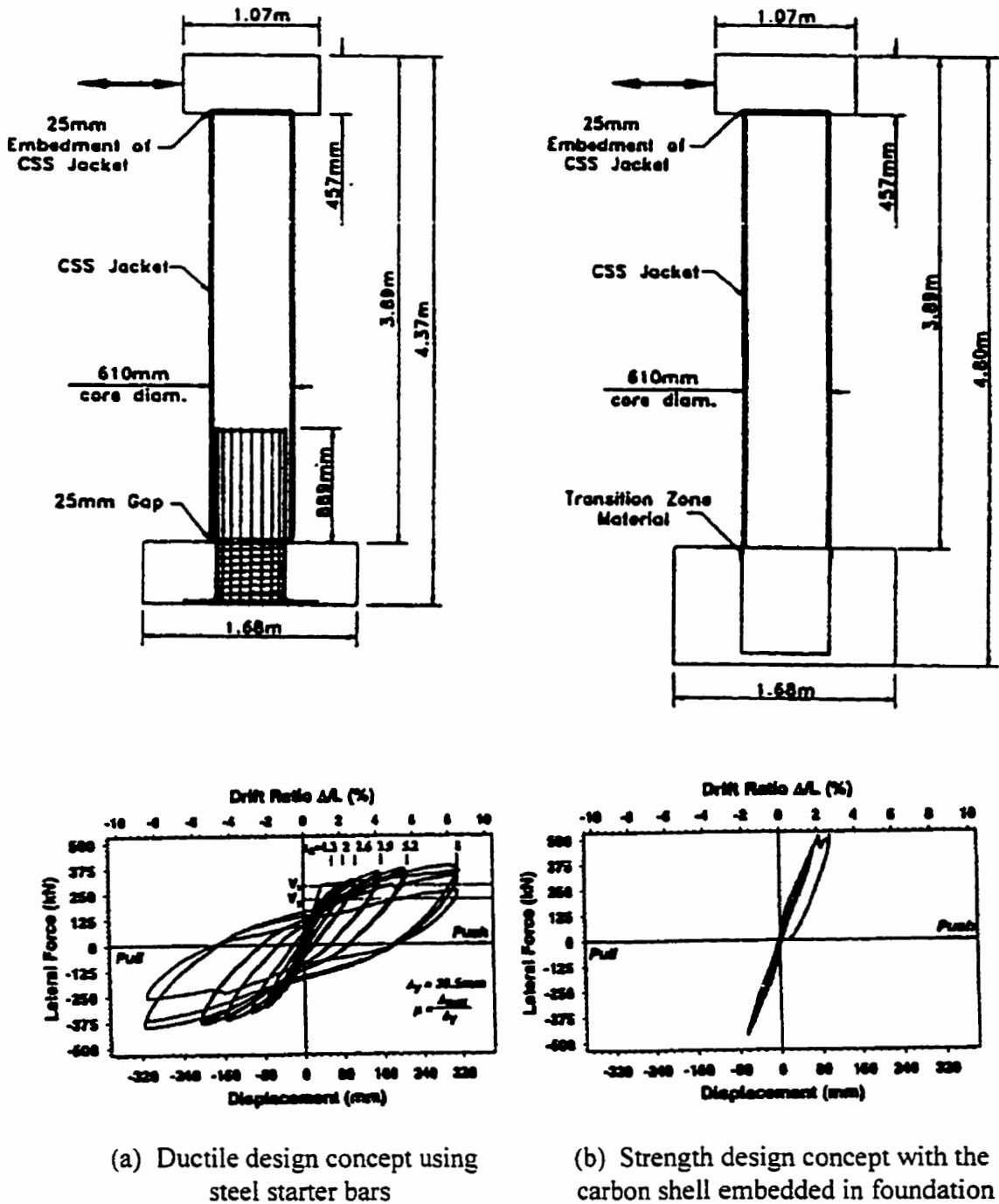


Fig. 2.9 Concrete-filled carbon shell column systems [Seible 1996]

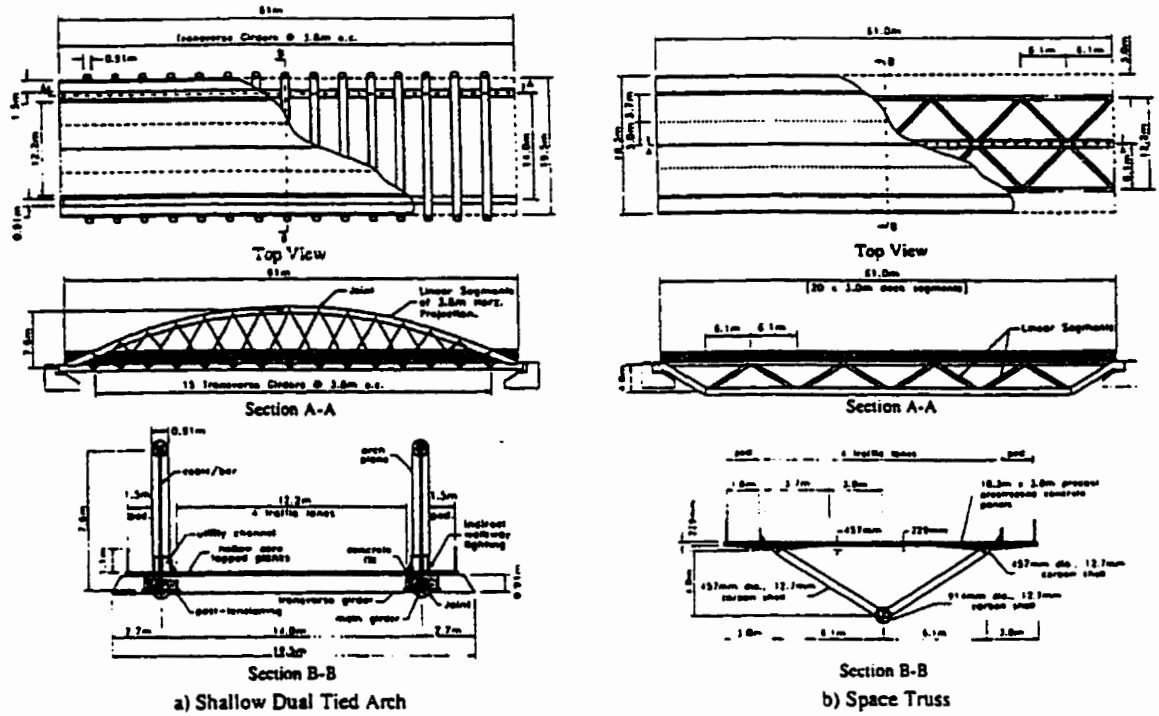


Fig. 2.10 Carbon shell space truss bridge systems [Seible 1996]

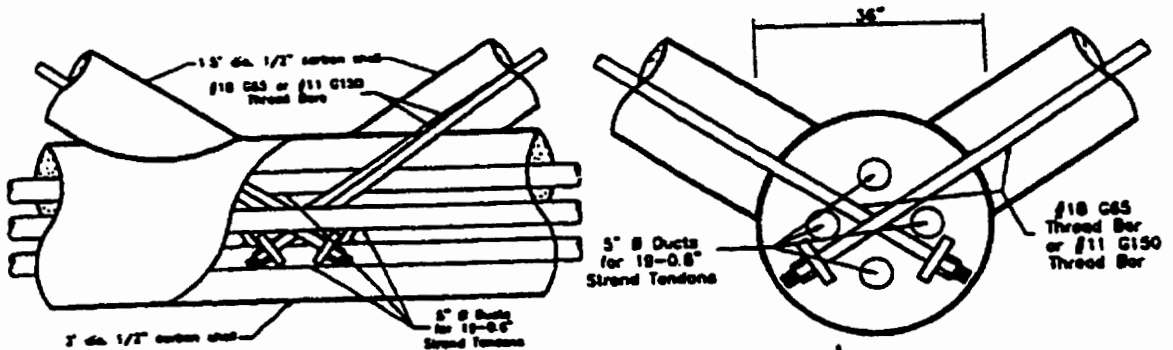


Fig. 2.11 Details of connections in space truss carbon shell bridge systems [Seible 1996]

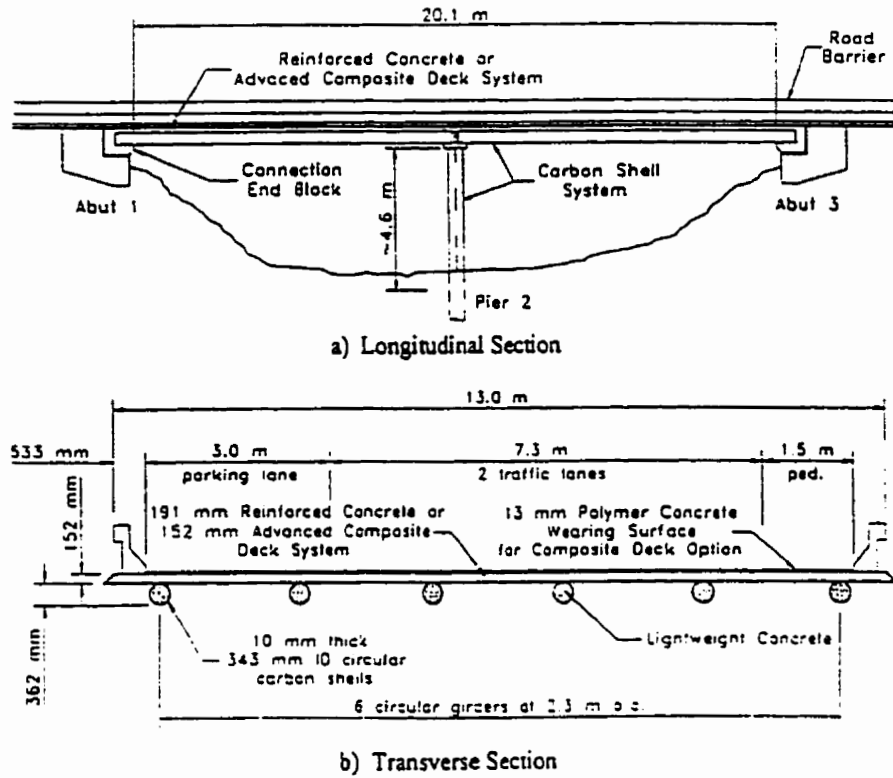


Fig. 2.12 Carbon shell girder-type bridge system [Seible et al 1997]

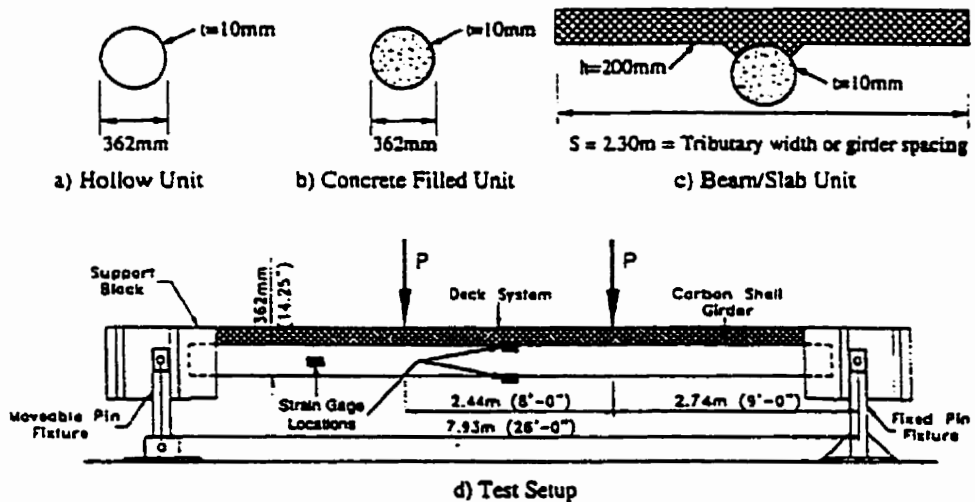


Fig. 2.13 Carbon shell girder bending tests [Karbhari et al 1998]

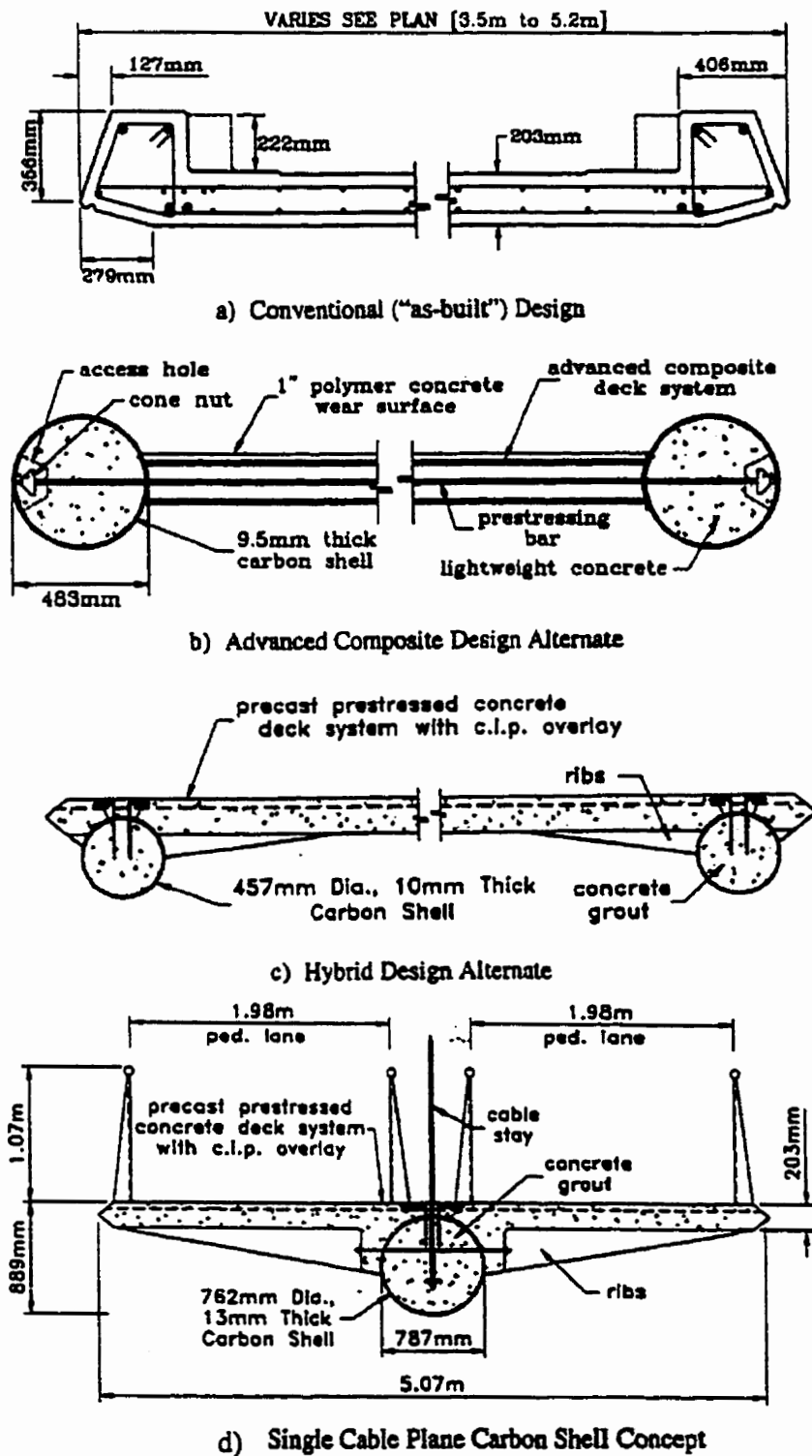


Fig. 2.14 Proposed systems for pedestrian bridge superstructures utilizing the carbon shell concept [Seible 1998]

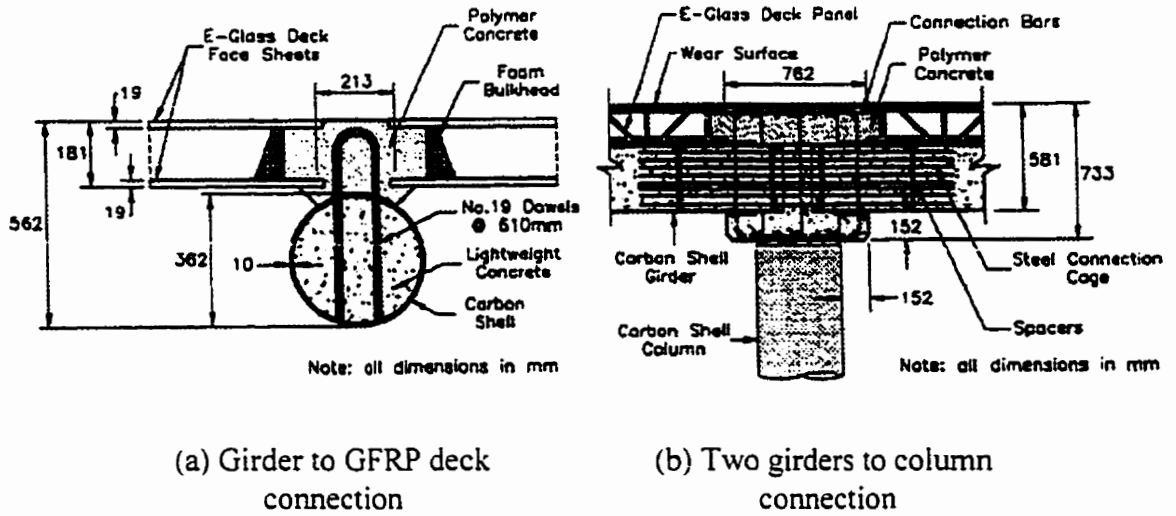


Fig. 2.15 Connection details of concrete-filled carbon shell system [Seible et al 1998]

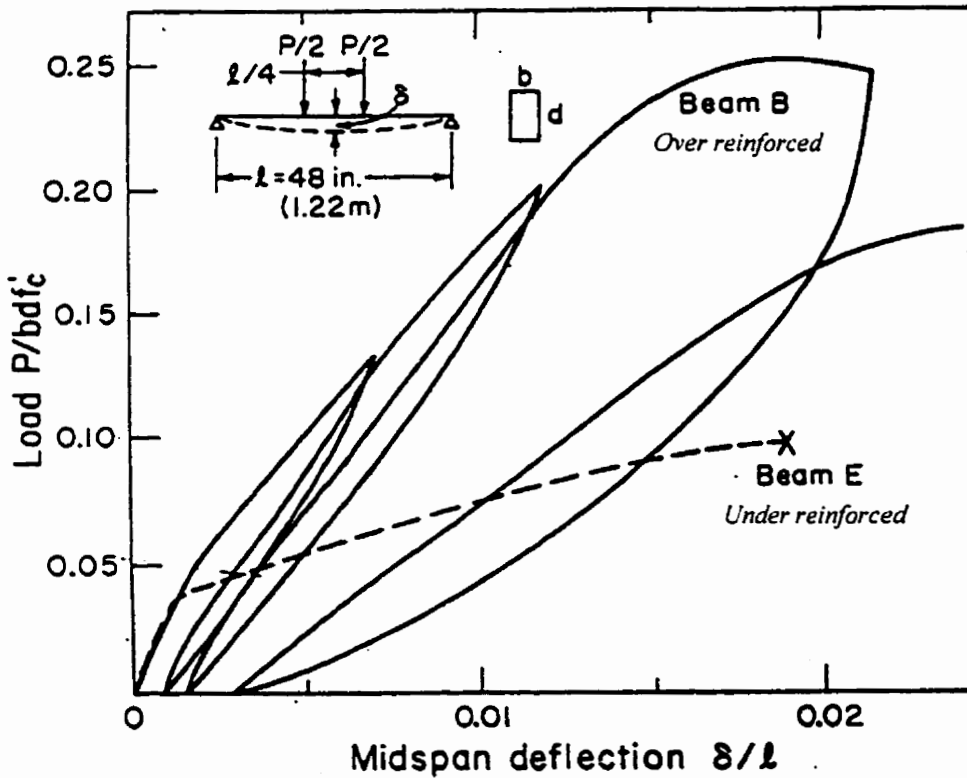


Fig. 2.16 Load-deflection behaviour of under and over-reinforced concrete-filled GFRP box sections [Fardis and Khalili 1981]

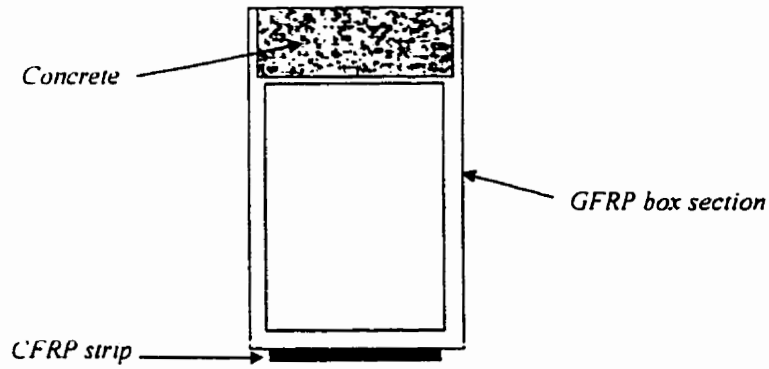


Fig. 2.17 Hybrid concrete/GFRP/CFRP rectangular section [Triantafillou and Meier 1992]

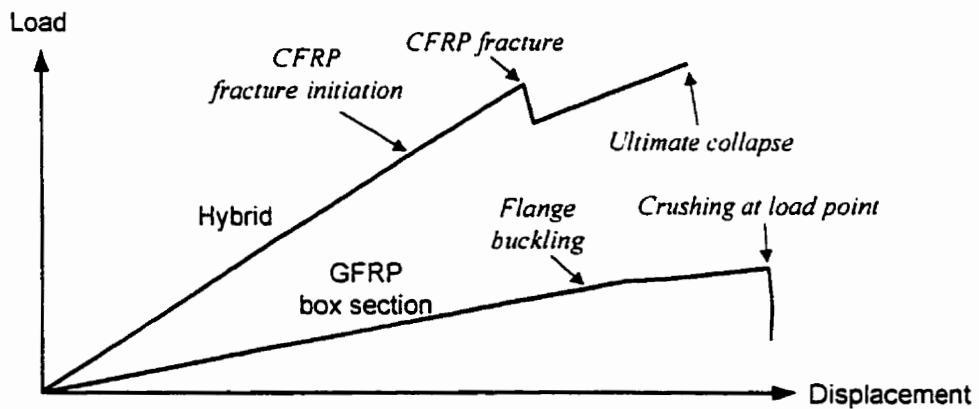


Fig. 2.18 Load-deflection behaviour of hybrid beam and the GFRP box section [Triantafillou 1995]

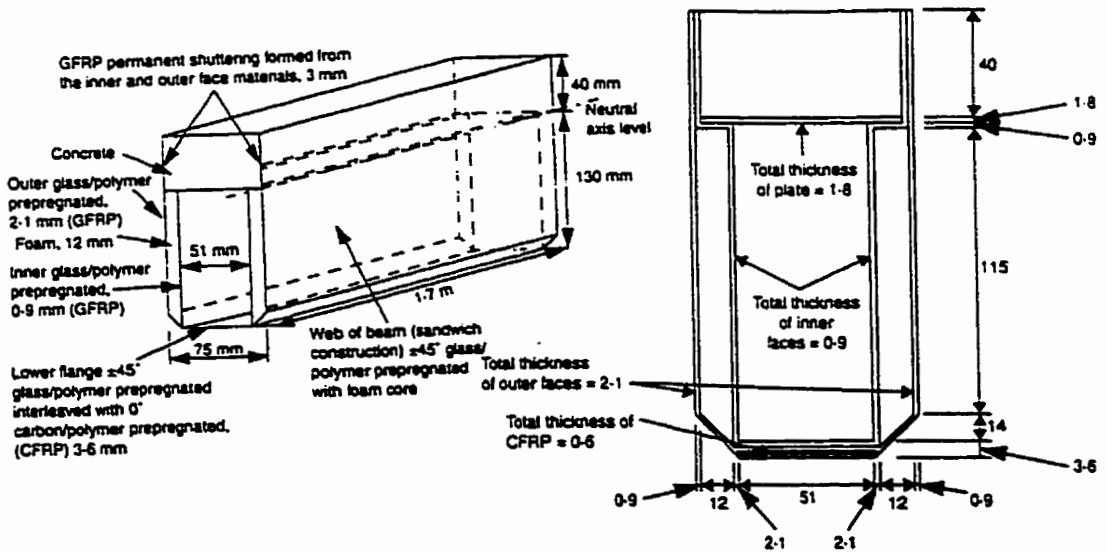


Fig. 2.19 Modified hybrid concrete/GFRP/CFRP rectangular section [Canning et al 1999]

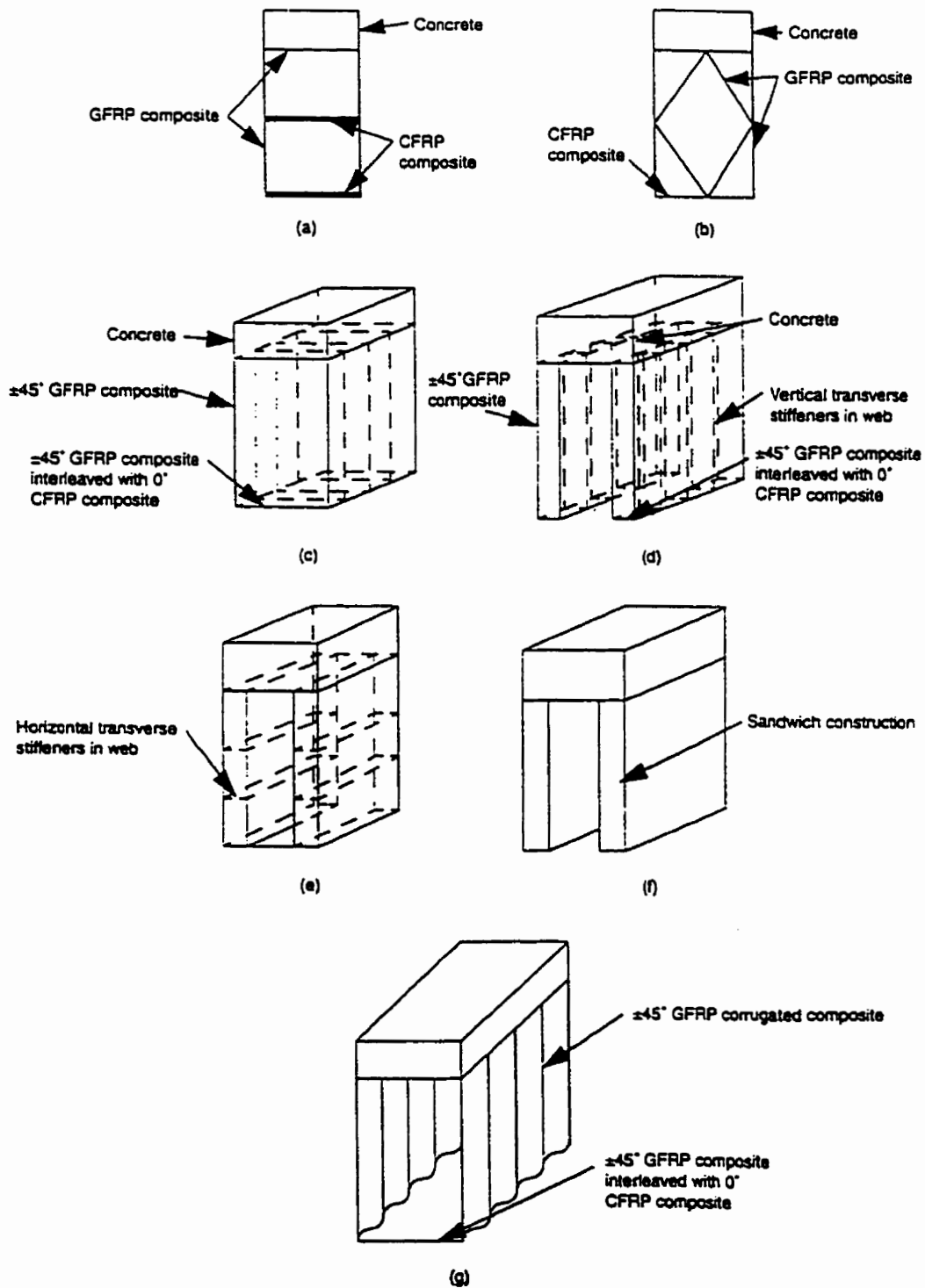


Fig. 2.20 Different configurations proposed for stronger web for the hybrid rectangular section. (a) Intermediate flange. (b) Diamond-shape stiffener. (c) Full diaphragm. (d) Web diaphragm. (e) Cellular web. (f) Foam sandwich. (g) Corrugated web [Canning et al 1999]

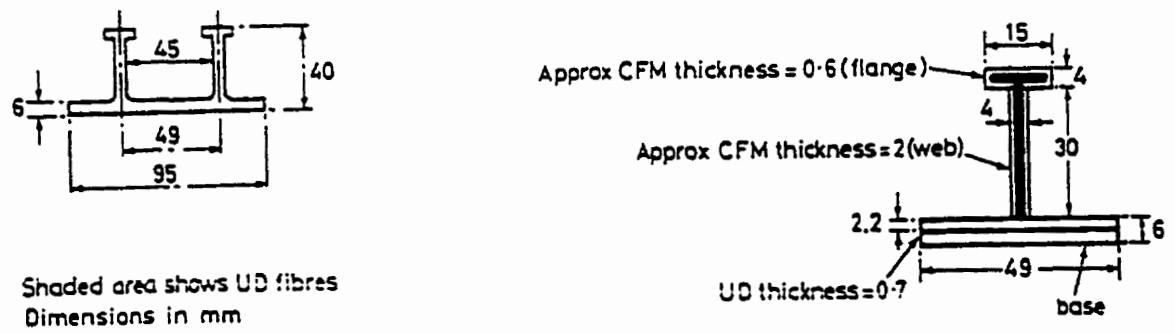


Fig. 2.21 Pultruded FRP panel [Hall and Mottram 1998]

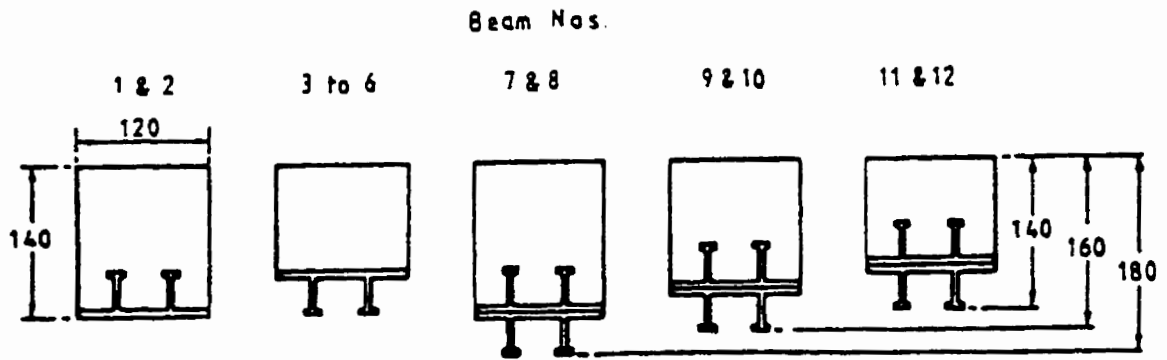


Fig. 2.22 Hybrid rectangular beam cross-section [Hall and Mottram 1998]

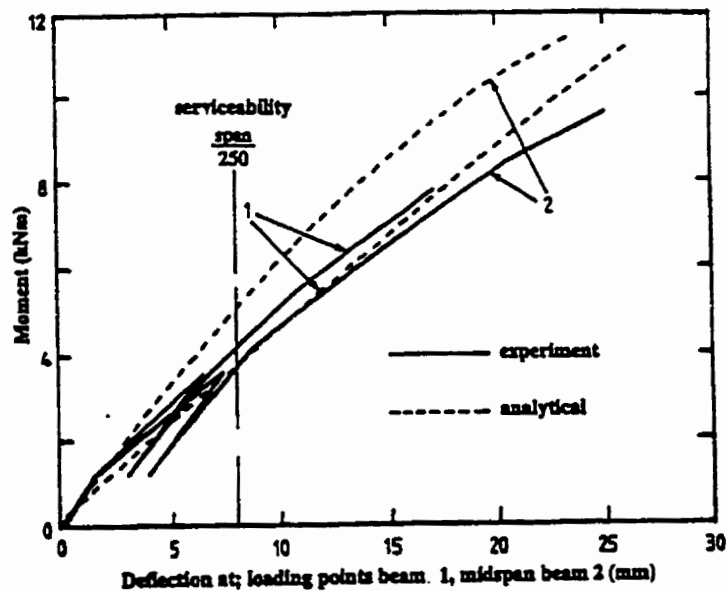


Fig. 2.23 Moment-deflection behaviour of hybrid beams 1 and 2 [Hall and Mottram 1998]

Chapter 3

The Experimental Program

3.1 Introduction

The experimental program was undertaken to study the structural performance of GFRP tubes totally and partially filled with concrete in flexure and under axial compression loading conditions. The study also included a concrete-filled steel tube as well as hollow GFRP and steel tubes as pilot specimens. The first phase, Phase I, is focused on the flexural behaviour through a series of eighteen beams tested under four-point bending. The parameters considered were the effect of concrete filling on the flexural behaviour as compared to hollow tubes, for both the GFRP and steel tubes, different cross-section configurations, and the laminate structure of the tubes including GFRP tubes with different laminate architectures and fibre orientations. Also the effect of the reinforcement ratio and size effect were studied. Phase II included twelve tubes totally and partially filled with concrete tested as short columns (stubs) under axial loads. The stubs were intended to examine the effects of most of the parameters studied in Phase I, but rather on the behaviour of axial members. The beam specimens were instrumented to measure the behaviour in terms of the following responses: load-deflection, moment-curvature, load-strain, and moment-neutral axis depth, while the stubs were instrumented to evaluate the behaviour in terms of load-axial and lateral strain responses. This chapter

presents details and properties of the materials used to fabricate the specimens. fabrication process, instrumentation, and testing of the specimens.

3.2 Materials used to fabricate the Specimens

This section provides description of the different tubes used to fabricate the specimens including manufacturing process, laminate structure, and mechanical properties. The concrete mixes used for filling the tubes are also introduced including the concrete mechanical properties.

3.2.1 Tubes

A total of eleven different cylindrical tubes were used to fabricate the specimens including GFRP filament-wound and pultruded tubes as well as steel tubes. The tubes ranged in diameter from 89 mm to 942 mm and in wall thickness from 2 mm to 10.2 mm. The tubes were given identification numbers ranging from 1 to 11, as shown in Table 3.1, in order to simplify identifying the specific tubes used to fabricate the different beams and stubs later. Table 3.1 provides detailed description of the tubes including their diameter, wall thickness, material of the tubes including GFRP and steel, fibre volume fraction, number of layers and laminate structure of the GFRP tubes. In some tubes, the inner surface had a layer of liner intended to facilitate the removal of the tubes from the mandrel during fabrication. For those tubes, the liner is not considered as part of the structural wall thickness of the tubes. Tubes 1, 3, 4, 5, 6, and 11 were received in 3050 mm lengths, tube 2 was 2500 mm long, tubes 7, 8, and 9 ranged in length from 5500 mm to 6090 mm, and tube 10 was 10970 mm long. Several tubes were received from each

size. The GFRP tubes were fabricated by Ameron International Fibreglass Pipe Group in Burkburnett, Texas, USA except for tube 2, which was fabricated by Faroex Ltd. in Gimli, Manitoba, Canada. The continuous filament-winding process adopted by Ameron International employs standard E-glass roving from either Owens Corning (Toledo, Ohio) or PPG Industries Inc. (Pittsburgh) packaged in especially long lengths wound on 3-inch (76 mm) spools. The resin is Epon 828 epoxy from Shell Chemical Co. (Houston) or DER 331 epoxy from Dow Chemical (Midland, Mich.). In some tubes such as tubes 2, 8, 9, and 10, polyester resin was used. The filament-winding machine at Ameron International is capable of producing cylinders in continuous lengths. As the cylinder is generated, it is rotated on the mandrel while the machine spirals from front to back, providing a fibre orientation which is very close to, but not exactly, circumferential and longitudinal. The process wraps alternating layers in the circumferential and longitudinal directions until the required number of layers is wrapped. The tubes are wound under controlled tension to prevent any loose or wavy glass fibres in the wall [Stapleman 1997]. Table 3.1 also provides the laminate structure and stacking sequence of the GFRP tubes including the thickness of the individual layers as well as the angle of the fibres with respect to the axial direction of the tube. Steel tube 11 was provided by a local supplier in Winnipeg, Manitoba.

3.2.1.1 Mechanical properties of the tubes

The mechanical properties of the tubes were obtained using experimental testing and verified using the data provided by the manufacturer as well as the classical lamination theory [Daniel and Ishai 1994] through computer program "CLASS" [Kibler 1987]. The

experimental testing included longitudinal strips and circular rings cut from the tubes and tested as tension specimens to evaluate the effective elastic modulus and tensile strength in the axial and circumferential directions. Although ideally it is better to test the whole cylindrical section rather than cutting strips to avoid the discontinuities of fibres at the edges, it was very difficult to grip and test large size tubes. Fig. 3.1a shows a schematic of a typical longitudinal tension coupon. Since the stress concentration at the gripping location can severely influence the strength of FRP coupons, the two ends of the GFRP strip were embedded inside hollow steel tubes, 305 mm long each, and secured in place using epoxy resin as a filler. The gripping was applied to the steel tubes and the size of the part of the GFRP coupon between the two steel tubes was 153 x 25 mm. Fig. 3.1b shows a picture of the failed specimens. Fig. 3.2a shows a schematic of a typical 25 mm wide GFRP ring tested in the hoop direction using the split-disk method. Two semi-circular stiff steel plates of a similar curvature to that of the GFRP rings were used to apply the tension force. Fig. 3.2b shows a picture of the failed ring specimens. Hollow tubes 1, 3, and 4 were also tested under axial compression in order to determine their compressive strength. All specimens were tested using a 267 kN RIEHLE universal testing machine. The elastic modulus of tube 3 in the axial direction was also determined later from a hollow tube beam test, beam 2a in Table 3.3, in order to compare with the tension coupon result. From the measured axial strains and moment in the beam test, the flexural stiffness was determined, and from which, the elastic modulus of 33 GPa was determined, which represents an average value of the GFRP tube in tension and compression. On the other hand, the elastic modulus obtained from the tension coupon test was 29 GPa, while that obtained from the axial compression test of the hollow tube

was 33 GPa. The average of the two values is very close to that obtained from the beam test. Mechanical properties of the steel tubes were determined from a beam test of the hollow tube, beam 1a in Table 3.3. For all specimens, strains were measured using electrical strain gauges produced by Tokyo Sokki Kenkyujo Co. Ltd., Japan of type FLA-6-11-5L and a resistance of 120 ohms, along with M-Bond 200 adhesive system. Table 3.2 provides the mechanical properties of the tubes in the axial and circumferential directions. Fig. 3.3 shows typical stress-strain curves of GFRP tube 8 based on the experimental axial tension test results, the manufacturer data, and the lamination theory.

3.2.2 Concrete

Two concrete mixes were designed to induce pressure fit into the tubes after hardening of the concrete to prevent possible separation due to shrinkage. This was achieved by adding expansive agents, commercially known as Conex or CPD, to the concrete mixes. The first mix, Mix 1, contains the following materials per unit cubic meter: 360 kg of type 10 cement, 89 kg of Conex, 803 kg of sand, 998 kg of 3/8 inches (9.5 mm) stone, 154 kg of water, 4.8 kg of super-plasticizer, and 5 percent of air content. The designed slump was 8 inches (203 mm) to provide good workability conditions. This mix is typically used in real applications involving concrete-filled FRP tubes for piles in marine environments. The second concrete mix, Mix 2, contains the following materials per cubic meter: 566 kg of type 10 cement, 5.7 kg of CPD, 768 kg of sand, 715 kg of 3/8 inches (9.5 mm) stone, and 228 kg of water. Three cylinders were tested from each mix according to ASTM C39 standards using a rate of loading of 0.1 mm/minute. The concrete-filled tubes were tested after a period of time ranging from two weeks to six

months from casting, therefore, the concrete compressive strength at time of tests ranged from 28 MPa to 67 MPa. Fig. 3.4 shows a sample of the stress-strain curves of the two concrete mixes used in this study.

3.3 Experimental Phase I - Beam Tests

This section describes the first phase of the experimental program undertaken to evaluate the flexural behaviour of concrete-filled GFRP tubes including description of the beam specimens, which were designed to cover a variety of parameters. Fabrication process, instrumentation, and testing of the beams are also discussed [Fam and Rizkalla 2000 (c) and (d)].

3.3.1 Test Specimens

A total of eighteen beams were tested in bending using four-point loads. Table 3.3 provides the details of the beams including their identification number, test span, spacing between the two applied loads, and the identification number as well as the material of the tubes used to fabricate the beams based on Table 3.1. Table 3.3 also provides the identification number of the concrete mix used in the beam as well as the concrete compressive strength at the time of the beam test based on cylinder tests. The cross-section configurations of the beams are also provided in Table 3.3. The objective of Phase I is to study the effect of the following parameters:

1. The effect of concrete filling of the tubes on the flexural behaviour as compared to that of hollow tubes. This includes both GFRP tubes [beams 2(a, b) and beams 3(a, b)] and steel tubes [beams 1 (a, b)].

2. Different cross-section configurations including totally and partially filled GFRP tubes. This includes a tube totally filled with concrete [beam 4], a partially filled tube with concentric voided core maintained by a non-structural tube [beam 5] and another partially filled tube with the inner void maintained by an additional GFRP tube in a tube-in-tube configuration with concrete filling in between [beam 6]. Additional beam with tube-in-tube configuration, where the inner tube is eccentric towards the tension side of the beam, was also included [beam 7].
3. Different GFRP laminate structures, by comparing beams similar in size and reinforcement ratio but have GFRP tubes of different laminate structures [beam 2(b) to beam 3 (b)], [beam 8 to beam 9] and [beam 10 to beam 11]. Beam 2b has a filament-wound tube, while beam 3b has a pultruded tube. Beam 8 has lower fibre content in the axial direction, 33 percent at 15 degrees, as compared to the hoop direction, 67 percent at 82 degrees, while beam 9 has all the fibres oriented at ± 30 degrees with the longitudinal axis. Beam 10 has similar fibre content in the two directions, at 3 and 88 degrees, while beam 11 has 70 percent of the fibre content at ± 34 degrees and 30 percent in the hoop direction at 80 degrees.
4. Size effect and reinforcement ratio by comparing beams with similar GFRP tubes but having different diameter-to-thickness ratios [beam 11, beam 12, and beam 13].

3.3.2 Fabrication of the Beams

The tubes were cut to the desired length of the beams, cleaned, and dried. Beams 1 to 9 were filled with concrete at the structures laboratory of the University of Manitoba. Fig.

3.5a shows the GFRP and steel tubes used to fabricate those beams before they were filled with concrete. Beams 10 to 13 were filled with concrete at a precast plant, Lafarge Canada, due to their large size. Fig. 3.5b shows the hollow GFRP tubes used to fabricate those beams at the plant before casting the concrete. A rough texture was created on the inner surface of the tubes used to fabricate beams 1 to 7 within ten percent of the length from both ends in order to enhance the bond between the tubes and concrete. This was done by applying a thin layer of epoxy to the inner surface of the tubes and silica sand was sprayed later on top of the tacky epoxy. For beams 6 and 7, the same process was also applied to the outer surface of the inner GFRP tubes to enhance their bond to concrete. Beams 2b, 3b, 8, and 9 were short enough to permit filling them with concrete in a vertical position. Beams 1b, 4, 5, 6, and 7 were cast in an inclined position as shown in Fig. 3.6. Strain gauges were installed on the tubes in the hoop direction before casting to measure the strains resulting from expansion of concrete during curing. The voided concrete core of beam 5 was maintained using a cardboard tube coated with wax. The cardboard tube as well as the inner GFRP tubes of beams 6 and 7 were secured in position through the wooden end plugs used to seal the ends of the beams. A tubular elbow joint was attached at the upper ends of the tubes to facilitate casting the concrete as shown in Fig. 3.6a. Ready-mix concrete (Mix 1) was delivered to the structures laboratory and concrete was cast from the upper ends of the tubes. External vibration was applied to the outer surface of the tubes. Later, after casting and before the complete hardening of concrete, the elbow joints were removed and the end surfaces were finished as shown in Fig. 3.6b. Immediately after casting, hoop strains were monitored during curing for seven weeks. The results of concrete expansion are presented in Chapter 4.

The large tubes used for beams 10, 11, 12, and 13 were filled with concrete at Lafarge Canada as shown in Fig. 3.7 using a setup with the same inclined position adopted for the smaller size beams. The ends of the tubes were sealed using wooden plugs and concrete of Mix 1 type was pumped from the upper end. Concrete was vibrated using an external vibrator attached to the supporting steel frame. Square wooden frames spaced at about 1.5 meters were used to brace beams 12 and 13 during casting and initial hardening of concrete. This was done, mainly to avoid the ovalization of the tubes under the high level of hydrostatic pressure of wet concrete resulting from the large volume of concrete and the height of the setup.

3.3.3 Instrumentation

The instrumentation of the beams was concentrated within the constant moment zone for strain and deflection measurements, as well as the two ends of the beam for slip measurements. Electrical strain gauges produced by Tokyo Sokki Kenkyujo Co. Ltd., Japan of type FLA-6-11-5L and a resistance of 120 ohms were used with M-Bond 200 adhesive system to measure strains in axial and circumferential directions of the tubes. Displacement gauges (PI-gauges) were also attached to the surfaces of the tubes to monitor the average longitudinal strains. Deflection at mid-span was monitored using Linear Motion Transducer (LMT). Mechanical dial-gauges were mounted at the ends to monitor any slip occurs between the concrete and the shell. Strains during curing were monitored using a digital strain indicator. Displacement and strain readings as well as the load and stroke of the machine were recorded during the tests using data acquisition

system. Fig. 3.8 shows schematic and pictures of the different instrumentation and their locations on the beam. In beams 6 and 7, the inner GFRP tubes were instrumented with additional strain gauges located at the same level of those installed on the outer GFRP tubes in order to check for the strain compatibility between the inner and outer shells.

3.3.4 Test Setup

All beams were tested under four-point bending using two concentrated loads to provide a zone of pure bending as shown in Fig. 3.9. The beams were simply supported on rollers at each end. The rollers were resting on stiff supports for all beams except for beams 2, 3, 8, and 9, where the roller supports were supported by the base of the machine. The loads were applied using a steel spreader beam, which transfers the loads to the round surface of the beams through curved loading plates connected to the spreader beam with another set of hinges. Beams 2, 3, 8, and 9 were tested under stroke control using a 267 kN RIEHLE universal testing machine with a rate of loading of approximately 1.25 mm/minute. The rest of the beams were also tested under stroke control using a closed-loop MTS 5000 kN cyclic loading testing machine with a rate of loading ranging from 0.5 to 1.5 mm/minute. Data was recorded at a rate of one sample per second using a 32 channels data acquisition system. Fig. 3.10 shows the test setup for beams 8 and 4. Beam 8 represents the small beams 2, 3, 8, and 9, which were all tested using the same setup, while beam 4 represents the medium size beams 1, 4, 5, 6, and 7. Fig. 3.11 shows the test setup of beams 11 and 13 representing the large size beams. Spans of all the beams and spacing between loads are given in Table 3.3.

3.4 Experimental Phase II - Stub Tests

This section describes the second phase of the experimental program undertaken to evaluate the behaviour of concrete-filled GFRP tubes under axial compression loading condition as short columns (stubs). The following sections include description of the stubs used to study the different parameters, fabrication process, instrumentation, and testing [Fam and Rizkalla 2000 (a) and (d)].

3.4.1 Test Specimens

A total of twelve stubs were tested under axial compression in order to evaluate the confinement effect on strength and ductility of concrete. Table 3.4 provides details of the stubs including their identification number, outer diameter as well as the inner diameter for partially filled tubes and the height, which is twice the outer diameter. Table 3.4 also provides the tubes identification numbers and material type (refer to Table 3.1) as well as the beams identification numbers from which the stubs were cut (refer to Table 3.3). The concrete compressive strengths and the cross-section configurations of the stubs are also provided in Table 3.4. The interface condition between the concrete core and the tube is also given in the Table, including a natural smooth interface as well as a rough interface. The following parameters were considered in Phase II:

1. Effect of material type of the tube on the behaviour of confined concrete including concrete-filled GFRP and steel tubes, [stubs 1 and 7].
2. Effect of laminate structure of the GFRP tube including a stub with filament-wound tube [stub 11] and a stub with pultruded tube [stub 12].

3. Different cross-section configurations including totally filled GFRP tubes [stubs 1 and 2], partially filled tubes with inner concentric voids [stubs 3 and 4], and partially filled tubes with the inner voids are maintained using additional GFRP tubes in a tube-in-tube configuration [stubs 5 and 6].
4. Different interface condition between the concrete and the tube including both smooth and rough interfaces [stubs 1 and 2, stubs 3 and 4, and stubs 5 and 6].
5. Different central void sizes for stubs identical in terms of the outer diameter and the GFRP tubes used, but having inner voids of different sizes [stubs 8, 9, and 10].
6. Effect of stiffness of the GFRP tubes in the hoop direction including GFRP tubes totally filled with concrete but having different stiffness in the hoop direction. The stiffness is governed by the circumferential effective elastic modulus as well as the diameter-to-thickness ratio of the tube [stubs 1, 2, 8, 11, and 12].
7. Effect of loading the GFRP tube in the axial direction with the concrete core as a composite system. In this study the axial loads were applied to both the GFRP tubes and the concrete cores, therefore, another study [Mirmiran and Shahawy 1997], which had the axial load applied to the concrete core only, was selected for comparison. The selected stubs had the same stiffness as stubs 1, 2, 8, 11 and 12.

3.4.2 Fabrication of Stubs

The stubs were cut to a length of twice the outer diameter from the ends of some of the beams tested in Phase I, far from the flexural failure region, using a diamond saw as shown in Fig. 3.12 and Fig. 3.13. Stubs 8, 9, and 10 were cut from concrete-filled tubes (tube 6 in Table 3.1) intended to produce the stubs and was not part of Phase I. The stubs

with rough interface between the tubes and the concrete core. stubs 1, 3, 5, 7, 11 and 12, were cut from the far ends of the tubes where a layer of epoxy and silica sand was applied to the surface before casting.

3.4.3 Instrumentation

Two strain gauges, 180 degrees apart in a cross-section plane, were installed on the surface at mid-height of the stubs in the axial direction. 100 mm displacement PI-gauges were also attached to the surface in the axial direction at mid height, 180 degrees apart from each other, but each was 90 degrees apart from the nearest strain gauge as shown in Fig. 3.14. Two other strain gauges were installed in the circumferential direction beside the axial strain gauges. This pattern allows for lateral strain measurements at two sides and axial strain measurements at four sides around the perimeter of the stub for more accuracy and also to check if load eccentricity, which is not intended, takes place in any direction. For stubs number 5 and 6, two extra strain gauges were installed on both the inner and outer shells in the circumferential direction, 40 mm from the top surface, above one of the strain gauge stations located at mid-height.

3.4.4 Test Setup

The stubs were intended to model practical applications of concrete-filled GFRP tubes, where the concrete core and the tube are acting as a composite member, therefore, the axial load was applied to the entire section including both the concrete core and the confining tube. Stubs were tested, as shown in Fig. 3.14, using a closed-loop 5000 kN MTS cyclic loading testing machine under stroke control with a 0.1 mm/minute rate of

loading, similar to that used for concrete cylinders according to ASTM C39. A thin layer of quick-set plaster was placed between the end faces of the stub and both the loading and supporting steel plates to ensure uniform loading pressure. Data were recorded during the test using a 32 channels data acquisition system.

Table 3.1 Dimensions and details of the tubes used to fabricate the beams and the stubs

Tube number	Outer diameter (mm)	Thickness *		Material type	Fiber / matrix	Fiber volume % age	Number of layers	Laminate structure and stacking sequence **										
		total (mm)	structural (mm)					Layer										
		1	2					3	4	5	6	7	8	9	10			
1	89	2.28	2.05	GFRP ^{FW}	E-glass / epoxy	51	9	Thickness (mm)	0.18	0.33	0.25	0.18	0.25	0.18	0.25	0.18	0.25	
								Angle (degrees)	+15	-82	-82	+15	-82	+15	-82	+15	-82	
2	90	2.0	2.0	GFRP ^{FW}	E-glass / polyester	56	6	Thickness (mm)	0.33	0.34	0.33	0.34	0.33	0.33				
								Angle (degrees)	+30	-30	+30	-30	+30	-30				
3	100	3.08	3.08	GFRP ^{FW}	E-glass / epoxy	51	9	Thickness (mm)	0.32	0.35	0.27	0.48	0.26	0.51	0.19	0.51	0.19	
								Angle (degrees)	-88	+3	-88	+3	-88	+3	-88	+3	-88	
4	100	3.09	3.09	GFRP ^P	E-glass / epoxy	51	1	Thickness (mm)	3.09									
								Angle (degrees)	0									
5	168	3.73	2.56	GFRP ^{FW}	E-glass / epoxy	51	9	Thickness (mm)	0.08	0.36	0.28	0.25	0.38	0.25	0.36	0.25	0.35	
								Angle (degrees)	+8	-86	-86	+8	-86	+8	-86	+8	-86	
6	219	3.7	2.21	GFRP ^{FW}	E-glass / epoxy	51	9	Thickness (mm)	0.23	0.23	0.23	0.25	0.25	0.28	0.25	0.24	0.25	
								Angle (degrees)	+15	-82	-82	+15	-82	+15	-82	+15	-82	
7	326	7.05	6.4	GFRP ^{FW}	E-glass / epoxy	51	10	Thickness (mm)	0.56	0.43	0.56	0.56	0.89	0.56	0.86	0.56	0.86	0.56
								Angle (degrees)	-88	+3	-88	-88	+3	-88	+3	-88	+3	-88
8	320	7.22	5.96	GFRP ^{FW}	E-glass / polyester	51	5	Thickness (mm)	1.04	1.04	1.8	1.04	1.04					
								Angle (degrees)	+34	-34	+80	+34	-34					
9	626	6.68	5.41	GFRP ^{FW}	E-glass / polyester	51	5	Thickness (mm)	0.94	0.95	1.63	0.94	0.95					
								Angle (degrees)	+34	-34	+85	+34	-34					
10	942	10.2	8.93	GFRP ^{FW}	E-glass / polyester	51	7	Thickness (mm)	1.14	1.15	2.07	1.14	1.15	1.14	1.14			
								Angle (degrees)	+34	-34	+86	+34	-34	+34	-34			
11	169	4.09	4.09	Steel														

* Some tubes have a liner at the inner surface to facilitate removing the tubes from the mandrel. The liner is not part of the structural wall thickness

** Angles of fibers are measured with respect to the longitudinal axis of the tube

GFRP^{FW} = Filament-wound GFRP tube















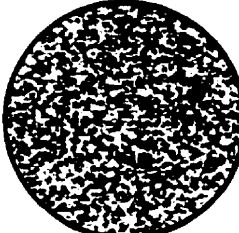
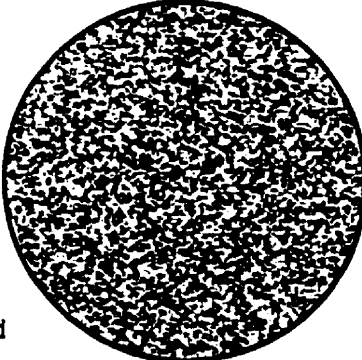
GFRP^P = Pultruded GFRP tube

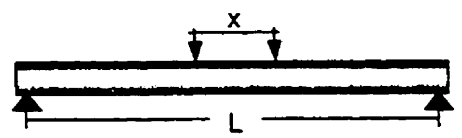
Table 3.2 Mechanical properties of the tubes used to fabricate the beams and the stubs

Tube number	Properties in the axial direction										Properties in the hoop direction								
	E (GPa)			f_u (Ten.) (MPa)			f_u (Comp.) (MPa)			ν ''			E (GPa)			f_u (Ten.) (MPa)			
	E*	M*	L*	E	M	L	E	M	L	E	M	L	E	M	L	E	M	L	
1			17.6			209			84			0.15			27.6			261	
2			22			171									9.7			108	
3	29		31	449		480	115		136						23			398	
4			37.7	629			161					0.24			8.7			193	
5	19.7	19.3	17.4	283	224	348	224	78		0.06	0.09			33.4	27.6	27.7	548	448	547
6	19.8		17.8	201		318	183	74		0.05	0.08			33.4	27.8	27.8	548		536
7	17	20.7	22.5	237	345	401	276	90		0.11	0.09				24.2			465	
8	14.7	15.2	16.4	178	207	249		103		0.57	0.34				17.1			326	
9	14.3	15.2	16.6	206	207	250		104		0.49	0.32				17.7			353	
10		15.2	17		207	244		104			0.39				15			216	
11	203			305	yield		305	yield		0.3			203				305	yield	

E* = Based on experimental testing M* = Based on manufacturer data L* = Based on lamination theory
 ** Poisson's ratio represents the circumferential / axial strain ratio due to axial loading













Table 3.3 Summary of experimental Phase I. test beams

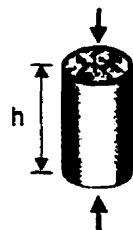
Beam number	Span, L (m)	Spacing between loads, x (m)	Tubes used from Table 3.1	Material of tube	Concrete mix	Concrete strength, f'_c (MPa)	Cross-section configuration
1 (a, b)	2.9	0.4	11	Steel	1	58	(a)  (b) 
2 (a, b)	1.3	0.2	3	GFRP	2	37	(a)  (b) 
3 (a, b)	1.3	0.2	4	GFRP	2	37	(a)  (b) 
4	2.9	0.4	5	GFRP	1	58	
5	2.9	0.4	5	GFRP	1	58	
6	2.9	0.4	5, 1	GFRP	1	58	
7	2.9	0.4	5, 1	GFRP	1	58	
8	1.07	0.2	1	GFRP	2	37	
9	1.07	0.2	2	GFRP	2	28	
10	5.5	1.5	7	GFRP	1	60	
11	5.5	1.5	8	GFRP	1	67	
12 (a, b)*	5.0	1.5	9	GFRP	1	33	
13 (a, b)*	10.4	1.5	10	GFRP	1	58	



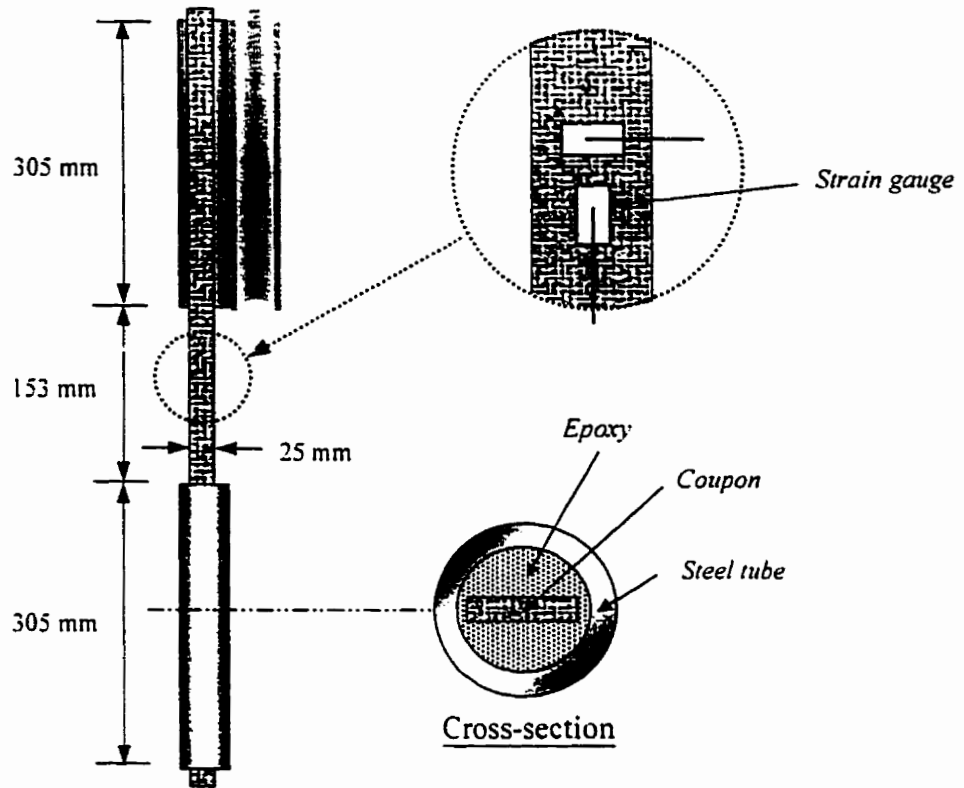
* Two identical beams, (a) and (b), were tested

Table 3.4 Summary of experimental Phase II. test stubs

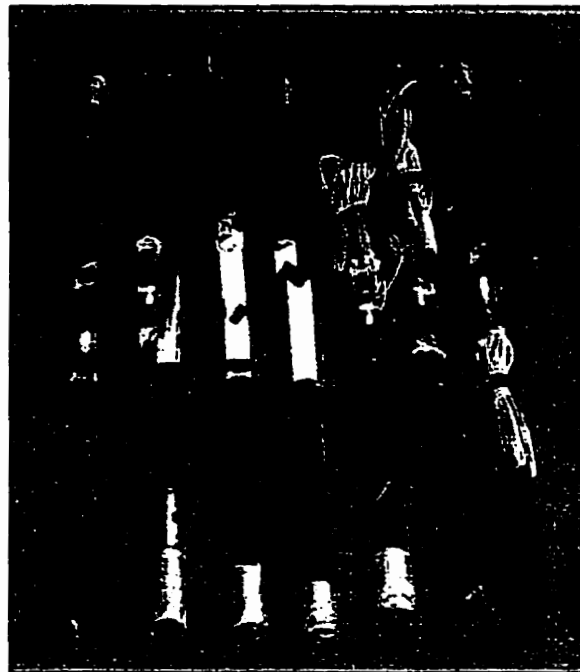
Stub number	Outer/inner Diameter (mm)	Height h (mm)	Tubes used from Table 3.1	Material of tube	The beam, the stub is cut from	Concrete strength, f'_c (MPa)	Interface condition	Cross-section configuration
1	168/0	336	5	GFRP	4	58	Rough	
2	168/0	336	5	GFRP	4	58	Smooth	
3	168/95	336	5	GFRP	5	58	Rough	
4	168/95	336	5	GFRP	5	58	Smooth	
5	168/84	336	5, 1	GFRP	6	58	Rough	
6	168/84	336	5, 1	GFRP	6	58	Smooth	
7	169/0	338	11	Steel	1(b)	58	Rough	
8	219/0	438	6	GFRP	*	58	Smooth	
9	219/95	438	6	GFRP	*	58	Smooth	
10	219/133	438	6	GFRP	*	58	Smooth	
11	100	200	3	GFRP	2 (b)	37	Rough	
12	100	200	4	GFRP	3 (b)	37	Rough	



* Stubs 8, 9, and 10 were cut from totally and partially-filled tubes (tube 6) which were not tested as beams

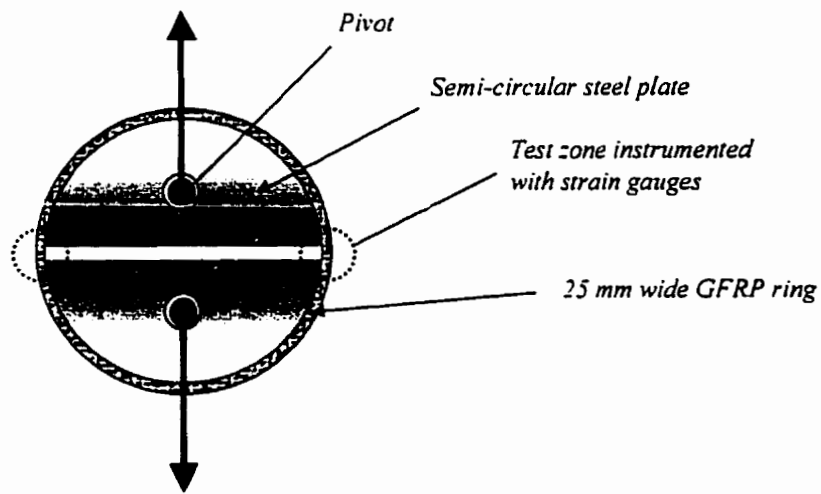


(a) Schematic of the tension coupon

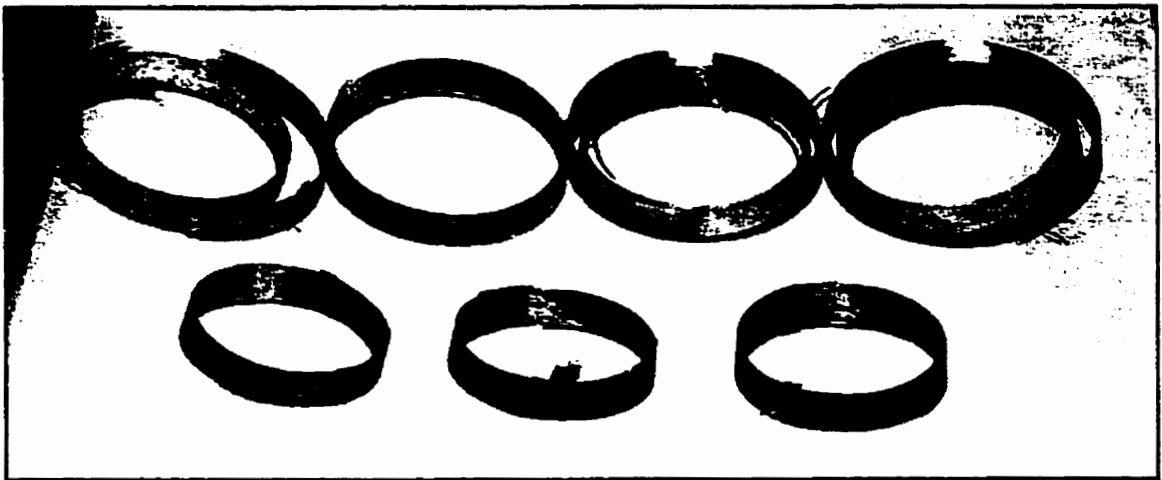


(b) Tension coupons after failure

Fig. 3.1 Tension coupons used to determine the mechanical properties of the tubes in axial direction



(a) Schematic of split-disk tension test



(b) GFRP rings after failure

Fig. 3.2 GFRP rings used to determine the mechanical properties in the circumferential direction using the split-disk test

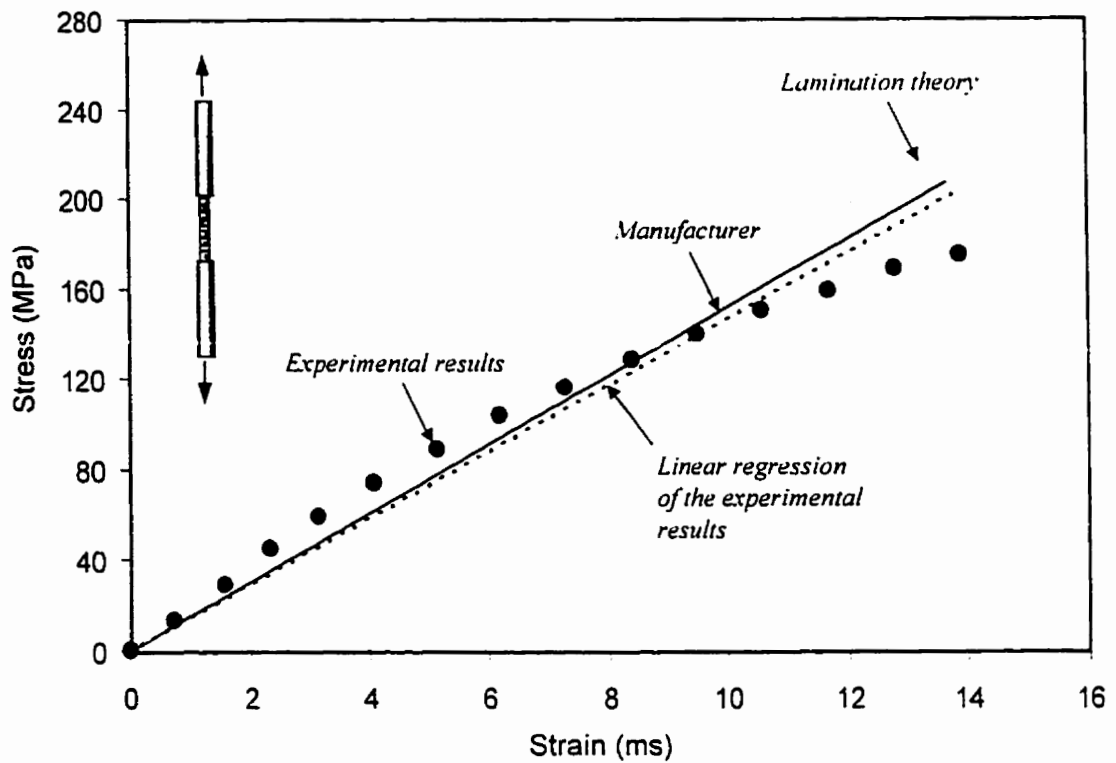


Fig. 3.3 Stress-strain curve of GFRP tube 8 under axial tension

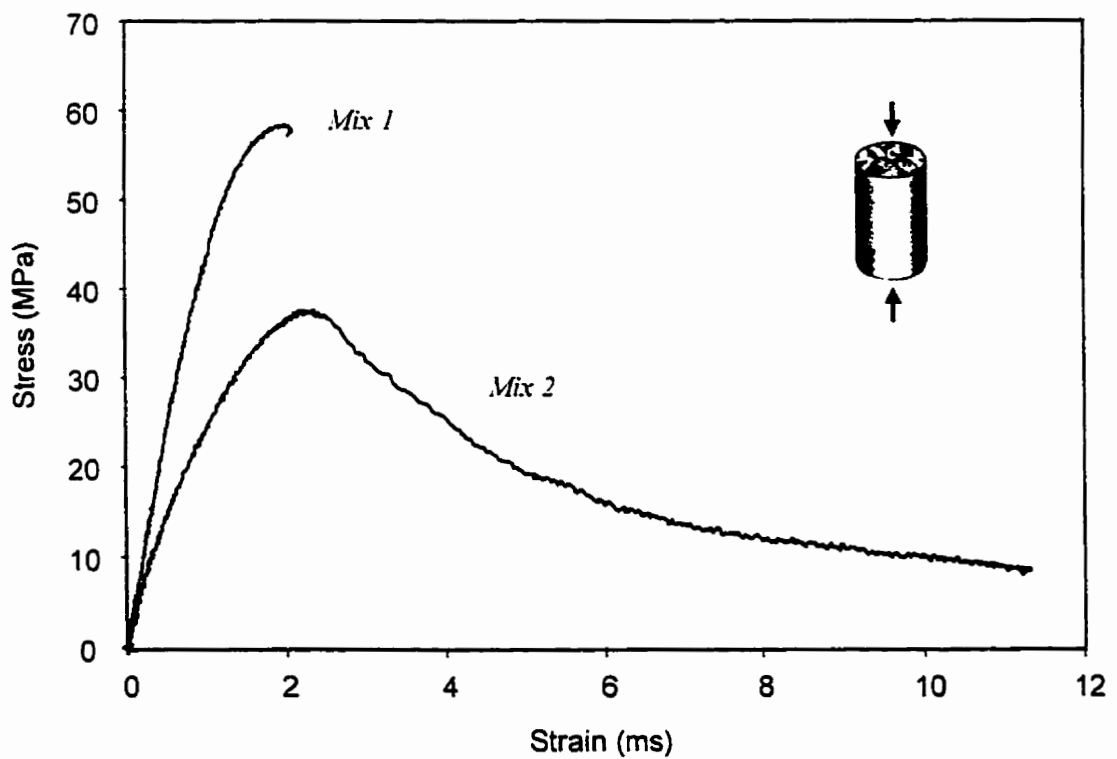
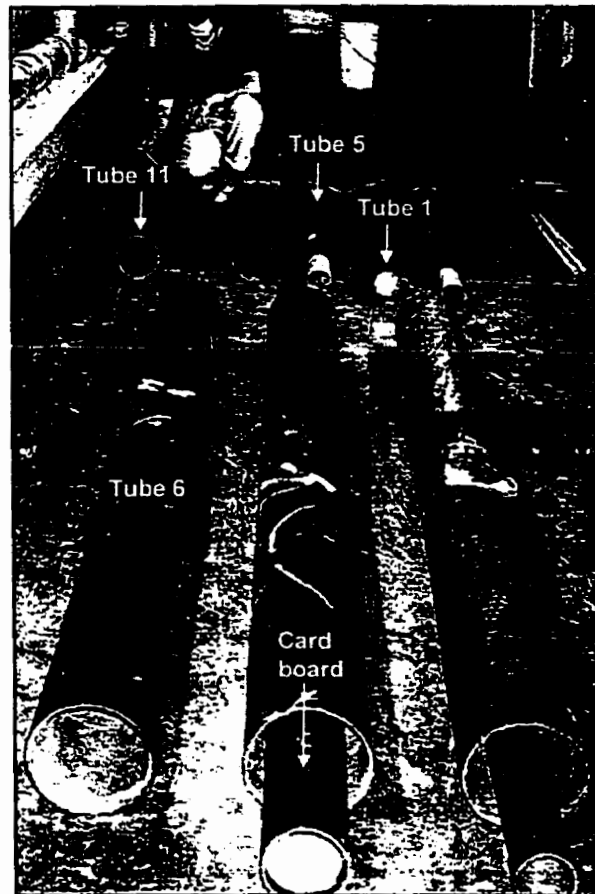
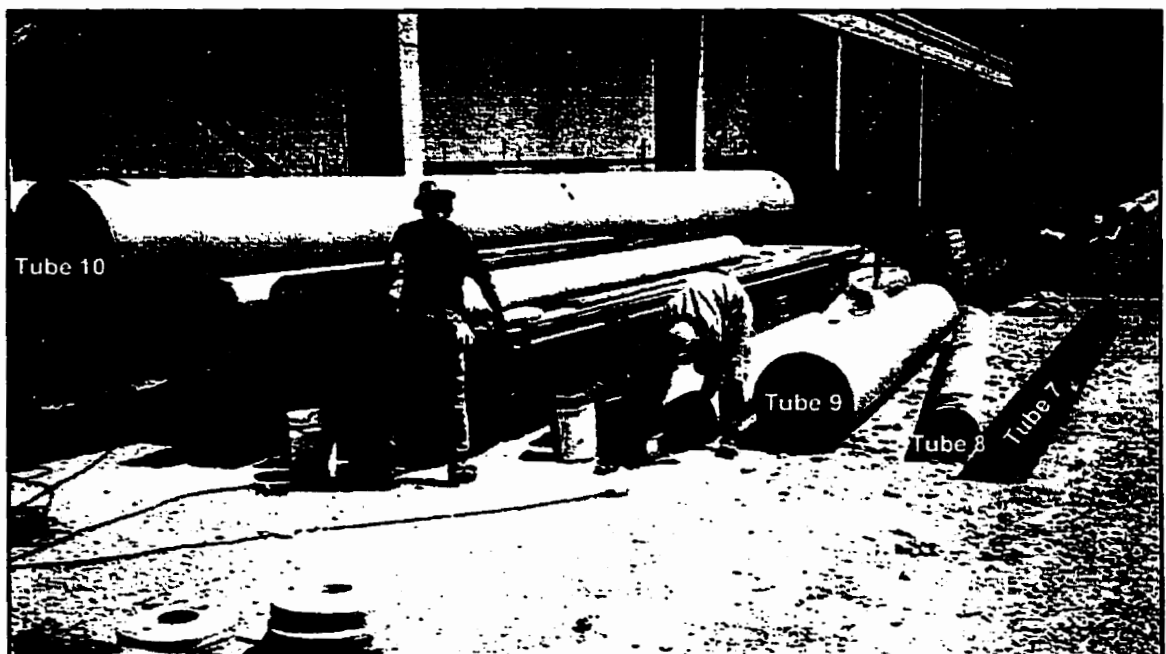


Fig. 3.4 Stress-strain curves of concrete under axial compression



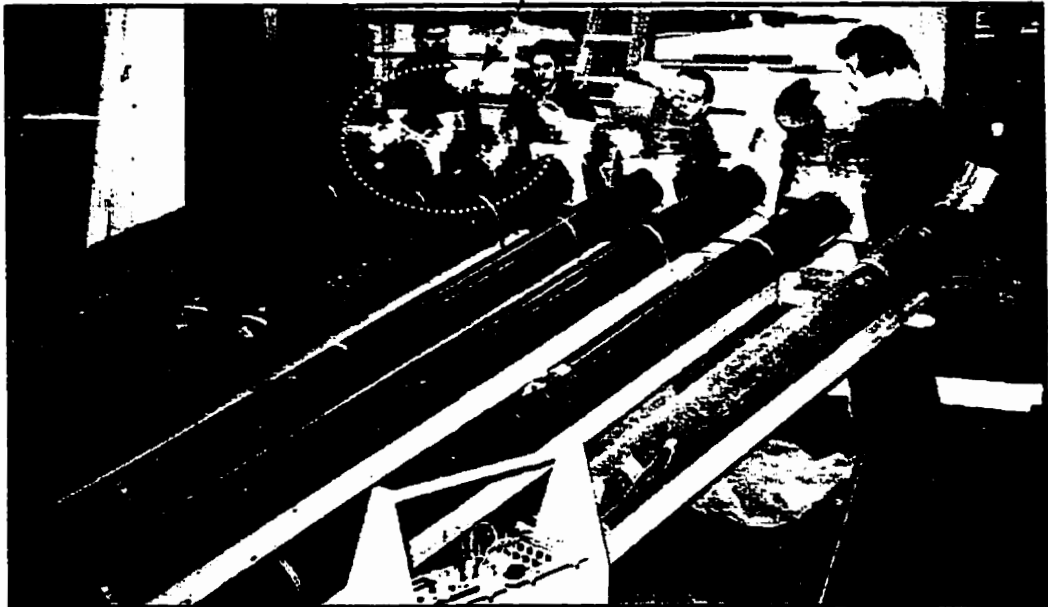
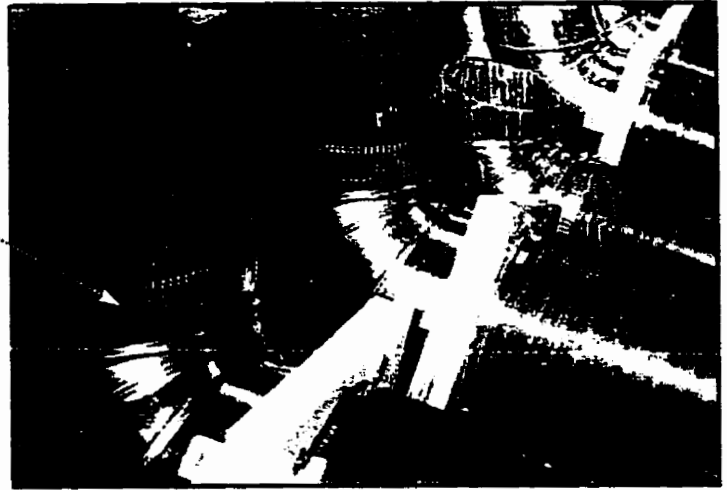
(a) Small tubes 1 to 6 and 11 at the structures laboratory



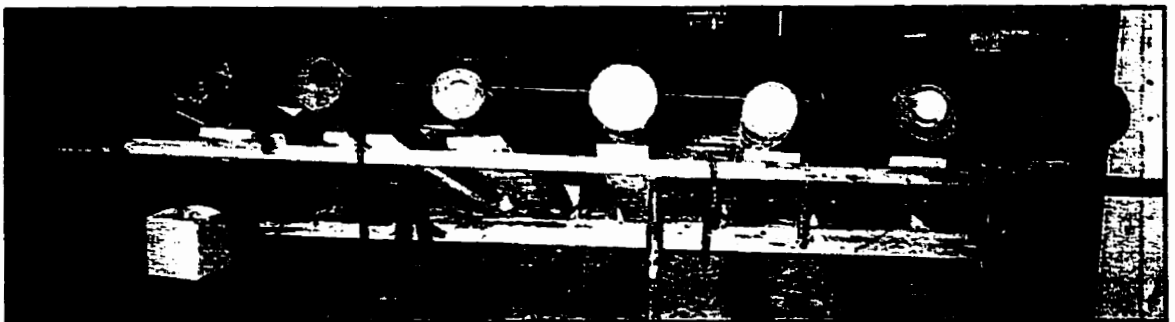
(b) Large tubes 7 to 10 at the precast plant

Fig. 3.5 GFRP and steel tubes before casting (See Table 3.1 for identification numbers)

Tubular elbow joints attached to the upper ends of the tubes to facilitate casting



(a) During casting



(b) After casting

Fig. 3.6 Casting setup of beams 1b, 4, 5, 6, and 7 at the structures laboratory

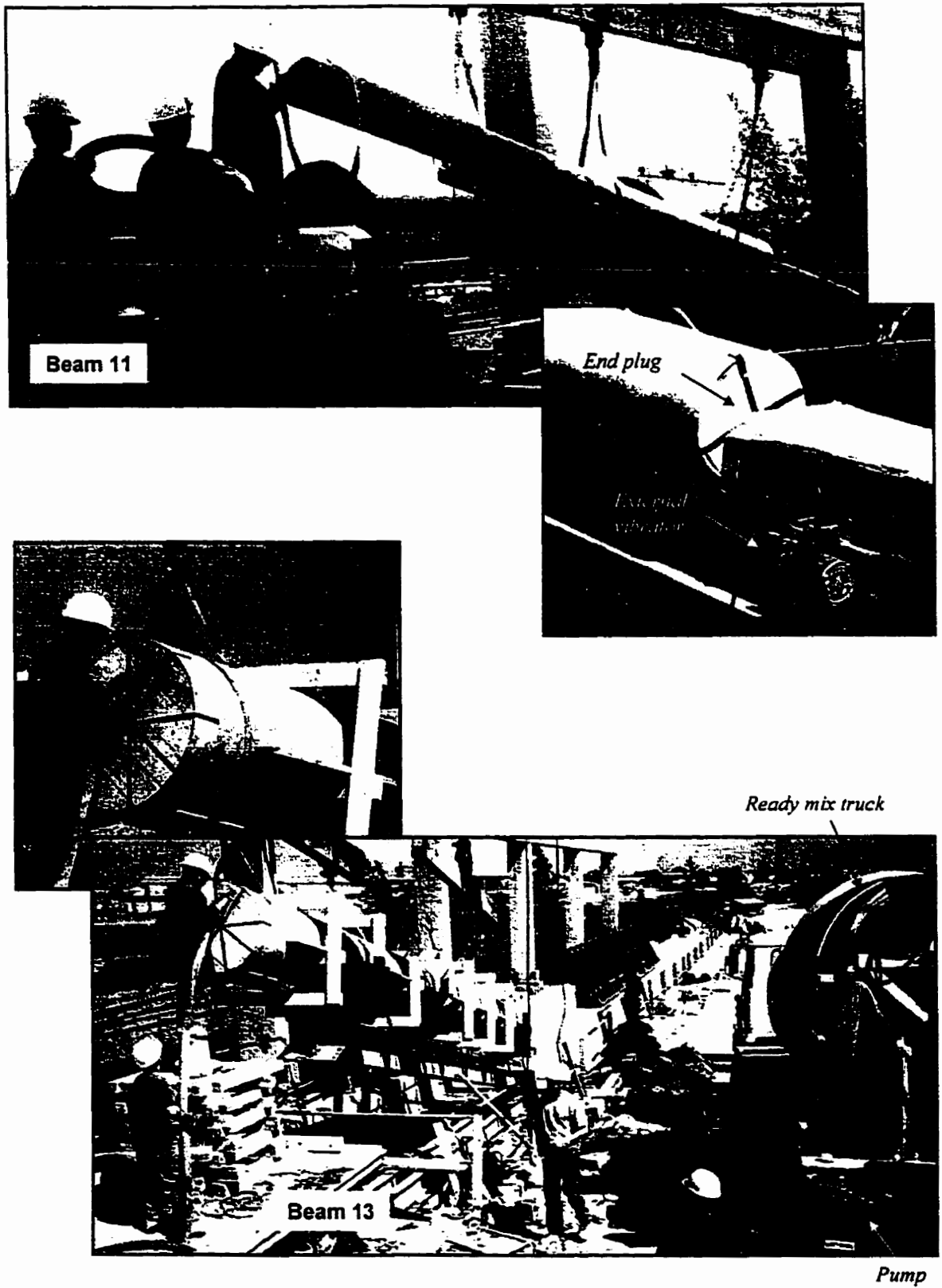
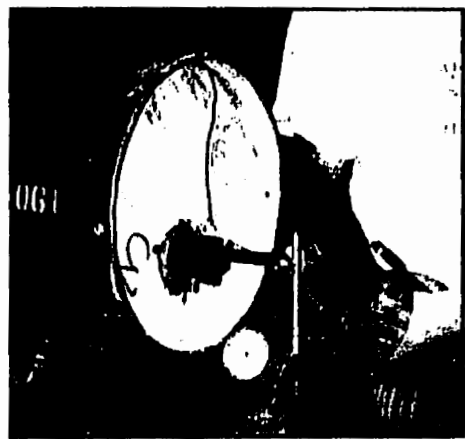
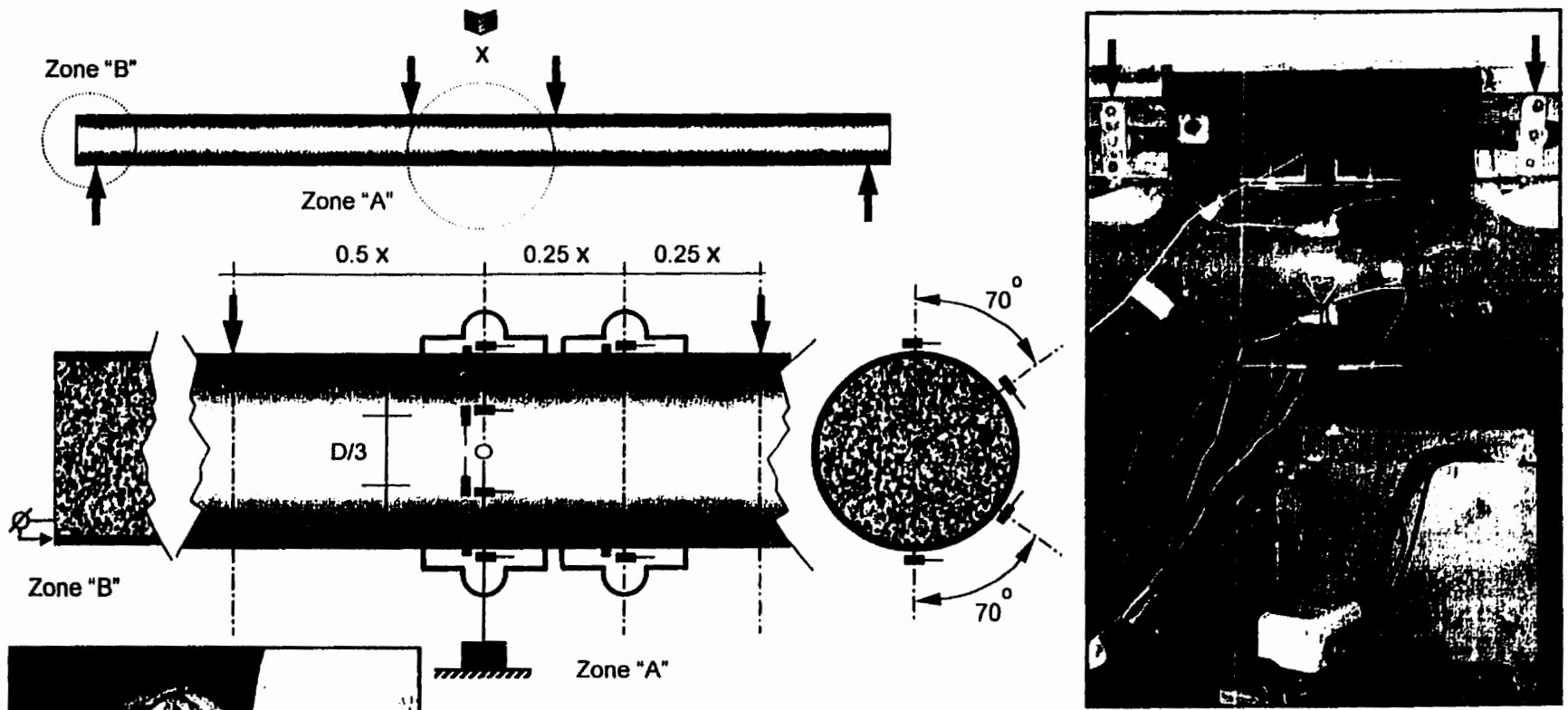


Fig. 3.7 Casting setup of beams 10, 11, 12, and 13 at a precast plant



Code	Type / brand		Function / output
	Strain gauge in the longitudinal direction	Produced by Tokyo Sokki Kenkyujo Co. Ltd., Japan of type FLA-6-11-5L and a resistance of 120 ohms	Strains in the two directions
	Strain gauge in the transverse direction		
	Displacement gauge (200-mm PI gauge)		Axial strains
	Linear Motion Transducer (LMT)		Mid-span deflection
	Mechanical dial-gauge		Relative slip
	Closed-loop 5000 kN MTS or 267KN RIEHLE universal testing machine		Stroke-control loading

Fig. 3.8 Instrumentation of test beams

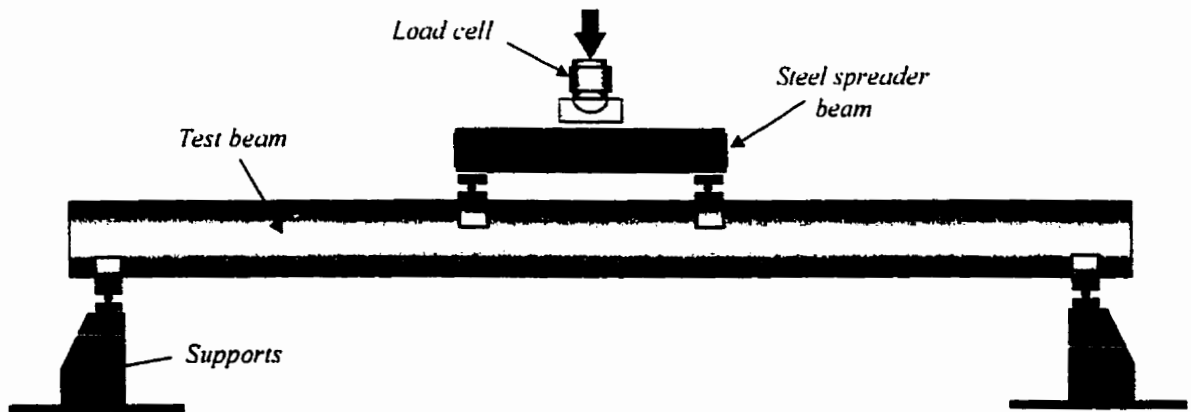


Fig. 3.9 Schematic of test setup for beams

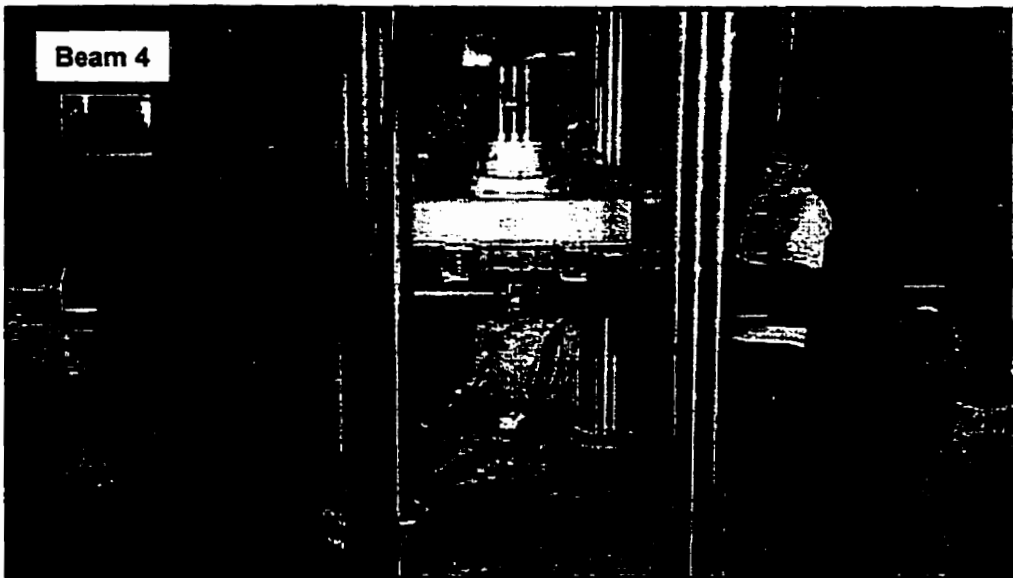
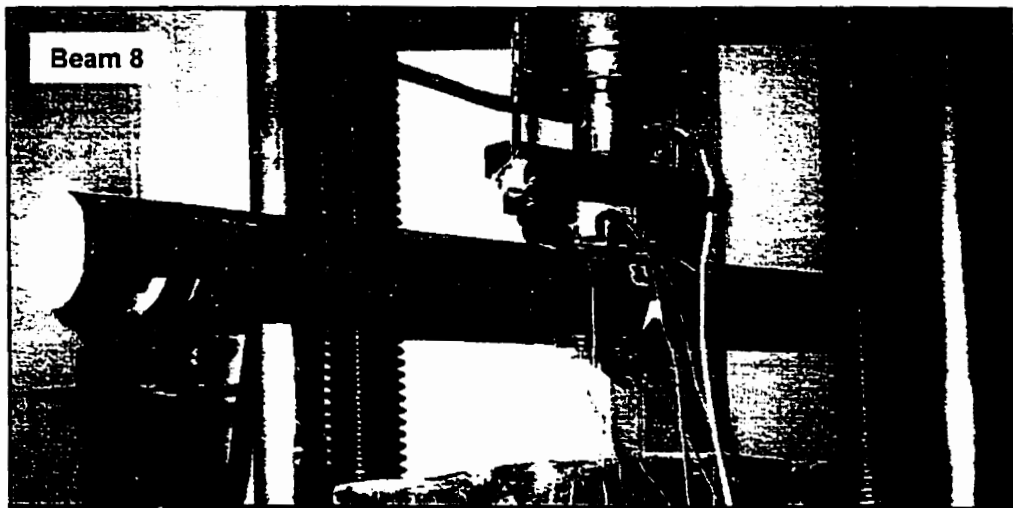


Fig. 3.10 Test setup of small and medium size beams, beams 8 and 4

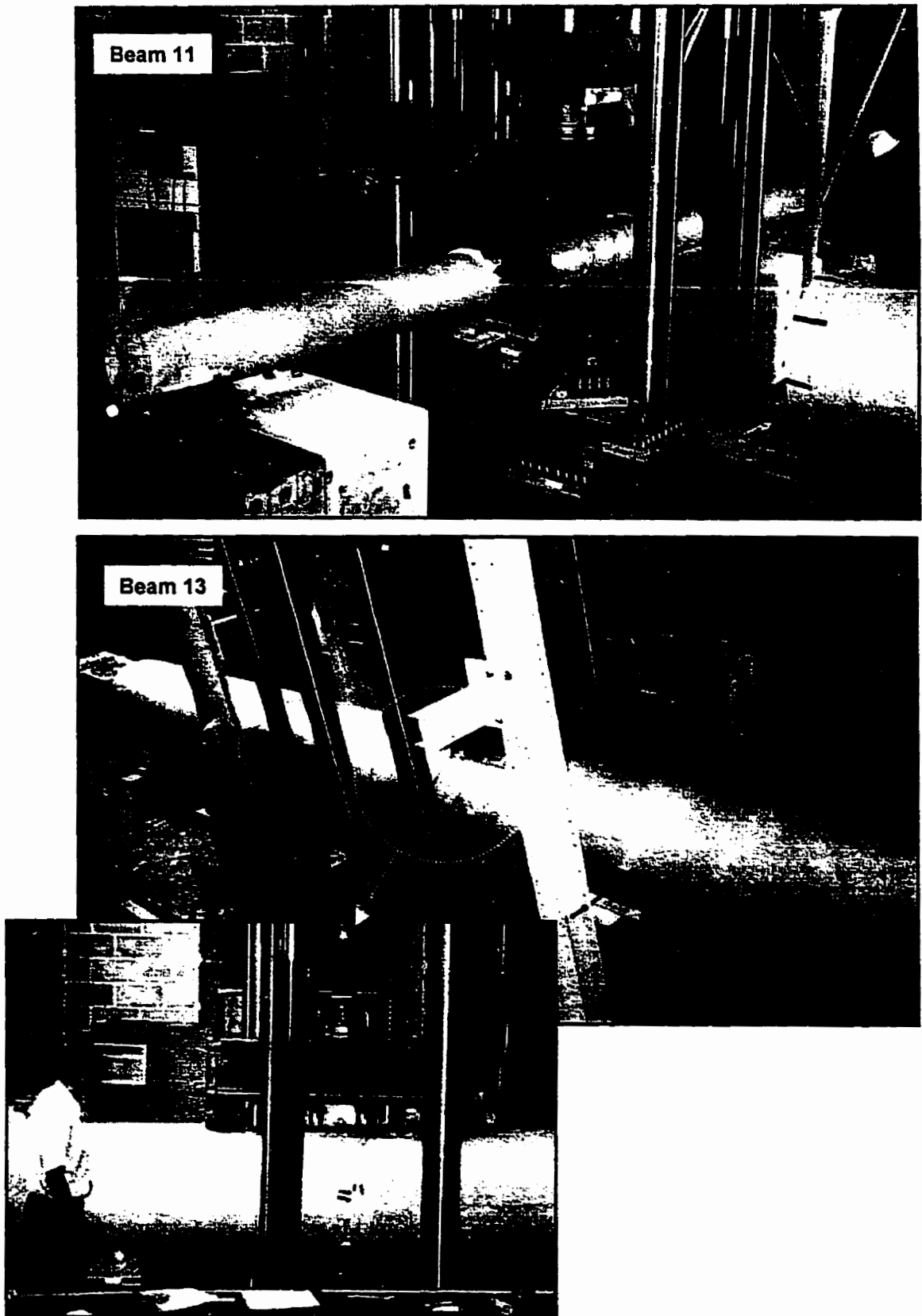


Fig. 3.11 Test setup of large beams, beams 11 and 13

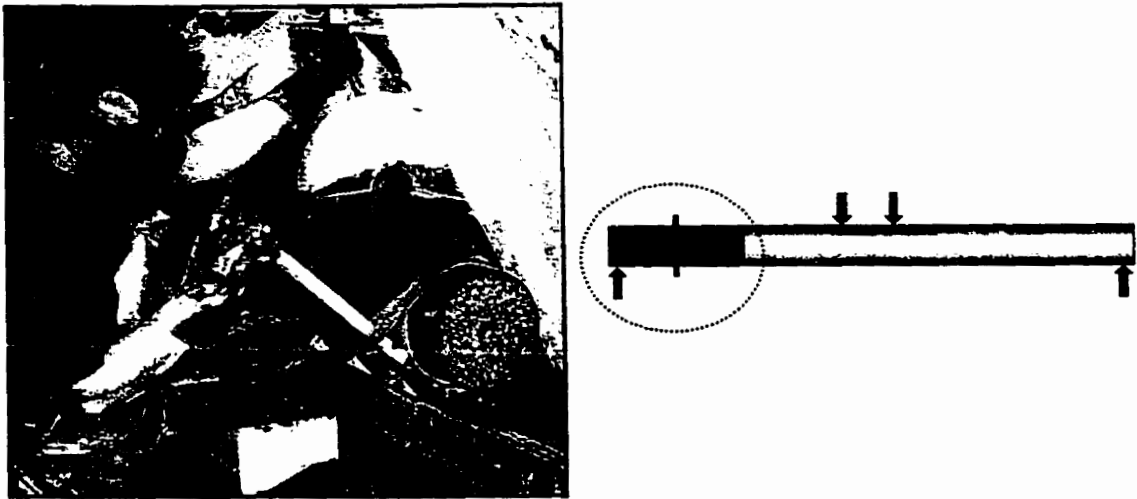


Fig. 3.12 Cutting the stubs from the ends of tested beams using a diamond saw

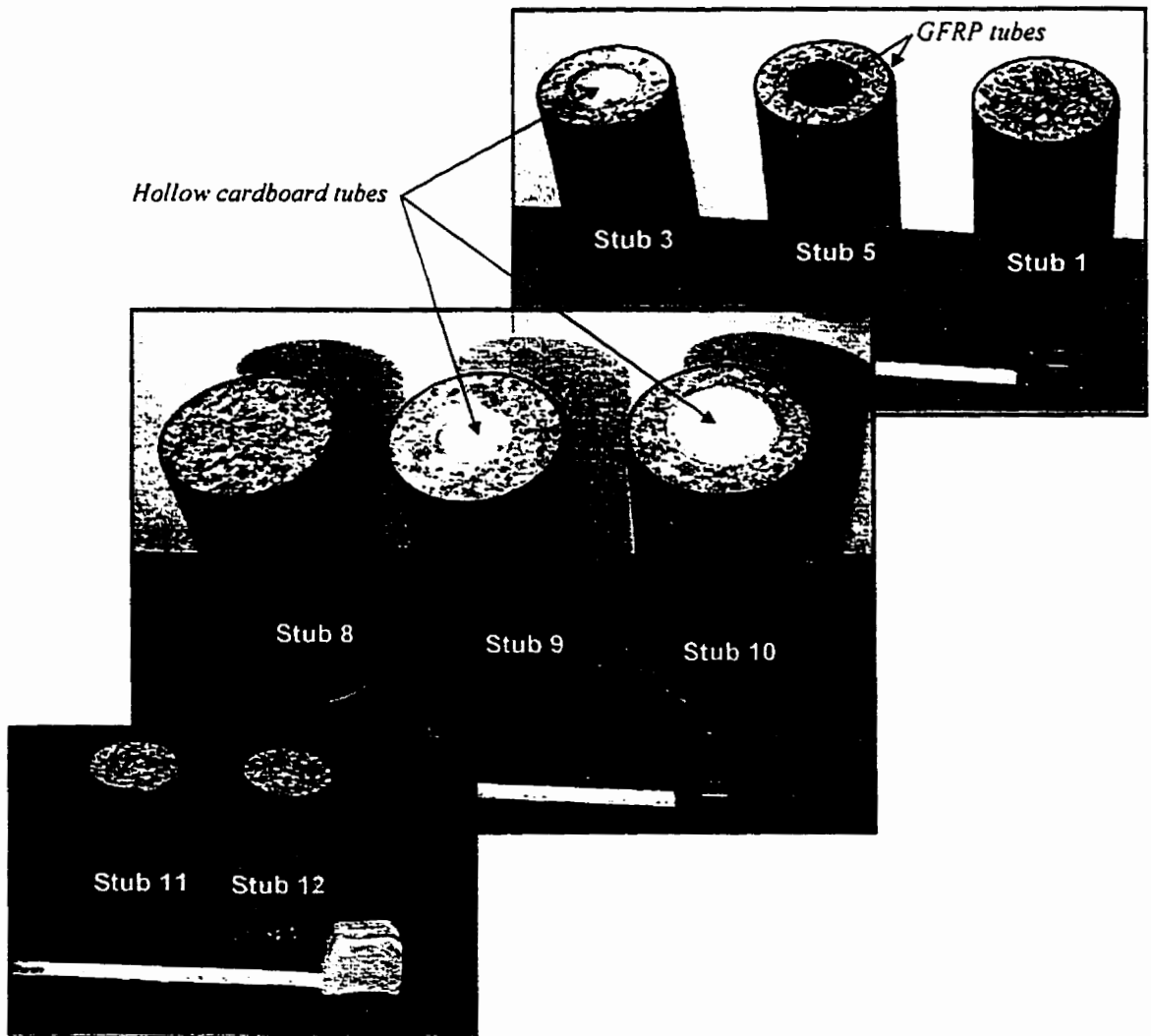


Fig. 3.13 Different stubs used in experimental Phase II

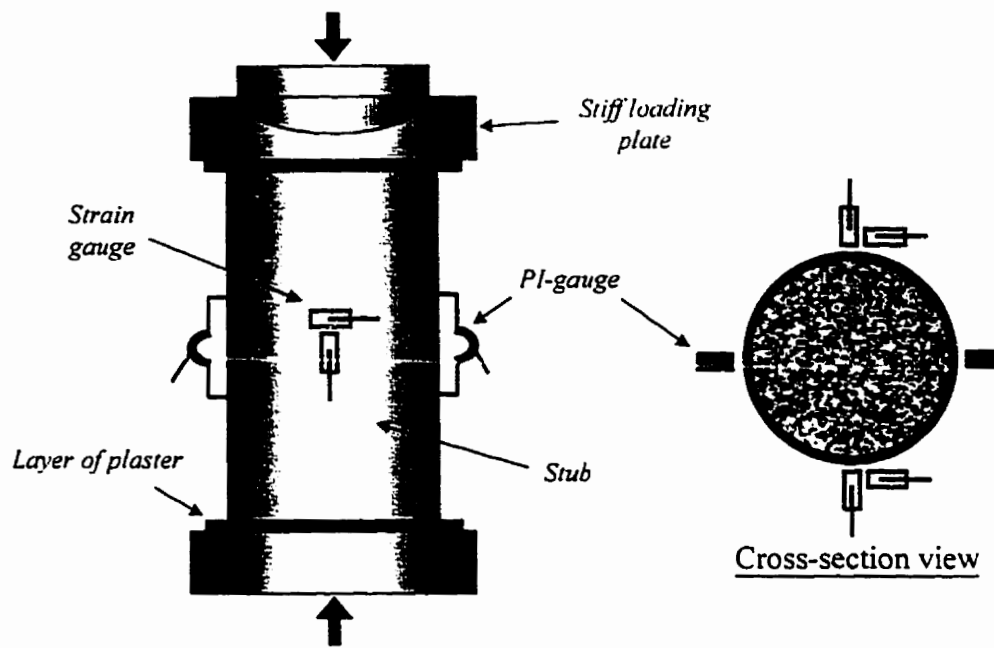


Fig. 3.14 Test setup and instrumentation of stubs tested under axial compression

Chapter 4

Results of the Experimental Program and Discussion

4.1 Introduction

This chapter presents the results of the experimental program including discussion of the behaviour and different failure modes. The experimental program included two phases intended to evaluate the behaviour of concrete-filled GFRP tubes under two different loading conditions. In Phase I. (Beam Tests), hollow GFRP and steel tubes as well as concrete-filled GFRP and steel tubes were tested in pure bending in order to evaluate their flexural behaviour and failure modes [Fam and Rizkalla 2000 (c) and (d)]. The flexural behaviour is evaluated in terms of the flexural stiffness and ultimate strength. In Phase II. (Stub Tests), the behaviour under axial compression loading conditions was examined by testing concrete-filled GFRP and steel tubes as short columns (stubs). The behaviour is evaluated in terms of the load-axial and lateral strain behaviour with emphasis on the confinement effect. The different failure modes are examined. Expansion behaviour of the concrete inside the tubes during curing is also discussed [Fam and Rizkalla 2000 (a) and (d)].

4.2 Phase I – Beam Tests

A total of eighteen beams were tested under four-point bending. The beams ranged from 89 mm to 942 mm in diameter and from 1.07 m to 10.4 m in span. Different parameters

were studied in this phase including the effect of filling hollow tubes with concrete, the effect of cross-section configurations including totally and partially filled tubes, tube-in-tube configuration and the effect of laminate structure of the shell. The reinforcement ratio as a function of the wall thickness-to-diameter ratio and the size effects are discussed. The definition of the reinforcement ratio is generalized in terms of a reinforcement index in order to account for tubes of different material properties, filled with concrete of different strengths. The strength due to cracking of the concrete is also studied. The following sections present the results of experimental Phase I.

4.2.1 Effect of Concrete Filling

4.2.1.1 Flexural behaviour

Fig. 4.1 shows the load-deflection behaviour of the hollow steel tube, beam 1a, compared to that of the concrete-filled steel tube beam 1b, given in Table 3.3. Fig. 4.2 shows the load-deflection behaviour of hollow and concrete-filled GFRP filament-wound tubes, beams 2a and 2b as well as the pultruded tubes beams 3a and 3b. Fig. 4.3 and Fig. 4.4 show the load-axial strain behaviour of the steel and GFRP tubes respectively, including both hollow and concrete-filled tubes. The figures indicate that the strength, stiffness and ductility are greatly improved by filling the tubes with concrete. The strength gain was 49.5 percent for the steel tube, 212 percent for the filament-wound GFRP tube, and 250 percent for the pultruded GFRP tube. The concrete provides internal support for the shell, which prevents local buckling and changes the behaviour and failure mode. This is evident from the measured lateral strains on the shell at the compression zone as shown in Fig. 4.5 for filament-wound tubes, beams 2a and 2b as well as the steel tubes, beams

1a and 1b. The figure indicates that lateral compressive strains develop in the compression side of the hollow tubes under bending. This behaviour is attributed to the ovalization of the hollow tube, which results in lateral bending on the upper part, placing the upper surface in a bi-axial state of compression. Ovalization results from the vertical components of the axial compression and axial tension forces acting on the cross-section as shown in Fig. 4.5. These vertical components are resisted by the concrete core in the case of concrete-filled tube, therefore ovalization is prevented and lateral tensile strains develop in the compression side of the tubes due to the Poisson's ratio effect of the tube. Fig. 4.6 shows the variation of the neutral axis depth with the applied moment for steel and GFRP hollow and concrete-filled tubes. The behaviour indicates that the neutral axis depth for the hollow tubes is equal to the radius of the tubes with almost no change during the loading history. In fact this behaviour indicates that the stiffness of the shell is similar under both compressive and tensile stresses, which supports the assumption adopted in the analysis of composite materials that Young's modulus is equal under both tension and compression loading conditions. In concrete-filled tubes, the neutral axis depth is equal to the radius of the tube, only before cracking. Once the concrete cracks, the neutral axis shifts up to balance the stresses in both the concrete and the shell. Insignificant change in the position of the neutral axis is observed during the loading history of both the concrete-filled GFRP and steel tubes. This is attributed to the linear characteristics of the shell in both tension and compression in the case of the GFRP shell, and to the fact that both tension and compression sides yielded, almost simultaneously, in the case of the steel tube. The neutral axis depth stabilized at a depth of about 40 percent of the diameter for beams 1b and 2b.

4.2.1.2 Failure modes

The hollow steel tube, beam 1a, showed an increasing ovalization of the cross-section within the constant moment zone and failed by yielding, followed by inward local buckling in the compression side as shown in Fig. 4.7. The concrete-filled steel tube, beam 1b, experienced a ductile failure as shown in Fig. 4.8. Once the steel shell yielded, excessive deformation was observed and later outward local buckling occurred. The concrete core forced the local buckling mode outward at a higher load level as compared to the hollow tube. Fig. 4.9 shows the failure modes of the hollow GFRP tubes. The filament-wound tube, beam 2a, failed by crushing of the shell on the compression side near the loading point. Prior to failure, ovalization of the cross-section was observed. The pultruded tube, beam 3a, failed by local crushing and lateral splitting of the shell at the loading point. Splitting occurred due to the lack of fibres in the hoop direction. Fig. 4.10 shows the failure modes of the concrete-filled GFRP tubes. The filament-wound concrete-filled tube, beam 2b, developed its full flexural strength and failed by rupture of fibres in the tension zone. The concrete-filled pultruded tube, beam 3b, failed prematurely in shear by splitting of the tube due to the lack of lateral strength. No slip was observed between the shell and the concrete core in any of the beams.

4.2.2 Effect of Cross-section Configuration

4.2.2.1 Flexural behaviour

The load-deflection behaviour of beams 4, 5, 6 and 7, given in Table 3.3, are compared in Fig. 4.11. All the beams have the same dimensions and identical outer GFRP shells.

Beam 4 is totally filled with concrete. Beam 5 has an inner concentric void. The void size was designed to achieve a concrete wall thickness equivalent to the expected size of the compression zone in beam 4. Beams 6 and 7 have a similar voided core but rather maintained by inner GFRP tubes, both concentric and eccentric. The load-axial strain behaviour of the beams is also shown in Fig. 4.12. The strengths of beams 4, 5, 6 and 7 are 31.2, 28.5, 33.0, and 42.9 kN respectively, while the strength-to-weight ratios are 19.6, 26.4, 28.1, and 36.6 respectively. The behaviour indicates that the absolute strength of beam 5 is only 9 percent less than that of beam 4, while its strength-to-weight ratio is 35 percent higher. Therefore, the designer could achieve comparable strength of the totally filled tube by using a hollow core to reduce the self-weight as long as the concrete wall thickness is equal to or larger than the depth of the compression zone of the totally filled tube. If the void is maintained by an additional GFRP tube as in beam 6, the strength can exceed that of the totally filled tube due to the additional reinforcement provided by the inner tube. When the inner tube was shifted towards the tension side as in beam 7, the strength significantly exceeded that of beam 6 with concentric inner tube by 30 percent since the inner tube is placed more effectively, further from the neutral axis. It should be noted, however, that the configuration of beam 7 is rather less practical, as most applications involve multi-direction loading which requires an axis-symmetric section, whereas this configuration is suitable if the loading is always applied in a specific direction. The strain gauge readings showed similar axial strains at the inner and outer shells at the same horizontal level within the cross-section. This indicates full composite action between the two shells and the concrete as also evident by the fact that no slip was observed in any of the four beams. The load-deflection behaviour shows

sudden change of stiffness after cracking due to the low Young's modulus of those tubes in the axial direction (19.7 GPa) as only one third of the amount of fibres is placed in the axial direction of the tube. Little reduction of stiffness is observed between cracking and failure, mainly due to the linear elastic behaviour of GFRP. The cracking load of beams 4, 5 and 6 is about 15 percent of the ultimate load, while that of beam 7, is about 4.7 percent of the ultimate load. Fig. 4.13 shows the variation of the neutral axis depth of the four beams during the loading history. Once the concrete cracks, the neutral axis shifts from the centre of the section upward to balance the stresses. The position of the neutral axis is almost similar for all the beams and stabilized at a level of about 30 percent of the diameter.

4.2.2.2 Failure modes

Beams 4, 5, 6 and 7 all failed in flexure by rupture of the outer GFRP shell in the tension side as shown in Fig. 4.14 for beam 5. Failure occurred near the mid-span within the constant moment zone for all beams except for beam 5 it took place at the loading point. The eccentric inner shell in beam 7 was also ruptured, whereas the concentric inner shell in beam 6 was not.

4.2.3 Effect of Laminate Structure of the Shell

4.2.3.1 Flexural behaviour

The behaviours of beams 2b and 3b are compared in Fig. 4.2 and Fig. 4.4. Both beams utilize concrete-filled GFRP tubes of identical dimensions and wall thickness. The main difference is the laminate structure of the tubes. Beam 2b has a filament-wound tube

with about two thirds of the fibres content oriented in the longitudinal direction at a 3 degrees angle and the rest are oriented at the hoop direction at an 88 degrees angle. whereas beam 3b has a pultruded tube. The effective elastic moduli in the axial direction were 29 and 37.7 GPa for beams 2b and 3b respectively. Fig. 4.2 indicates that the stiffnesses of the beams after cracking are almost proportional to the effective axial elastic moduli of the laminates. Beam 2b achieved higher strength than beam 3b, which failed prematurely by horizontal shear failure due to the lack of strength in the hoop direction.

Fig. 4.15, 4.16, and 4.17 compare the behaviour of beams 8 and 9 in terms of load-deflection, load-axial strain and variation of the neutral axis depth respectively. Both beams utilize concrete-filled GFRP filament wound tubes of similar dimensions and wall thickness. Beam 8 has only one third of the fibres content wound at an angle of 15 degrees with the longitudinal axis and the two thirds are placed on the hoop direction at 82 degrees angle. Beam 9 has all the fibres content wound at ± 30 degrees angle with the longitudinal axis. The two different laminate structures resulted in an effective elastic modulus for beams 8 of about 80 percent of that of beam 9. Also the concrete strength of beam 8 is 32 percent higher than that of beam 9. Fig. 4.15 indicates that the stiffness of the beams after cracking is somewhat proportional to the effective axial elastic moduli of the shells. Although both beams achieved a similar strength, the failure modes were completely different as will be discussed in section 4.2.3.2. The neutral axis depth in beams 8 and 9 stabilized at a level of about 30 and 33 percent, respectively, of the diameter as shown in Fig. 4.17. No slip was observed during testing of either beam.

Fig. 4.19 and Fig. 4.20 show the load-deflection and load-axial strain behaviour of beams 10 and 11. Beam 10 has 48 percent of the fibres content in the axial direction at 3 degrees angle and 52 percent at 88 degrees in the hoop direction. Beam 11 was proposed as an alternative by the manufacturer of the tube used in beam 10. It includes 70 percent of the fibres content at ± 34 degrees with the axial direction and 30 percent close to the hoop direction at 80 degree, mainly to facilitate producing larger size tubes compared to the tubes used in beam 10. The two beams have comparable stiffnesses, however beam 10 achieved a 25 percent higher strength. This is attributed to the difference in tensile strength of the tubes as indicated by the ultimate tensile strains measured on the tubes as shown in Fig. 4.20 as well as the slight difference in dimensions of the tubes. Fig. 4.21 also shows that the neutral axis depth in both beams stabilized at a level of about 25 percent of the diameter. By visual examination of the cross-section of beam 11 after failure, the compression zone was identified from the different surface texture of the cross-section as shown in Fig. 4.21. The depth of the compression zone was 95 mm, which agrees very well with the stabilized value on the graph. Since no additional surface preparations were done in beams 10 and 11 to enhance the bond, a 1.0 mm total slip was measured at each end of beam 10, whereas a 2.1 mm was measured at each end of beam 11 as shown in Fig. 4.22. It should be noted, however, that this slip reflects the accumulation occurring over a 5.5 m span. The slip in beam 10 occurred gradually, while in beam 11 occurred in a sudden step-wise pattern, as shown the figure, which is believed to have accompanied cracking. It is also believed that this minor slip had an insignificant effect on the strength as indicated from the analysis and predictions.

4.2.3.2 Failure modes

The failure modes of beams 2b and 3b were discussed in section 4.2.1.2 and shown in Fig. 4.10. Fig. 4.18 shows the failure modes of beams 8 and 9. Beam 8 had a flexural tension failure by rupture of the fibres in the axial direction. Beam 9, on the other hand, experienced a flexural compression failure in the GFRP shell. The shell gradually cracked at the ± 34 degrees directions of the fibres and the fibres buckled in the compression side as indicated by the measured axial strain on the compression side in Fig. 4.16. Later the concrete was found crushed in the compression zone. Beam 9 is the only beam that had such a compression failure mode in the entire set of beams in this program and it is also the only beam that do not have fibres wound in the hoop direction. This clearly shows the function of fibres placed in the hoop direction to confine the other longitudinal fibres. This failure mode resulted in significant loss of stiffness near the end as evident by the highly non-linear behaviour in Fig. 4.15.

Fig. 4.23 shows the failure mode of beams 10 and 11. Both beams had a flexural tension failure. Beam 10 failed by rupture of the fibres in the axial direction and splitting of the fibres in the hoop direction. In beam 11, the fibres at ± 34 degrees failed on the tension side. It is also interesting to compare the failure modes of beams 9 and 11. Although both beams have comparable diameter-to-thickness ratio as well as the main fibres wound at large angles, ± 30 and ± 34 respectively; each had a different failure mode. The main difference is the lack of fibres in the hoop direction in beam 9, which could be the reason

behind the compression failure. On the other hand, compression failure was avoided in beam 11.

4.2.4 Reinforcement Ratio and Size Effects

4.2.4.1 Flexural behaviour

Beams 11, 12 (a, b), and 13 (a, b) were all fabricated using same GFRP composite materials, same process, and similar laminate structure. The difference in concrete strength, which was not intended in the mix design, is ignored since the failure mode in all beams was flexural tension failure and the bending strength is mainly governed by the GFRP tube as also shown by analysis. Therefore, the main difference is the size of the tubes, which resulted in different reinforcement ratios. The reinforcement ratio ρ in this case is defined by the ratio of the cross-sectional area of GFRP tube-to-the area of the concrete core. For large diameter-to-thickness ratios, this ratio can be reduced to:

$$\rho = \frac{4t}{D_o} \quad (4.1)$$

Where D_o is the outer diameter of the tube and t is the structural wall thickness. The reinforcement ratios for beams 11, 12, and 13 were 7.4, 3.5, and 3.8 percent respectively. Two identical tests were done for each of beams 12 and 13 as denoted by (a) and (b) to confirm the findings. The flexural behaviour of beam 11 was discussed in section 4.2.3 and shown in Figures 4.19, 4.20, 4.21 and 4.22. The self-weight effect was considered in all the beams tested in this category. Before comparing beams 11, 12, and 13, the results of beams 12 (a, b) and 13 (a, b) are first introduced.

Fig. 4.24 and Fig. 4.25 show the load-deflection and load-axial strain behaviours of beams 12 (a, b). The difference in strength between beam 12a and 12b is about 6 percent. Since the tests were conducted under stroke control, the behaviour shows a sudden drop in load after first cracking due to the low stiffness and reinforcement ratio of the beam. Similar drops of load with recovery occurred after. If the tests were performed under load control, horizontal shifts in the curves would have been expected instead, indicating increase of deflection under the same load. The drops in load were accompanied by loud sounds and slip between the concrete and the shell, where the concrete core moves out of the shell in the axial direction. The total slip measured at the end of the test, at both ends of each beam, was 9.0 and 10.0 mm for beam 12a and 7.0 and 11.0 mm for beam 12b. At each end, the value of slip between the concrete and the top surface of the shell was equal to that between the concrete and the bottom surface of the shell. Fig. 4.26 shows the variation of the neutral axis depth with the moment. The figure indicates that before cracking the neutral axis was located at the centre of the beam. Once the concrete cracked, the neutral axis shifted up to balance the stresses on the section. It should be noted, however, that slip took place simultaneously with first cracking and continued thereafter during the test, therefore, the composite action was partially lost and the zero stress level for the shell Z' does not necessarily coincide with the lower boundary Z of the compression zone in concrete. In this case the measured depth Z' in Fig. 4.26 does not exactly indicate the depth of the compression zone Z in concrete since it was based on strain measurements on the shell surface. The difference in neutral axis depth between beam 12a and 12b immediately after cracking in Fig. 4.26 could be attributed to different initial slip values accompanied first cracking in the two beams. This difference gradually

disappears towards the end of the test since the final total slip values were almost identical in the two tests. Fig. 4.26 also shows that the horizontal drops in moment level are accompanied by sudden shift in the neutral axis level Z' towards the centre of the circular cross-section. Again this is attributed to the slip, which results in partial loss of the concrete contribution and gradually leading the system to behave more like a hollow tube, which would normally have the neutral axis located at the centre of the cross-section. In fact after failure of beam 12b, the cross-section was examined and the measured compression zone in concrete was only about 150 mm in depth as shown in Fig. 4.26. which is significantly less than the stabilized value given in the graph at failure, about 225 mm. This is completely different from the case of beam 11 in Fig. 4.21 due to the larger slip in this case, which confirms the discussion given above.

Fig. 4.27 and Fig. 4.28 show the load-deflection and load-axial strain of beams 13(a. b). The difference in strength between beam 13a and 13b was less than 3 percent. A very similar behaviour to that of beams 12 (a. b) was observed in terms of cracking, slip, and the accompanied noise. However, in this case, when some of the load drops were recovered, they were accompanied by excessive deflection. The total slip measured at one end of beam 13b was 23 mm at the bottom. In beam 13a, the total slips at the top and bottom levels were 14.0 and 10.0 mm respectively at the left end and 22.0 and 15.0 mm at the right end. The load-axial strain curve also indicates that the vertical load-drops were also accompanied by lateral shifts in the strains. In the case of top strains, the shifts indicate increase in the compressive strains, whereas on the tension side, the shifts indicate reduction in the tensile strains. This indicates that the tube is suddenly

compressed top and bottom, which could be attributed to the impact effect of the outward movement of the large mass of concrete when it slips. Fig. 4.29 shows the variation of the neutral axis depth with the moment. The behaviour is very similar to that of beams 12 (a, b) in terms of the effect of slip on the shift of neutral axis of the shell Z' , which does not coincide with the lower level of the compression zone in concrete Z . This is also evident from the measured depth of the compression zone after the test, which was about 225 mm rather than the 340 mm indicated by the graph at failure. It is believed that the slip in beams 12 and 13 did not have a significant effect on the ultimate strength as indicated from the analysis.

Fig. 4.30 compares the load-deflection behaviour of beams 11, 12a, and 13a. Since the span-to-depth ratios as well as the diameters were different, Fig. 4.30 can not be used to compare the behaviour in order to examine the effect of reinforcement ratio, but rather a normalization technique needs to be adopted to study a single variable at a time. To overcome the effect of different spans, the moment-curvature behaviour is compared rather than the load-deflection. The curvature is based on the slope of the axial strain profile along the depth of the section. To overcome the effect of variable diameter, the moments are divided by D_c^3 in a normalized form of stress, and the curvatures are multiplied by D_c in a dimensionless format, independent of the size [Park and Paulay 1974]. Fig. 4.31 shows the normalized moment-curvature response of beams 11, 12a and 13a, which is used to illustrate the effect of reinforcement ratio. The normalized behaviour of beams 12a and 13a is almost identical as expected due to the similar reinforcement ratios. This observation provides confidence in this method of

normalization to be used to compare the effects of different parameters using beams of different sizes. Beam 11 showed higher strength and stiffness due to the higher reinforcement ratio. In fact both, strength and stiffness were almost directly proportional to the reinforcement ratio.

The size effect can be examined by comparing beams 12 and 13 since both beams have the same reinforcement ratio. The main difference is the size, where beam 13 is 1.5 times larger than beam 12. Fig. 4.31 indicates that both beams achieved the same normalized flexural strength of about 2 MPa, regardless of the size difference.

4.2.4.2 Failure modes

The failure mode of beam 11 is shown in Fig. 4.23 and discussed in section 4.2.3.2. The failure mode of beams 12 (a, b) is shown in Fig. 4.32. The beams had flexural tension failure within the constant moment zone by rupture of the fibres in the ± 34 degrees direction. The failure in beam 12a was scattered over a larger area than in beam 12b. Fig. 4.33 shows the failure mode of beams 13 (a, b). The beams had a flexural tension failure below the left loading point by rupture of the fibres. The failure in beam 13b also covered larger area than in beam 13a. Failure of beam 13a occurred due to rupture of the tube at the location of a wide flexural crack. Therefore, the lack of shear resistance of concrete under the impact effect of failure caused the shell to show this localized failure. However, the flexural strength was not affected as evident from the similar strength of beams 13 (a, b) and the fact that both beams reached a similar ultimate tensile strain in the shell as indicated from Fig. 4.28.

4.2.5 The Reinforcement Index

Most of the GFRP tubes were made of different laminate structures, which resulted in different axial effective tensile strengths, and also were filled, with concrete of different strengths. Therefore, the definition of the reinforcement ratio ρ introduced in Equation 4.1 is limited to beams made of similar GFRP tubes and filled with concrete of the same strength. The reinforcement index ω introduced in Equation 4.2 allows for comparing beams of different GFRP tubes and concrete strengths. The reinforcement index is defined as the reinforcement ratio multiplied by the ratio of the axial tensile strength of the GFRP tube f_u to the concrete compressive strength f'_c as follows:

$$\omega = \frac{4t}{D_o} \frac{f_u}{f'_c} \quad (4.2)$$

Beams 2b, 4, 8, 10, 11, 12, and 13 are selected to study the correlation between the reinforcement index and the flexural strength, the curvature at ultimate and the neutral axis depth. All the beams are totally filled GFRP tubes and had a flexural tension failure. Table 4.1 shows the reinforcement ratio ρ , the reinforcement index ω , the axial tensile strength of the GFRP tubes f_u , the concrete compressive strength f'_c , the ultimate moment M_u , the neutral axis depth at failure Z , and the ultimate curvature ψ for the selected beams. For beams 12b and 13b, the neutral axis depth is based on the measured depth of the compression zone after failure rather than the axial strain distribution because of the slip that took place. The neutral axis depth at ultimate is normalized with respect to the diameter to overcome the size difference of the beams as follows:

$$\bar{Z} = \frac{Z}{D_n} \quad (4.3)$$

The ultimate moment is normalized with respect to the diameter and the concrete strength in a dimensionless format as follows:

$$\bar{M} = \frac{M_u}{D_n^3 f_c'} \quad (4.4)$$

The ultimate curvature is also normalized with respect to the diameter and both the shell and concrete strengths in a dimensionless format as follows:

$$\bar{\psi} = \psi D_n \frac{f_u}{f_c'} \quad (4.5)$$

Fig. 4.34 shows the variation of the normalized moment capacity \bar{M} with the reinforcement index ω . Linear correlation is observed as given by Equation 4.6:

$$\bar{M} = 0.0015 \omega + 0.016 \quad (4.6)$$

Where ω is a percentage and \bar{M} is dimensionless. From Equations 4.2, 4.4 and 4.6, the following equation is obtained for the ultimate moment capacity:

$$M_u = 600 t D_n^2 f_u + 16 D_n^3 f_c' \quad (4.7)$$

Where t and D_n are in meters, f_u and f_c' are in MPa and M_u is in kN.m.

Fig. 4.35 shows the variation of the normalized ultimate curvature $\bar{\psi}$ with the reinforcement index ω . Linear correlation is observed as given by Equation 4.8:

$$\bar{\psi} = 3.365 \omega + 18.446 \quad (4.8)$$

Where ω is a percentage and $\bar{\psi}$ is dimensionless ($\times 10^{-3}$). From Equations 4.2, 4.5 and 4.8, the following equation is obtained for the ultimate curvature:

$$\psi = 1346 \frac{t}{D_o^2} + 18.45 \frac{f_c'}{D_o f_u} \quad (4.9)$$

Where t and D_o are in meters. f_u and f_c' are in MPa and ψ is in $(\text{meter})^{-1} \times 10^{-3}$.

Fig. 4.36 shows the variation of the normalized neutral axis depth \bar{Z} with the reinforcement index ω . Linear correlation is obtained as given by Equation 4.10:

$$\bar{Z} = 0.0007 \omega + 0.2424 \quad (4.10)$$

Where both ω and \bar{Z} are dimensionless. From Equations 4.2, 4.3 and 4.10, the following equation is obtained for the neutral axis depth at ultimate:

$$Z = 0.28 t \frac{f_u}{f_c'} + 0.242 D_o \quad (4.11)$$

Where Z , t and D_o are in meters. f_u and f_c' are in MPa.

Equations 4.7, 4.9, and 4.11 are obtained using the test beams shown in Table 4.1. The beams covered a wide range of variables. The diameter ranged from 89 mm to 942 mm. The shell thickness ranged from 2.05 mm to 8.93 mm. The GFRP shells varied in laminate structure, which resulted in axial tensile strength ranging from 209 MPa to 725 MPa. The concrete strength ranged from 32.7 MPa to 67.3 MPa. Therefore, in absence of detailed analysis, Equation 4.7 provides a simple and quick method to predict the ultimate moment capacity of concrete-filled FRP tubes failing in tension in terms of the material and cross-section properties. Also Equation 4.9 can be used to predict the ultimate curvature, which can be used to estimate the ultimate deformations of flexural members.

4.2.6 Cracking Strength of the Beams

The cracking load of concrete-filled GFRP tubes is normally small compared to the ultimate load. The beams that showed a distinct cracking load during testing with an obvious change in stiffness, mostly the large size beams, were selected to evaluate the cracking behaviour of concrete. Table 4.2 shows the selected beams and their properties including their concrete strength f'_c , cracking moment M_{cr} (accounting for self-weight), and their transformed moment of inertia I_t . The transformed moment of inertia is calculated using the following equation:

$$I_t = I_c + \frac{E_{t(axial)}}{E_c} I_s \quad (4.12)$$

Where $E_{t(axial)}$ is the modulus of elasticity of the shell in the axial direction and E_c is the concrete modulus of elasticity, calculated as $5000 \sqrt{f'_c}$ [CSA Standard A23.3-94]. I_c and I_s are the moments of inertia of the concrete core and the GFRP shell respectively and are calculated as follows:

$$I_c = \frac{\pi (D_o - 2t)^4}{64} \quad (4.13)$$

$$I_s = \frac{\pi (D_o^4 - (D_o - 2t)^4)}{64} \quad (4.14)$$

Where D_o is the outer diameter and t is the thickness of the shell.

Using the measured cracking moment M_{cr} and the transformed moment of inertia I_t , the concrete cracking strength inside the tube, f_{cr} , was estimated as shown in Table 4.2 using the following equation:

$$f_{cr} = \frac{M_{cr}}{I_t} \left((D_o - 2t)/2 \right) \quad (4.15)$$

The ACI Building Code [ACI 318-95] uses the following equation to predict the cracking strength:

$$f_{cr} = k \sqrt{f_c'} \quad \text{Where } k = 0.6 \quad (4.16)$$

The CEB-FIP Model Code [Ghali and Favre 1993] uses the following equation:

$$f_{cr} = k (f_c')^{2/3} \quad \text{Where } k = 0.205 \text{ to } 0.398 \quad (4.17)$$

The measured cracking strengths of the beams, f_{cr} , were normalized with respect to f_c' according to the code Equations 4.16 and 4.17. The coefficient k was estimated for each beam based on the two codes as shown in Table 4.2 and Fig. 4.37. The average values of k obtained based on the ACI and CEB-FIP formulas were 1.0 and 0.51 respectively. These values are about 68 percent higher than the values proposed by the codes, which indicates higher cracking strength of the beams. This behaviour could be attributed to the containment of concrete inside the shell and the restrained expansion of concrete during curing, which might have induced a state of chemical prestressing of the concrete.

4.3 Phase II – Stub Tests

A total of twelve short columns (stubs) were tested under axial compression loading condition. The effects of confinement on the behaviour of axially loaded concrete are demonstrated. The behaviour of concrete-filled steel tube is compared to that of a concrete-filled GFRP tube to study the effect of the material type of the shell. Concrete-filled GFRP tubes with different laminate structures including filament-wound and pultruded GFRP tubes are compared. The behaviour of totally filled GFRP tube is

compared to that of partially filled GFRP tubes with central voids including tube-in-tube configuration. Partially filled GFRP tubes with different void sizes are compared to study the effect of void size on the confinement level. The effect of the GFRP shell/concrete interface condition is examined. The effects of the stiffness of the shell on the confinement effectiveness, as well as, the effects of loading the GFRP shell in the axial direction are examined. The axial-lateral strain behaviour of the shell is analyzed and compared. Failure modes are also introduced. The following sections provide the experimental results of the stub tests.

4.3.1 Confinement Effect on Concrete

4.3.1.1 Behaviour under axial load

In order to evaluate the beneficial effect of confinement on the total load carrying capacity of concrete-filled FRP tubes, the measured axial load-strain behaviour of stub 11 is given in Fig. 4.38. On the same figure, the behaviour is also compared to a hypothetical response obtained by superposition of the responses of the individual constituent components of the stub including the hollow GFRP tube and the plain concrete core. The axial load-strain behaviour of the hollow GFRP shell, tube 3 in Table 3.1, was obtained by testing the hollow tube in compression. At strain of about 0.004, the hollow GFRP shell suffered local damage at the loading end and failed. The axial load-strain behaviour of the plain concrete core is obtained using the measured stress-strain curve of a tested standard concrete cylinder from the same concrete mix. The figure clearly indicates that the capacity of the composite stub significantly exceeds the load sharing capacity of the two individual components by about 60 percent, and exceeds the

capacity of the concrete core only by about 143 percent. In fact, the estimated behaviour using superposition matches the measured response of the composite stub very well up to the vicinity of the unconfined plain concrete strength. This observation strongly emphasises the beneficial effect of confinement beyond this stage, when concrete starts to expand excessively at a stress level of about 87 percent of the unconfined strength [Avram et al 1981] and the confinement mechanism is activated through the confining GFRP shell.

4.3.1.2 Failure modes

Fig. 4.39 shows the failure modes of the plain concrete, the hollow GFRP tube, and the composite system. The plain concrete suffers from excessive lateral expansion due to unstable propagation of the internal micro-cracks, which causes the strain softening behaviour and eventually the concrete mass loses its integrity and fails. The hollow GFRP shell fails prematurely due to the brooming effects at the end, which causes localized damage. However, if these end effects are eliminated, the hollow tube is still expected to fail prematurely by local buckling. The concrete-filled GFRP tube failed by fracture of the GFRP shell under a bi-axial state of stress including tensile stresses in the hoop direction due to expansion of concrete and compressive stresses in the axial direction due to the axial load applied to both the concrete and the tube. This indicates that the hybrid system fully utilizes the two materials. The concrete supports the shell and prevents premature failure while the shell confines the concrete and restrains its excessive expansion.

4.3.2 Effect of Material Type of the Confining Shell

4.3.2.1 Behaviour under axial load

The behaviour of GFRP confined concrete, stub 1, is compared to that of steel confined concrete, stub 7, in terms of load-axial strain and load-lateral strain behaviours in Fig. 4.40. The axial strains represent the average of readings monitored at four sides around the perimeter of the stub, while the lateral strains represent the average of readings taken at two opposite sides. The plain concrete behaviour is also shown for comparison. Although the structural wall thickness of the GFRP shell is 37 percent less than that of the steel shell, they both achieved the same axial strength. The behaviour of GFRP confined concrete is characterized by a bi-linear response with a transition zone near the vicinity of unconfined concrete strength. The stiffness beyond this point, second slope, is governed by the stiffness of the confining GFRP shell, whereas, the ultimate strength of the column is governed by the strength of the GFRP shell. Once the shell reached its tensile strength in the hoop direction, in presence of the axial compressive stress, it fractured and the stub failed. On the other hand, steel confined concrete behaved almost linearly till the shell yielded, followed by a plastic plateau with large deformations. The strain hardening response of FRP-confined concrete is attributed to the continuously increasing confining pressure as the concrete core expands, due to the linear nature of FRP as also indicated by the excessive increase in lateral strains at the level of unconfined strength as shown in Fig. 4.40. On the other hand, once the steel shell yields, the confining pressure becomes stable regardless of the degree of concrete expansion. Therefore, the increase in lateral strains after yielding, shown in Fig. 4.40, is not accompanied by increase in the confining pressure.

The figure also shows that the measured strength of the GFRP/concrete hybrid system, stub 1, is 41 percent higher than the combined load capacities of the unconfined concrete core and the GFRP shell added together, whereas the increase in capacity for the steel/concrete system, stub 7, is only 18 percent. Generally speaking, the steel shells before yielding tend to attract more sharing of the axial load as compared to GFRP shells under the same axial strain level. This is mainly attributed to the higher elastic modulus of steel as compared to GFRP. It should also be noted that the wall thickness of the steel tube is 1.59 times that of the GFRP tube.

4.3.2.2 Failure modes

Fig. 4.41 shows the failure modes of steel-confined concrete, stub 7, and GFRP-confined concrete, stub 1. The GFRP shell fractured under a combined hoop tensile stresses and axial compressive stresses. Once the shell fractured the column failed in a brittle manner. On the other hand, the steel shell yielded and sustained large axial deformations. When the shell yielded, the column started to bulge in the lateral direction.

4.3.3 Effect of Laminate Structure of the Shell

4.3.3.1 Behaviour under axial load

Stubs 11 and 12 were identical in size, concrete strength, and wall thickness of the shell. The main difference is that the GFRP shell in stub 11 is filament-wound, where the fibres are oriented in both longitudinal and hoop direction with a ratio of about 2:1, whereas the GFRP shell of stub 12 is pultruded with all the fibres oriented in the axial direction. Fig.

4.42 compares the load-axial and lateral strain behaviours for both stubs. The figure clearly illustrates the advantage of fibres in the hoop direction for confinement, which results in much higher strength. The pultruded tube fails to confine the concrete at the vicinity of the peak unconfined strength when concrete starts to expand excessively and the tube splits immediately due to the lack of stiffness and strength in the hoop direction as evident by the limited lateral strains measured on the shell. This is also indicated by comparing the failure load of stub 12, 395 kN, to the calculated ultimate load based on superposition of the load capacities of the hollow tube and the concrete core, 367 kN. The gain in strength is insignificant, 7 percent only. On the other hand, Fig. 4.38 shows that in stub 11, the estimated gain in strength due to confinement at ultimate was 60 percent.

4.3.3.2 Failure modes

Fig. 4.43 shows the failure modes of stubs 11 and 12. The pultruded tube of stub 12 is split parallel to the fibres, whereas the filament-wound tube of stub 11 is fractured.

4.3.4 Effect of Cross-section Configuration and Interface

Condition

4.3.4.1 Behaviour under axial load

Fig. 4.44 shows the load-axial and lateral strain behaviours of stubs 1 to 6 including totally filled GFRP tubes, stubs 1 and 2, partially filled GFRP tubes with concentric voids, stubs 3 and 4, and the tube-in-tube system with concrete filling in between, stubs 5 and 6. Stubs 1, 3, and 5 had a rough interface surface between the shell and the concrete,

whereas, stubs 2, 4, and 6 had a smooth interface. The confinement effectiveness can be detected by the slope of the second part of the bi-linear response. It is evident that the totally filled tube is more effective in confinement compared to the tubes with voided core. However, it is also evident that providing an additional inner GFRP tube, as in stubs 5 and 6, could enhance the confinement. The behaviour of stubs 5 and 6 shows a similar flat response to that of stubs 3 and 4 at the unconfined strength level, but soon the stiffness increases and the slope of the second part of the response approaches a comparable value to that of stubs 1 and 2 due to the activation of the inner shell in the confinement mechanism. This is also evident from the lateral strain response on both the inner and outer GFRP shells of stubs 5 and 6, as shown in Fig. 4.45. At early stages of loading, before concrete expands, both shells were under lateral tensile strains due to Poisson's ratio effect for tubes under axial compression. Once the concrete starts to expand excessively, it presses against both shells. At this stage the outer shell is subjected to higher hoop tensile strains, whereas the hoop strain of the inner shell starts to reverse direction toward the compression side. At this point the stiffness is comparable to a totally filled tube. It should be noted that this behaviour is more obvious in stub 5 (with rough interface) than in stub 6 (with smooth interface) due to the better bond, which insures strain compatibility. The lateral strains in the inner shell of stub 6 reached a peak tensile strain and just before reversing direction to compression, the stub failed. In general, from Fig. 4.44, the interface condition had an insignificant effect on the behaviour of stubs 1 to 4. More pronounced effect is recognized for stubs 5 and 6 due to the larger surface area of GFRP in contact with concrete, yet the maximum strength was not affected.

4.3.4.2 Failure modes

The stubs failed immediately once the outer GFRP shell fractured. The outer shell is subjected to hoop tensile stresses in presence of axial compressive stresses. The hoop tensile stresses are induced through the expanding concrete core, while the axial compressive stresses are due to the direct loading on the shell. In most cases, the apparent failure mode is rupture of the shell in the hoop direction. Stub 5 showed additional signs of crushing in the axial direction. The fracture of the totally filled GFRP tube is more spread than that of the partially filled tubes as shown in the Fig. 4.46. This could be attributed to the higher radial confining pressure developed in the totally filled tubes as compared to partially filled tubes at failure as will be discussed in section 4.3.5. The inner GFRP shell in stubs 5 and 6 is subjected to bi-axial compressive stresses at failure. Stub 5 showed signs of crushing of the inner shell at failure.

4.3.5 Effect of Void Size

4.3.5.1 Behaviour under axial load

The effect of void size is illustrated through two groups of stubs including stubs 8, 9, and 10, as well as stubs 2 and 4. The stubs within each group have a similar GFRP outer shell and different void sizes inside the concrete core. The load-axial and lateral strain behaviour of stubs 2 and 4 is shown in Fig. 4.44, and that of stubs 8, 9, and 10 is shown in Fig. 4.47. The figures show that the larger the size of the void, the lower the strength. However, in order to compare the confinement effect on the concrete core, which normally affect the second slope of the bi-linear response, the normalized behaviour in

terms of the stress-strain response of the concrete core should be compared rather than the load-strain response. The stress-strain response of the concrete core is estimated by deducting the contribution of the GFRP shell, P_f , from the total measured load, P_T . The remaining load, P_c , divided by the net concrete cross-sectional area, gives the concrete stress. The equilibrium equation is given as follows:

$$P_T = P_c + P_f \quad (4.18)$$

$$P_f = E_{f(axial)} A_f \varepsilon_{(axial)} \quad (4.19)$$

$$\text{From Equations 4.18 and 4.19: } P_c = P_T - E_{f(axial)} A_f \varepsilon_{(axial)} \quad (4.20)$$

Where A_f is the area of the cross-section of the GFRP shell, $E_{f(axial)}$ is the elastic modulus of the tube in the axial direction, and $\varepsilon_{(axial)}$ is the axial strain, which is similar in both the shell and the concrete. The stress-strain responses of the confined concrete of stubs 2 and 4 as well as stubs 8, 9, and 10 are determined and compared in Fig. 4.48. The behaviour clearly shows that the larger the size of the void, the less confinement, and consequently less strain hardening effect or rather strain softening instead. The effect is more pronounced in stubs 2 and 4 since the GFRP shell of those stubs is significantly stiffer than that used in stubs 8, 9, and 10 as will be shown in section 4.3.6.

The peak confined strengths of the partially filled tubes, $f'_{cc(voided)}$, are normalized with respect to the peak confined strengths of the totally filled tubes, $f'_{cc(solid)}$, and were related to the inner-to-outer diameter ratio (D_i/D_o) as shown in Fig. 4.49. The reduction in strength with increasing the void size is attributed to the fact that voided cores provide an inwards displacement degree of freedom for concrete when it expands under axial compression, relieving part of the contact pressure and reducing the confinement effect.

4.3.5.2 Failure modes

Fig. 4.50 shows the stubs 8, 9, and 10 after failure. The failure mode is similar to the other stubs discussed before, mainly fracture of the GFRP shell due to hoop tensile stresses in presence of axial compressive stresses. The totally filled tube showed more spread failure than the partially filled ones due to the higher confining pressure as compared to partially filled tubes.

4.3.6 Effect of Stiffness of the Shell in the Hoop Direction

The confinement effectiveness, (f'_c / f'_c) , is the ratio between the maximum strength of the concrete-filled tube and the strength of the unconfined concrete. This ratio is affected by both the strength and stiffness of the shell in the hoop direction, which control the level of confinement. Stubs 1, 2, 8, 11, and 12 were selected to examine the effect of stiffness of the shell on the confinement effectiveness of totally filled GFRP tubes. The stiffness of the GFRP tube in the hoop direction, $(E_{f(hoop)} t / R)$ is defined based on the relationship relating the confining pressure of the concrete core σ_R to the hoop tensile strain in the shell $\varepsilon_{(hoop)}$ as shown in Fig. 4.51 and given in Equation 4.23. Equilibrium of radial pressure and forces in the hoop direction is given in the following equation:

$$T = R \sigma_R \quad (4.21)$$

Where T is the hoop tensile force per unit length of the shell and R is the radius of the shell. T is also related to the hoop strain in the shell $\varepsilon_{(hoop)}$ as follows:

$$T = E_{f(hoop)} \varepsilon_{(hoop)} t \quad (4.22)$$

Where t is the thickness of the shell and $E_{r(hoop)}$ is the elastic modulus of the shell in the hoop direction. From Equations 4.21 and 4.22, the following equation is driven:

$$\sigma_R = \frac{E_{r(hoop)} t}{R} \epsilon_{(hoop)} \quad (4.23)$$

Table 4.3 provides the dimensions, properties and stiffness of the selected stubs. The confinement ratio (f'_{cc}/f'_c) is calculated for each stub and plotted as a function of the stiffness of the tube in Fig. 4.52. The figure shows the increase in the strength of confined concrete by increasing the stiffness of the shell. This could be achieved either by using a higher thickness-to-radius ratio or using GFRP shells with higher elastic moduli in the hoop direction.

4.3.7 Effect of Loading the Shell in the Axial Direction

The effect of loading the shell in the axial direction, simultaneously with the concrete core, can be illustrated by comparing the results of stubs 1, 2, 8, 11, and 12 with another group of stubs, which have an equivalent range of stiffnesses of the GFRP shells, where the concrete cores only were axially loaded. In 1997, Mirmiran and Shahawy tested concrete-filled GFRP tubes with a range of stiffnesses very similar to that experienced in this study for the selected stubs. The strength of the GFRP shells in the hoop direction was also very similar to that of stubs 1, 2, and 8. Table 4.4 provides the details of those stubs. The 152.5x305 mm stubs a, b, and c included GFRP shells with 1.3, 2.1, and 3.0 mm wall thickness, filled with 31.5 MPa concrete, and tested in compression by loading the concrete core only. The shells consisted of a filament-wound angle ply of polyester resin with E-glass fibres at ± 15 degrees with the hoop direction, resulting in elastic

moduli of 37.2 to 40.7 GPa and strengths of 524 to 641 MPa in the hoop direction. The results of their study in terms of the confinement effectiveness (f'_c/f'_c) are shown in Fig. 4.52 for comparison. It is clearly shown that the present study showed less confinement effectiveness under the same stiffness level. This is mainly attributed to the fact that the GFRP shells in the present study were axially loaded, therefore, they expanded outward due to Poisson's ratio effect under their own share of axial load, which results in less contact pressure (confinement) with concrete. Another factor is that the shells were also bi-axially loaded under axial compression and lateral tension, which reduces their tensile strength in the hoop direction. On the other hand, the GFRP shells in the other study were fully utilized in the hoop direction only, under uniaxial tensile stresses, which allows the development of their full tensile strengths. This comparison shows that ignoring the stiffness of the shells in the axial direction by winding all the fibres in the hoop direction, and/or loading the concrete core only in order to preserve the strength and stiffness of the shells to be fully utilized in the hoop direction, could overestimate the beneficial effect of confinement. Most practical applications require a full composite action as well as longitudinal strength and stiffness of the shells for combined loading cases.

4.3.8 Strain Behaviour of the FRP Tube

The strain behaviour of the shell in the axial and lateral directions is a good indicator of the initiation of the confinement mechanism. Fig. 4.53a shows the axial versus lateral strain behaviour for the totally filled GFRP and steel tubes, stubs 2 and 7, as well as stubs with voided core and tube-in-tube, stubs 4 and 6. The behaviour of totally filled tubes is

generally characterized by a bi-linear response, with an initial slope slightly higher than Poisson's ratio of the shell due to the small elastic lateral expansion of the concrete at the stable micro-cracking stage, which induces small tensile strains in the shell. Once the concrete starts to expand excessively near the vicinity of the unconfined strength, the shell is fully activated in confinement and the rate of lateral straining increases as shown by the increase of the slope. The figure also shows that under the same axial strain level, the lateral strain in stub 4 is less than that of stub 2, which indicates less confinement due to the voided core as explained before. The figure also confirms that using an additional GFRP tube to maintain the voided core improves the confinement as indicated by the slope of the second branch for stub 6 in Fig. 4.53a. Steel shell shows a similar behaviour with a higher lateral strain level due to the higher Poisson's ratio of steel, compared to GFRP, to start with. Fig. 4.53b shows the axial-lateral strain behaviour of stubs 8, 9, and 10, which show similar behaviour to stubs 2 and 4 in terms of lower lateral strains with increasing the void size. Fig. 4.53c shows the axial-lateral strain behaviour of stubs 11 and 12. The filament-wound tube of stub 11 shows the typical change of slope, which indicates the initiation of confinement, whereas the pultruded tube of stub 12 failed before developing confinement as indicated by the absence of the second slope.

4.4 Concrete Expansion during Curing

Fig. 4.54 and Fig. 4.55 show the history of hoop strains developed after casting and during curing of the concrete in the tubes used to fabricate the beams and stubs. Fig. 4.54 shows the history for the tubes used to fabricate stubs 1, 3, 5, and 7. The behaviour reflects the resultant of two mechanisms taking place over time including the internal

pressure developed due to expansion of concrete, as well as the drying shrinkage. The behaviour shows that the hoop strains reached the maximum values at about 20 days regardless of the cross-section configuration or the material type of the shell (GFRP or steel). The strains were almost stabilized with little reduction over time, which indicates that the shrinkage process might have lasted longer than the expansion process. Knowing the stiffness of the shells in the hoop direction, $(E_{f(hoop)} t/R)$, one can estimate the sustained radial pressure resulting from expansion at the interface between concrete and the shell, σ_{Ro} , using Equation 4.23, where $\varepsilon_{(hoop)}$ is the stabilized hoop strain measured on the shell as given in Fig. 4.54. The estimated pressures were 0.63, 0.49, 0.42, and 5.13 MPa for stubs 1, 3, 5, and 7 respectively. The higher pressure in stub 7 is attributed to the higher stiffness of the tube, mainly due to the higher elastic modulus of steel, 203 GPa compared to that of GFRP, 33.4 GPa, as well as the difference in wall thickness. The behaviour in Fig. 4.54 also shows that less pressure is built up in the specimens with central voids. This is also illustrated in Fig. 4.55 for the tubes used to fabricate stubs 8, 9, and 10 by comparing the history of concrete expansion of totally filled tube, stub 8, and partially filled tubes with small and large voids, stubs 9 and 10. The lower pressure developed in the stubs with central voids is attributed to the radial displacement degree of freedom for inward expansion, which provides some relief of the internal pressure. Also in partially filled tubes, there is less volume of concrete to produce as much expansion as that produced in a totally filled tube. Fig. 4.56 shows the sustained pressure due to expansion of concrete, σ_{Ro} , as a function of the stiffness of the shell in the hoop direction, $(E_{f(hoop)} t/R)$ for the totally filled tubes, based on concrete-filled steel tube, stub 7, and concrete-filled GFRP tubes, stubs 1 and 8. The effect of void size (D_i/D_o) on

the sustained pressure ratio $\left(\frac{\sigma_{Ro(voided)}}{\sigma_{Ro(solid)}}\right)$ is also shown in Fig. 4.57 based on stubs 1 and 3 as well as stubs 8, 9, and 10 with two different values of stiffness. $\sigma_{Ro(voided)}$ and $\sigma_{Ro(solid)}$ are the pressures built in the partially and totally filled tubes respectively, for the same GFRP shell. D_i and D_o are the inner void diameter and the outer diameter respectively. The figure clearly indicates the reduction of the pressure with increasing the size of the inner void. The strain due to expansion in the axial direction was also monitored for the tube used to fabricate stub 1 and the sustained axial strain was about 57 percent of the sustained strain in the hoop direction. The induced strain in the axial direction reflects the good bond between the GFRP tube and the concrete core. This is mainly due to the skin friction in the tube.

Table 4.1 Details of the beams used to study the effect of reinforcement index on ultimate moment, curvature, and neutral axis depth

Beam	ρ (%)	f_u (MPa)	f'_c (MPa)	M_u (kN.m)	Z (mm)	$\psi \times (10^{-3})$ (m^{-1})	ω (%)	\bar{Z}	\bar{M}	$\bar{\psi}$ $\times (10^{-3})$
2b	12.32	725	37.7	14.1	41	425	236.9	0.41	0.374	817.3
4	6.09	342	58.0	19.51	51	145	35.9	0.30	0.071	143.6
8	9.26	414	37.7	4.04	27	370	101.7	0.30	0.152	361.6
10	7.85	340	60.3	155	86	84	44.3	0.26	0.074	154.4
11	7.45	232	67.3	125	88	67	25.6	0.27	0.057	73.9
12a	3.46	218	32.7	506			23.0		0.063	
12b	3.46	209	32.7	467	150*	29.3*	22.1	0.24	0.058	117.1
13a	3.79	235.5	57.5	1681			15.3		0.035	
13b	3.79	243.2	57.5	1632	225*	21.2*	15.8	0.24	0.034	84.5

* Neutral axis depth and curvatures are based on the measured depth of the compression zone after the test rather than using the axial strain distribution because of the slip.

Notes:

f_u = Tensile strength of the GFRP tube in the axial direction (obtained using the ultimate strains of the beams)

f'_c = Compressive strength of the concrete

M_u = Ultimate moment capacity of the beam

Z = Neutral axis depth at ultimate state based on the axial strain distribution

ψ = Ultimate curvature based on the axial strain distribution

ρ (Reinforcement ratio) = $\frac{4t}{D_o}$ Where t is the structural wall thickness and D_o is the outer diameter of the tube

ω (Reinforcement index) = $\rho \frac{f_u}{f'_c}$

\bar{Z} (Normalized neural axis depth) = $\frac{Z}{D_o}$

\bar{M} (Normalized ultimate moment) = $\frac{M_u}{D_o^3 f'_c}$

$\bar{\psi}$ (Normalized ultimate curvature) = $\psi D_o \frac{f_u}{f'_c}$

Table 4.2 Details of the beams used to compare the cracking strength to different codes

Beam	D_o (mm)	f'_c (MPa)	M_{cr} (kN.m)	I_t (m ⁴)	f_{cr} (MPa)	Comparison with ACI code			Comparison with CEB-FIP code		
						$\frac{f_{cr}}{\sqrt{f'_c}}$	k_{mean}	k_{ACI}	$\frac{f_{cr}}{f'_c{}^{2/3}}$	k_{mean}	k_{CEB}
4	168	58.0	3.58	0.000037	8.11	1.07	} 1.0 0.6	0.54	} 0.51	0.205 (min.)	
10	326	60.3	24.52	0.000512	7.80	1.01		0.51			
11	320	67.3	29.15	0.000471	9.89	1.21		0.59			
12a	626	32.7	119.6	0.007323	5.71	1.00		0.56			0.398
12b	626	32.7	133.8	0.007323	5.11	0.89		0.50			0.205 (max.)
13a	942	57.5	532.2	0.037143	6.74	0.89		0.45			
13b	942	57.5	540.4	0.037143	6.85	0.90		0.46			

Notes:

D_o = Outer diameter of the beam

f'_c = Compressive strength of the concrete

M_{cr} = Cracking moment of the beam

I_t = Transformed moment of inertia of the cross-section

f_{cr} = Cracking strength of concrete

$$I_t = I_c + \frac{E_{f(axial)}}{E_c} I_f \quad \text{Where } I_c \text{ and } I_f \text{ are the moments of inertia of the concrete core and the FRP shell respectively. } E_{f(axial)} \text{ is the elastic modulus of the shell in the axial direction and } E_c \text{ is concrete elastic modulus.}$$

$$f_{cr} = \frac{M_{cr}}{I_t} ((D_o - 2t)/2)$$

ACI code: $f_{cr} = k\sqrt{f'_c} \quad (k = 0.6)$

CEB-FIP code: $f_{cr} = k(f'_c)^{2/3} \quad (k = 0.205 - 0.398)$

Table 4.3 Details of the stubs used to study the effect of stiffness of the shell on the confinement effectiveness

stub	Radius	Thickness	Elastic mod.	f'_c	f'_{cc}	$\frac{f'_{cc}}{f'_c}$	$\frac{E_{f(hoop)} t}{R}$
	R (mm)	t (mm)	$E_{f(hoop)}$ (GPa)				(GPa)
1	82.7	2.56	33.4	58.0	97.1	1.674	1.03
2	82.7	2.56	33.4	58.0	94.5	1.625	1.03
8	108.4	2.21	33.4	58.0	70.1	1.209	0.68
11	48.5	3.08	23.0	37.7	81.0	2.149	1.46
12	48.5	3.09	8.7	37.7	50.3	1.334	0.55



Table 4.4 Details of the stubs tested by Mirmiran and Shahawy (1997) and used in this study to examine the effect of loading the shell in the axial direction

stub	Radius	Thickness	Elastic mod.	f'_c	f'_{cc}	$\frac{f'_{cc}}{f'_c}$	$\frac{E_{f(hoop)} t}{R}$
	R (mm)	t (mm)	$E_{f(hoop)}$ (GPa)				(GPa)
a	76.3	1.3	37.2	31.5	60.5	1.920	0.634
b	76.3	2.1	40.3	31.5	77.2	2.450	1.109
c	76.3	3.0	40.7	31.5	85.5	2.715	1.600



$$\text{Confinement effectiveness} = \frac{f'_{cc}}{f'_c}$$

$$\text{Stiffness of the shell} = \frac{E_{f(hoop)} t}{R}$$

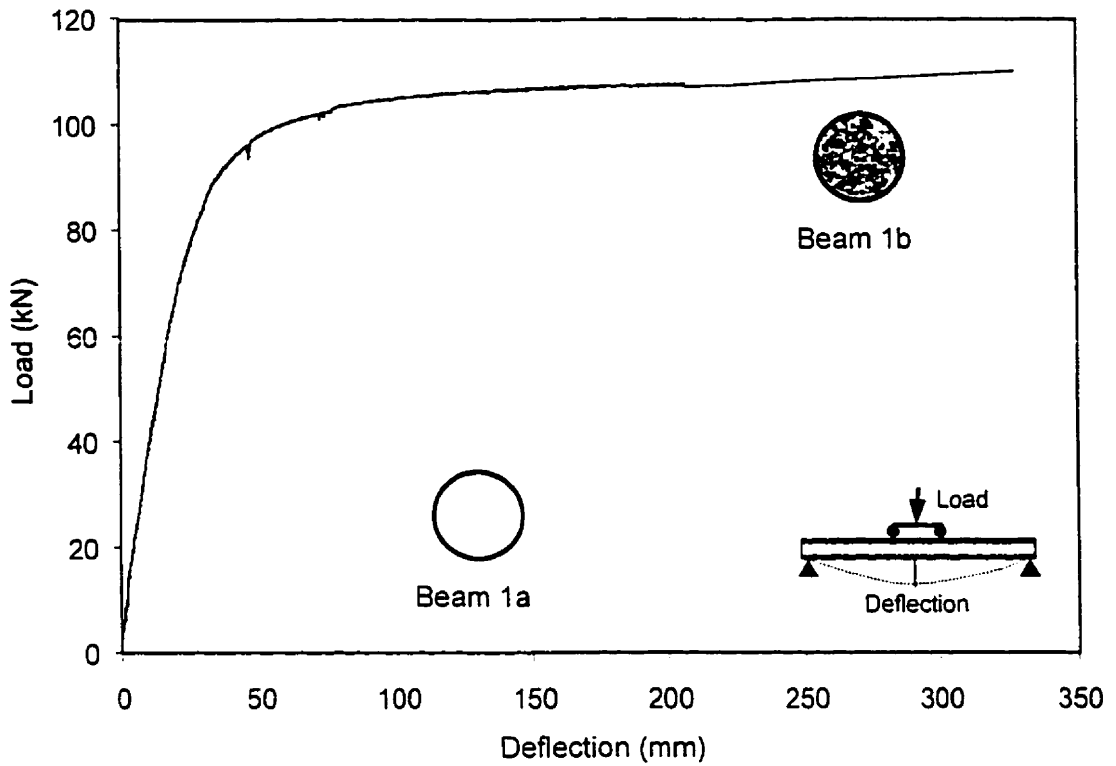


Fig. 4.1 Load-deflection behaviour of hollow and concrete-filled steel tubes

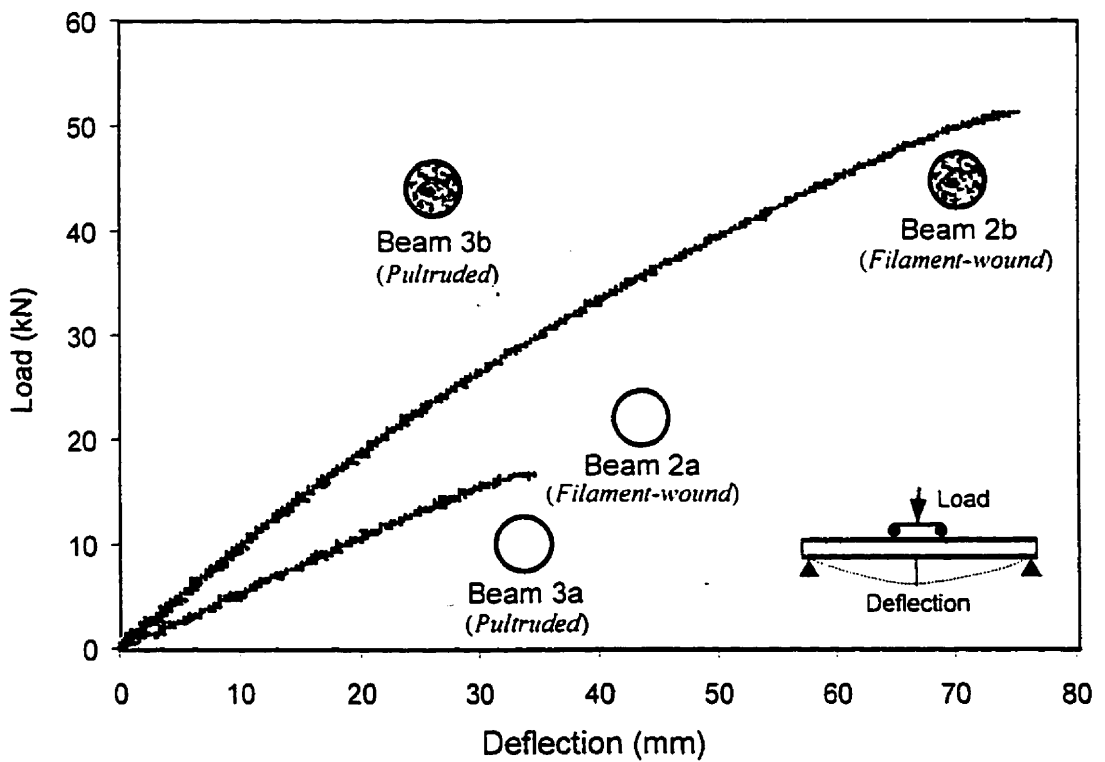


Fig. 4.2 Load-deflection behaviour of hollow and concrete-filled GFRP tubes

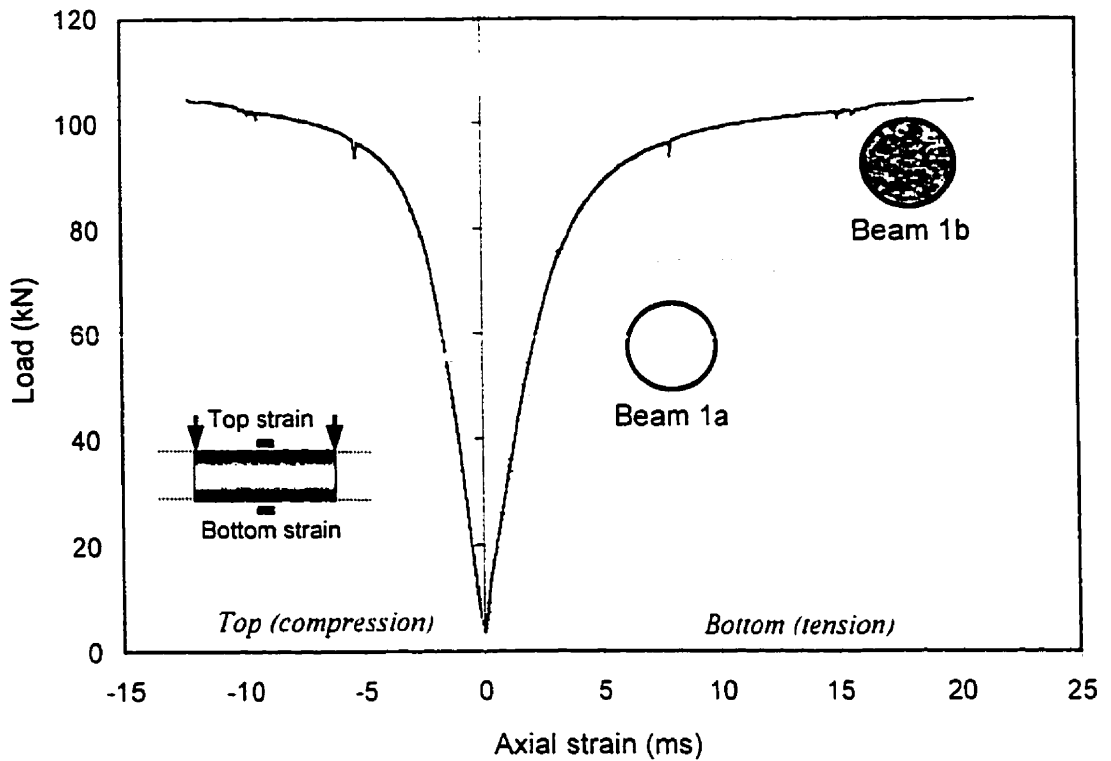


Fig. 4.3 Load-axial strain behaviour of hollow and concrete-filled steel tubes

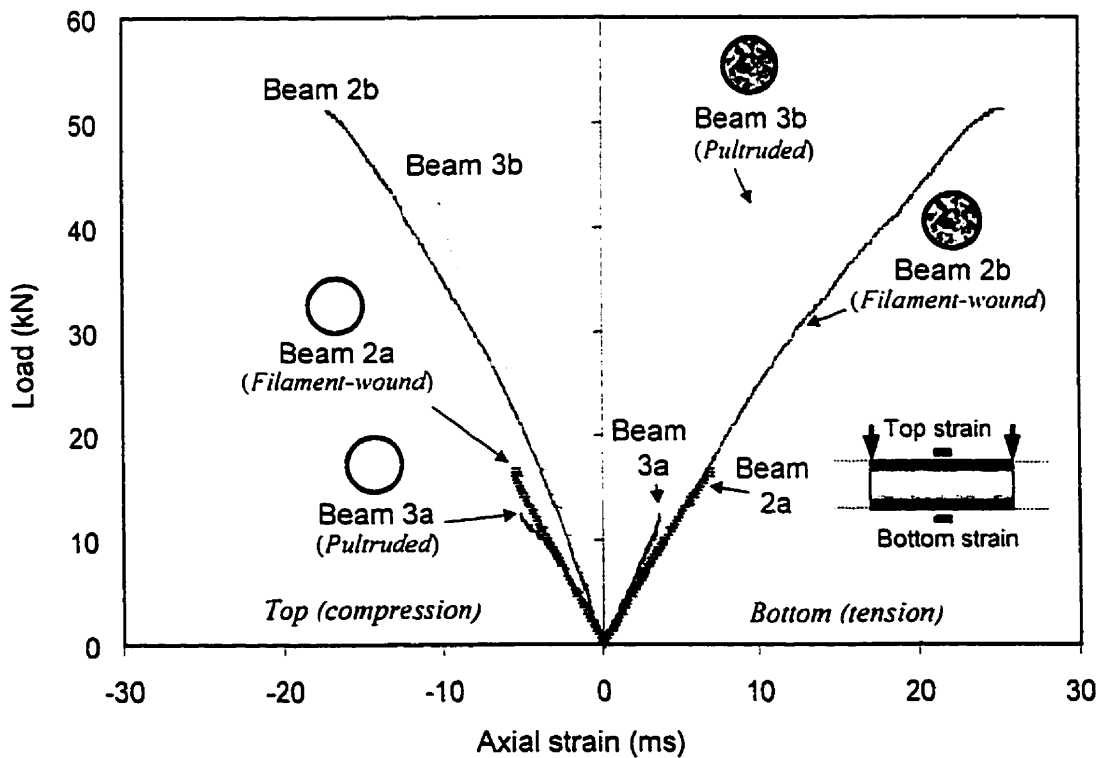


Fig. 4.4 Load-axial strain behaviour of hollow and concrete-filled GFRP tubes

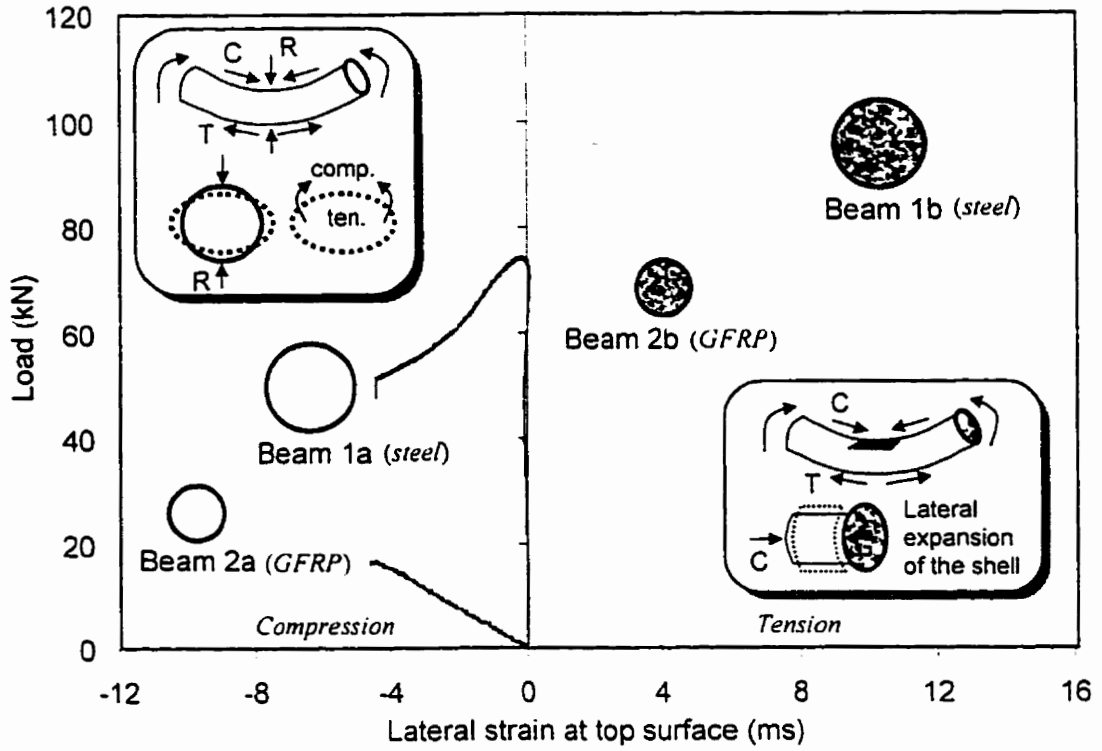


Fig. 4.5 Load-lateral strain behaviour at compression side of hollow and concrete-filled tubes

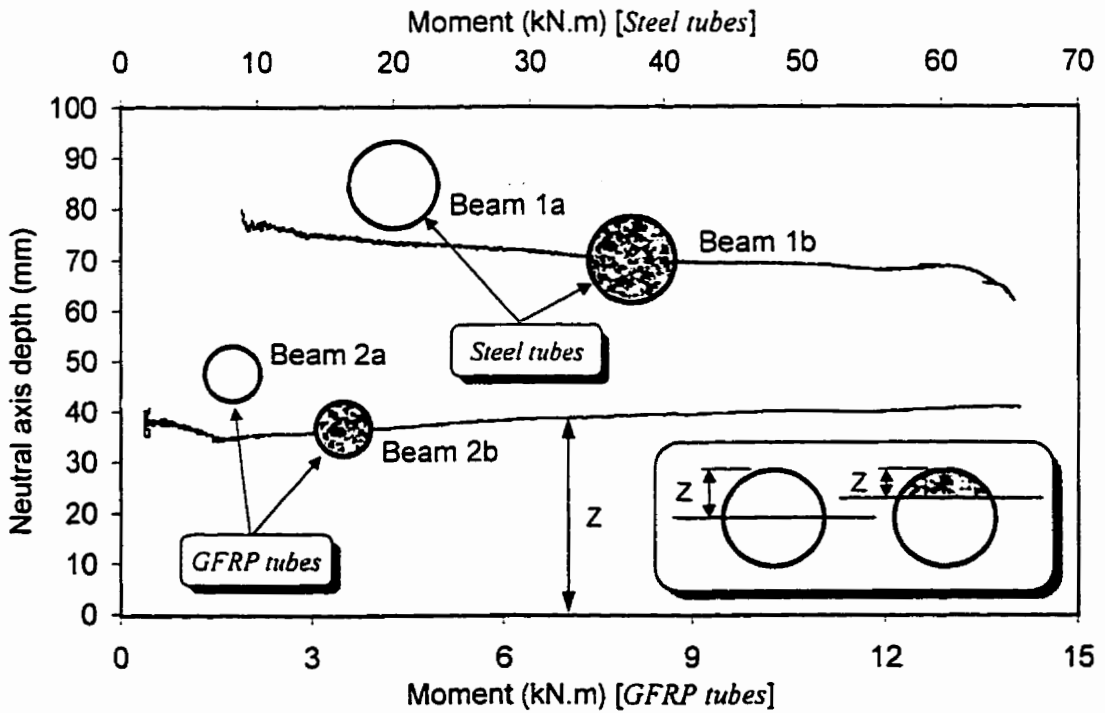


Fig. 4.6 Variation of neutral axis depth with the moment for hollow and concrete-filled GFRP and steel tubes

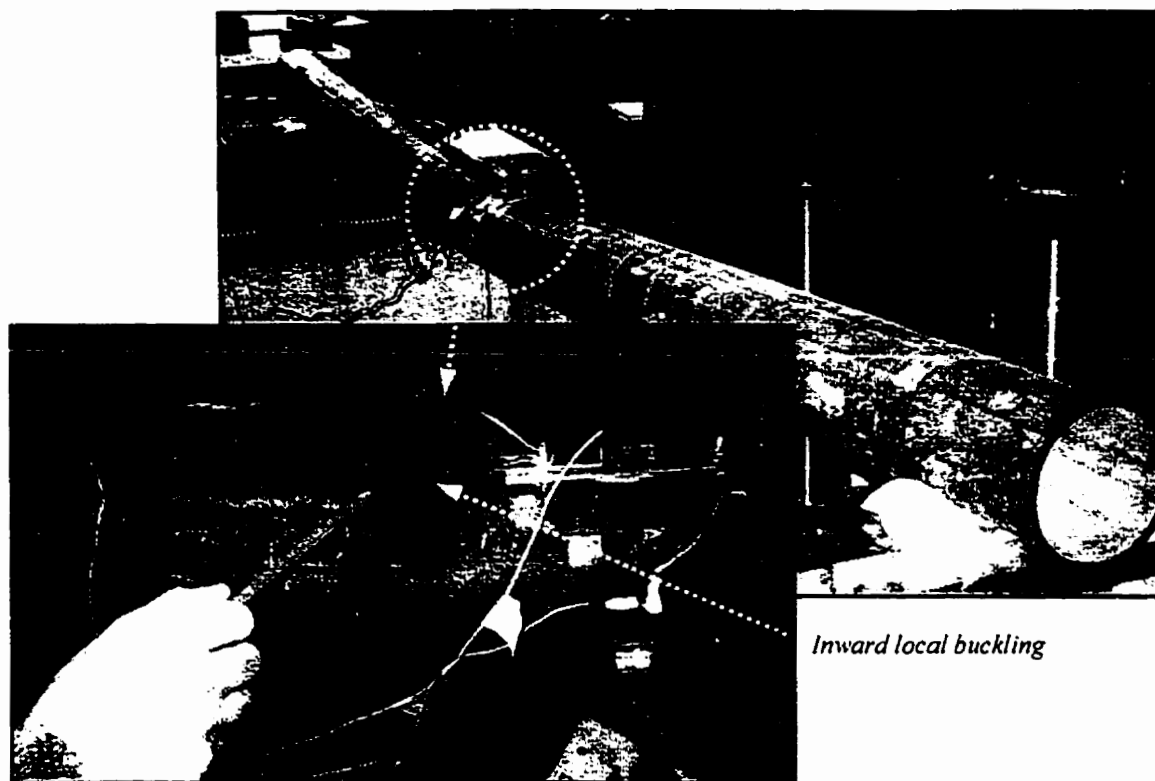


Fig. 4.7 Failure mode of hollow steel tube, beam 1a

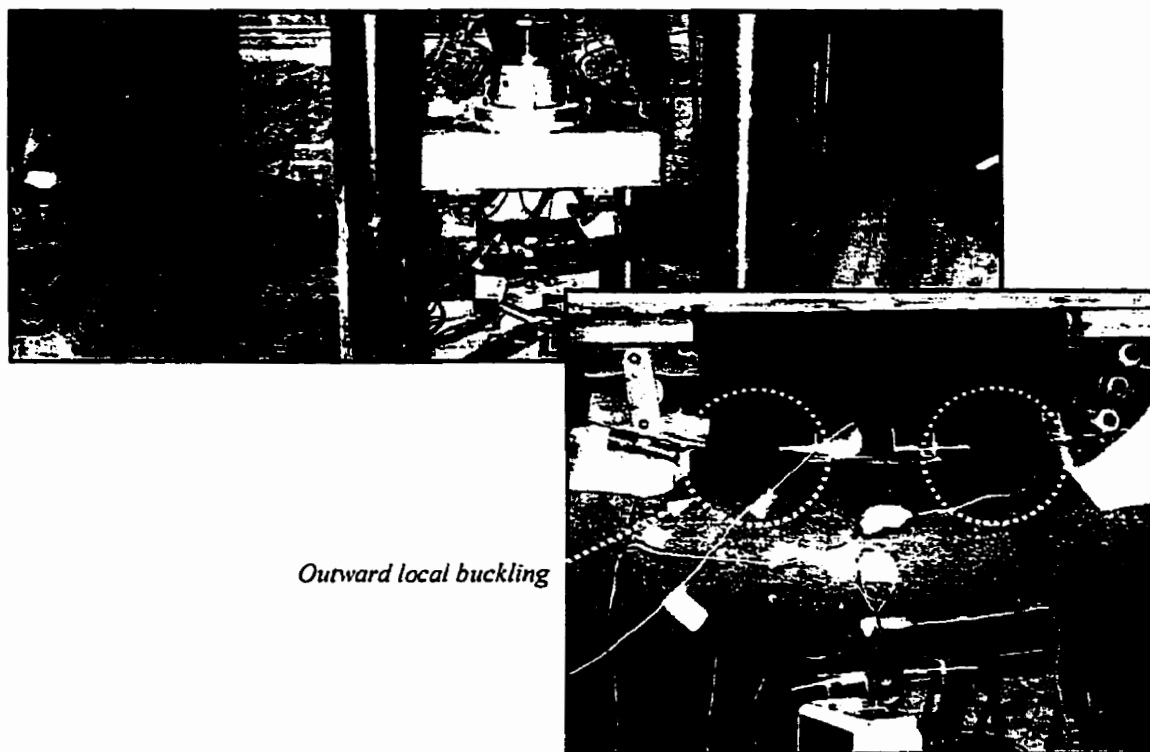


Fig. 4.8 Failure mode of concrete-filled steel tube, beam 1b

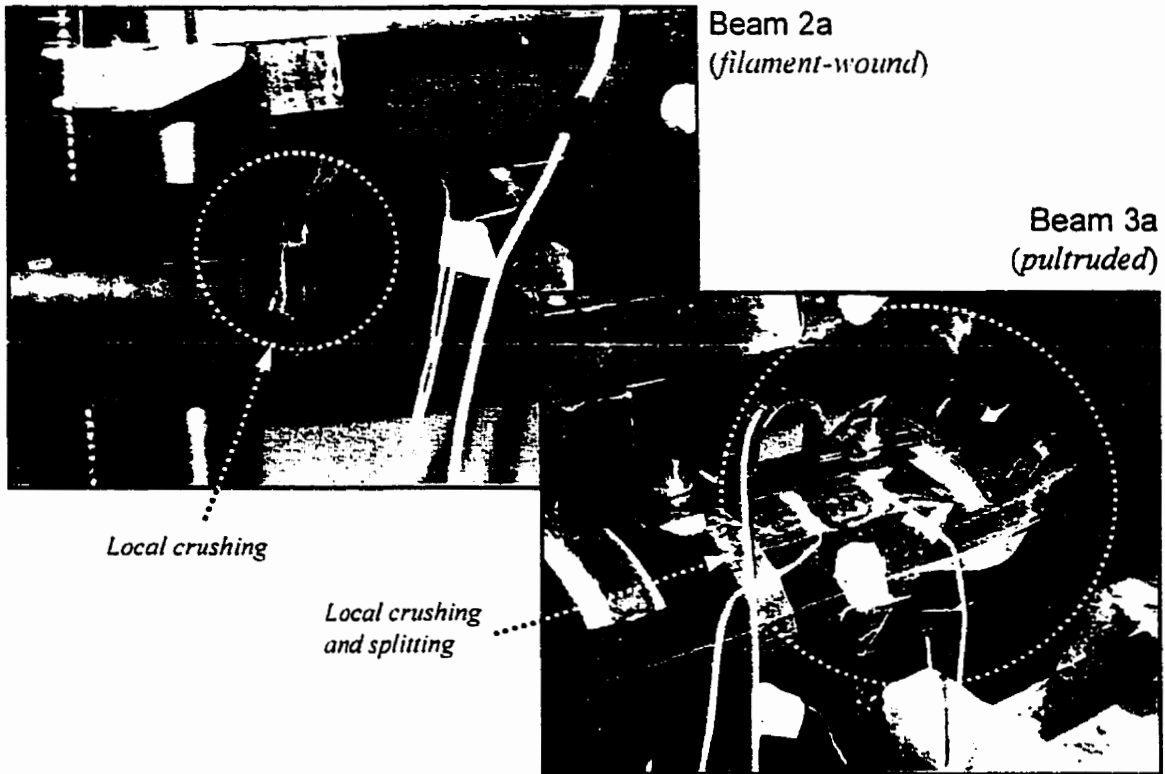
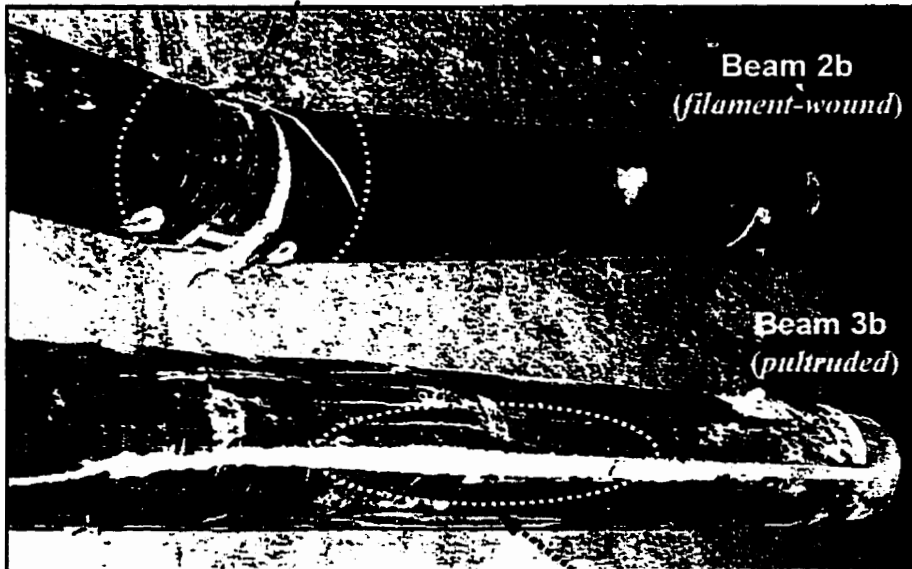


Fig. 4.9 Failure modes of hollow GFRP tubes, beams 2a and 3a

Rupture of fibers in the tension side due to bending



Splitting of tube due to shear

Fig. 4.10 Failure modes of concrete-filled GFRP tubes, beams 2b and 3b

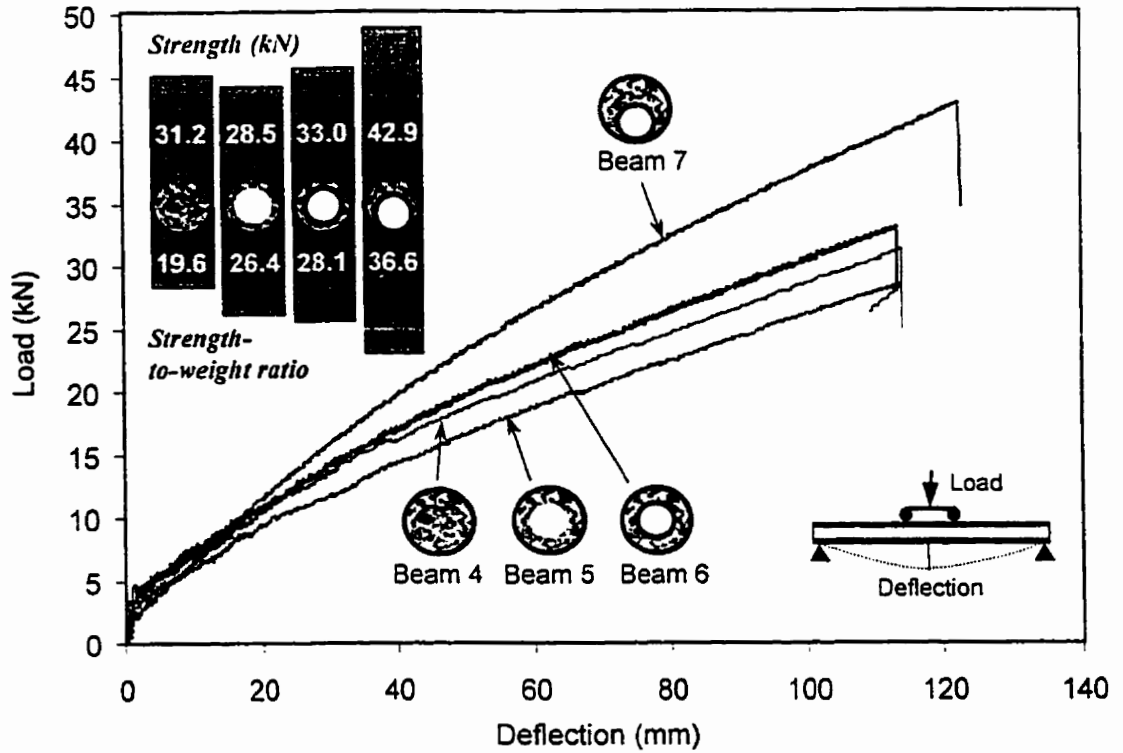


Fig. 4.11 Load-deflection behaviour of totally and partially filled GFRP tubes

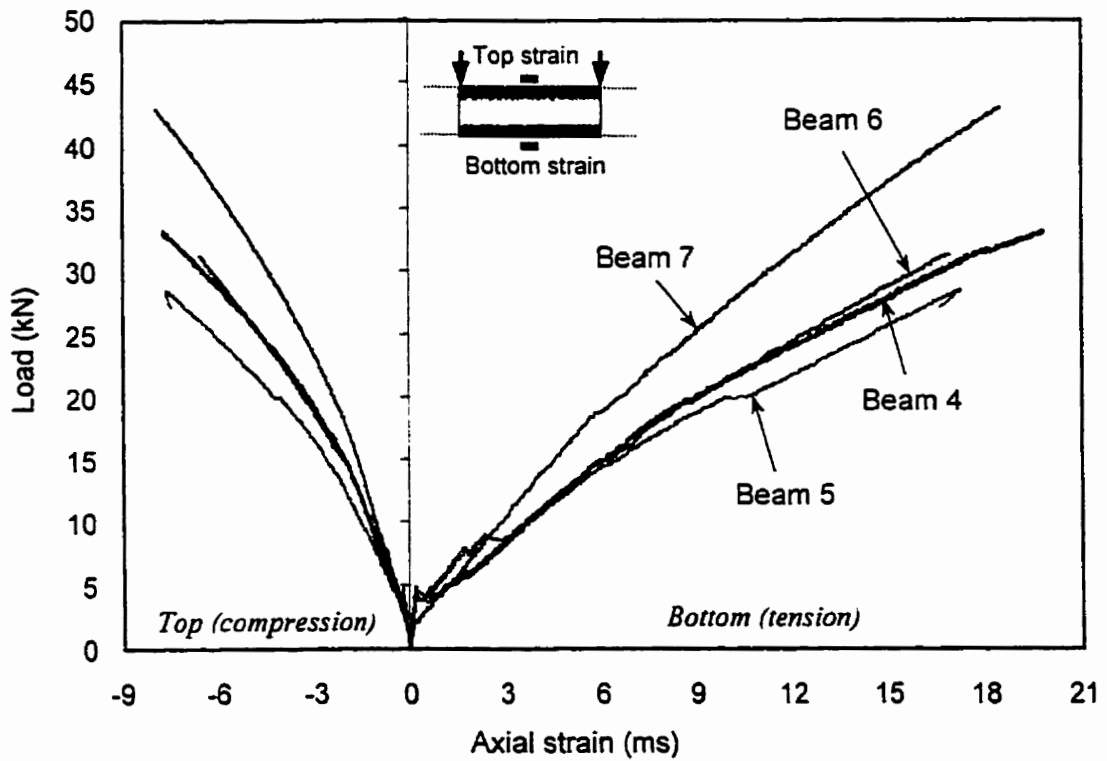


Fig. 4.12 Load-axial strain behaviour of totally and partially filled GFRP tubes

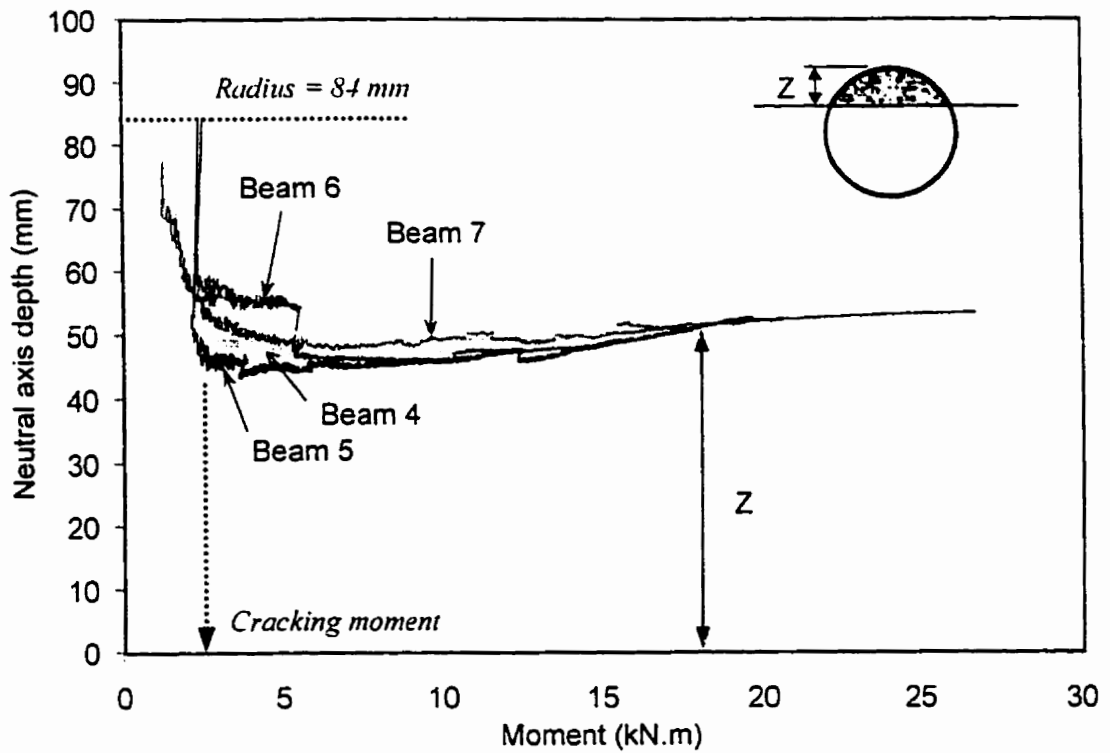


Fig. 4.13 Variation of neutral axis depth with the moment for totally and partially filled GFRP tubes

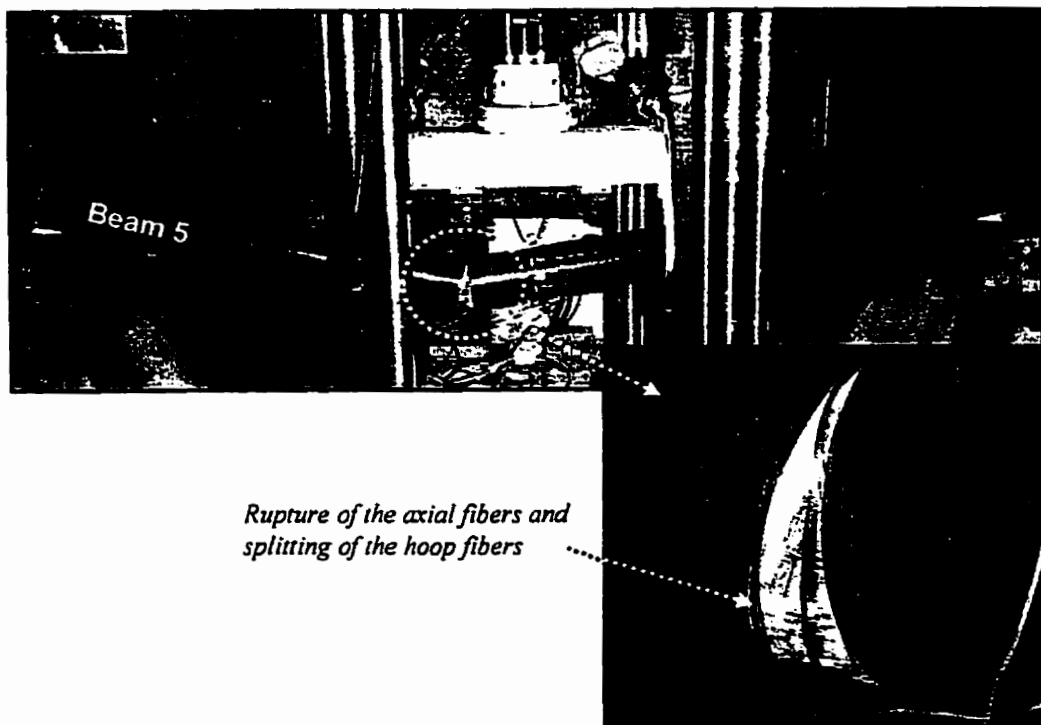


Fig. 4.14 Failure mode of beams 4, 5, 6 and 7

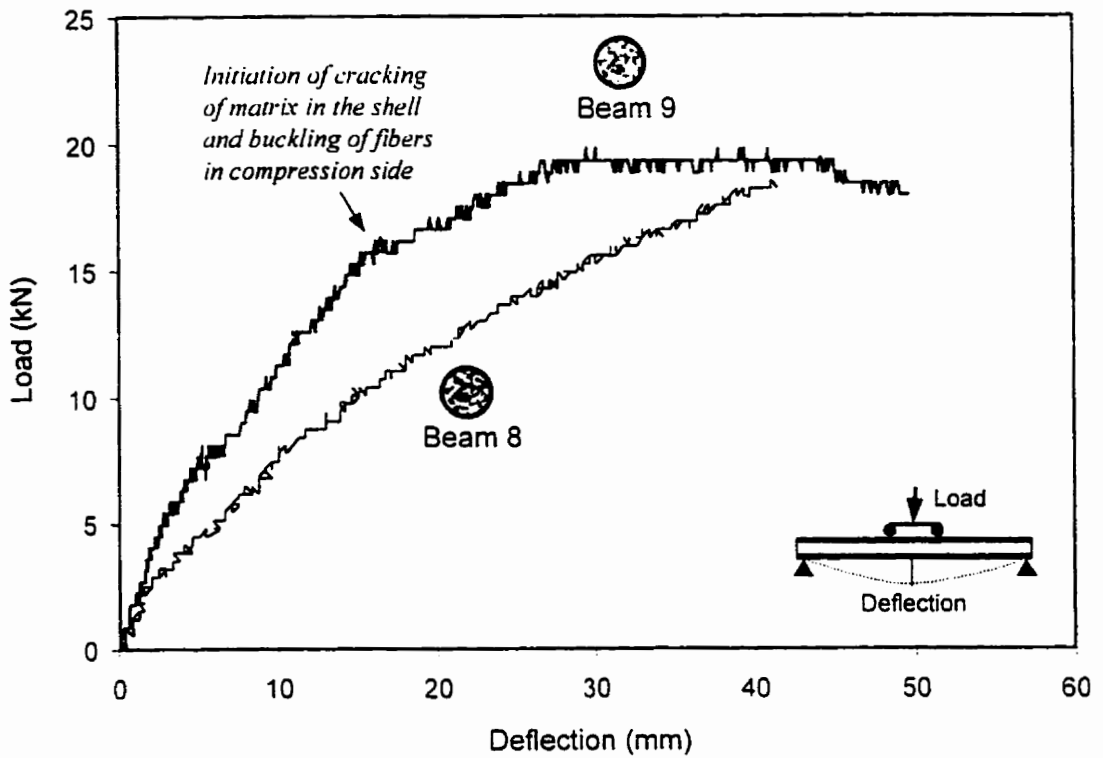


Fig. 4.15 Load-deflection behaviour of beams 8 and 9 with different laminate structures

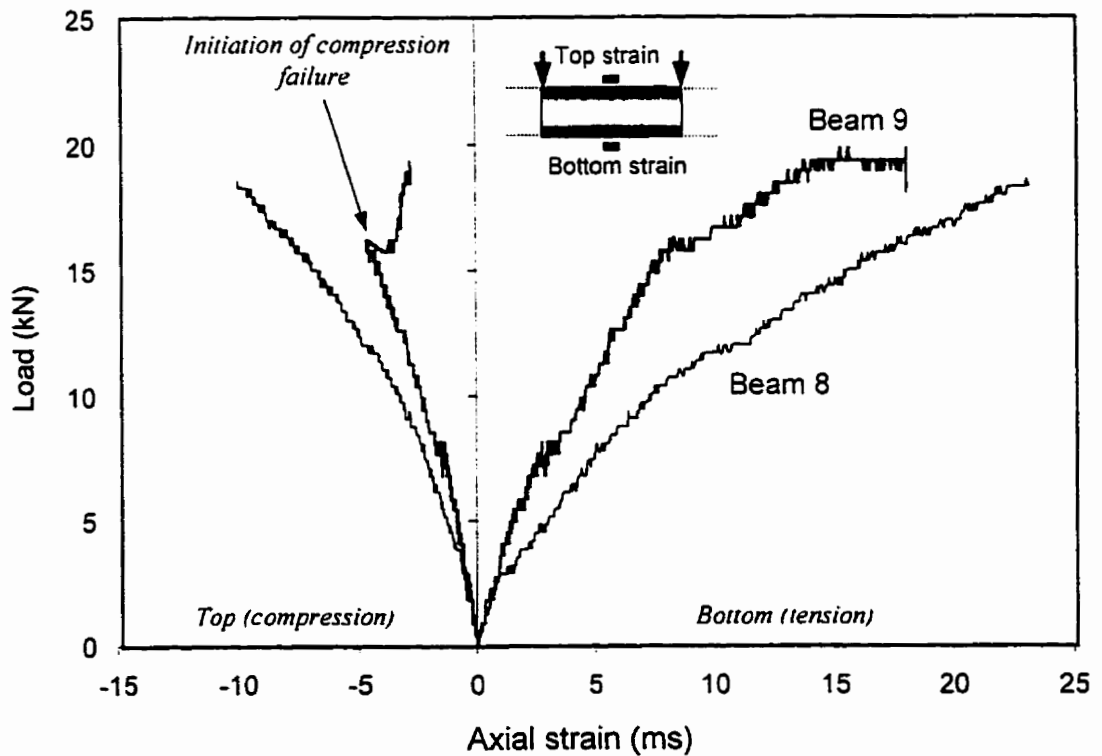


Fig. 4.16 Load-axial strain behaviour of beams 8 and 9

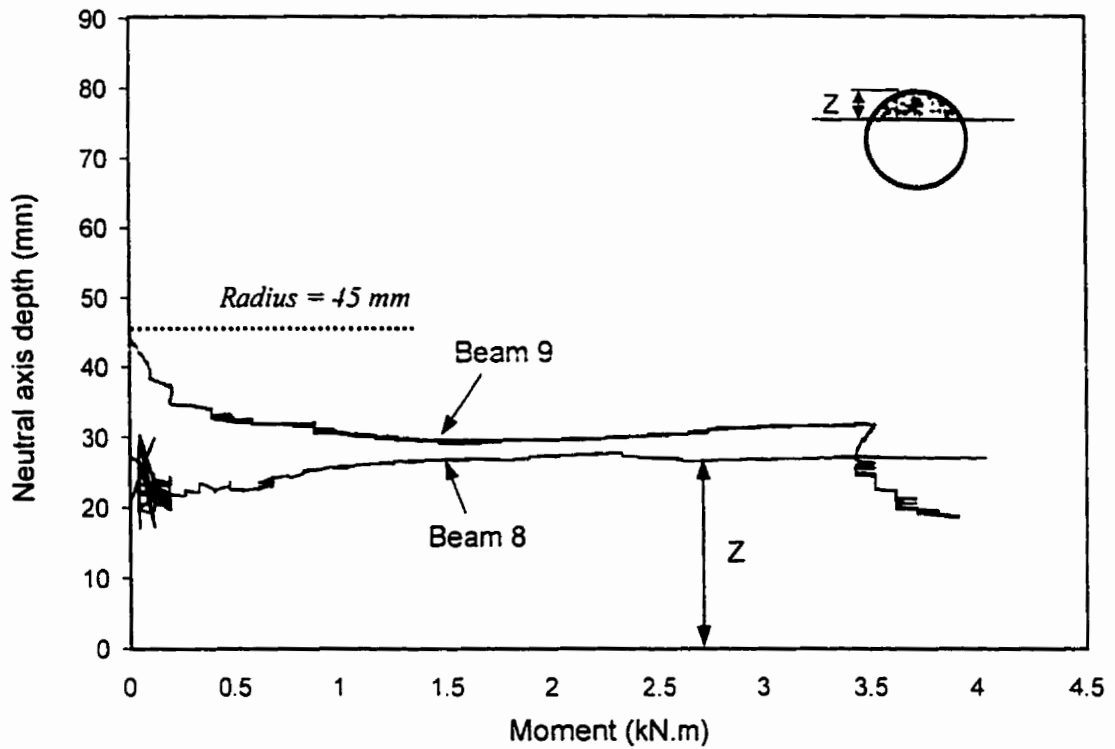


Fig. 4.17 Variation of neutral axis depth with the moment in beams 8 and 9

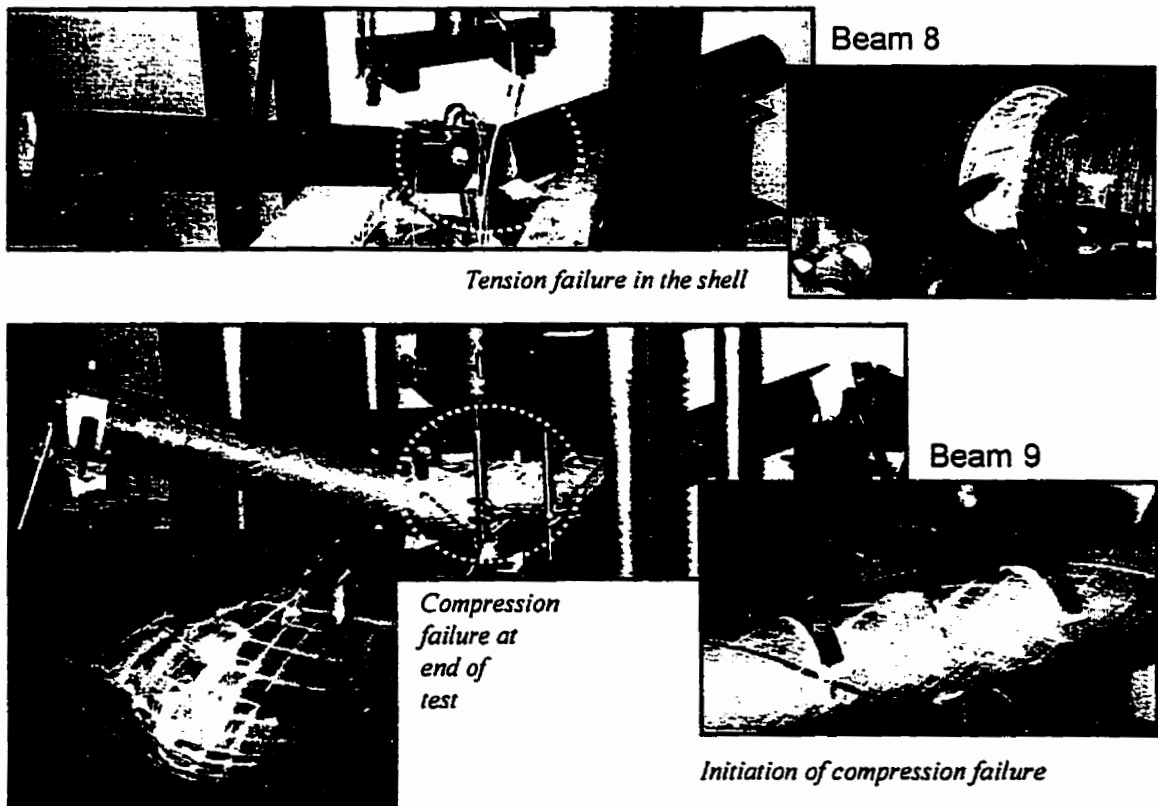


Fig. 4.18 Failure modes of beams 8 and 9

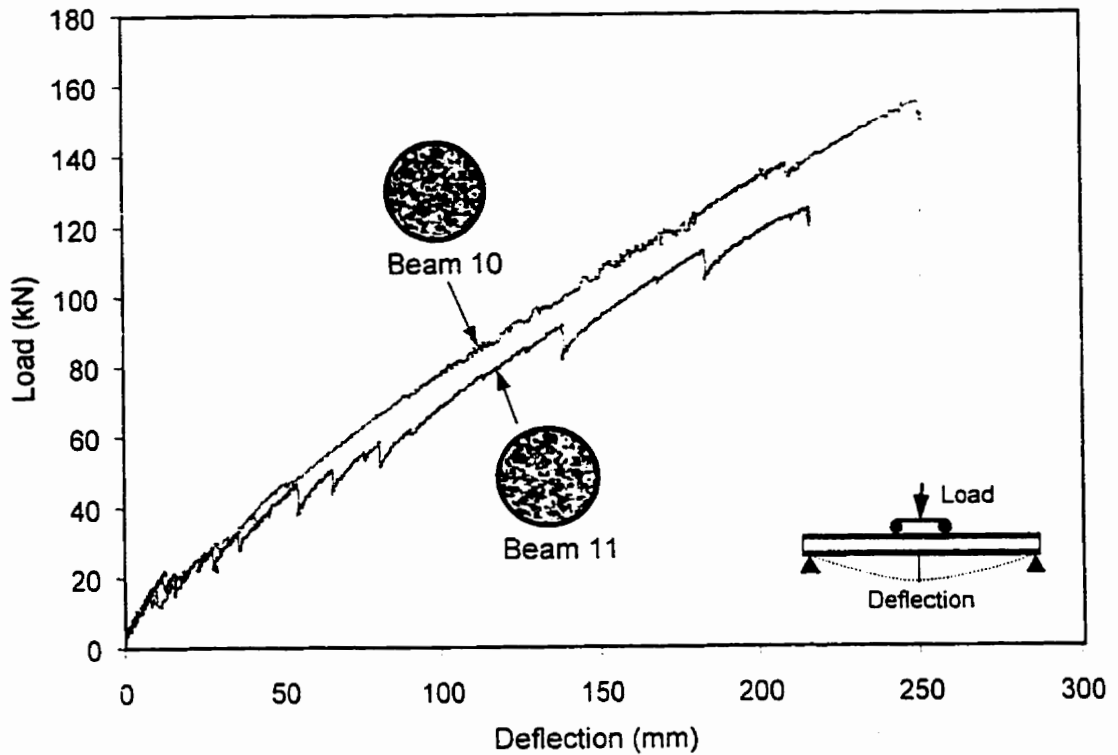


Fig. 4.19 Load-deflection behaviour of beams 10 and 11 with different laminate structures

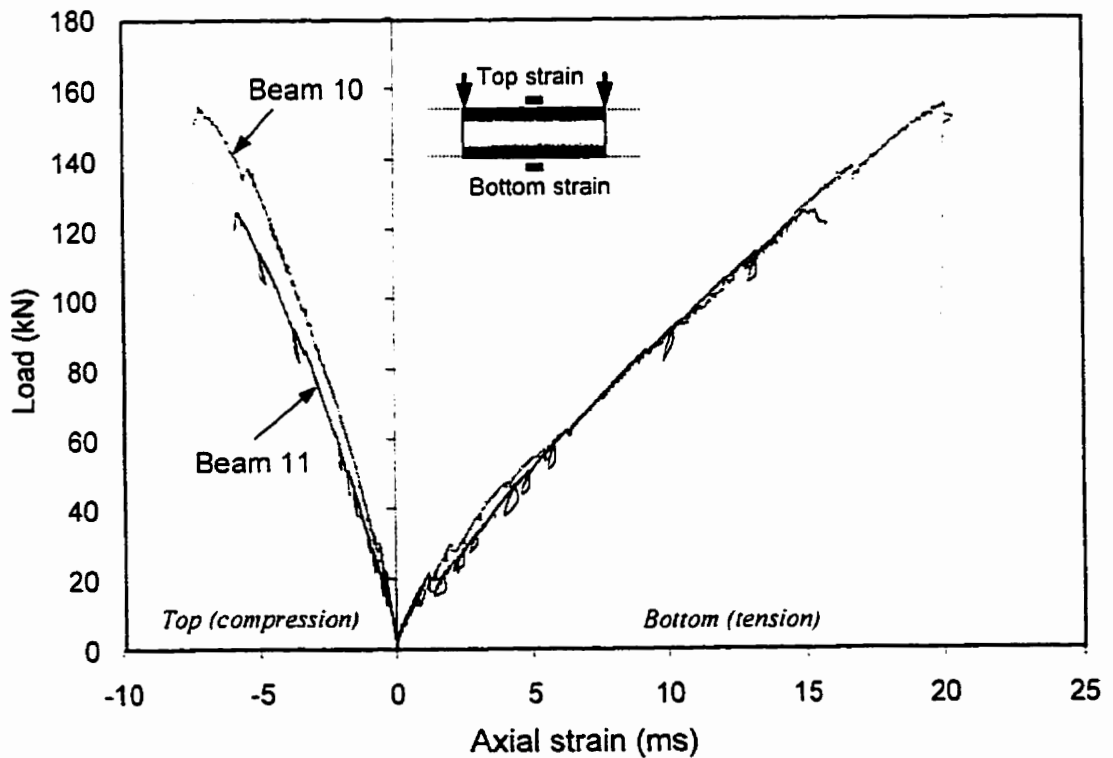


Fig. 4.20 Load-axial strain behaviour of beams 10 and 11

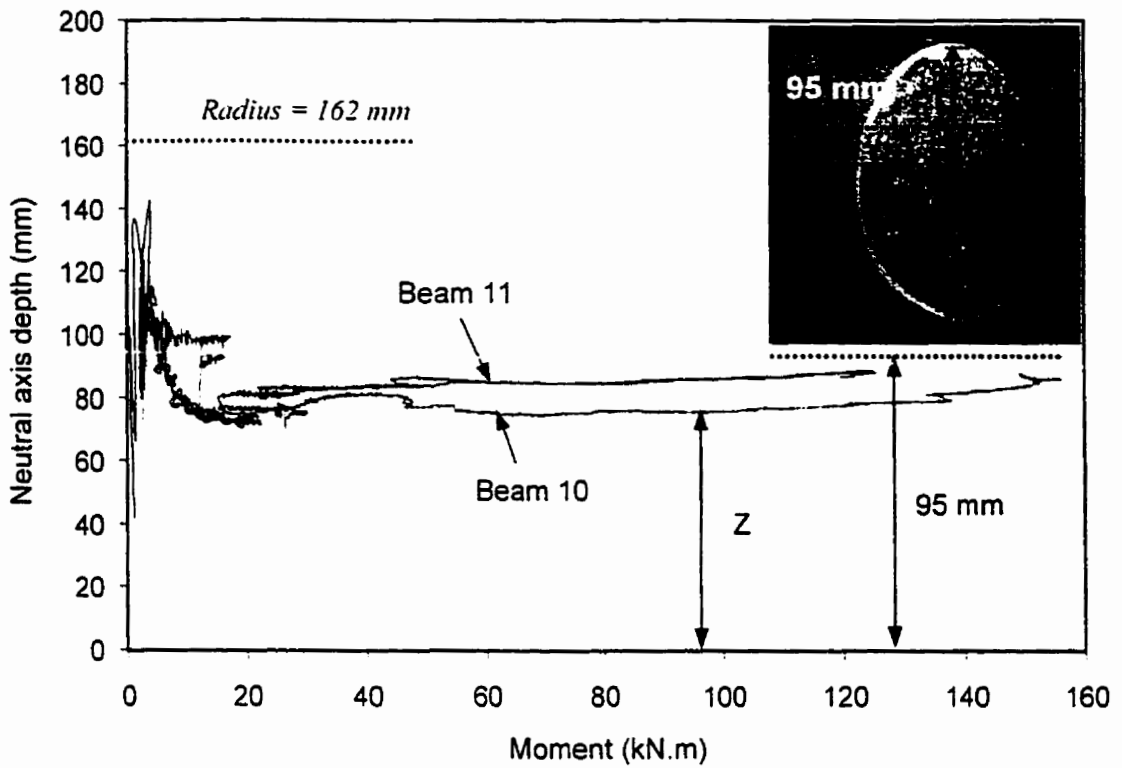


Fig. 4.21 Variation of neutral axis depth with the moment in beams 10 and 11

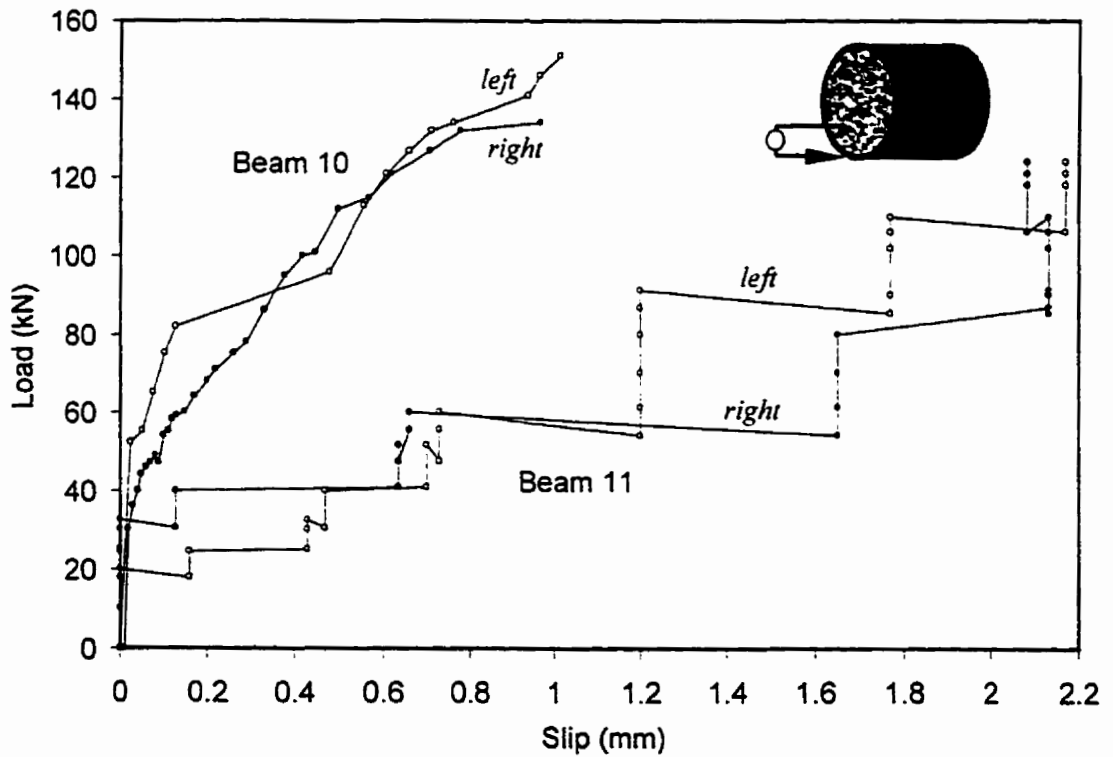


Fig. 4.22 Load-slip behaviour of beams 10 and 11

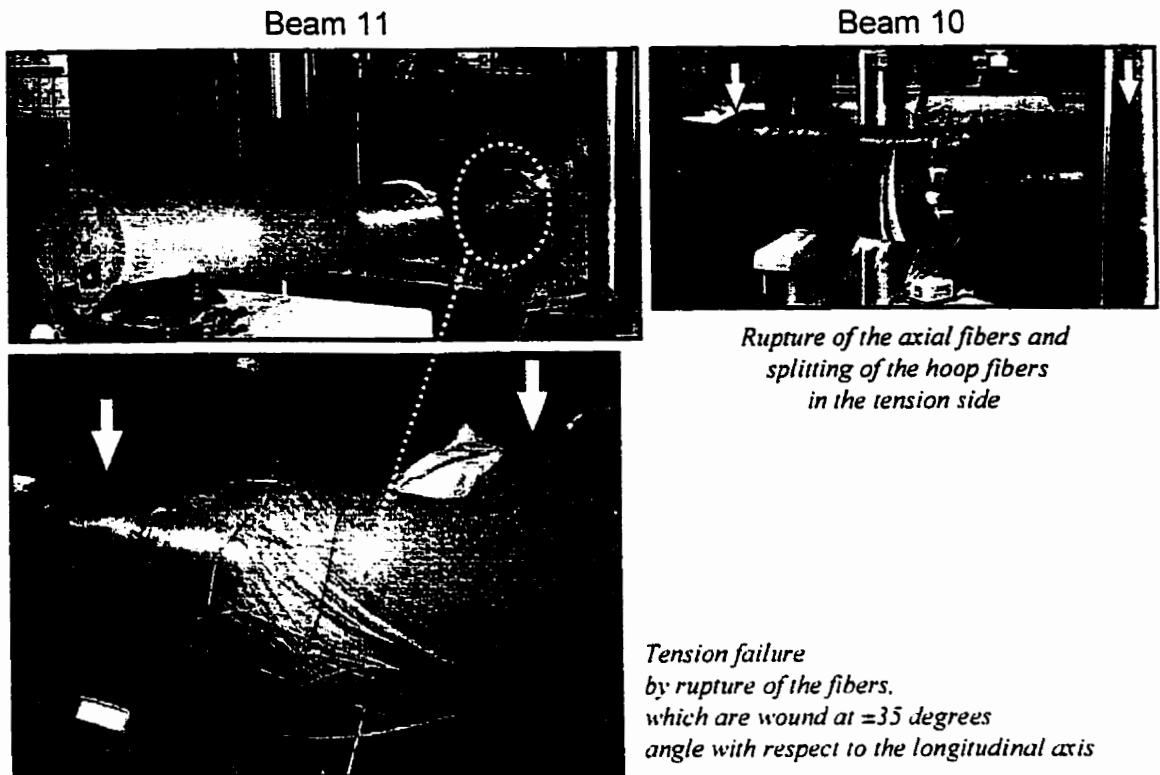


Fig. 4.23 Failure modes of beams 10 and 11

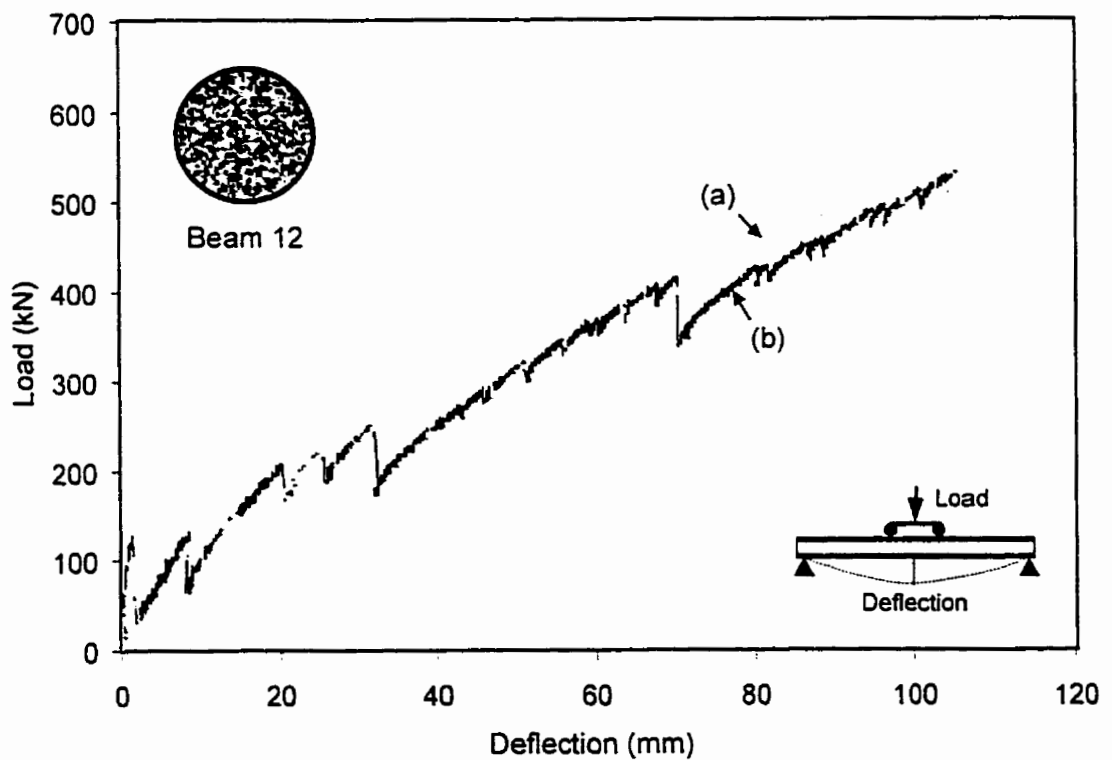


Fig. 4.24 Load-deflection behaviour of beams 12 (a, b)

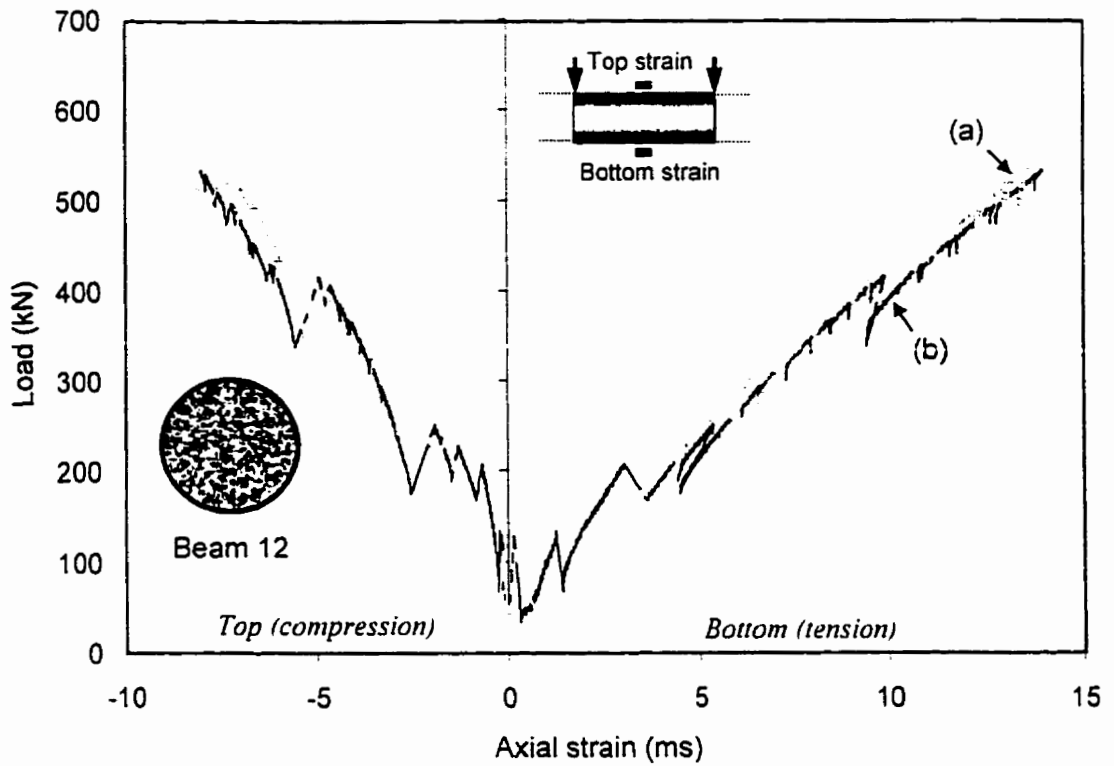


Fig. 4.25 Load-axial strain behavior of beams 12 (a, b)

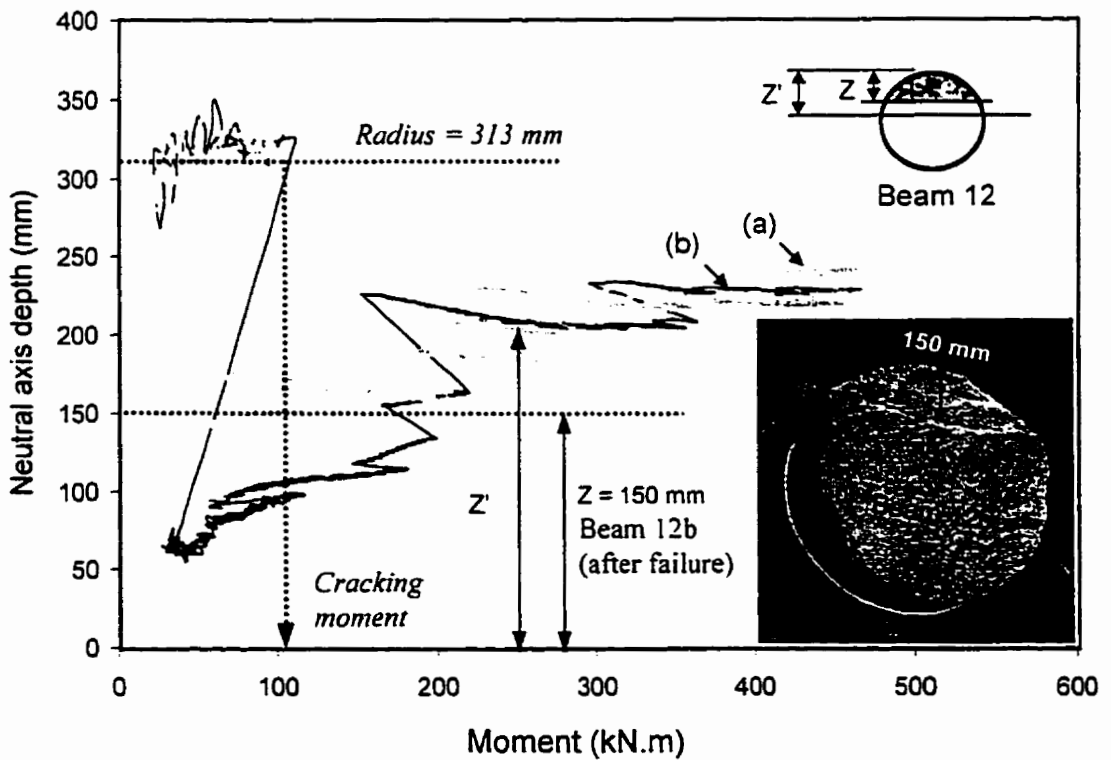


Fig. 4. 26 Variation of the neutral axis depth in beams 12 (a, b)

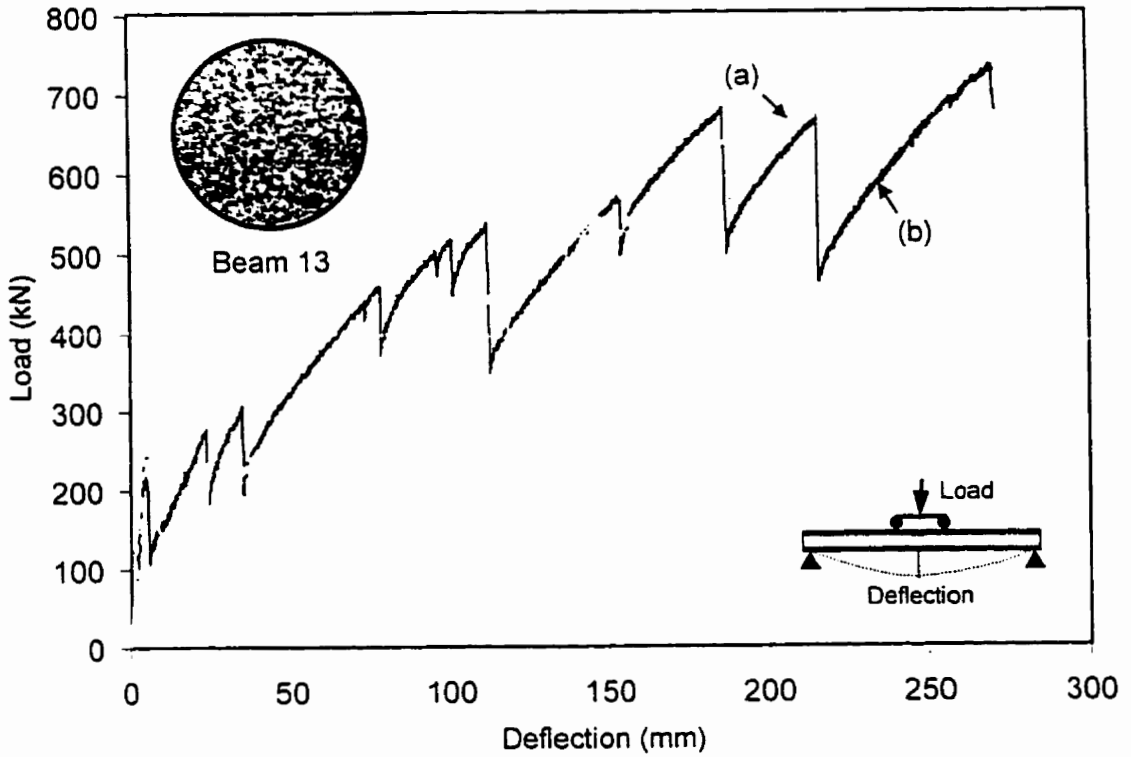


Fig. 4.27 Load-deflection behavior of beams 13a and b

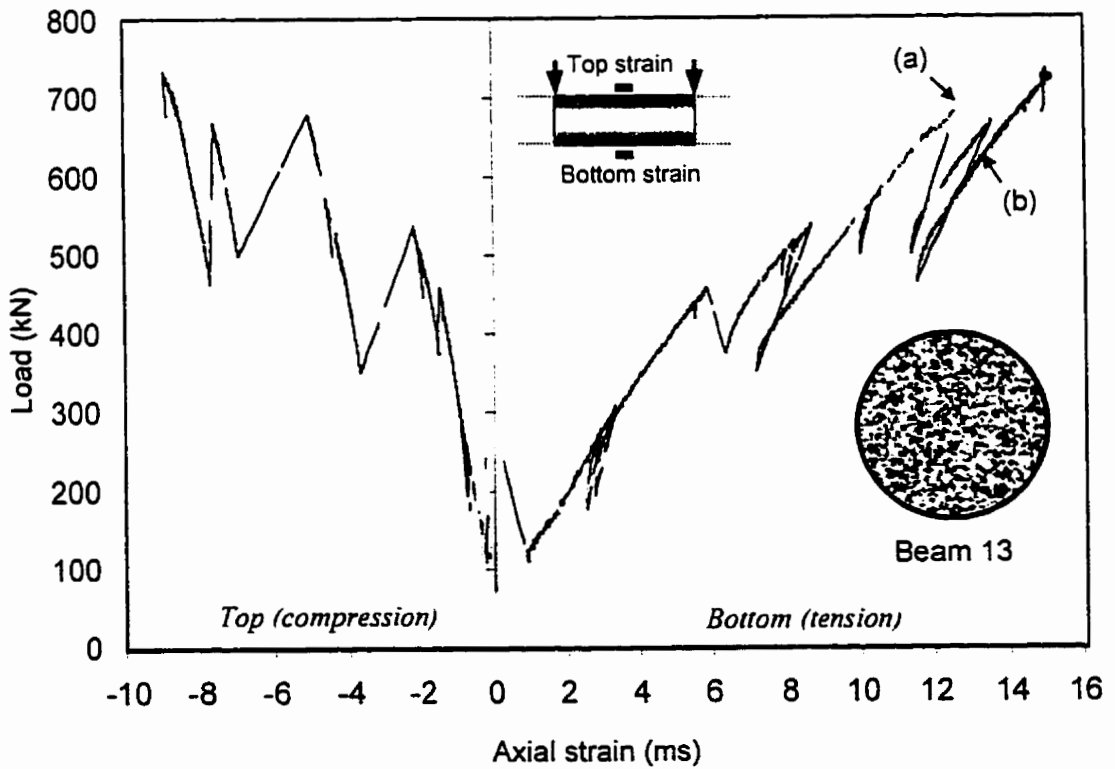


Fig. 4.28 Load-axial strain behavior of beams 13 (a, b)

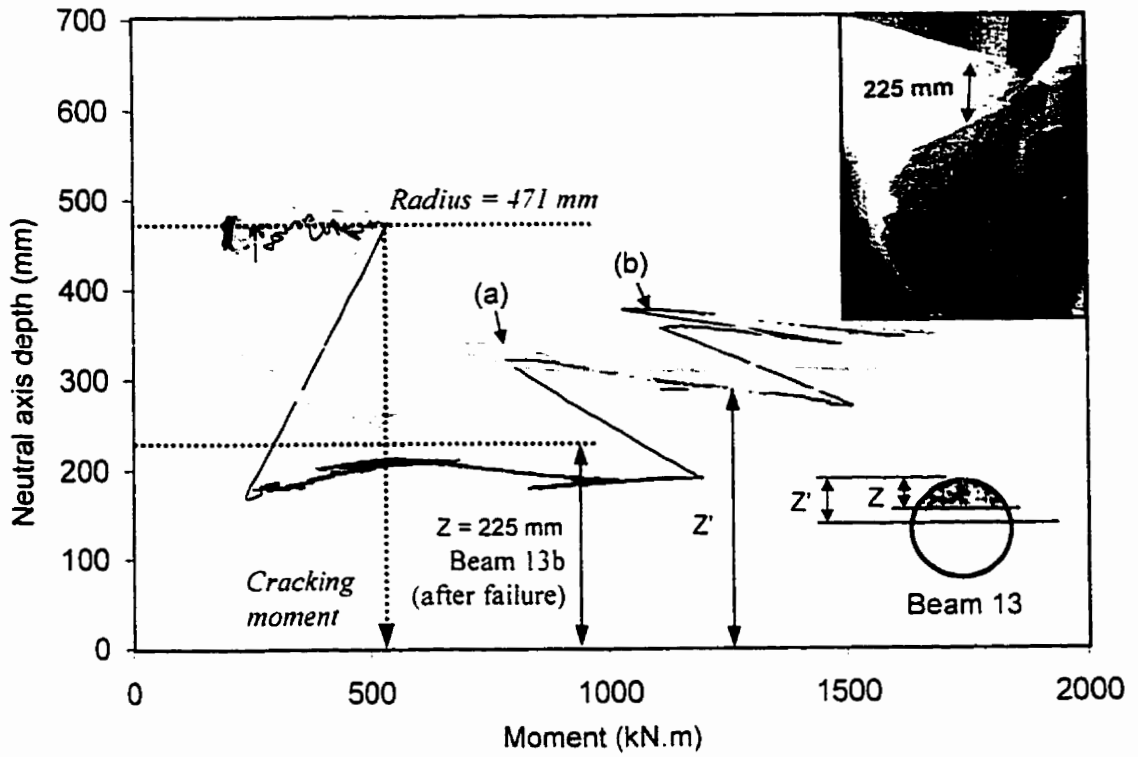


Fig. 4.29 Variation of the neutral axis depth in beams 13 (a, b)

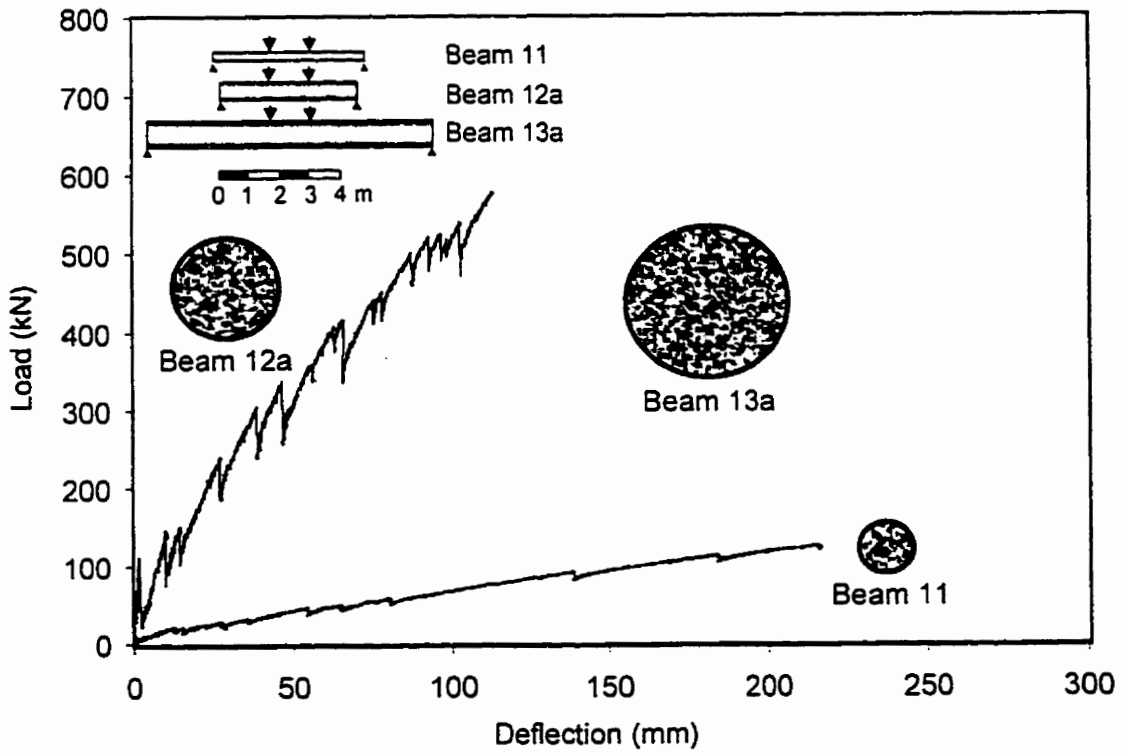


Fig. 4.30 Load-deflection behaviour of beams 11, 12a, and 13a

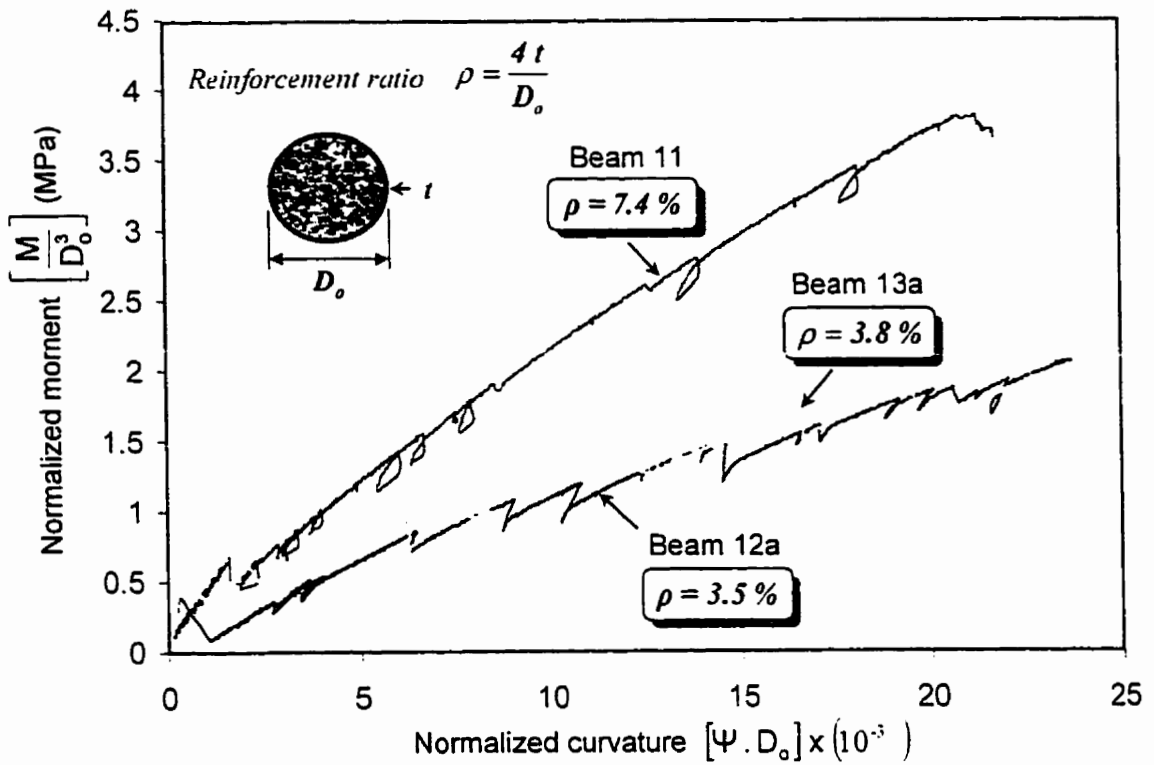


Fig. 4.31 Normalized moment-curvature response of beams 11, 12a, and 13a

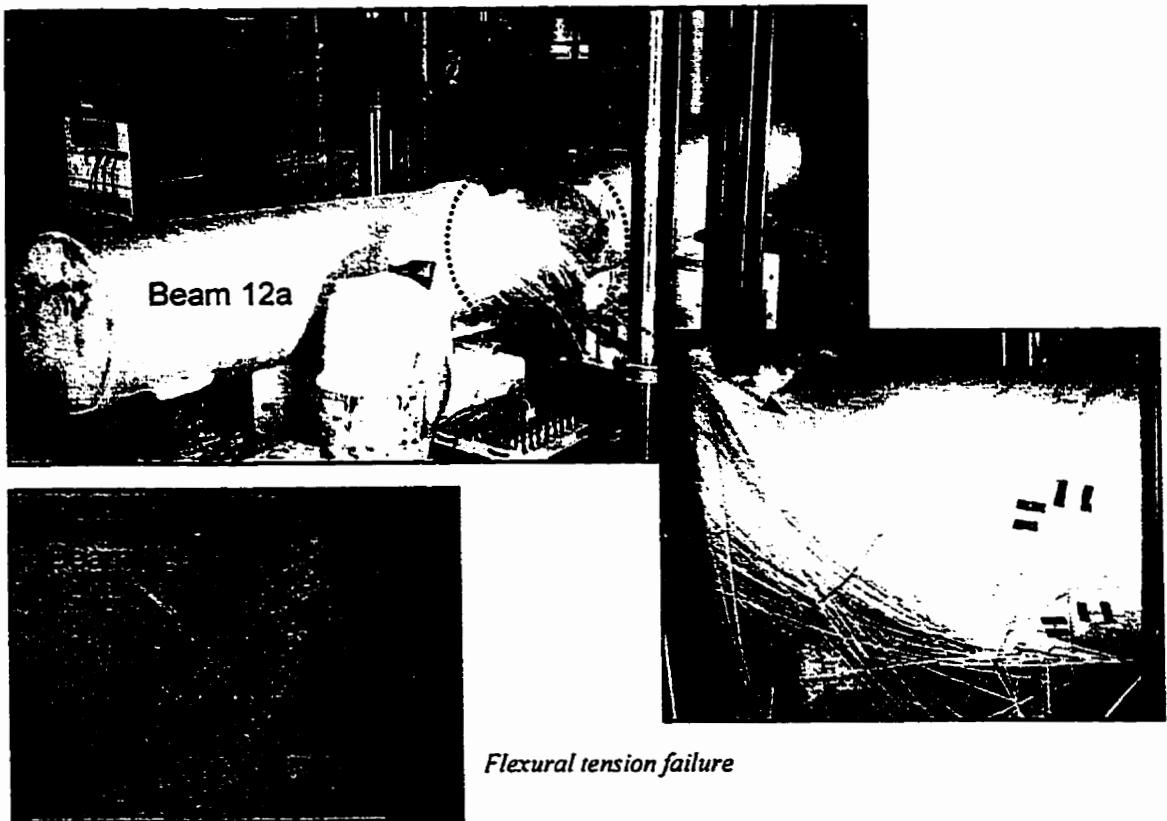


Fig. 4.32 Failure mode of beams 12 (a, b)

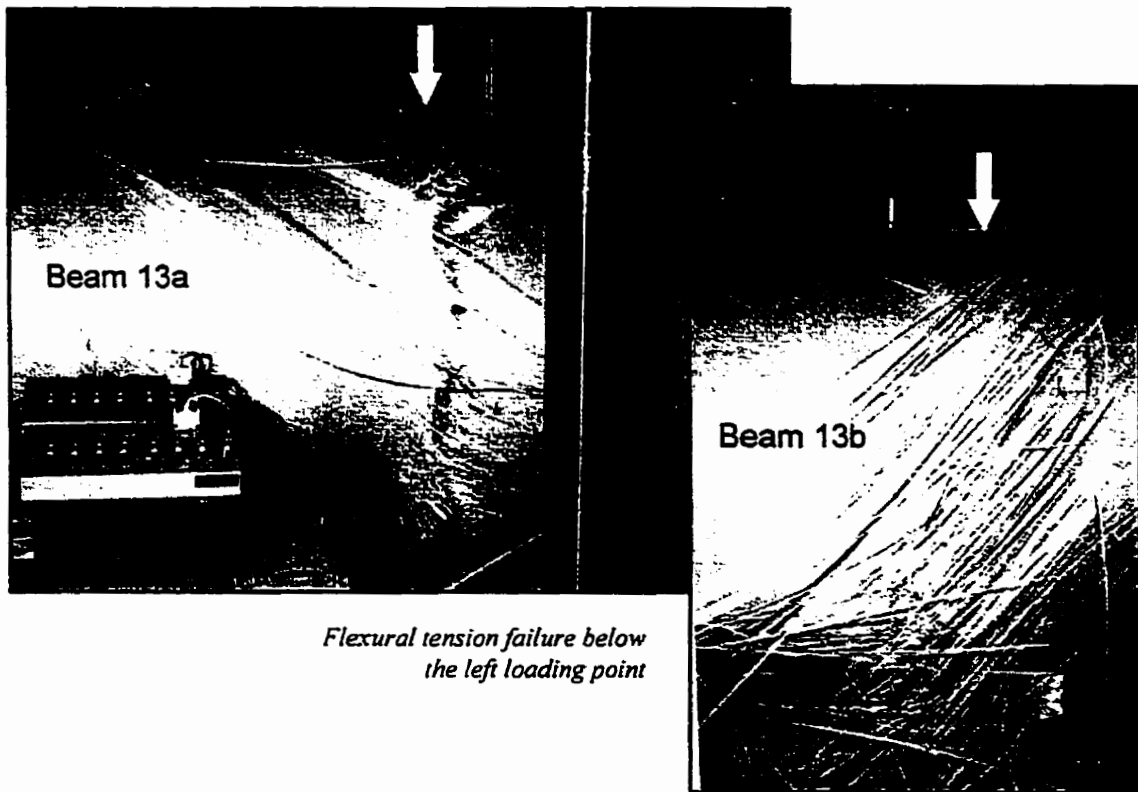
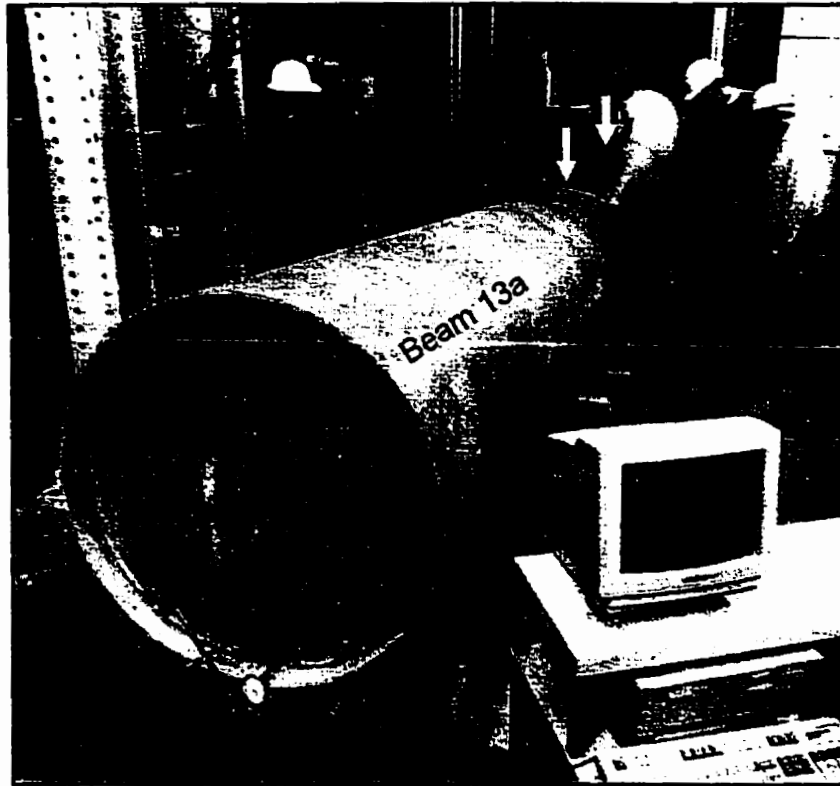


Fig. 4.33 Failure mode of beams 13 (a, b)

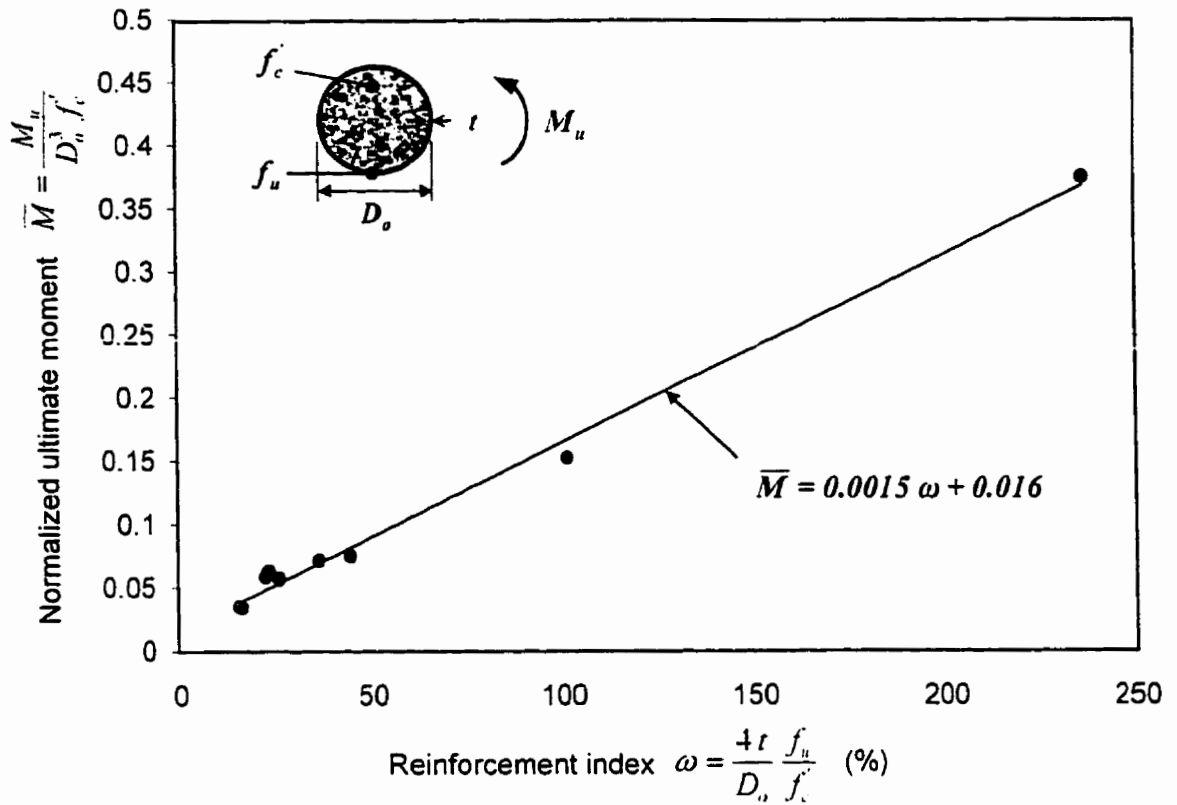


Fig. 4.34 Variation of the normalized ultimate moment with the reinforcement index

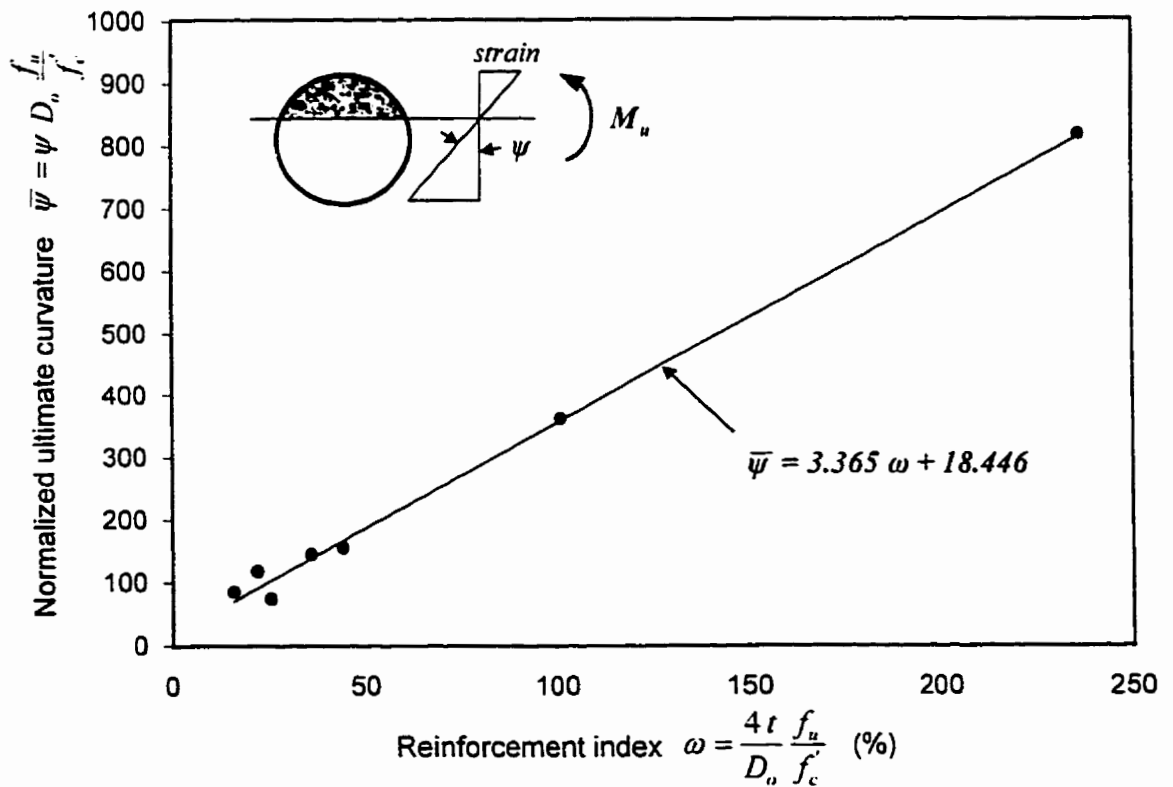


Fig. 4.35 Variation of the normalized ultimate curvature with the reinforcement index

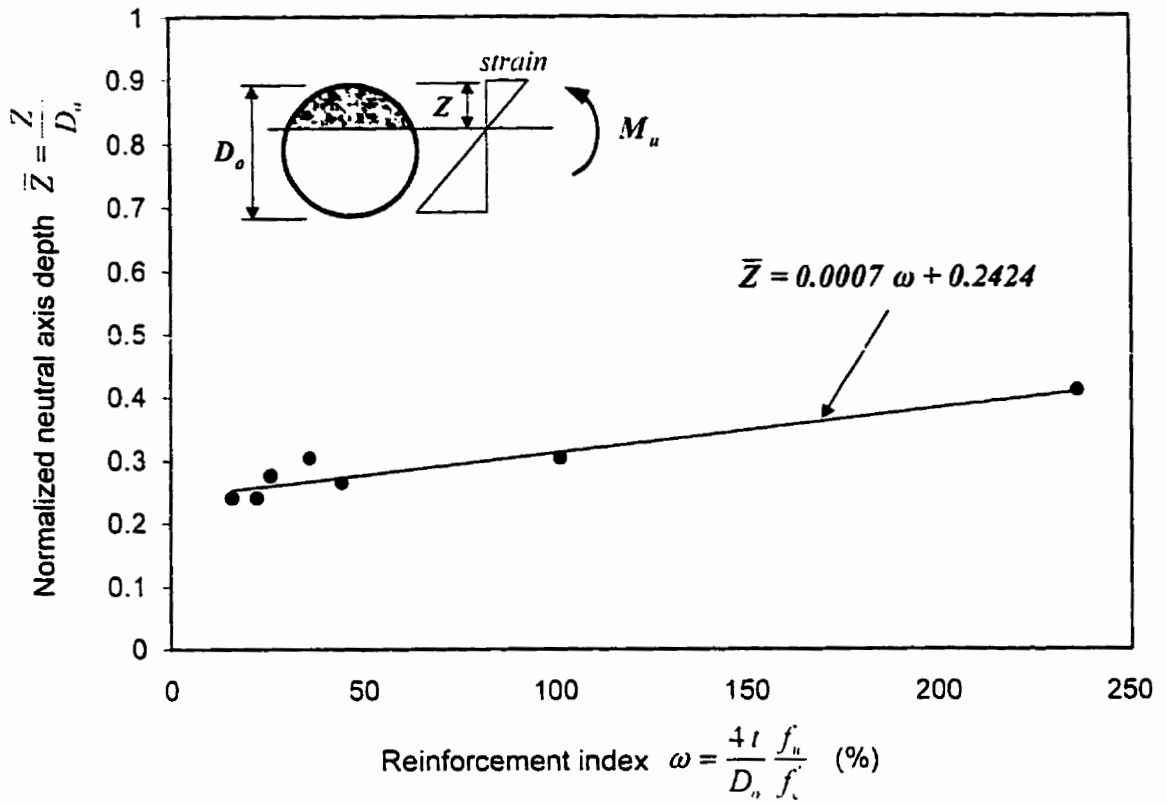


Fig. 4.36 Variation of the normalized neutral axis depth with the reinforcement index

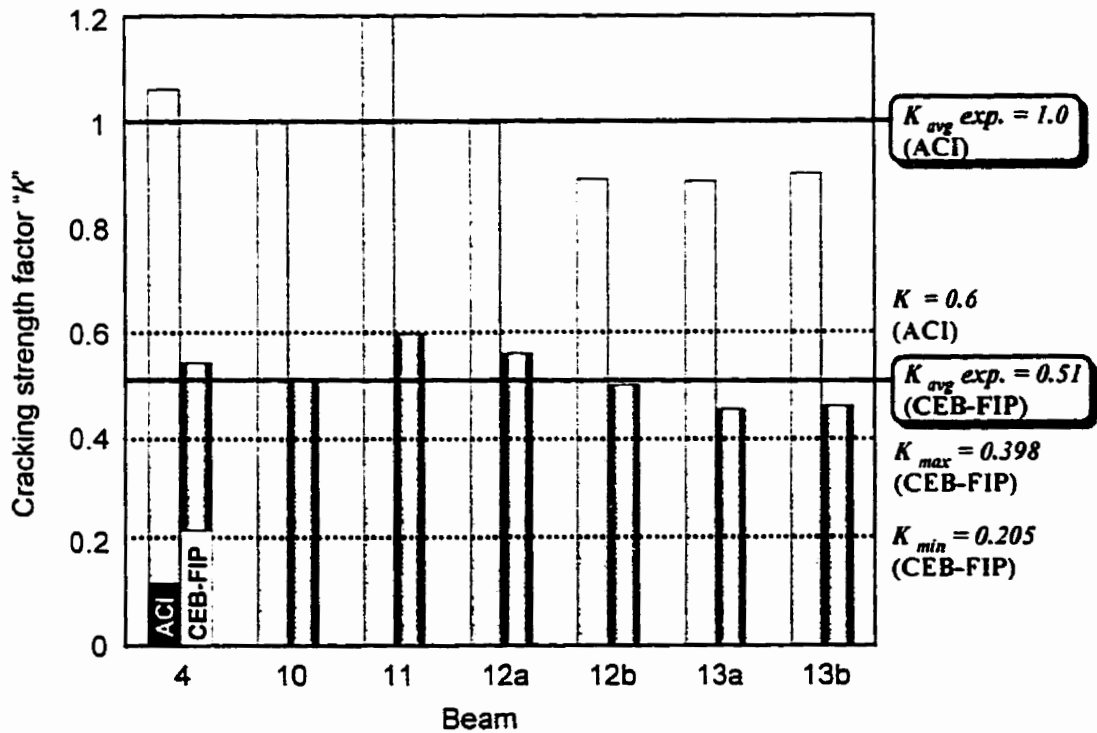


Fig. 4.37 Concrete cracking strength factor of beams versus different codes

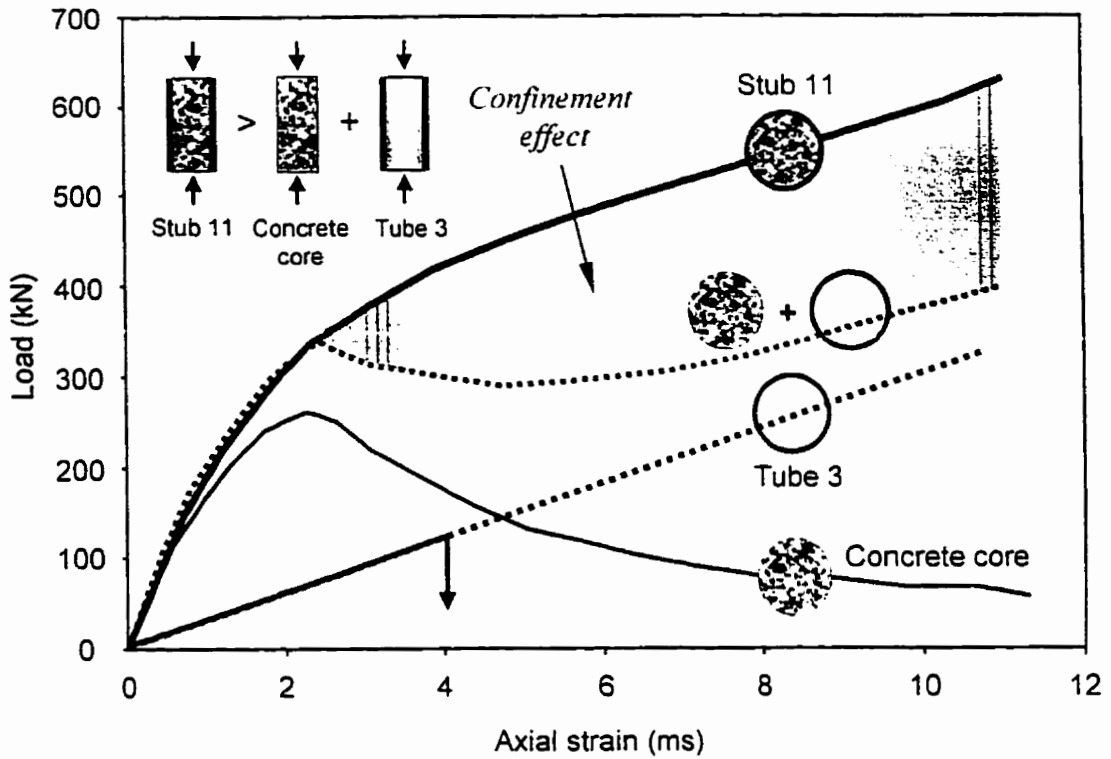


Fig. 4.38 Confinement effect on axial load-strain behaviour of stub 11

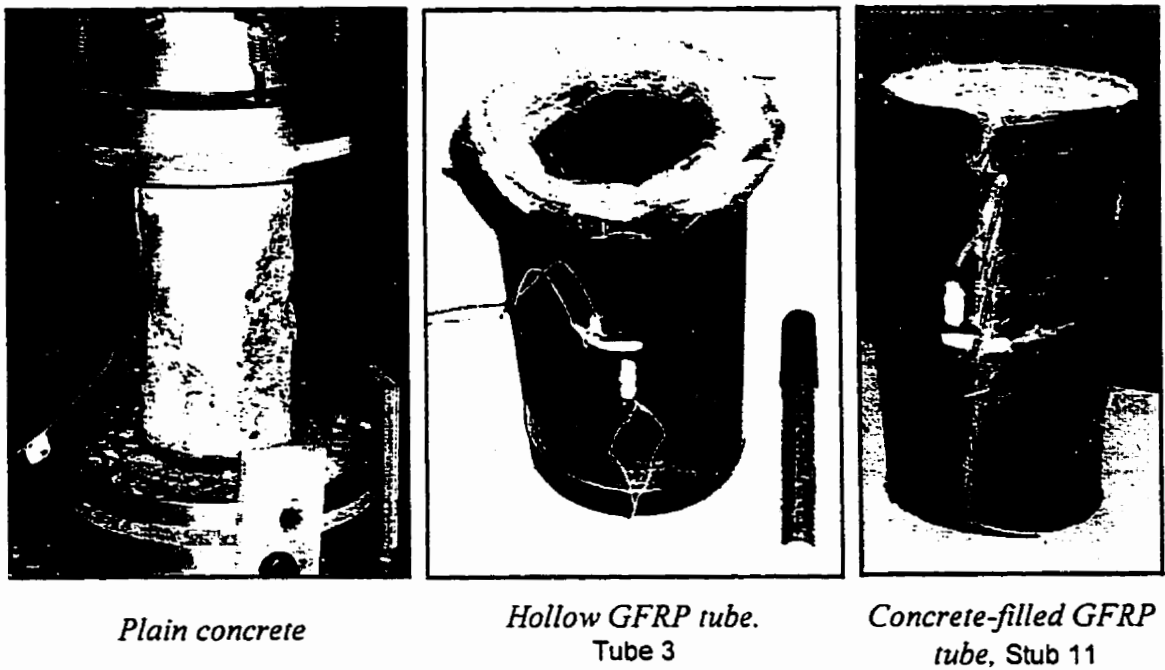


Fig. 4.39 Failure modes of plain concrete, hollow GFRP tube, and concrete-filled GFRP tube

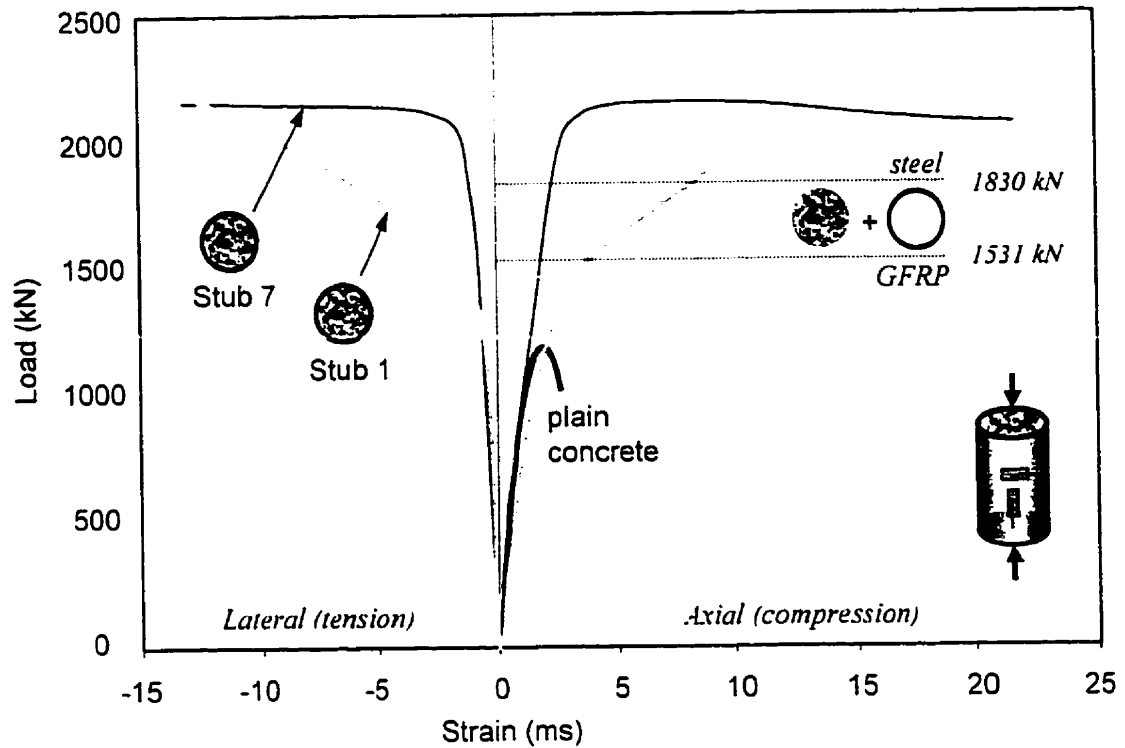


Fig. 4.40 Load-strain behaviour of GFRP-confined concrete, stub 1, and steel-confined concrete, stub 7

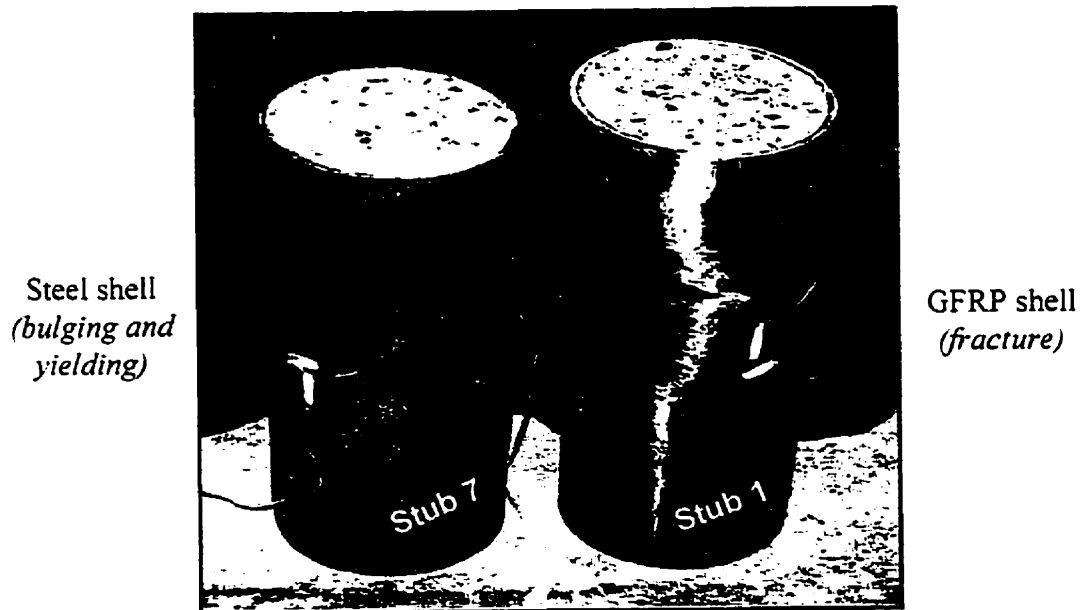


Fig. 4.41 Failure modes of GFRP-confined concrete, stub 1, and steel-confined concrete, stub 7

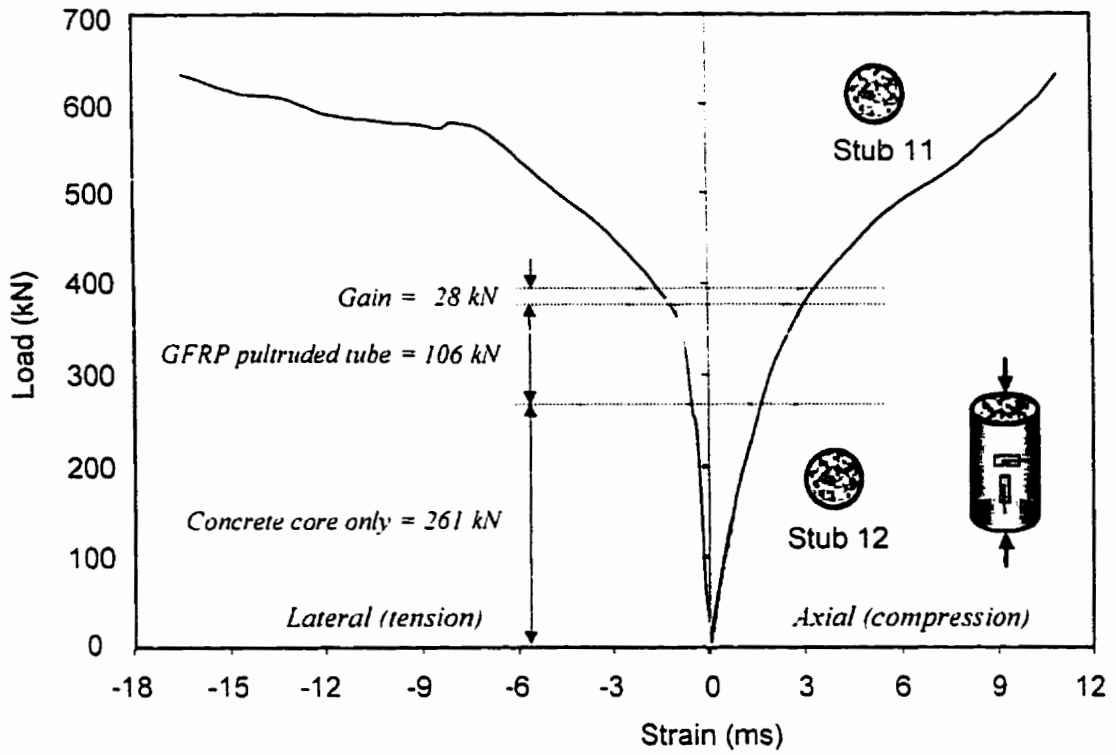


Fig. 4.42 Load-strain behaviour of concrete confined using filament-wound GFRP tube. stub 11. and pultruded GFRP tube. stub 12

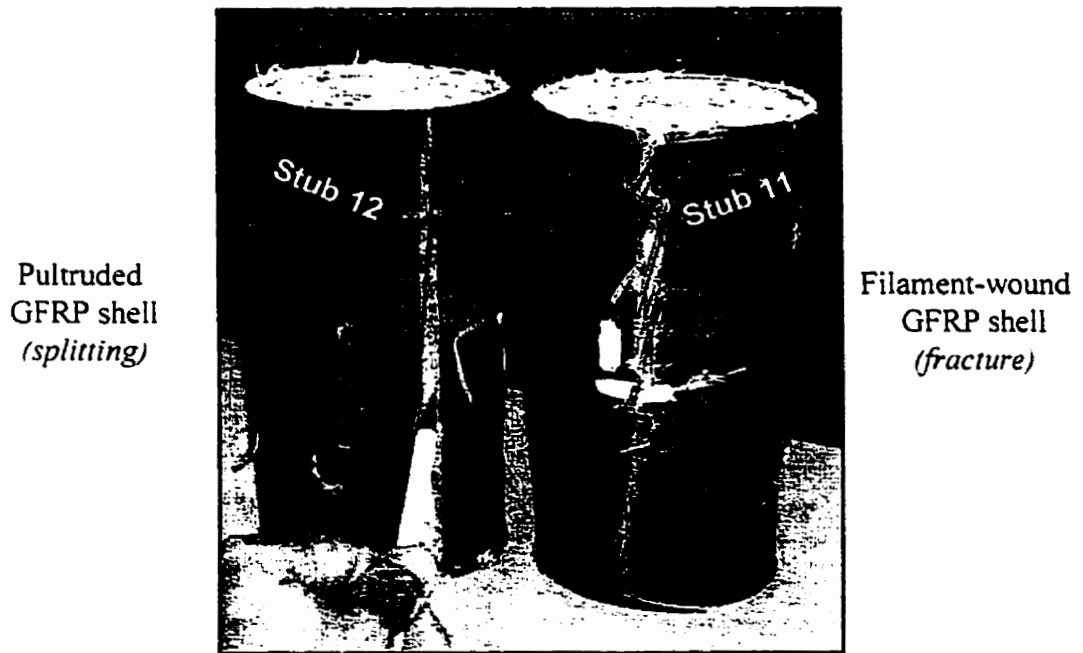


Fig. 4.43 Failure modes of concrete confined using filament-wound GFRP tube, stub 11, and pultruded GFRP tube. stub 12

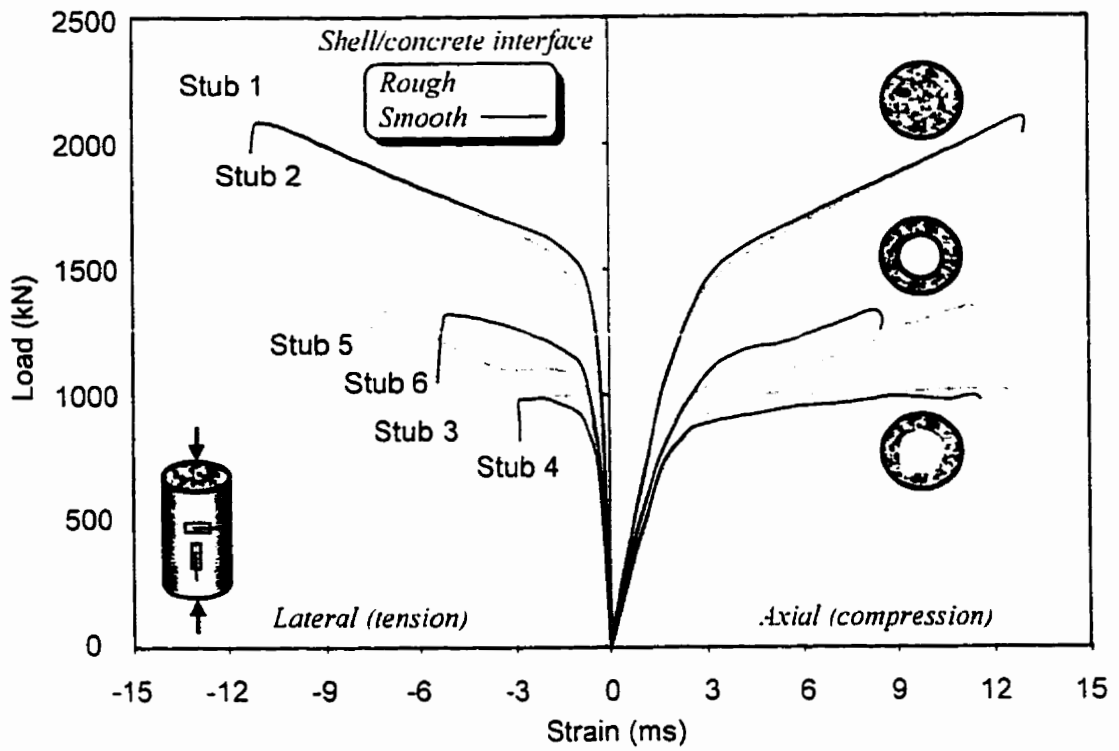


Fig. 4.44 Load-strain behaviour of stubs 1 to 6 with different cross-section configurations and different interface conditions

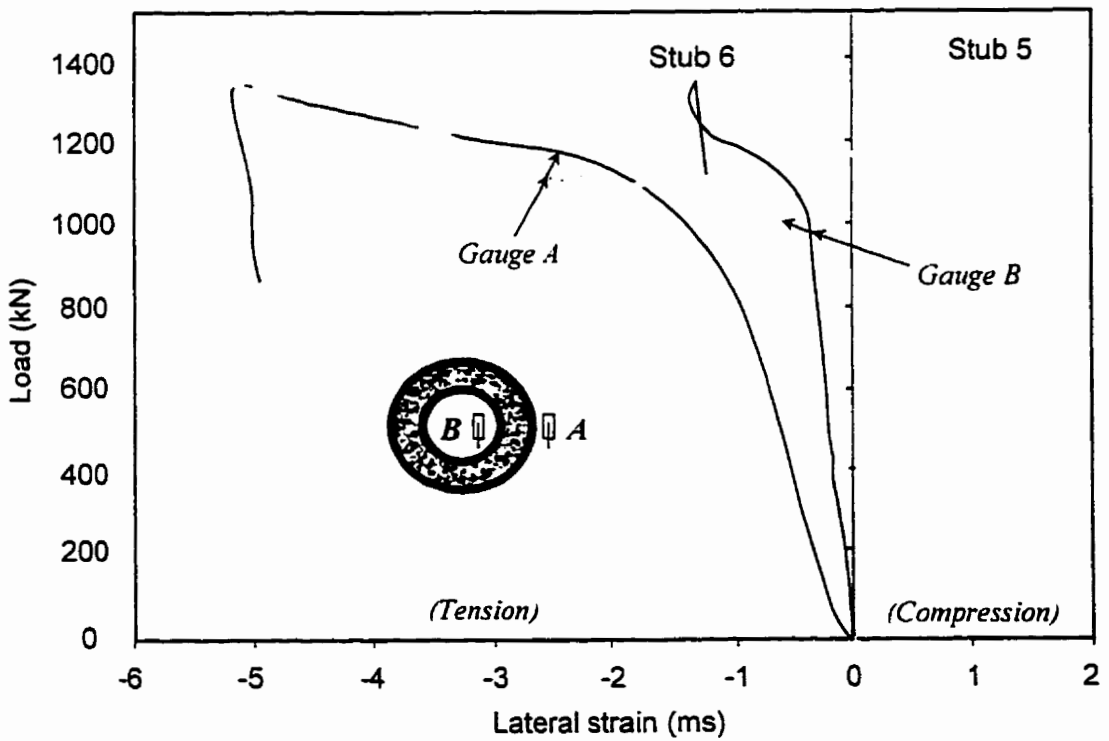


Fig. 4.45 Load-lateral strain behaviour of the inner and outer shells of stubs 5 and 6

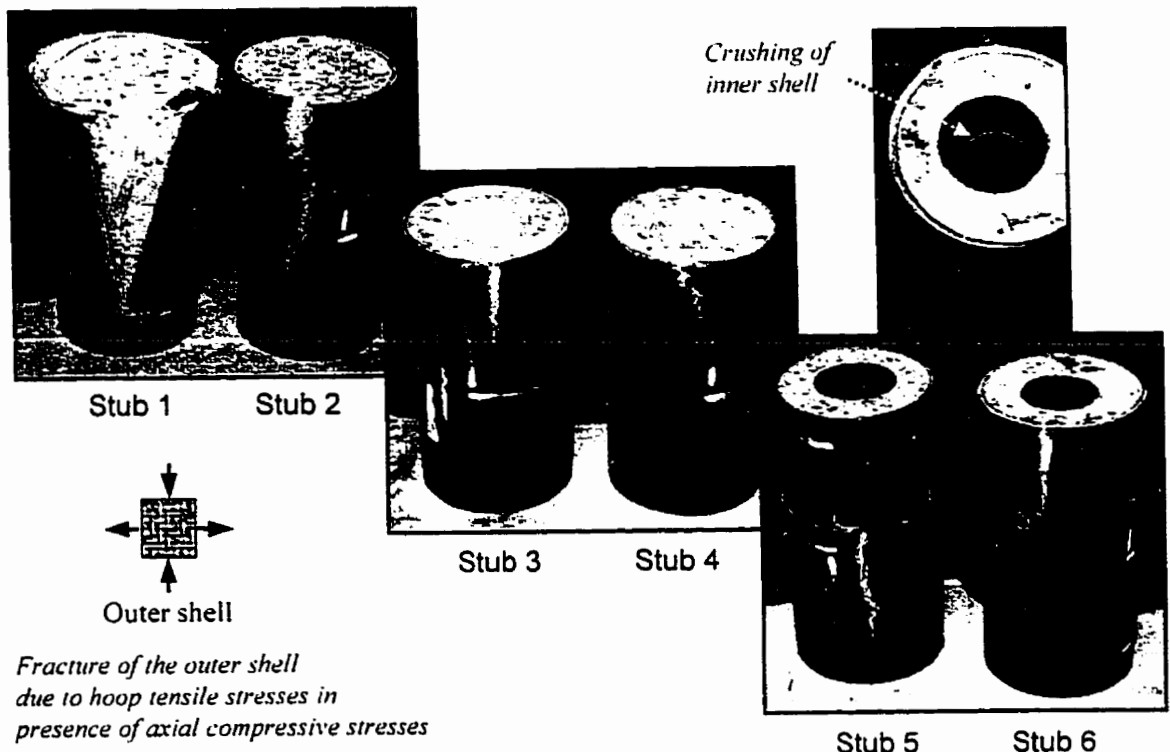


Fig. 4.46 Failure modes of stubs 1 to 6 with different cross-section configurations

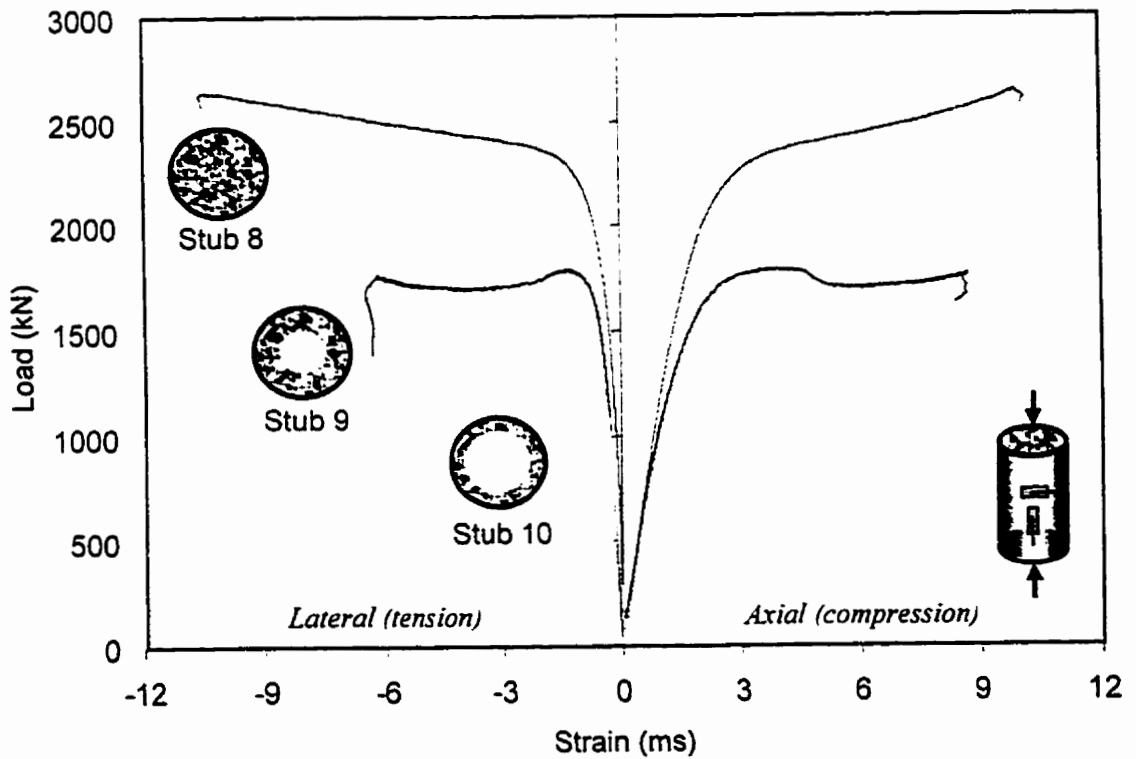


Fig. 4.47 Load-strain behaviour of stubs 8, 9, and 10 with different void sizes

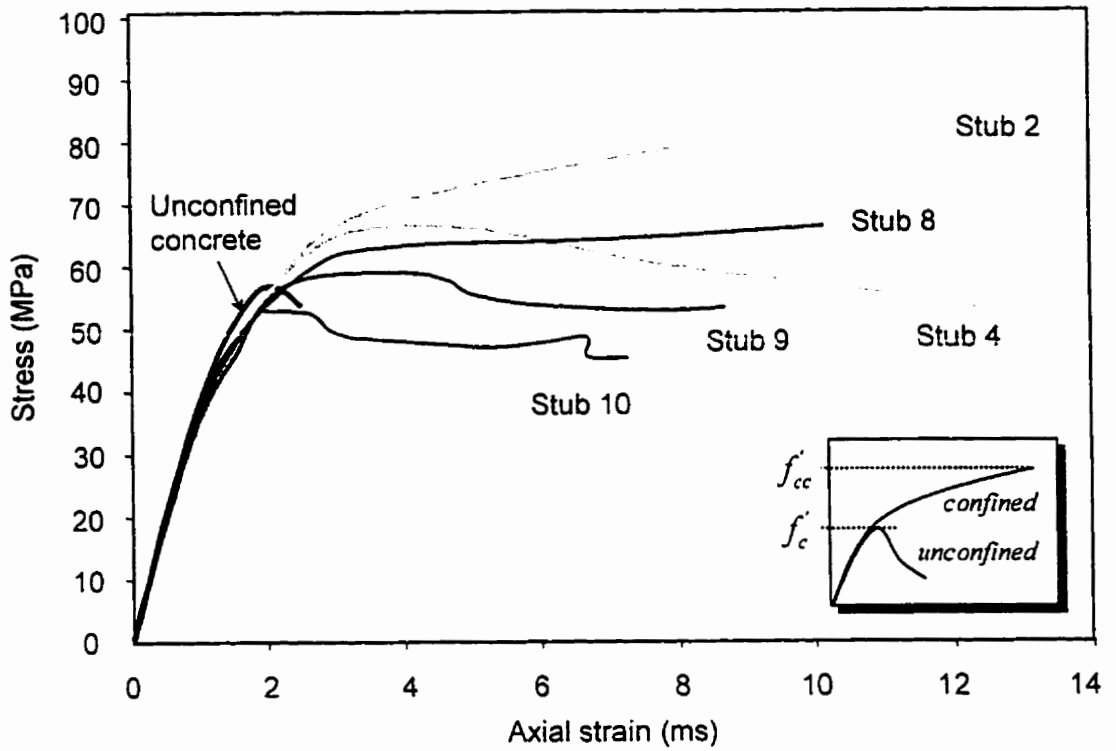


Fig. 4.48 Effect of void size on stress-strain behaviour of concrete confined by GFRP shells

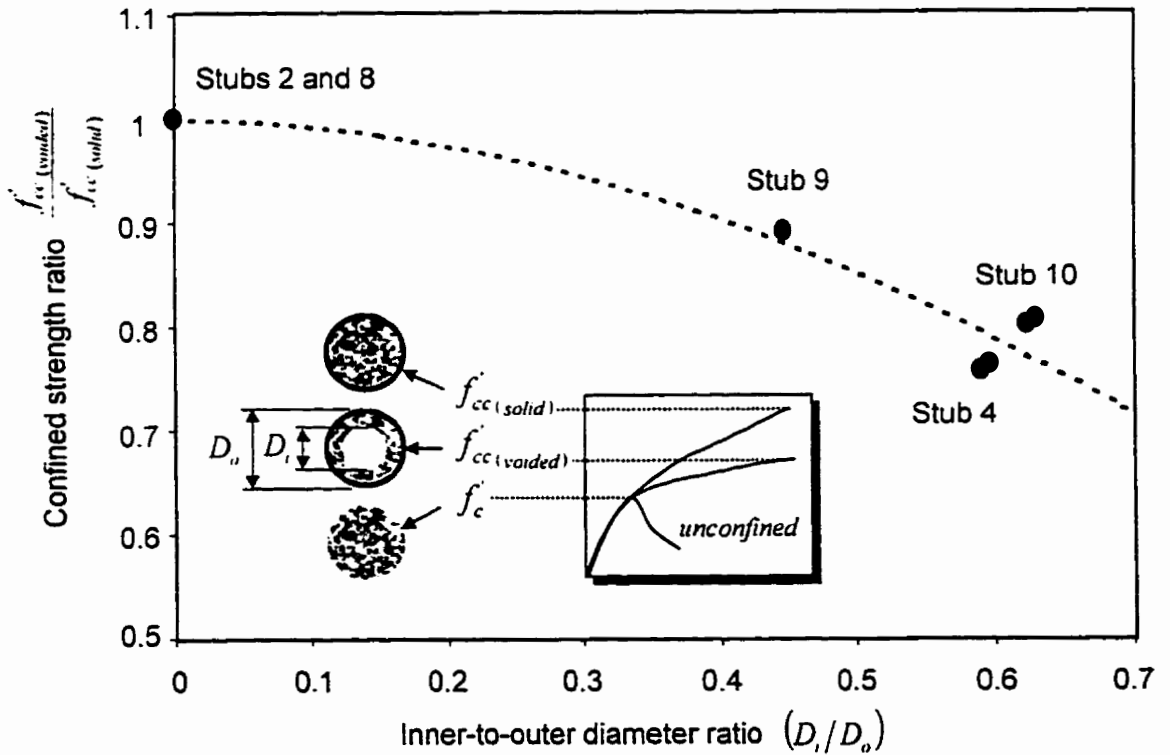


Fig. 4.49 Variation of confined strength ratio with the inner-to-outer diameter ratio

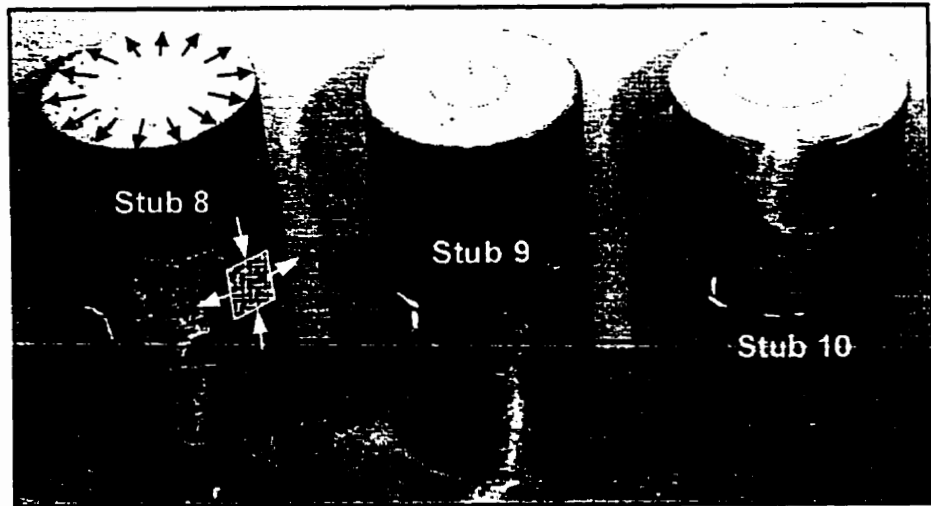


Fig. 4.50 Failure modes of stubs 8, 9, and 10 with different void sizes

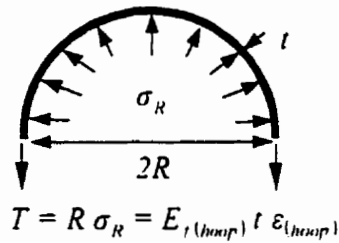


Fig. 4.51 Equilibrium of internal pressure and the hoop tensile stress

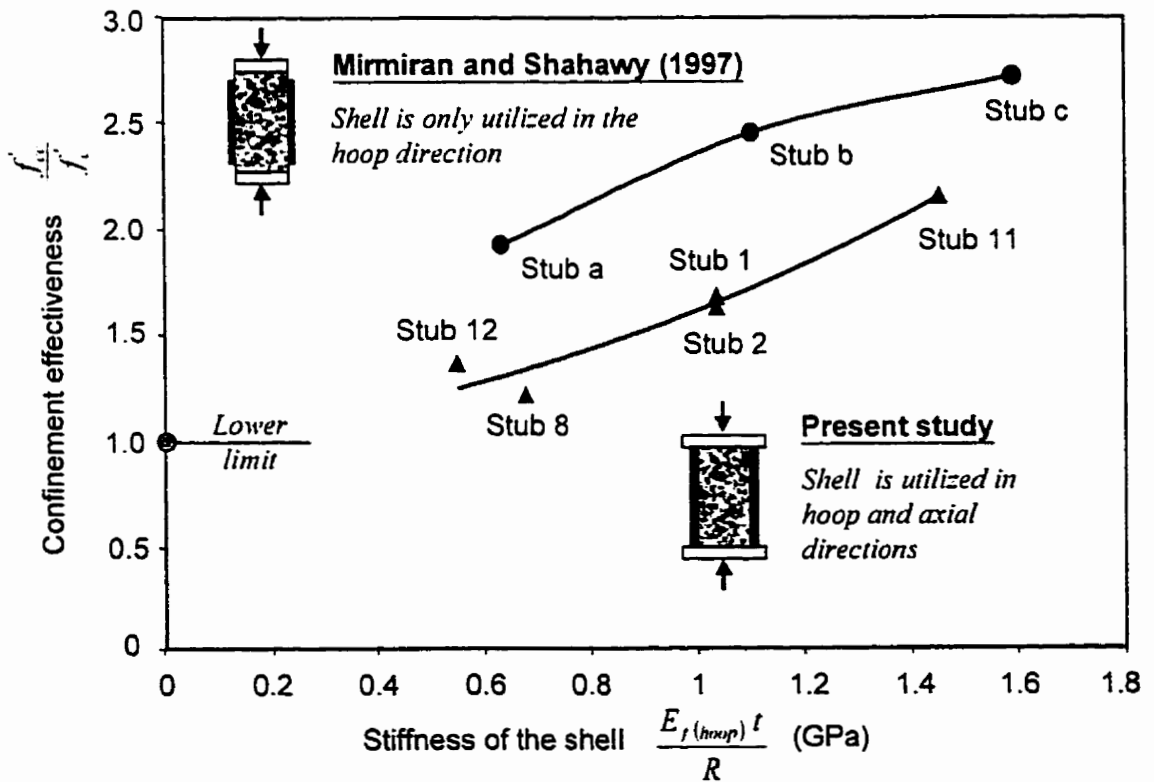


Fig. 4.52 Effect of stiffness of the shell on confinement effectiveness

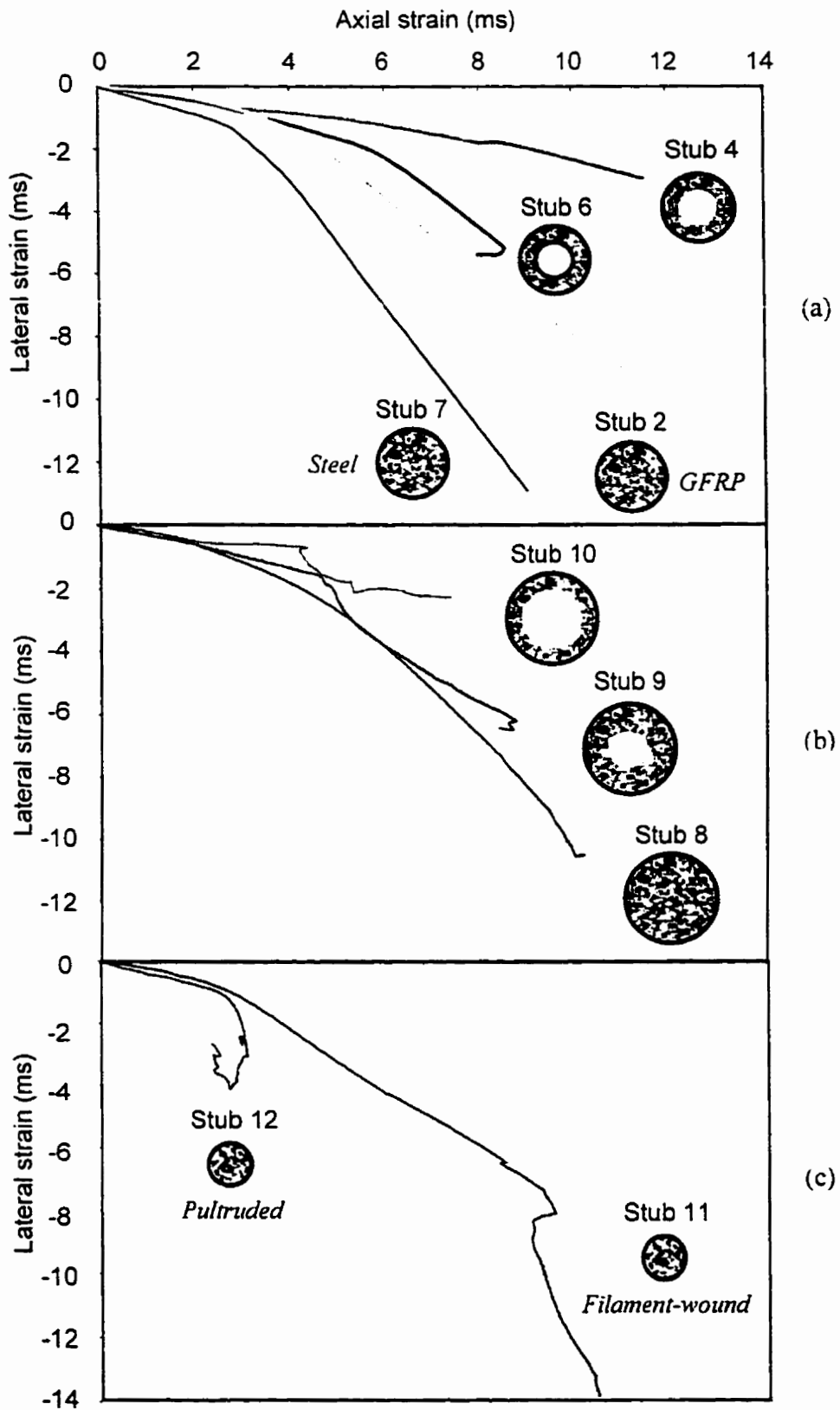


Fig. 4.53 Variation of lateral strains at different axial strain levels

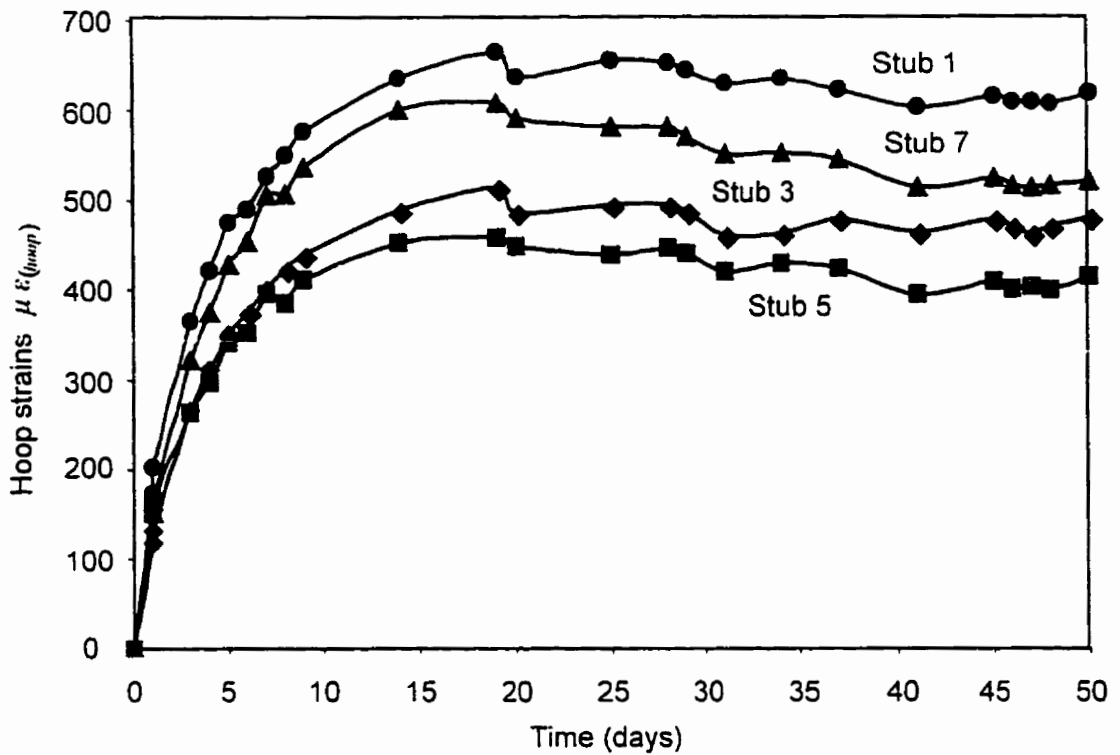


Fig. 4.54 Development of hoop strains over time due to expansion of concrete in stubs 1, 3, 5, and 7

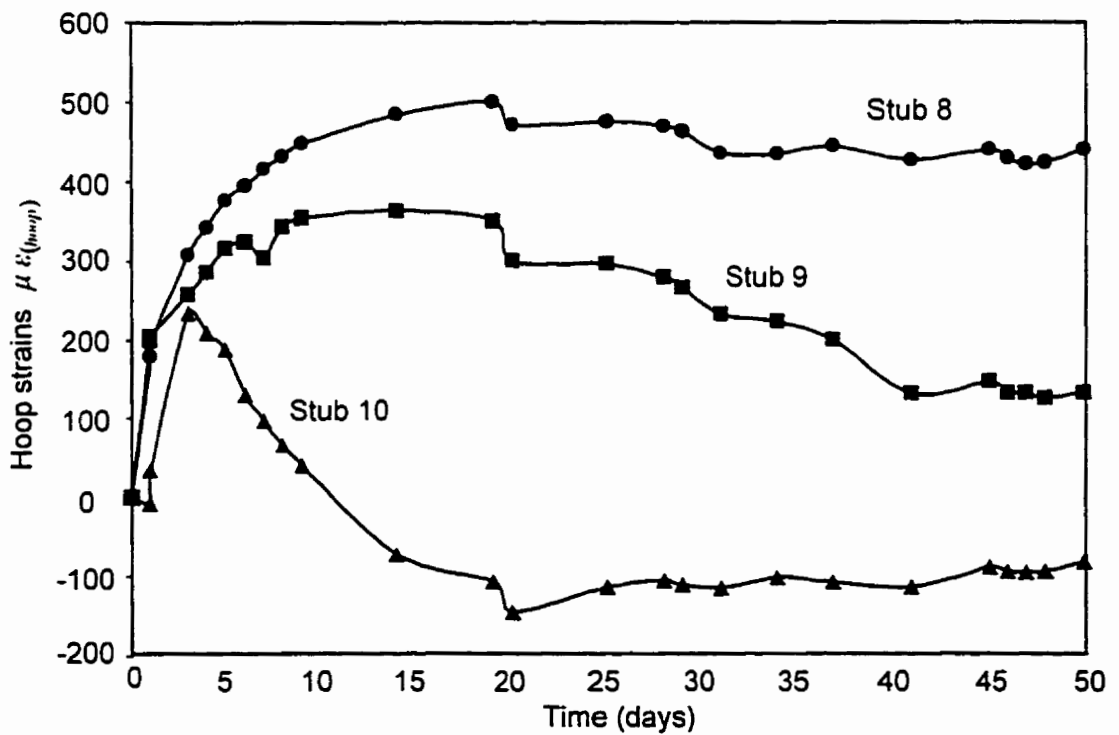


Fig. 4.55 Development of hoop strains over time due to expansion of concrete in stubs 8, 9, and 10

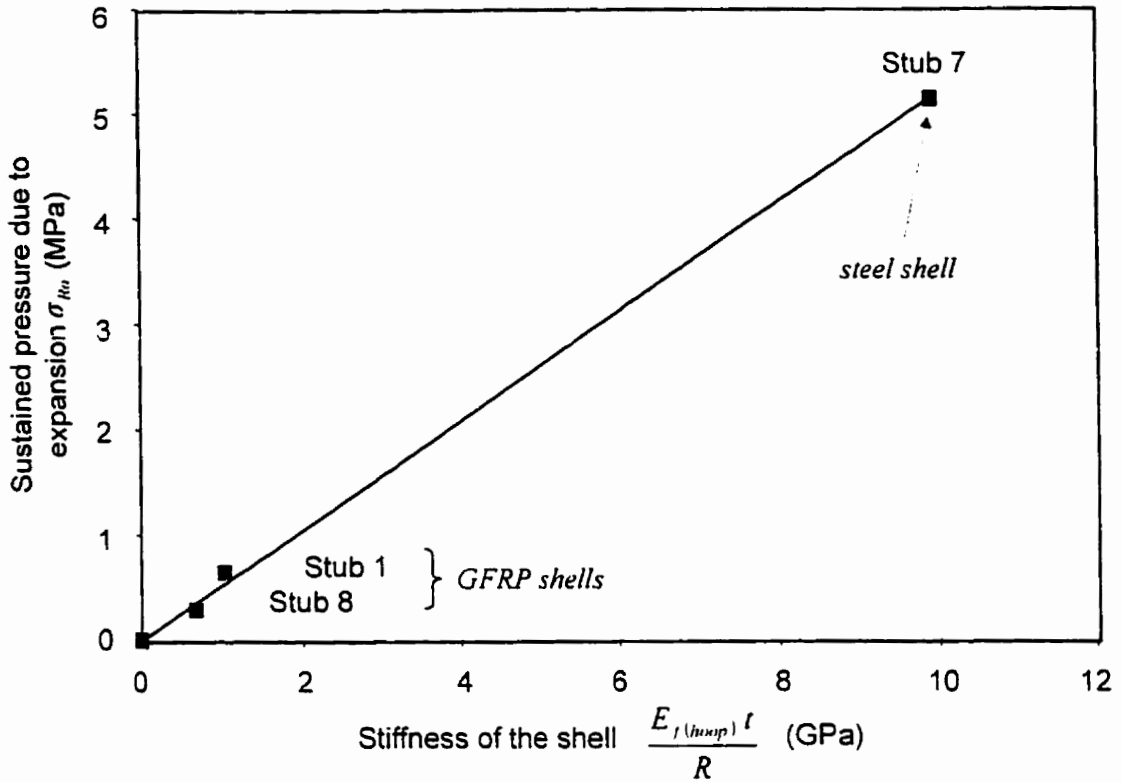


Fig. 4.56 Variation of pressure due to expansion of concrete with stiffness of the shell

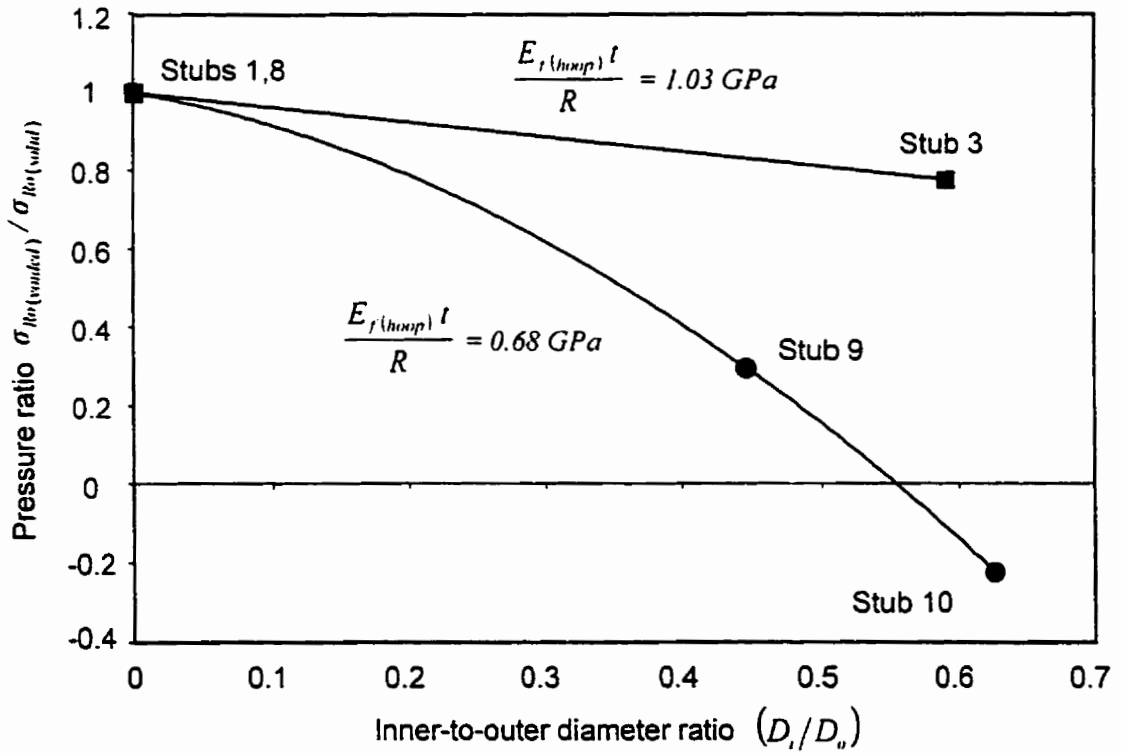


Fig. 4.57 Effect of the void size on the pressure due to expansion of concrete

Chapter 5

Analytical Modelling

5.1 Introduction

This chapter discusses the analytical modelling of concrete-filled FRP tubes used for both axially loaded members and flexural members. An analytical model has been developed for axially loaded members to predict the stress-strain behaviour of concrete confined using FRP jackets under axial compression loading condition [Fam and Rizkalla 2000 (b)]. The model utilizes a step-by-step technique based on a variable confining pressure, which is dependent on the stiffness of the confining jacket as well as the expanding concrete core. The model has been verified using the experimental results of the stubs tested in this study as well as experimental results presented by other researchers. A parametric study has also been performed using the confinement model to study the effects of the thickness of the FRP shell, fibre orientation, loading condition, and the void size inside the concrete core. Section 5.2 of this chapter presents the proposed confinement model for axially loaded members, verification of the model and the parametric study.

The analytical model for the flexural behaviour of concrete-filled FRP tubes is based on equilibrium, strain compatibility, and material constitutive relationships. It also accounts for the tension stiffening effect of concrete in tension. The model showed very good

agreement with the experimental results. It has been shown that in flexure, the concrete confinement in the compression zone is insignificant, however, the concrete filling adds strength and stability to the tubes as demonstrated both experimentally and analytically. This is attributed to the fact that premature failure due to local buckling is prevented. Also the concrete filling adds compressive strength to the section. A method is introduced to optimize the size of the void inside the concrete core to minimize the self-weight. A parametric study has been performed using the strain compatibility/equilibrium model to study the effect of axial stiffness of the tubes on the flexural behaviour. Different laminate structures and different wall thicknesses were used to vary the stiffness. The effect of the concrete strength has been studied. The effect of concrete filling in low and high stiffness tubes has also been studied. Section 5.3 of this chapter presents the analytical model for flexural members, verification of the model, and the parametric study.

5.2 Variable Confinement Model for Axially Loaded Concrete Confined by FRP Shells

Strength and ductility of plain concrete are highly dependent on the degree of confinement. As a concrete mass is axially compressed, the rate of lateral expansion is a function of the axial shortening by a stable value of Poisson's ratio up to approximately 50 percent of the compressive strength. During this stage stable propagation of the bond cracks occurs, and negative volumetric strain indicates consolidation of the concrete mass. At about 50 percent of the strength, micro cracks develop within the matrix, causing the concrete to behave nonlinearly, and the lateral strain also increases

nonlinearly, yet the volumetric strain is still negative up to a critical stress level, about 87 percent of the compressive strength. Past this loading stage, the volumetric strain starts to increase and the material degradation proceeds to a much higher rate of micro crack system merging into a dominant crack, which propagates within the concrete mass causing failure [Avram et al 1981]. It is, therefore, believed that controlling the lateral expansion of concrete by confinement is the key to enhance the strength and ductility of concrete. One of the methods used to achieve confinement is to cast concrete in FRP or steel tubes, or to wrap the concrete with FRP sheets. When the concrete is axially loaded, lateral expansion is then partially restrained by the tube, resulting in radial pressure at the interface. The amount of radial pressure depends on the stiffness of the tube in the circumferential direction. As the load increases, the tendency for lateral expansion increases and the confining pressure also increases, provided that the material properties of the FRP tubes are perfectly linear elastic. This behaviour can be categorized as variable confinement [Mirmiran and Shahawy 1997]. For steel tubes, the confining pressure is stable and independent of the axial load level as the steel yields, and therefore, it can be categorized as constant confinement [Kilpatrick and Rangan 1997].

Most of the reported experimental and analytical modelling of this problem has considered the case of FRP shells totally filled with concrete or solid concrete cylinders wrapped with FRP sheets [Parent 1997 and Spoelstra and Monti 1999]. In most cases, the fibres in the shells or sheets were mainly oriented in the hoop direction, to provide maximum stiffness and strength for confinement [Picher et al 1996 and Samaan et al 1998]. Other researchers considered the case of applying the axial load to the concrete

core only, for optimum use of the FRP shell in confinement [Mirmiran and Shahawy 1997]. However, in practical applications, FRP tubes filled with concrete are mainly used to carry axial compression loads and possibly bending moments, therefore, their overall strength and stiffness are essential. In some cases, they may also have voided concrete core to minimize their self-weight.

5.2.1 Significance of the Model

The following sections discuss an analytical model proposed to simulate the behaviour of concrete confined by FRP tubes. The model accounts for totally and partially filled tubes with central voids, composite action including the case of axial load applied to both the concrete core and the shell, and FRP shells designed to provide strength and stiffness in axial and hoop directions. The model is also applicable to concrete members wrapped with FRP sheets. The model is based on equilibrium and radial displacement compatibility as well as variable confinement using a step-by-step strain increment technique utilizing the equations proposed by Mander in 1988 for concrete under constant confining pressure. Mander's model has been selected as the starting point for the proposed variable confinement model since literature indicates that the model has been extensively tested against experimental data [Spolestra and Monti 1999].

5.2.2 Constant Confinement Model by Mander (1988)

In 1988, Mander et al proposed a unified stress-strain approach for confined concrete members subjected to axial compressive stresses as shown in Fig. 5.1. The model utilizes the equation given by Popovics in 1973, originally developed to represent the stress-

strain response of unconfined concrete. This confinement model by Mander is based on a constant confining pressure, σ_R , acting during the entire loading history. The axial stress of the confined concrete, f_{cc} , for any given strain, ε_{cc} , is related to the peak confined strength, f'_{cc} in Equation 5.1 as follows:

$$f_{cc} = \frac{f'_{cc} x^r}{r - 1 + x^r} \quad (5.1)$$

$$x = \frac{\varepsilon_{cc}}{\varepsilon'_{cc}} \quad (5.2)$$

Where ε'_{cc} is the strain at the peak strength f'_{cc} .

$$r = \frac{E_{cu}}{E_{cu} - E_{sec}} \quad (5.3)$$

Where E_{cu} is the tangent elastic modulus of unconfined concrete, and can be estimated as $5000\sqrt{f'_c}$ (MPa). E_{sec} is the secant modulus of confined concrete and can be estimated as $f'_{cc}/\varepsilon'_{cc}$. The peak confined strength, f'_{cc} , is a function of the unconfined strength f'_c and the constant lateral confining pressure σ_R as follows:

$$f'_{cc} = f'_c \left(2.254 \sqrt{1 + \frac{7.94 \sigma_R}{f'_c}} - 2 \frac{\sigma_R}{f'_c} - 1.254 \right) \quad (5.4)$$

The strain at peak confined strength, ε'_{cc} , is given as a function of the strain at peak unconfined strength of concrete, ε'_c , by:

$$\varepsilon'_{cc} = \varepsilon'_c \left[1 + 5 \left(\frac{f'_{cc}}{f'_c} - 1 \right) \right] \quad (5.5)$$

Given a value of the unconfined strength f'_c , and the confining pressure σ_R , Equation 5.4 can be used to evaluate f'_{cc} . The corresponding strain ϵ'_{cc} can be estimated using Equation 5.5. Using the ratio r from Equation 5.3, the entire stress-strain response of the confined concrete can be determined using Equations 5.1 and 5.2. This model can predict the behaviour only under a constant confinement level, for example the case of yielded steel jacket, where σ_R can be found from the following equation:

$$\sigma_R = \frac{f_y t}{R} \quad (5.6)$$

Where f_y is the yield strength, t and R are the thickness and radius of the tube respectively. It is evident from Equation 5.6 that the confining pressure in this case is constant and independent of loading level. In the case of FRP shell, the confining pressure is continuously increasing due to the linear characteristics of the FRP materials. The following sections are an attempt to estimate the behaviour under a variable confining pressure as a function of the loading level.

5.2.3 Variable Confining Pressure

The following basic fundamentals are provided to define the criteria used to formulate the interaction between the concrete and the confining surface utilizing the radial displacement compatibility at the interface between the cylindrical core and the outer thin shell. In this analysis, the loading is considered by imposing an axial strain ϵ_{cc} . The radial displacements of different components are introduced in section 5.2.3.1. In section 5.2.3.2, the condition of radial displacement compatibility is applied.

5.2.3.1 Radial displacements of the individual components

* *Solid Cylinder under Axial Pressure:*

Consider a solid cylinder, shown in Fig. 5.2a, subjected to axial strain ϵ_{cc} . As the cylinder is free to expand laterally, the radial displacement at the free edge, u_R , can be evaluated as:

$$u_R = \nu_c R \epsilon_{cc} \quad (5.7)$$

Where ν_c is Poisson's ratio, and R is the radius of the cylinder.

* *Solid Cylinder under Radial Pressure:*

Consider a solid cylinder, shown in Fig. 5.2b, subjected to external radial stress σ_R . In a cross-section plane, the cylinder is subjected to a bi-axial state of stress and the radial displacement at the free edge, u_R , can be calculated as follows [Young 1989]:

$$u_R = \frac{1 - \nu_c}{E_c} R \sigma_R \quad (5.8)$$

Where E_c is the elastic modulus of the cylinder.

* *Thin Shell under Internal Radial Pressure:*

Consider a thin shell, shown in Fig. 5.2c, subjected to internal radial stress σ_R . The hoop stress and radial displacement in the shell are given as follows [Young 1989]:

$$\sigma_\phi = \frac{\sigma_R R}{t} \quad (5.9)$$

$$u_R = \frac{\sigma_R R^2}{E_\phi t} \quad (5.10)$$

Where E_s is the elastic modulus of the shell in the hoop direction, R is the radius of the shell, and t is the wall thickness.

*** Thin Shell under Axial Pressure:**

Consider a thin shell, shown in Fig. 5.2d, subjected to axial strain loading, ϵ_{cc} . The radial displacement, u_R , is calculated as follows [Young 1989]:

$$u_R = \nu_s R \epsilon_{cc} \quad (5.11)$$

Where ν_s is Poisson's ratio of the shell.

5.2.3.2 Radial displacement compatibility

Now consider that the solid cylinder is placed inside the thin shell, as shown in Fig. 5.2e. The hybrid system can be analyzed for the following two cases:

(1) The cylindrical core only is subjected to a uniform axial strain loading, ϵ_{cc} . In order to estimate the interface pressure, σ_R , both equilibrium and radial displacement compatibility are considered. The outward radial displacement of the outer surface of the core due to both the axial strain ϵ_{cc} and the radial pressure σ_R must be equal to the outward radial displacement of the shell due to the same radial pressure σ_R . Utilizing Equations 5.7, 5.8, and 5.10, the unknown interface radial pressure can be found at any axial loading stage from the following equation:

$$\sigma_R = \frac{\nu_c}{R \left(\frac{1 - \nu_c}{E_c} + \frac{1}{E_s t} \right)} \epsilon_{cc} \quad (5.12)$$

Where R was assumed the same for both the core and the shell for large (R/t) ratios.

(2) Both the cylindrical core and the shell are axially loaded with the same strain level, ε_{cc} . As the concrete core tends to expand outwards, the shell expands as well with a different rate related to the relative Poisson's ratios of the two materials. Therefore, the developed interface pressure is a direct function of the relative radial displacements. Similarly, σ_R is estimated from the radial displacement compatibility, utilizing Equations 5.7, 5.8, 5.10 and 5.11 as follows:

$$\sigma_R = \frac{(\nu_c - \nu_s)}{R \left(\frac{1 - \nu_s}{E_s t} + \frac{1 - \nu_c}{E_c} \right)} \varepsilon_{cc} \quad (5.13)$$

Two points of special interest can be noted from examining Equations 5.12 and 5.13. The higher the values of both stiffness of the shell in the hoop direction ($E_s t/R$) and Poisson's ratio of the concrete core, ν_c , the higher the confining pressure σ_R . More importantly is that, if Poisson's ratio of the shell is higher than that of the concrete at a given load level, Equation 5.13 gives a negative value. This indicates that the shell is separated from the concrete core and there is no confinement, which strongly agrees with the observations by other researchers [Fardis and Khalili 1981 and Wei et al 1995]. Both research groups stated that steel tubes are less effective in confinement when axially loaded with the concrete core, as Poisson's ratio of concrete at early stages (0.15 ~ 0.2) is lower than that of steel (0.3), and they tend to separate from each other. On the other hand, FRP shells could be more effective by having a lower Poisson's ratio, depending on the laminate structure [Shahawy and Mirmiran 1998].

If the cylindrical core has a central void, and is treated as a thick-walled cylinder [Young 1989] under axial and radial stresses, following the same procedure, an equation similar to Equation 5.12 for the radial interface pressure in terms of the outer radius R_o and the inner radius R_i , has also been driven:

$$\sigma_r = \frac{(R_o - R_i)\nu_c}{R_o \left(\frac{R_o^2 + R_i^2}{R_o^2 - R_i^2} - \nu_c \right)} \varepsilon_{cc} \quad (5.14)$$

$$E_c \left(\frac{R_o^2}{E_c} + \right)$$

It is evident from the formula that providing a voided core reduces the confinement stress. This was also observed in the experimental results.

So far, Equations 5.12, 5.13, and 5.14 are based on elasticity formulation, which considers linear elastic behaviour, however it is well known that the concrete core behaves nonlinearly. This non-linearity is represented in the material parameters E_c and ν_c in Equations 5.12, 5.13 and 5.14. The goal of the next section is to develop a technique to account for the non-linear characteristics of the concrete, represented by E_c and ν_c at different loading levels, ε_{cc} .

5.2.4 Material Parameters

5.2.4.1 Variable secant modulus of concrete

Consider a general non-linear stress-strain curve, shown in Fig. 5.3a. This behaviour can be expressed in two different ways. One can consider a single continuous non-linear function relating the stress to strain and valid at any point, such as parabolic variation in the case of concrete. On the other hand, the behaviour can also be described in a linear

form: $f_i = E_{ci} \varepsilon_i$, where E_{ci} is a variable slope. In this case E_{ci} is the secant modulus at point "i", except for the first point, "o". E_{co} is the tangential initial slope as shown in Fig. 5.3a. This concept is adopted in the model using the secant modulus at any point. The goal is to construct the confined stress-strain diagram incrementally, point-by-point. The initial tangential modulus of the unconfined concrete, E_{co} is used to obtain the first point, "1" on the confined stress-strain curve, $(f_{cc1}, \varepsilon_{cc1})$, under the first axial strain loading, ε_{cc1} . Thus, when the axial strain is increased to a new level, ε_{cc2} , in order to obtain the next point "2", the concrete is treated as a new material with a new secant modulus, $E_{c1} = f_{cc1} / \varepsilon_{cc1}$. As the confined stress-strain curve is constructed, each point is obtained using the secant modulus of the previous point as given in Equation 5.15 and shown in Fig. 5.3b.

$$(E_c) \text{ to be used to obtain point "i"} = \frac{(f_{cc})_{i-1}}{(\varepsilon_{cc})_{i-1}} \quad (5.15)$$

5.2.4.2 Variable Poisson's ratio of concrete

Consider a typical relationship between axial and lateral strain for concrete in compression, Fig. 5.3c. The slope at the beginning, ν_{co} , represents the initial Poisson's ratio, which is reported to be between 0.1 to 0.3, with most values between 0.15 and 0.2 [Park and Paulay 1975]. As the load increases, the rate of lateral strain increases. Similar to the technique adopted for the concrete modulus, the variable secant Poisson's ratio is used to obtain the lateral strain at a given axial strain in the incremental approach adopted in the model.

Under the confinement conditions, the dilation of concrete is reduced because of the controlled micro cracking, therefore the Poisson's ratio, at a given axial strain level, is expected to be lower in the presence of confining pressure. In fact both concrete and rock behave in a very similar manner in this regard as evident from literature [Gowd and Rummel 1980]. In 1969, Gardner tested 29 MPa concrete cylinders under different confining hydrostatic pressures of 0, 8.62, 17.24, and 25.86 MPa and reported the axial-lateral strain behaviour. The results of Gardner's tests are used in this study to correlate the Poisson's ratio to the axial strain levels for the different confinement pressures. The results of the cylinder tests under the 17.24 MPa confining pressure were excluded from the correlation analysis as the author indicated lack of confidence and inconsistency in those particular test results [Gardner 1969]. Fig. 5.4 shows the axial-lateral strain behaviour of the concrete cylinders under the different confining pressures. The data reported by Gardner were selected in this study mainly due to the fact that the range of the hydrostatic pressures he used in the experimental program is very similar to that experienced by concrete confined by FRP tubes or sheets at different loading stages. Also the results he reported represent the average of at least three identical tests for each case. The axial-lateral strain behaviour followed a second order polynomial of the following form:

$$\varepsilon_l = A\varepsilon_{cc}^2 + B\varepsilon_{cc} \quad (5.16)$$

Where ε_l and ε_{cc} are the lateral and axial strains respectively. A and B are constants. The secant Poisson's ratio ν_c which is the ratio ($\varepsilon_l / \varepsilon_{cc}$) was estimated at different axial strain levels ε_{cc} . A simple linear relation is proposed as given in Equation 5.17 based on

the fact that the axial-lateral strain behaviour followed a second order polynomial as shown in Equation 5.16.

$$\nu_c = A\varepsilon_{cc} + B \quad (5.17)$$

In order to obtain a general simple expression for the variable Poisson's ratio, ν_c is normalized with respect to the initial Poisson's ratio ν_{c0} and ε_{cc} is normalized with respect to the strain at peak strength, ε'_{cc} as shown in Equation 5.18:

$$\left(\frac{\nu_c}{\nu_{c0}} \right) = C \left(\frac{\varepsilon_{cc}}{\varepsilon'_{cc}} \right) + H \quad (5.18)$$

Where C and H are constants. At zero axial strain ε_{cc} , Poisson's ratio $\nu_c = \nu_{c0}$, therefore $H = 1$.

$$\left(\frac{\nu_c}{\nu_{c0}} \right) = C \left(\frac{\varepsilon_{cc}}{\varepsilon'_{cc}} \right) + 1 \quad (5.19)$$

The constant C was correlated to the different confinement ratios (σ_R / f'_c) using a simple linear relationship as given in Equation 5.20 and shown in Fig. 5.5.

$$C = 1.914 \left(\frac{\sigma_R}{f'_c} \right) + 0.719 \quad (5.20)$$

Equations 5.19 and 5.20 can be used to estimate Poisson's ratio ν_c at any axial strain level ε_{cc} for a given confinement ratio (σ_R / f'_c).

5.2.5 Applying the Model using Step-by-step Approach

This section shows how the variable confining pressure approach based on variable material parameters can be combined with the confinement model by Mander using a

step-by-step approach to construct the stress-strain diagram of concrete confined by FRP shells. The flowchart is given in Fig. 5.6 and explained as follows for the simple case of totally filled FRP tube, where only the concrete core is axially loaded:

Data given:	Average radius of FRP shell	R
	Thickness of FRP shell	t
	Elastic modulus of the shell in hoop direction	E_s
	Tensile strength of the shell in hoop direction	σ_{su}
	Unconfined concrete strength	f'_c
	Strain at f'_c (normally 0.002)	ϵ'_c
	Initial Poisson's ratio (normally 0.15 ~ 0.2)	ν_{co}
	Initial elastic modulus	$E_{co} = 5000\sqrt{f'_c}$

A typical loop through the flowchart to obtain point "i" on the confined stress-strain curve will be as follows:

1. Input the axial strain level (ϵ_{cc})_i.
2. Determine (E_c)_i from Equ. 5.15 using the output of previous step. (f_{cc} , ϵ_{cc})_{i-1} and (ν_c)_i from Equ. 5.19 using (σ_R)_{i-1} and (ϵ'_{cc})_{i-1}. For point $i = 1$, use E_{co} and ν_{co} .
3. Determine (σ_R)_i using Equ. 5.12

4. Check the hoop stress in the jacket $(\sigma_r)_i$ using Equ. 5.9. If $(\sigma_r)_i \geq \sigma_{ur}$ then failure has occurred and the last point is $(f'_{cc}, \varepsilon'_{cc})_{i-1}$. If $(\sigma_r)_i < \sigma_{ur}$ then continue
5. Calculate $(f'_{cc})_i$ from Equ. 5.4
6. Determine $(\varepsilon'_{cc})_i$ from Equ. 5.5
7. Calculate $(E_{sec})_i = (f'_{cc})_i / (\varepsilon'_{cc})_i$
8. Determine $(r)_i$ from Equ. 5.3
9. Calculate $(x)_i$ from Equ. 5.2
10. Determine the confined stress at point "i", $(f'_{cc})_i$ from Equ. 5.1
11. Plot $(f'_{cc})_i$ from step 10 versus $(\varepsilon'_{cc})_i$ from step 1 as a point on the confined stress-strain curve.
12. Go to step 1 for a new axial strain level using a new modulus $(E_c)_{i+1} = (f'_{cc})_{i+1} / (\varepsilon'_{cc})_{i+1}$

The model is also capable of predicting the lateral (hoop) strain response. At point "i", the lateral strain $(\varepsilon_r)_i$ is:

$$(\varepsilon_r)_i = \frac{(\sigma_r)_i}{E_c} \quad (5.21)$$

5.2.6 Failure Criteria

Failure of confined concrete is a result of failure of the confining shell. As described in the previous section, in step 4, the hoop stress in the shell is checked at every loading level, and once it reaches the strength in the hoop direction, failure is indicated. In fact, this simple form only applies to the case where the axial load is applied to the concrete

core only and the shell is utilized in the hoop direction under simple uni-axial tension as shown in Fig. 5.7a. If the shell is axially loaded with concrete, it behaves as a bi-axially-loaded membrane under axial compression and hoop tensile stresses as shown in Fig. 5.7b. The presence of axial compression in this case weakens the shell in the hoop direction, and a bi-axial failure criteria must be adopted to account for the combined stresses. The most widely used criteria in the analysis of composite shells is the interactive tensor polynomial theory, Tsai-Wu [Daniel and Ishai 1994], which provides a failure envelope in the bi-axial stress plane as shown in Fig. 5.7c. In this case, at each axial strain level, the combination of stress in the shell in axial and hoop directions $(\sigma_x, \sigma_y)_s$ is compared to the interaction failure envelope in step 4. The axial and hoop stresses in the shell are given in Equation 5.22 in terms of the axial and lateral strains, as well as the elastic moduli E_x and E_y , and the Poisson's ratios ν_{xy} and ν_{yx} of the shell in the two directions. These parameters of the orthotropic shell are obtained using the classical lamination theory [Daniel and Ishai 1994].

$$\begin{aligned}\sigma_r &= \frac{E_x}{1 - \nu_{xy}\nu_{yx}} (\varepsilon_r + \nu_{yx}\varepsilon_l) \\ \sigma_l &= \frac{E_y}{1 - \nu_{xy}\nu_{yx}} (\nu_{xy}\varepsilon_r + \varepsilon_l)\end{aligned}\quad (5.22)$$

Knowing the axial strain level in the shell, ε_l , which is equal to that induced in the concrete core in step 1 of the flowchart, ε_{cc} , due to axial strain compatibility, and the hoop stress, σ_r , which is σ_l in Equation 5.9, the lateral strain ε_x and axial stress σ_x can be estimated.

5.2.7 Comments on the Model

1. The resulting stress-strain response of the FRP-confined concrete using this variable-confinement model is schematically illustrated in Fig. 5.8a. The final response crosses through a family of hypothetical constant confinement curves representing the response under different levels of constant confining pressures (each is applied throughout the entire loading history) as predicted by Mander's model. Each point at which the predicted stress-strain curve crosses these hypothetical curves, indicates a unique level of confinement experienced by the concrete inside the FRP shell at that specific instant. On the other hand, steel-confined concrete will experience the same behaviour only until the steel shell yields, then the response will follow a single constant confinement curve rather than crossing through the other curves as shown in Fig. 5.8b.
2. The Poisson's ratio variation is also illustrated in Fig. 5.9. based on the equations developed in section 5.2.4.2. The behaviour is also crossing through a family of curves each represents the variation of Poisson's ratio with respect to the axial strain level for a given confining pressure.
3. For axially loaded shells, if $(\sigma_R)_i$ in step 3 of section 5.2.5 is calculated using Equation 5.13, and a negative value is obtained, indicating a higher Poisson's ratio of the shell than that of concrete, $(\sigma_R)_i$ should be given a zero value at this step. Eventually, concrete dilation will overcome the expansion of the shell and confinement could be activated at a later stage.
4. If the shell is axially loaded, the total lateral strain is calculated as follows:

$$(\varepsilon_l)_i = \frac{(\sigma_c)_i}{E_c} + \nu_s (\varepsilon_{cs})_i \quad (5.23)$$

This represents the combined effects of both the expanding concrete core inducing hoop tensile strains as well as the Poisson's ratio effect of the shell when subjected to axial compression.

5. If the shell is axially loaded it provides additional load capacity to that of the confined concrete. In this case if the model is used to verify the experimental response, the contribution of the shell in the axial direction, which is normally small due to the lower elastic modulus of FRP, must be deducted from the total measured load, P_l at every axial strain level as shown in Equation 5.24. The remaining part of the load, P_c is then, divided by the concrete cross-sectional area to represent the experimental confined stress-strain behaviour to be compared to the predicted response by the model.

$$P_c = P_l - (EA)_{shell} \varepsilon_{cs} \quad (5.24)$$

Where $(EA)_{shell}$ is the stiffness of the shell in the axial direction.

5.2.8 Verification of the Model

The model has been applied to ten different concrete cylinders confined with FRP shells including specimens tested in this program as well as specimens tested and reported by four other research groups [Kawashima et al 1997, Nanni and Bradford 1995, Picher and Labossiere 1996, and Mirmiran and Shahawy 1997]. The specimens covered a wide range of variables including glass and carbon fibre shells, totally and partially filled tubes with different void sizes, standard and large size cylinders, specimens with both axially

loaded core and shell, as well as axially loaded core only, and shells with different laminate structures. It should be noted, however, that the development of the analytical model was completely independent of the experimental results of those axially loaded stubs.

5.2.8.1 Present study

Stubs 2 and 4 as well as stubs 8, 9 and 10, given in Table 3.4, were selected to examine the model. It should be noted that stubs 1 and 3 are also similar to stubs 2 and 4 respectively since both the concrete core and the FRP shell are axially loaded in both cases. The stubs included GFRP tubes totally and partially filled with 58 MPa concrete. The GFRP tubes used to fabricate the stubs, tubes 5 and 6 in Table 3.1, were filament-wound using E-glass fibres and epoxy resin with fibre volume fraction of 51 percent. The bi-axial failure envelope of the shells was established using the Tsai-Wu failure criteria and used to define the axial and lateral stress combination at failure. Computer program "CLASS" was used to establish the failure envelope [Kibler 1987]. Fig. 5.10a shows the failure envelope of tube 5 used to fabricate stubs 2 and 4 and Fig. 5.10b shows the failure envelope of tube 6 used to fabricate stubs 8, 9, and 10. The figure also shows the bi-axial stress path during the loading history using the step-by-step analysis. Once the stress path intersects the failure envelope, failure is detected. Fig. 5.11a and 5.11b show the experimental versus the predicted stress-strain behaviour of the confined concrete for the five specimens. Good agreement is observed in these graphs, however, the ultimate axial strains of stubs 9 and 10 were overestimated.

5.2.8.2 Tests by Kawashima et al (1997)

Kawashima et al performed a set of experiments on cylindrical reinforced concrete specimens confined with carbon fibre sheets with different elastic moduli and thicknesses. The specimens were 200 mm in diameter and 600 mm in height and were provided with a longitudinal steel reinforcement ratio of 1 percent with yield strength of 295 MPa. In 1999, Spoelstra and Monti reported the behaviour of two of those specimens, where the contribution of the steel was deducted from the measured stresses. The specimens were wrapped with a 439 GPa high modulus CFRP sheet, and had two different jacket thicknesses of 0.338 and 0.676 mm with tensile strengths of 2810 and 2327 MPa respectively. The unconfined concrete strength was 39 MPa. The stress versus axial and lateral strain response was predicted and compared to the measured values in Fig. 5.12 for the two specimens. Good agreement is achieved. The slightly lower failure load measured in the specimens could be attributed to a bi-axial state of stress that might have developed in the jacket due to some share of the axial stresses, which weakens the jacket as explained before.

5.2.8.3 Tests by Nanni and Bradford (1995)

A total of 15 (152.5x305 mm) concrete cylinders confined by FRP jackets were tested. The cylinders were made with a central rod. They were then placed on a filament-winding machine and wrapped with one, two, four, or eight plies of E-glass fibres and either vinyl ester or polyester resin. The reported hoop strength and elastic modulus of the FRP jacket by the manufacturer were 583 MPa and 52 GPa, respectively. The unconfined concrete strength was 36.3 MPa. Fig. 5.13 shows the test results and the

predicted stress-strain response for one of the four-ply specimens with a 1.2 mm thick shell and hoop fibres at 90 degrees orientation, which was reported by Samaan et al (1998). Good agreement is noted in the behaviour except for the fact that lower failure load is predicted if the 583 MPa hoop strength value is used. This is attributed to the fact that this value, reported by the manufacturer, is overly conservative. However, one can predict the ultimate strength of uni-axial E-glass/polyester lamina by knowing the elastic modulus, 52 GPa. The fibre volume fraction was worked out to be 70 percent using reversed analysis, and the strength of the laminate was then found to be 1365 MPa. The behaviour was also predicted using this laminate strength and presented in the same figure.

5.2.8.4 Tests by Picher and Labossiere (1996)

Tests were carried out on four confined 152 x 304 mm concrete cylinders using different configurations of carbon fibre sheets. The sheets consisted of 3 layers, 0.3 mm thick each, wrapped around the cylinders with winding angles $[0_3]$, $[\pm 6/0]$, $[\pm 12/0]$, and $[\pm 18/0]$ using epoxy resin. The unconfined concrete strength was 39.7 MPa. The hoop strength and stiffness for the $[0_3]$ laminate were 1245 MPa and 83 GPa, respectively. Although the ultimate tensile strain of the sheet in the hoop direction is 0.015, failure occurred at 0.0084 hoop strain in the tested stubs. The researchers reported that failure was caused by a bi-axial loading condition. Therefore the 1245 MPa hoop strength overestimates the capacity if used in the model, and a bi-axial failure envelope has to be established. This, however, requires detailed information about the laminate, which was not reported by the researchers. Therefore, in order to comply with this, the ultimate strength of the sheet

was considered 697 MPa, based on the 0.0084 hoop strain at failure. The load-strain behaviour was predicted and showed excellent agreement as shown in Fig. 5.14.

5.2.8.5 Tests by Mirmiran and Shahawy (1997)

A total of 24 (152.5x305 mm) concrete-filled GFRP tubes were tested. The unconfined concrete strength ranged from 29.6 to 32 MPa. The FRP tubes consisted of filament-wound angle-ply laminate of polyester resin and E-glass fibres at a winding angle of ± 15 degrees. Direct interaction between the jacket and the concrete in the axial direction was prevented. Specimens included GFRP jackets of 6, 10, and 14 layers with 1.3, 2.1, and 3 mm wall thickness, respectively. The hoop strength ranged from 524 to 641 MPa and the modulus of elasticity ranged from 37.23 GPa to 40.74 GPa, respectively. Eight stubs were tested for each jacket thickness. The full response is predicted and compared to the experimental data in Fig. 5.15 for the stub with the 10 layers GFRP shell. The scattered experimental points at failure represent the failure points of the seven similar tests of the same case. Although the predicted strength is very satisfactory, the axial strain was slightly underestimated.

5.2.9 Parametric Study using the Confinement Model

The study was extended to examine the effect of the stiffness of the shell in both the hoop and axial directions under two loading conditions, as well as the effect of void size. For this study, a typical 150 mm diameter concrete-filled GFRP tube using 40 MPa concrete is considered, with 0.002 strain at peak unconfined strength and 0.18 initial Poisson's ratio. Two extreme laminate structures were considered for the GFRP shell, including all

fibres oriented in the hoop direction, or axial direction, in order to provide the maximum and minimum stiffness in both directions. This parameter was studied for a GFRP shell of 2 mm thickness. A typical E-glass/epoxy GFRP shell with a 55 percent fibre volume fraction was used [Daniel and Ishai 1994]. The major and minor elastic moduli are 39 and 8.6 GPa and the major and minor Poisson's ratios are 0.28 and 0.06, respectively. The effect of shell thickness was studied for the case of fibres oriented in the hoop direction by varying the thickness from 0.5 mm to 8 mm. The effect of void size was considered by varying the diameter of the void from zero to 125 mm for the case of the 2 mm GFRP shell with maximum stiffness in the hoop direction.

5.2.9.1 Effect of shell thickness

Fig. 5.16a shows the confined stress-strain curves of concrete using different shell thicknesses to provide different levels of stiffness in the hoop direction. The variation of the confined peak strength is shown in Fig. 5.16b as a function of the stiffness (Ei/R), where t and R are the thickness and radius of the shell respectively, and E is the elastic modulus in the hoop direction. The figure shows the enhanced strength with increasing the stiffness of the shell; however, the rate of strength gain is reduced with increasing the stiffness. Figure 5.16b also shows that below a certain stiffness level, there is no gain in strength, due to the post-peak softening behaviour, which results from the lower confining pressure. This is illustrated in Fig. 5.16a for the case of 0.5 mm FRP shell. The figure shows that the strength at ultimate is smaller than the peak strength.

5.2.9.2 Effect of fibre orientation and loading condition

Fig. 5.17a shows the confined stress-strain behaviour of concrete using a 2 mm GFRP shell. The behaviour is given for both the [90] laminate where all fibres are oriented in the hoop direction for maximum hoop stiffness and minimum axial stiffness, and also for the [0] laminate with all fibres in the axial direction. Figures 5.17b and 5.17c show the bi-axial failure envelopes for both laminates. For each laminate, the load was applied either to the concrete core only, or to both the core and the shell. When the load is applied to the core only, the shell is fully utilized in the hoop direction and develops the full strength. In this case the [90] laminate provides maximum gain in the strength due to its high tensile strength and modulus, 1080 MPa and 39 GPa, respectively, whereas the [0] laminate is less effective due to its lower strength and stiffness in the hoop direction, 39 MPa and 8.6 GPa, respectively. When the load is applied to both the core and the shell, significant reduction in performance in terms of both strength and stiffness is observed, especially in the [90] laminate. The reduced strength is attributed to the bi-axial state of stress developed in the shell. Figures 5.17b and 5.17c show the bi-axial stress path during the loading history till failure for both laminates. The reduced stiffness is attributed to the outward expansion of the shell due to its Poisson's ratio effect, which reduces the confining pressure. In this regard the [90] shows a smaller reduction due to its smaller Poisson's ratio, 0.06, compared to the 0.28 of the [0] laminate. Fig. 5.17c also shows that at the beginning of the bi-axial stress path, development of hoop stresses in the shell is delayed till the concrete expansion overcomes the shell expansion for the [0] shell, due to the higher Poisson's ratio of the shell, 0.28, compared to that of concrete initially, 0.18.

5.2.9.3 Effect of void size

Fig. 5.18a shows the confined stress-strain response of concrete confined with a 2 mm [90] GFRP shell and having an inner void of different sizes. Fig. 5.18b shows the developed confining pressures for the different void sizes. Fig. 5.18c shows the reduction of both peak axial strength and maximum confining pressure with increasing the void size. Fig. 5.18c also shows that for an inner-to-outer diameter ratio higher than 0.67 there is no gain in strength for this particular case due to the post-peak softening behaviour resulting from the lower confining pressure, which results in strength at ultimate, lower than the peak strength.

5.3 Analytical Modelling of Flexural Behaviour of Concrete-Filled FRP Tubes

This section presents the analytical model developed for concrete-filled FRP round tubes subjected to pure bending. Fig. 5.19 illustrates description of the problem under consideration. A strain compatibility/equilibrium model has been developed to predict the moment curvature response of the section. The curvatures along the span of the flexural member are integrated to predict the displacements. The model accounts for the tension stiffening effect of concrete in the tension side. The issue of confinement of concrete in the compression side is addressed. The benefits of concrete filling of the FRP tubes are demonstrated analytically. For partially filled FRP tubes with a voided concrete core, a method is presented to optimize the void size in order to minimize the self-weight of the member. The model is also used to perform a parametric study to investigate the

effects of different variables including the concrete strength, stiffness and strength of the FRP tube, and the reinforcement ratio.

5.3.1 Strain Compatibility/Equilibrium Model

The model is based on the assumption that plain sections remain plain after deformation, which indicates linear strain distribution along the depth of the concrete-filled tubes subjected to bending. Also the strain compatibility assumption is valid, which indicates that at any given level along the depth of the section, the strain in the concrete core equals the strain in the FRP tube and no slip occurs. The model assumes a linear behaviour of the FRP tube in both tension and compression and accounts for the concrete's material non-linearity. A cracked section analysis is performed using a layer-by-layer approach in order to sum the forces along the cross-section depth using numerical integration.

5.3.1.1 Geometry of the problem

Unlike the conventional reinforced concrete sections, the concrete-filled tubes are rather more sophisticated in terms of both geometry and stress analysis. The stresses, which are variable along the depth, are distributed over an area of variable width. The reinforcement, which is the circular tube itself, is a continuous surface extending along the depth in both the tension and compression sides. This is different from the case of discrete reinforcing bars located at specific distance from the neutral axis. The problem is addressed using a layer-by-layer approach in order to allow for the numerical integration of the stresses over the cross-sectional area. Fig. 5.20 shows both the cross-

section and the idealized geometry. The average diameter of the tube, D , is considered and given as follows:

$$D = D_o - t \quad (5.25)$$

Where D_o is the outer diameter and t is the thickness of the tube. The diameter D is divided into a number of layers, n , which has the same thickness hi , given as follows:

$$hi = \frac{D}{n} \quad (5.26)$$

For a given strip i , the depth of the centre of the strip from the top level, $h(i)$ can be determined as:

$$h(i) = hi(i - 0.5) \quad (5.27)$$

The length of the part of the perimeter of the tube within the strip on one side, $L(i)$ is:

$$L(i) = 0.5 D [\phi_2(i) - \phi_1(i)] \quad (5.28)$$

Where $\phi_1(i)$ and $\phi_2(i)$ are the angles in radians between the vertical centre line of the section and the two radiuses bounding the length of the arc $L(i)$ and are given as follows:

$$\phi_1(i) = \cos^{-1} \left[\frac{0.5 D - h(i) + 0.5 hi}{0.5 D} \right] \quad (5.29)$$

$$\phi_2(i) = \cos^{-1} \left[\frac{0.5 D - h(i) - 0.5 hi}{0.5 D} \right] \quad (5.30)$$

The area of the part of the tube at the two sides within the strip, $A_f(i)$ is:

$$A_f(i) = 2 L(i)t \quad (5.31)$$

The net area of concrete within the strip, $A_c(i)$ is:

$$A_c(i) = 2 B(i)hi - 0.5 A_f(i) \quad (5.32)$$

Where $B(i)$ is half the width of the strip and is given as follows:

$$B(i) = 0.5 D \sin \phi(i) \quad (5.33)$$

$\phi(i)$ is the angle between the vertical centre line of the section and the radius reaching to the perimeter at the level of the mid thickness of the strip and is given as follows:

$$\phi(i) = \cos^{-1} \left[\frac{0.5 D - h(i)}{0.5 D} \right] \quad (5.34)$$

Equations 5.31 and 5.32 are used to calculate the stress resultant at each strip as will be shown in section 5.3.1.3.

5.3.1.2 Stress distribution and material constitutive relationships

At a general stage of loading, the section is assumed to be cracked under a bending moment M . The depth of the compression zone from the top surface of the tube is c . Fig. 5.21 shows the section and the linear strain distribution with the top compressive strain is ε_t and the bottom tensile strain is ε_b in the FRP tube. The strain at the extreme fibres of concrete in compression is ε_c . The strain at a given strip i , $\varepsilon(i)$, can be determined as follows:

$$\varepsilon(i) = \frac{\varepsilon_t [D - h(i)] + \varepsilon_b h(i)}{D} \quad (5.35)$$

The FRP tube is assumed to have a linear stress-strain curve in both tension and compression as shown in Fig. 5.22. The elastic moduli in both tension and compression in the axial direction are E_{ft} and E_{fc} respectively. The ultimate tensile and compressive strains are ε_{tu} and ε_{tc} respectively. Fig. 5.21 shows the stress distribution in the FRP tube along the depth of the section. The stress is also linear and proportional to the strain distribution. The stress in the FRP tube at the level of the strip i , $f_t(i)$ is:

$$\text{In tension:} \quad f_t(i) = E_{tt} \varepsilon(i) \quad (5.36)$$

$$\text{In compression:} \quad f_c(i) = E_{cc} \varepsilon(i) \quad (5.37)$$

For concrete in compression, the unconfined stress-strain curve is used. This assumption is very well confirmed by a number of evidences including experimental results as will be shown in section 5.3.2. The model given by Popovics [Mander et al 1988] has been selected due to its accurate representation of the material non-linearity. Fig. 5.22 shows the stress-strain curve of concrete in compression. The compressive stress in strip i , $f_c(i)$ is determined as follows:

$$f_c(i) = \frac{f_c' x(i)r}{r - 1 + x(i)^r} \quad (5.38)$$

Where f_c' is the concrete unconfined compressive strength. $x(i)$ is given as follows:

$$x(i) = \frac{\varepsilon(i)}{\varepsilon_c'} \quad (5.39)$$

Where ε_c' is the strain at peak strength f_c' for the concrete. r is given as follows:

$$r = \frac{E_{cv}}{E_{cv} - E_{sec}} \quad (5.40)$$

Where the secant and tangent moduli are $E_{sec} = f_c' / \varepsilon_c'$ and $E_{cv} = 5000\sqrt{f_c'}$ (MPa).

Although the concrete is cracked in the tension side, the "tension stiffening" effect, which is the contribution of concrete between cracks, is accounted for using the model suggested by Vecchio and Collins [Collins and Mitchell 1997]. The tensile stress in concrete at layer i , $f_c(i)$ is:

$$\text{For } \varepsilon(i) < \varepsilon_{cr}: \quad f_c(i) = E_{cv} \varepsilon(i) \quad (5.41)$$

$$\text{For } \varepsilon(i) > \varepsilon_{cr}: \quad f_c(i) = \frac{\alpha_1 \alpha_2 f_{cr}}{1 + \sqrt{500 (\varepsilon(i) - \varepsilon_{cr})}} \quad (5.42)$$

Where f_{cr} is the cracking strength of concrete and related to the cracking strain ε_{cr} as follows:

$$f_{cr} = E_{co} \varepsilon_{cr} \quad (5.43)$$

α_1 is a factor accounting for the bond characteristics of the reinforcement. A value of 0.3 has been suggested for the GFRP tubes used in this study and showed good agreement with the experimental results as will be shown in section 5.3.3.1. α_2 is a factor accounting for the nature of loading. $\alpha_2 = 1.0$ for short-term monotonic loading.

5.3.1.3 Internal forces and moments

The internal forces in the section, which are the resultants of the stress distribution, have to be balanced in the compression and tension sides for equilibrium. These internal forces are calculated using numerical integration of the stresses over the cross-sectional area. Fig. 5.21 shows the forces acting on a strip i . The compression force in concrete, $CC(i)$, is calculated as follows:

$$CC(i) = f_c(i) A_c(i) \quad (5.44)$$

Where $f_c(i)$ is given in Equation 5.38 and $A_c(i)$ is given in Equation 5.32. The compression force in FRP, $CF(i)$, is calculated as follows:

$$CF(i) = \varepsilon(i) E_{fc} A_f(i) \quad (5.45)$$

Where $\varepsilon(i)$ is given in Equation 5.35 and $A_f(i)$ is given in Equation 5.31. The tension force in concrete, $TC(i)$, is calculate as follows:

$$TC(i) = f_c(i) A_c(i) \quad (5.46)$$

Where $f_c(i)$ is given in Equations 5.41 and 5.42 and $A_c(i)$ is given in Equation 5.32. The tension force in FRP, $TF(i)$, is calculated as follows:

$$TF(i) = \varepsilon(i) E_f A_f(i) \quad (5.47)$$

Where $\varepsilon(i)$ is given in Equation 5.35 and $A_f(i)$ is given in Equation 5.31.

The total compressive forces in concrete and FRP, CCC and CFF respectively, which are the sum of forces acting on all the strips located above the neutral axis are:

$$CCC = \sum_{i=1}^{\left(\frac{c-0.5t}{D}\right)_n} CC(i) \quad (5.48)$$

$$CFF = \sum_{i=1}^{\left(\frac{c-0.5t}{D}\right)_n} CF(i) \quad (5.49)$$

The total tension forces in concrete and FRP, TCC and TFF respectively, which are the sum of forces acting on all the strips located below the neutral axis are:

$$TCC = \sum_{i=\left(\frac{c-0.5t}{D}\right)_n}^{i=n} TC(i) \quad (5.50)$$

$$TFF = \sum_{i=\left(\frac{c-0.5t}{D}\right)_n}^{i=n} TF(i) \quad (5.51)$$

Equilibrium of internal forces requires that the following condition be satisfied:

$$CCC + CFF = TCC + TFF \quad (5.52)$$

Once this condition is satisfied, the internal moment can be calculated. The total moments of compression and tension forces in both concrete and FRP are calculated from the following set of Equations:

$$MCC = \sum_{i=1}^{i=\left(\frac{c-0.5t}{D}\right)^n} [CC(i)y(i)] \quad (5.53)$$

$$MCF = \sum_{i=1}^{i=\left(\frac{c-0.5t}{D}\right)^n} [CF(i)y(i)] \quad (5.54)$$

$$MTC = \sum_{i=\left(\frac{c-0.5t}{D}\right)^n}^{i=n} [TC(i)y(i)] \quad (5.55)$$

$$MTF = \sum_{i=\left(\frac{c-0.5t}{D}\right)^n}^{i=n} [TF(i)y(i)] \quad (5.56)$$

Where $y(i)$ is the distance from the neutral axis to the force acting on layer i and is calculated as follows:

$$\text{For compression forces: } y(i) = c - 0.5t - h(i) \quad (5.57)$$

$$\text{For tension forces: } y(i) = h(i) - c + 0.5t \quad (5.58)$$

The total moment is the sum of the internal moments and is calculated as follows:

$$\text{Moment} = MCC + MCF + MTC + MTF \quad (5.59)$$

The corresponding curvature of the section, which is the slope of the strain profile, is calculated as follows:

$$\text{Curvature} = \frac{\epsilon_c}{c-t} \quad (5.60)$$

5.3.1.4 Procedure of analysis

Fig. 5.23 shows the flow chart of the analytical model used to predict the moment-curvature response of the section utilizing the equations presented in the previous sections. The procedure can be summarized in the following steps:

1. Input the dimensions, material properties, and the number of layers, n .
2. Input a value for the compressive strain in concrete ε_c .
3. Assume a value for the neutral axis depth c .
4. Calculate the extreme fibre compressive and tensile strains, ε_c and ε_t , in the FRP, and compare them to the ultimate strains of the material to check if failure occurred.
5. For all the layers ($i = 1$ to n), calculate the areas of concrete and FRP, $A_c(i)$ and $A_f(i)$, within each layer.
6. Calculate the total compressive and tensile forces in both concrete and FRP, CCC , CFE , TCC , and TFE .
7. Check for equilibrium by satisfying the condition that the absolute value of the difference between the total compression force and the total tension force is less than the allowable tolerance accepted for the difference, "error".
8. If the equilibrium is not satisfied, go to step 3 and assume another value of c . The process is repeated until the equilibrium is satisfied.
9. Once the equilibrium is satisfied, the internal moments are calculated for concrete and FRP in compression and tension, MCC , MCF , MTC , and MTF .
10. The total moment corresponding to the strain level entered in step 2 is the sum of all the internal moments, and the corresponding curvature is the slope of the strain profile based on this strain and the neutral axis depth that satisfied the equilibrium condition.
11. Go to step 2 to enter a new strain level and repeat the process till the complete moment-curvature response is constructed.

5.3.1.5 Cracking moment

The cracking moment is calculated from the following equation:

$$M_{cr} = f_{cr} \frac{I_t}{((D-t)/2)} \quad (5.61)$$

Where I_t is the transformed moment of inertia and calculated as follows:

$$I_t = I_c + \frac{E_f}{E_{co}} I_f \quad (5.62)$$

Where E_f is the effective elastic modulus of the FRP tube in the axial direction. If the modulus is different in tension and compression, E_f can be assumed as the average of E_{ft} and E_{fc} . I_c and I_f are the moments of inertia of the concrete core and the FRP tube respectively and calculated as follows:

$$I_c = \frac{\pi (D-t)^4}{64} \quad (5.63)$$

$$I_f = \frac{\pi (D_o^4 - (D-t)^4)}{64} \quad (5.64)$$

The cracking strength of concrete f_{cr} can be calculated as follows:

$$f_{cr} = k \sqrt{f_c} \quad (5.65)$$

Where $k = 0.6$ [ACI 318-95], however, it was shown that a value of 1.0 correlates better to the experimental results as shown in Fig. 4.37 and Table 4.2 of Chapter 4.

5.3.1.6 Load-deflection calculations

Once the moment-curvature response of the section ($M-\psi$) is obtained, the load-deflection response of the member ($P-y$) can be estimated for a given loading scheme. The deflection y is calculated by integrating the curvatures along the span using the

moment-area method [Ghali and Neville 1989] as shown in Fig. 5.24 and given by the following equations:

$$\psi = \frac{d^2 y}{d x^2} \quad (5.66)$$

$$y = \iint \psi \, dx \, dx \quad (5.67)$$

The deflection at a point is the moment of the curvature diagram, which is considered as elastic load acting on the conjugate beam.

5.3.2 Confinement of Concrete in the Compression Zone

Fig. 5.25 shows a typical concrete-filled tube subjected to bending. Unlike the sections subjected to high level of axial loads, the size of the compression zone in the pure bending case is relatively small compared to the total cross-sectional area. Both the strain distribution and the width of the section are variable. The compression force of the concrete is obtained by integrating the stress diagram with the area in compression. The large stresses near the top fibres are integrated with small areas due to the narrow width, while the large area at the base of the compression zone is integrated with the small stresses near the neutral axis. The resultant compressive force in concrete is also very close to the neutral axis, therefore, the moment due to the compressive force of the concrete is small in case of bending. Up to a compressive strain of about 0.002, shown as stage "1" in Fig. 5.25, there is no confinement effect on the concrete stress-strain behaviour and the compression force in concrete is $C1$ as shown in the figure. At strain levels higher than 0.002, stage "2", the difference between the stress-strain diagrams of the confined and unconfined concrete is little and is integrated with even smaller part of

the compression zone, therefore, its contribution to the total force, ΔC , is very small. It should also be noted that in most cases, the beams fail in tension due to rupture of the tubes before developing the full stress-strain curve of the concrete in the compression zone. In addition, flexural members are normally made of laminates that provide more strength and stiffness in the axial direction than in the hoop direction, consequently, very little confinement is provided even if the member is subjected to pure axial load. Therefore, in the proposed model for flexural analysis, the material constitutive relationship of the unconfined concrete, Equation 5.38, is used.

The measured response of axial strain versus lateral strain in beams also verifies the above conclusion. Fig. 5.26 shows the axial-lateral strain behaviour of concrete-filled tubes tested under pure axial load and under pure bending. In case of bending, the axial-lateral strain behaviour is measured in the compression zone. Fig. 5.26a shows the behaviour of beam 1b and stub 7 of the same concrete-filled steel tube. Fig. 5.26b shows the behaviour of beam 4 and stub 2 of the same concrete-filled GFRP tube, which has only one third of the fibres content oriented in the axial direction. Fig. 5.26c shows the behaviour of beam 2b and stub 11 of the same concrete-filled GFRP tube, which has two thirds of the fibres content oriented in the axial direction. The figures clearly show that in stubs, the behaviour is bi-linear with the initial slope representing Poisson's ratio of the shell. At an axial strain level of 0.002 ~ 0.003, the concrete expands excessively and the shell is loaded more in the hoop direction, therefore, the rate of lateral strain increases as indicated by the second slope. On the other hand, in the compression zone of beams, the axial-lateral strain behaviour followed the same initial slope up to failure, which occurred

due to rupture of the FRP in the tension zone. The behaviour confirms the lack of confinement of concrete in the compression zone in pure bending.

5.3.3 Verification of the Model

The strain compatibility/equilibrium model is applied to several beams selected to cover the various types and sizes of the GFRP tubes including beams 2, 4, 10, 11, 12, and 13. The details of the beams in terms of dimensions and material properties were given in Tables 3.1, 3.2, and 3.3 of Chapter 3. This section presents the predicted flexural behaviour in terms of moment-curvature, load-deflection, and moment-strain behaviour as well as the neutral axis depth for beams 4, 10, 11, 12, and 13. The prediction of beam 2 is given in section 5.3.4, as it demonstrates the effect of concrete filling on the flexural behaviour, since beam 2 was tested as hollow tube, beam 2a and as concrete-filled tube as well, beam 2b.

5.3.3.1 Beam 4

Beam 4 represents the beams with FRP tubes having lower strength and stiffness in the axial direction as compared to the hoop direction. Tube 5 of Table 3.1 is used to fabricate this beam. The tube has only 33 percent of the fibres oriented towards the axial direction at 8 degrees and 67 percent of the fibres oriented towards the hoop direction at 86 degrees. Fig. 5.27 shows the experimental versus the predicted moment-curvature response of beam 4. The experimental curvature is based on the slope of the measured axial strain profile along the depth. The predicted response was obtained using the model developed in section 5.3.1 utilizing the material properties obtained from the coupon test

for the GFRP tube and the cylinder tests for the concrete strength. The cracking moment is calculated according to section 5.3.1.5 where the coefficient k in Equation 5.65 for the cracking strength is taken as 1.0. Four different cases were considered including the unconfined and confined concrete material models as well as tension stiffening being considered or ignored. The confined concrete model was obtained using the confinement model given in section 5.2, which resulted in the stress-strain curve shown in Fig. 5.11(a) for stub 2. The figure shows that the best prediction is obtained by considering the tension stiffening and ignoring the concrete confinement as explained before. The figure also shows the predicted failure point based on the failure strain of the tension coupon test as well as the failure strain based on the beam test. The coupon test slightly underestimates the failure strength of the GFRP tube. Fig. 5.28, 5.29, and 5.30 show the experimental versus the analytical load-deflection, moment-strain, and neutral axis depth behaviours respectively. Good agreement is observed. As indicated in section 5.3.1.2, a value of 0.3 is recommended for the bond factor α_1 in the concrete model in tension, which is used to account for the tension stiffening effect. In order to illustrate this observation, Fig. 5.31 shows the experimental versus the predicted moment-curvature response of the beam based on different bond factors. The figure is focused on the immediate part of the behaviour after cracking since it is the most affected by tension stiffening. The bond factor ranges in value from zero to 1.0, where zero indicates unbonded reinforcement and the tension stiffening is completely ignored, while 1.0 indicates the maximum level of tension stiffening due to a perfectly bonded reinforcement [Collins and Mitchell 1997]. The figure clearly indicates that the value of 0.3 very well represents the behaviour.

5.3.3.2 Beam 10

Beam 10 represents the beams with FRP tubes having similar stiffness in both the axial and hoop directions. Tube 7 of Table 3.1 is used to fabricate this beam. The tube has 48 percent of the fibres oriented towards the axial direction at 3 degrees and 52 percent of the fibres oriented towards the hoop direction at 88 degrees. Figures 5.32, 5.33, 5.34, and 5.35 show the predicted versus the experimental moment-curvature, load-deflection, moment-strain, and variation of the neutral axis depth diagrams respectively. The behaviours are predicted with and without the tension stiffening effect, and ignoring the confinement effects of concrete in compression. Good prediction is observed, however, the failure point based on the tension coupon test slightly underestimates the failure load.

5.3.3.3 Beams 11, 12 (a, b) and 13 (a, b)

Beams 11, 12, and 13 were all fabricated using GFRP tubes of the same laminate structure, which has almost similar stiffness in both directions, as in the case of beam 10, yet the laminate structure is completely different from that used in beam 10. In this case, 70 to 77 percent of the fibres content are oriented at ± 34 degrees with respect to the axial direction and 23 to 30 percent towards the hoop direction at 80 to 86 degrees. Beams 11, 12, and 13, however, represent three different sizes with different reinforcement ratios. Figures 5.36, 5.40, and 5.44 show the predicted versus the experimental moment-curvature diagrams. It should be noted that two identical beams (a and b) were tested for both beams 12 and 13. Figures 5.37, 5.41, and 5.45 show the load-deflection responses of the beams. Figures 5.38, 5.42, and 5.46 show the moment-strain responses. Figures

5.39, 5.43, and 5.47 show the variation of the neutral axis depth. In general good agreement is observed between the experimental and analytical responses except for beams 12 and 13 some difference is observed. This is attributed to the fact that, in beams 12 and 13, slip occurred between the tube and the concrete core, therefore, the strain compatibility assumption used in the model is not fully satisfied in those beams. This is clearly illustrated in Figures 5.42 and 5.46 for the load-strain behaviour, especially in the compression side and also in Figures 5.43 and 5.47 for the history of the neutral axis depth. The concrete slip results in some loss of stiffness, over loading of the tube in compression and shifting of the neutral axis depth of the tube.

5.3.4 Significance of Concrete Filling

As discussed before in section 4.2.1, the concrete filling has two functions. It provides support for the FRP shell to prevent ovalization and to prevent premature failure due to local buckling. Also it adds to the resistance of the section in the compression zone and increases both the overall stiffness and strength of the member. Beam 2 is selected to demonstrate this mechanism as it was tested with and without concrete filling. Fig. 5.48 shows the experimental and predicted moment-curvature responses of the hollow and concrete-filled tubes, beams 2a and 2b respectively. The moment-curvature response of the hollow tube is calculated using the following equation:

$$M = (EI)_{shell} \psi \quad (5.68)$$

Where $(EI)_{shell}$ is the axial flexural rigidity of the hollow tube based on the moment of inertia of the section and the effective elastic modulus of the shell in the axial direction. The predicted failure load of beam 2a is based on the measured compressive strain of the

GFRP tube at failure in the beam test, which is considerably lower than the ultimate strain of the tube in compression. In fact for the other beams, beams 4, 10, 11, 12, and 13 no hollow tubes were tested in bending, however, the moment-curvature response of the hollow tubes can be predicted using the expression given in Equation 5.68. The approximation involved is the assumption that the moment of inertia of the section is constant and is based on the original circular geometry, however the inertia reduces with increasing the load due to the ovalization of the section. The failure load is predicted using a formula developed by Keward (1978) and presented by Ibrahim (2000). The formula is given in Equation 5.69 and it calculates the critical bending moment M_{crit} due to local buckling of hollow composite cylindrical tube subjected to pure bending.

$$M_{crit} = \frac{4\sqrt{2}}{3\sqrt{3}} \sqrt{\frac{D_{xx}}{E_y t}} E_y \pi R t \quad (5.69)$$

t and R are the wall thickness and the original radius of the tube. E_y is the effective modulus in the longitudinal direction of the composite laminate. D_{xx} is the circumferential bending stiffness of the tube calculated using the lamination theory [Daniel and Ishai 1994]. The calculated circumferential bending stiffness of the hollow tubes were 0.044, 0.617, 0.202, 0.168, and 0.613 kN.m for beams 4, 10, 11, 12, and 13, respectively. The resulting critical bending moments of the beams were 13.4, 141.6, 70.7, 123.7, and 472.3 kN.m respectively. Fig. 5.49 shows the moment-curvature response of beams 4, 10, 11, 12, and 13. Also shown on the same graphs the predicted moment-curvature response of the same beams if were tested as hollow tubes with the critical moment level pointed out on the curves. The figure indicates that beams 4, 10, and 11 would have a material compressive failure before local buckling, while beams 12 and 13 would fail prematurely in local buckling before reaching the material strength.

The figure also indicates that the concrete filling adds a significant contribution to the strength and stiffness of the beams. This is particularly true for beams with relatively low flexural stiffness as will be discussed in section 5.3.6.4. As shown in Table 4.1 of Chapter 4, the reinforcement ratios of beams 4, 10, 11, 12, and 13 ranged from 3.46 to 7.85 percent. On the other hand, Fig. 5.48 shows that the gain in stiffness of beam 2 due to concrete filling was smaller. This is attributed to its relatively high stiffness, as the reinforcement ratio for this beam, 12.32 percent, is relatively higher than that of the other beams.

5.3.5 Optimization of Void Size in Flexural Members

As discussed in section 4.2.2.1 and shown in Figures 4.11 of Chapter 4, the behaviour of beams 4 and 5 is very similar although the configuration of the cross-section is different. This is attributed to the fact that the void inside the concrete core of beam 5 is located within the tension side of the beam. The fact that the neutral axis depths of these beams were similar and stable during the loading history as shown in Fig. 4.13 can be utilized in design to optimize the self-weight of the member. The designer can perform the cracked section analysis for the totally filled tubes using the analytical model given in section 5.3.1 and find the neutral axis depth that satisfies the equilibrium and strain compatibility conditions at failure. A concentric circular void can then be provided in the core such that the remaining concrete wall thickness is equal to the estimated neutral axis depth as shown in Fig. 5.50. This will minimize the self-weight without sacrificing the strength of the member. In fact the best technique to fabricate such members would be the concrete

spinning technique, originally developed to produce ordinary reinforced concrete or prestressed poles and piles [Rodgers 1984], however, this is out of the scope of this study.

5.3.6 Parametric Study using the Proposed Model for Flexural Analysis

In this section a parametric study is performed using the proposed model to study the effects of stiffness of the tube in the axial direction and the concrete strength on the flexural behaviour. Both the reinforcement ratio and the laminate structure affect the stiffness of the tube. The concrete contribution in low and high stiffness tubes is also studied. A 300 mm diameter GFRP tube with a $[0/90]_s$ symmetric crossply laminate is selected for the analysis. The laminate structure was changed by varying the proportions of the fibres in the axial and hoop directions of the tube for the same wall thickness and concrete strength. A 9:1, 3:1, 1:1, and 1:3 ratios were included in the study. A 3:1 laminate, for example, indicates that the amount of fibres oriented in the axial direction is three times that in the hoop direction, or that 75 percent of the wall thickness is composed of layers with fibres oriented in the axial direction. This also indicates that the tube is stiffer and stronger in the axial direction compared to the hoop direction. A 1:1 laminate indicates that the tube has the same strength and stiffness in the two directions. It should be noted however that the strength and stiffness in the axial direction are significant for flexural resistance of concrete-filled tubes. The reinforcement ratio is controlled by varying the wall thickness of the tube for the same diameter, laminate structure, and concrete strength. Based on the definition given in Equation 4.1, the reinforcement ratios included in the study are 2.67, 5.33, 10.67, and 21.33 percents, based on wall thicknesses

of 2, 4, 8, and 16 mm respectively. The effect of concrete strength was studied by varying the concrete compressive strength for the same reinforcement ratio and laminate structure. For all the cases the cracking strength of concrete was calculated using Equation 5.65 where, the k factor equals 1.0. Also the tension stiffening effect was accounted for in the analysis. Fig. 5.51 shows the stress-strain curves of the three different concrete materials used in the study including 20, 50, and 80 MPa strengths. The curves in the compression side were developed using the model by Popovics, which is given in Equations 5.38 to 5.40. It is interesting to observe the sensitivity of the model to the fact that low strength concrete is more ductile with higher plasticity compared to high strength concrete. The stress-strain curves in the tension side were developed using the model by Vecchio and Collins, which is given in Equations 5.41 and 5.42. Fig. 5.52 shows the stress-strain curves of the four GFRP laminates used for the tubes. These curves represent the behaviour in the axial direction and were developed for a realistic E-glass/epoxy laminate with fibre volume of 0.55 [Daniel and Ishai 1994]. The curves also show the reduction in stiffness and strength of the laminate with reducing the amount of fibres in the axial direction.

5.3.6.1 Effect of laminate structure

Figures 5.53, 5.54, and 5.55 show the moment-curvature, moment-strain, and moment-neutral axis depth behaviours for four GFRP tubes with four different laminates filled with concrete. All the tubes were 4 mm thick and filled with 50 MPa concrete. The figures show that increasing the amount of fibres in the axial direction increases the overall strength and stiffness of the beam, however, the failure mode could be changed.

The beam with (1:3) laminate failed in tension, while the beams with (3:1) and (9:1) laminates failed in compression. The beam with (1:1) had the tension and compression sides of the tube reaching the ultimate strengths almost simultaneously, which is referred to as balanced failure. The behaviour before cracking is almost identical for all the beams. The neutral axis depth shifts down towards the tension side near the end to balance the stresses on the section when concrete starts to soften excessively. Fig. 5.62 shows the effect of the laminate structure, represented in the form of reinforcement index, on the normalized flexural strength. Also shown on the same figure Equation 4.6, which was developed based on experimental results in Chapter 4 to predict the strength of concrete-filled FRP tubes failing in tension. The equation predicted well the flexural strength of the beam with (1:3) laminate since it is the only beam among the four cases that failed in tension.

5.3.6.2 Effect of the reinforcement ratio

Figures 5.56, 5.57, and 5.58 show the moment-curvature, moment-strain, and moment-neutral axis depth behaviours for four concrete-filled GFRP tubes with thickness ranging from 2 to 16 mm. The laminates of all the tubes were (1:1) and the concrete strength was 50 MPa. The figures show the increase in the stiffness and strength of the beams with increasing the wall thickness. In fact increasing the wall thickness has the same effect as increasing the stiffness of the laminate of the tube, as both increase the flexural rigidity of the section. This is evident from comparing the moment curvature responses of the beam with (9:1) laminate and 4 mm wall thickness in Fig. 5.53 to the beam with (1:1) laminate and 8 mm wall thickness in Fig. 5.56. The moment-curvature responses for the

two beams are almost identical. Also the stiffer the GFRP tube, whether by changing the laminate structure or increasing its thickness, the closer the level of the neutral axis depth to the centre of the circular section as shown in Figures 5.55 and 5.58. This is attributed to the fact that the stiffer the shell, the smaller the effect of the concrete on the location of the centroid of the transformed section and the behaviour would be more similar to the behaviour of hollow tubes. Fig. 5.62 shows the effect of increasing the wall thickness, represented in the form of reinforcement index, on the normalized flexural strength. In fact the trend is identical to that representing the increase of axial stiffness of the laminate on the same graph as evident by the overlap of the two curves. Also Equation 4.6, represented by the dotted curve, predicted well the strength of the beam with 2 mm wall thickness since it failed in tension.

5.3.6.3 Effect of concrete strength

Figures 5.59, 5.60, and 5.61 show the moment-curvature, moment-strain, and moment-neutral axis depth behaviours for GFRP tubes with 4 mm wall thickness, (1:1) laminates, and filled with 20, 50, and 80 MPa concrete. The figures show that while the concrete strength slightly improves the behaviour at cracking, it has insignificant effect on the behaviour at ultimate. In fact it is interesting to note that the beam with highest concrete strength, 80 MPa, had the lowest strength as shown in Fig. 5.59. This can be explained by examining the material stress-strain curves of concrete in Fig. 5.51. The 80 MPa concrete has a sudden drop in the stress once the peak strength is achieved, while the lower strength concrete has an extended ductility and sustained stress level. This affects

the internal moment resistance of the section. when integrating the distributed stresses in the compression zone with the area of concrete.

5.3.6.4 Concrete contribution in cases of low and high stiffness tubes

Fig. 5.63 shows the moment-curvature response of hollow and concrete-filled (1:1) GFRP tubes of two different wall thicknesses, 2 and 16 mm. The 2 mm tube represents a case of low stiffness tube while the 16 mm tube represent a very stiff tube. The failure of the 16 mm hollow tube was governed by the compressive strength of the shell, while that of the 2 mm hollow tube was governed by local buckling rather than material failure as predicted by Equation 5.69. The circumferential bending stiffness D_{θ} in the equation was estimated as 0.023 and 12.01 kN.m for the 2 mm and 16 mm tubes respectively, assuming a [90/0/90] stacking sequence. The figure clearly shows that the concrete filling significantly improves the strength and ductility of low stiffness tubes, while its effect is very little in stiff tubes. The effect of concrete filling in low stiffness tubes is reflected in two aspects. It prevents the premature local buckling failure in compression. In fact it could change the failure mode to tension failure as shown in the figure. It also significantly contributes to the internal moment resistance of the section as evident by comparing the dotted curve, which represents a hypothetical case beyond local buckling failure, to the solid line representing the behaviour of the 2 mm tube, which is filled with concrete.

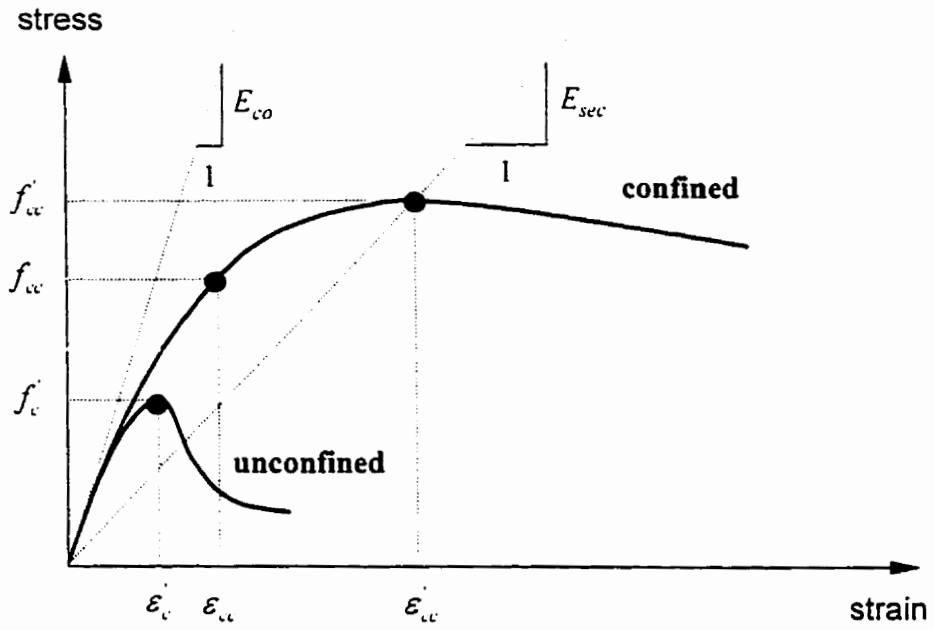


Fig. 5.1 Constant confinement model by Mander (1988)

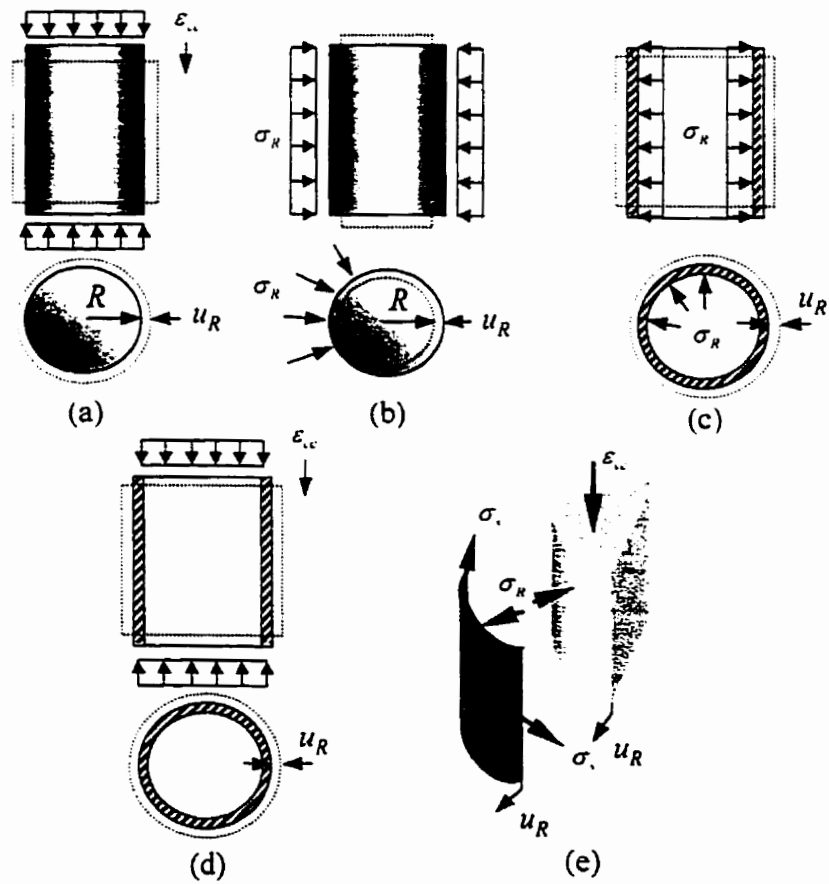
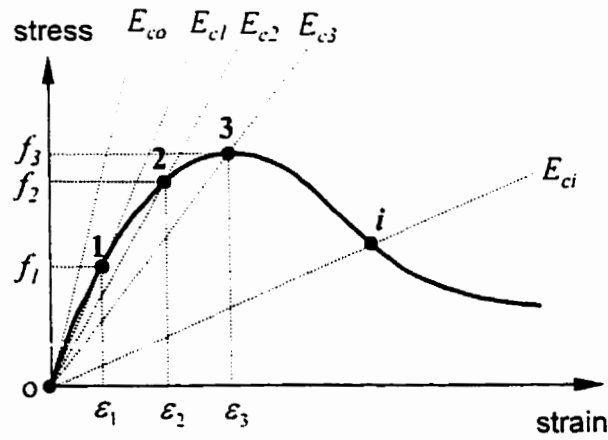
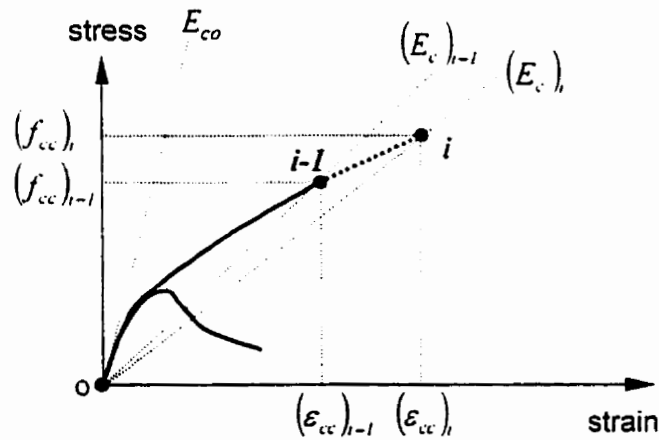


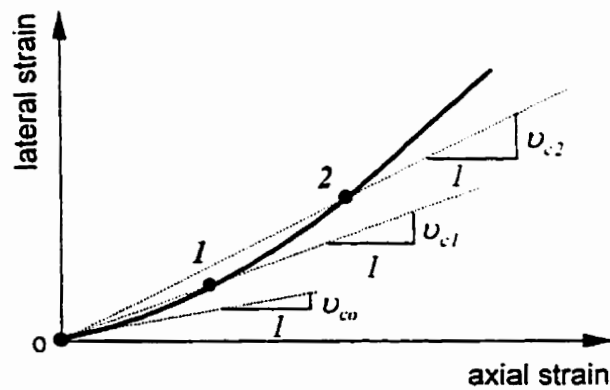
Fig. 5.2 Solid cylinder and thin shell under different stresses



(a) Representing nonlinear materials using variable secant modulus



(b) Construction of the confined stress-strain diagram using the instantaneous modulus



(c) Variable Poisson's ratio approach

Fig. 5.3 Variable material parameters for concrete

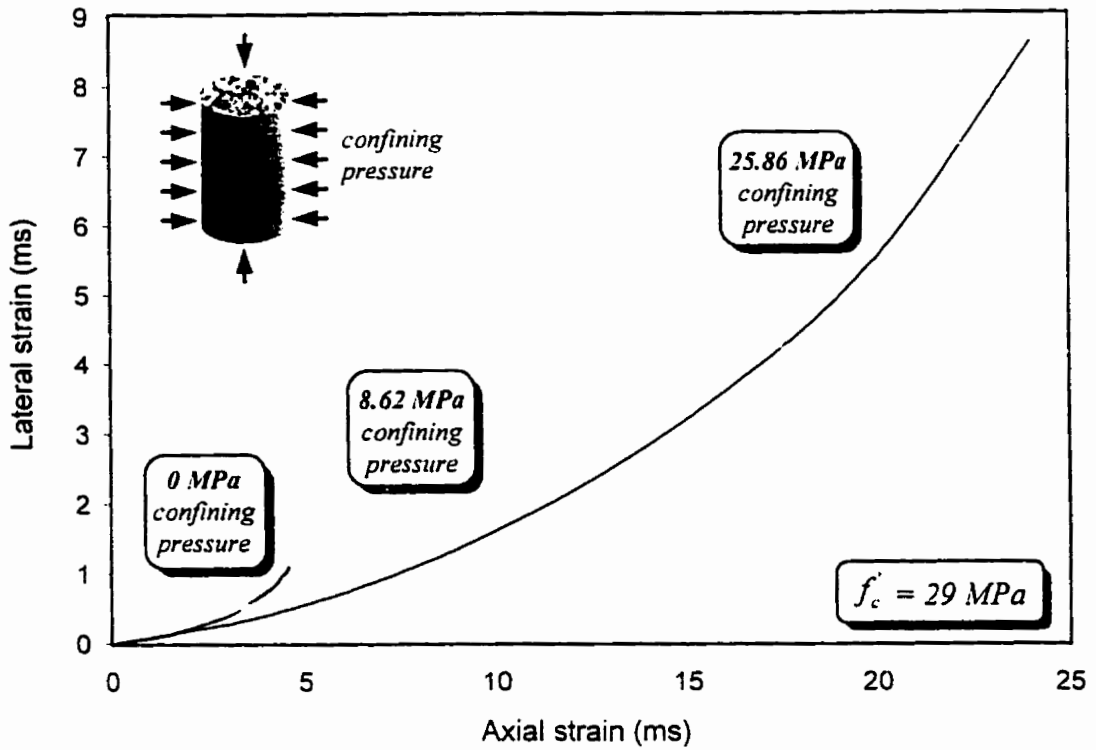


Fig. 5.4 Average axial-lateral strain behaviour under different confinement pressures [Gardner 1969]

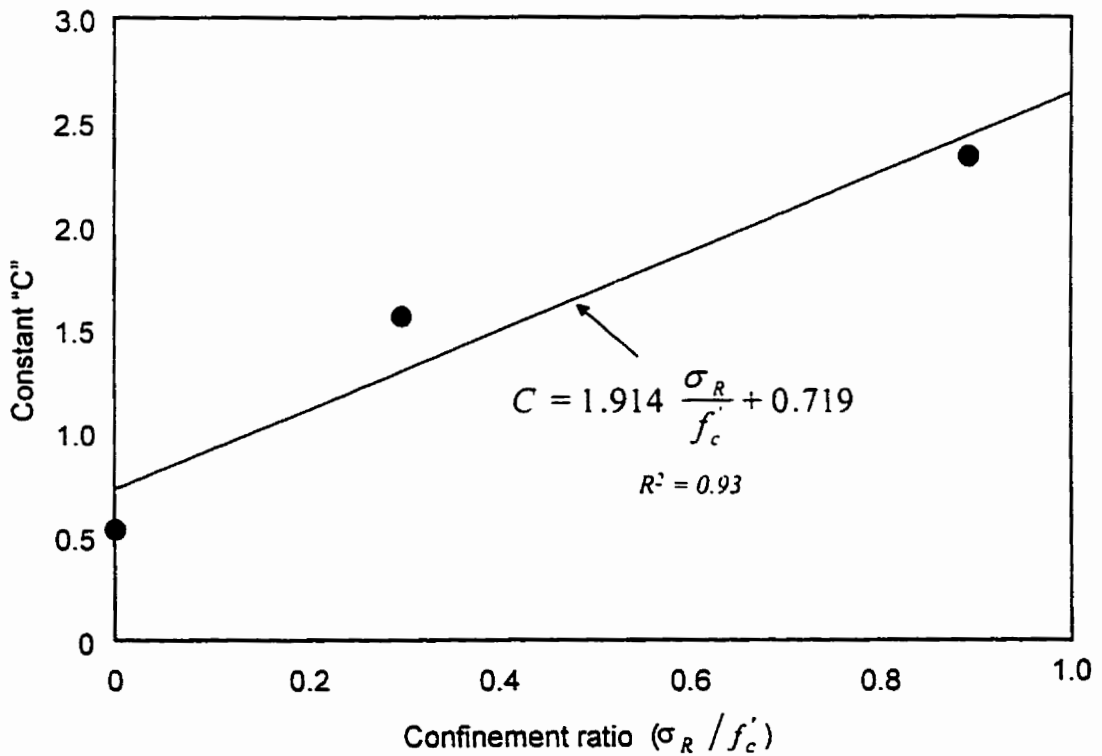


Fig. 5.5 Variation of constant "C" at different confinement ratios

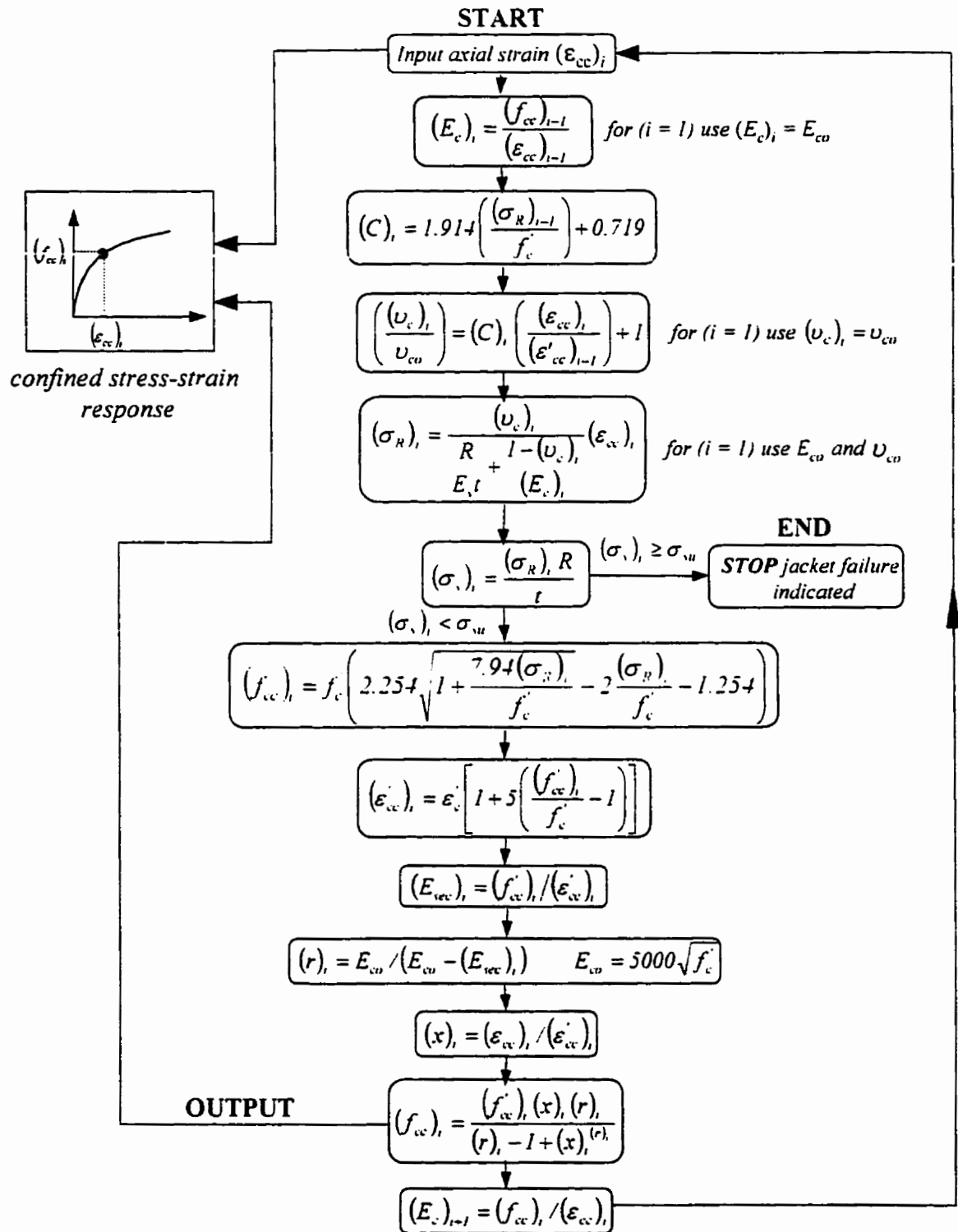


Fig. 5.6 Flowchart of the proposed incremental variable confinement model

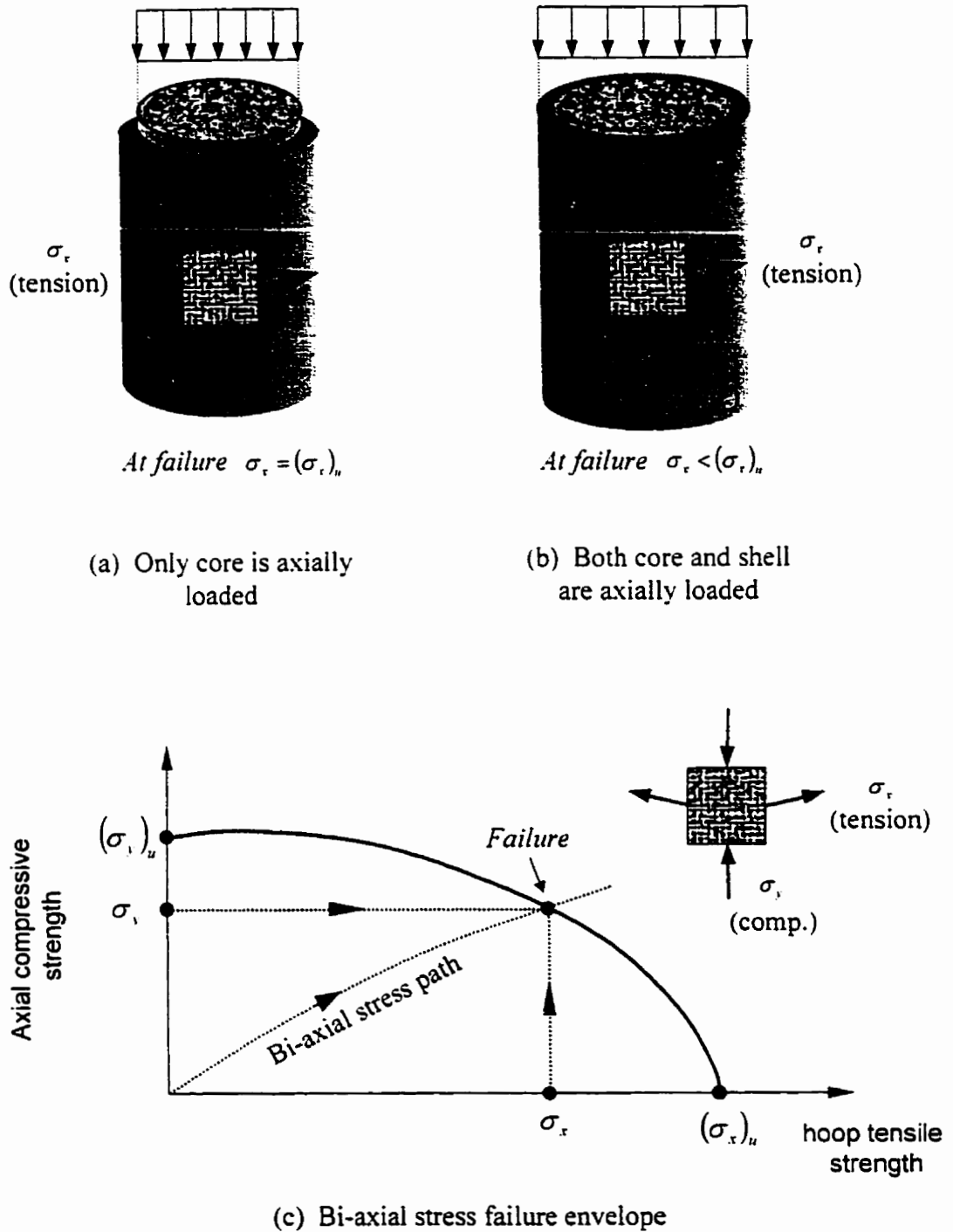
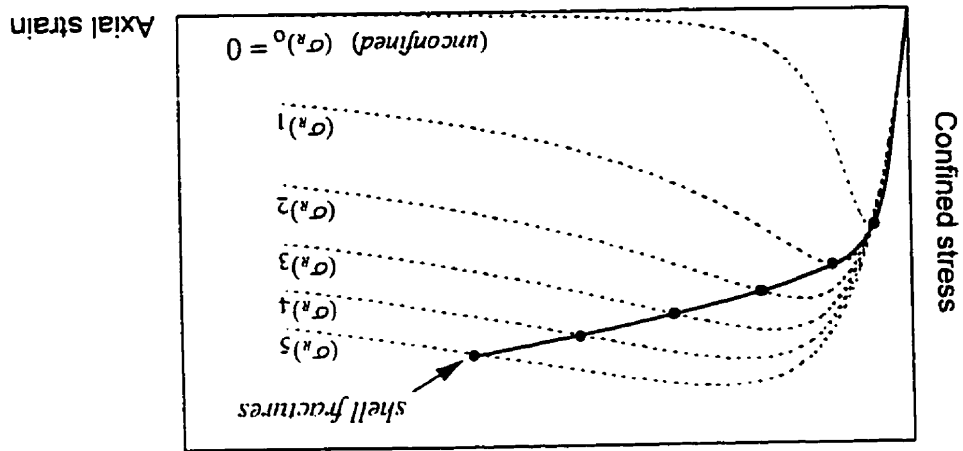
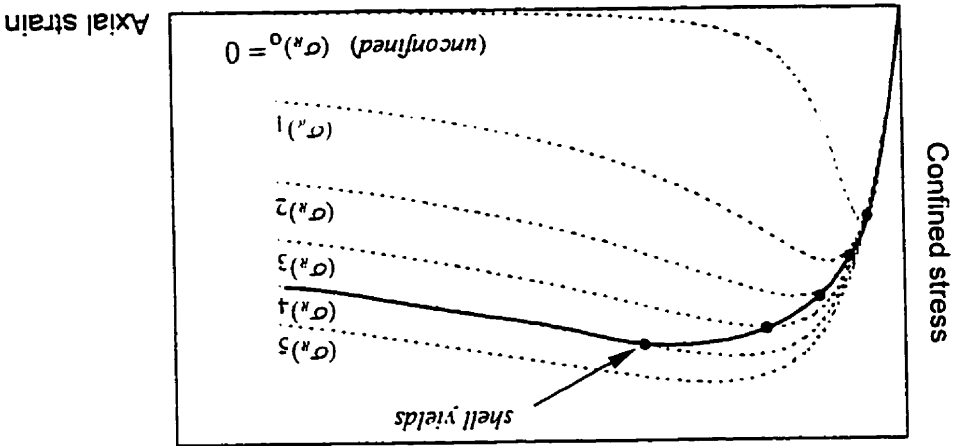


Fig. 5.7 Effect of the axial loading conditions on the strength of FRP shell



(a) FRP-confined concrete



(b) Steel-confined concrete

Fig. 5.8 Schematic stress-strain behaviour of FRP and steel confined concrete (Not to scale)

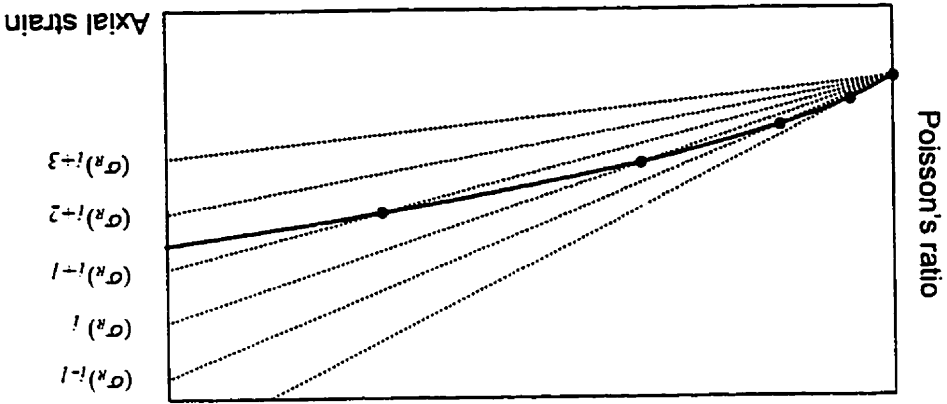
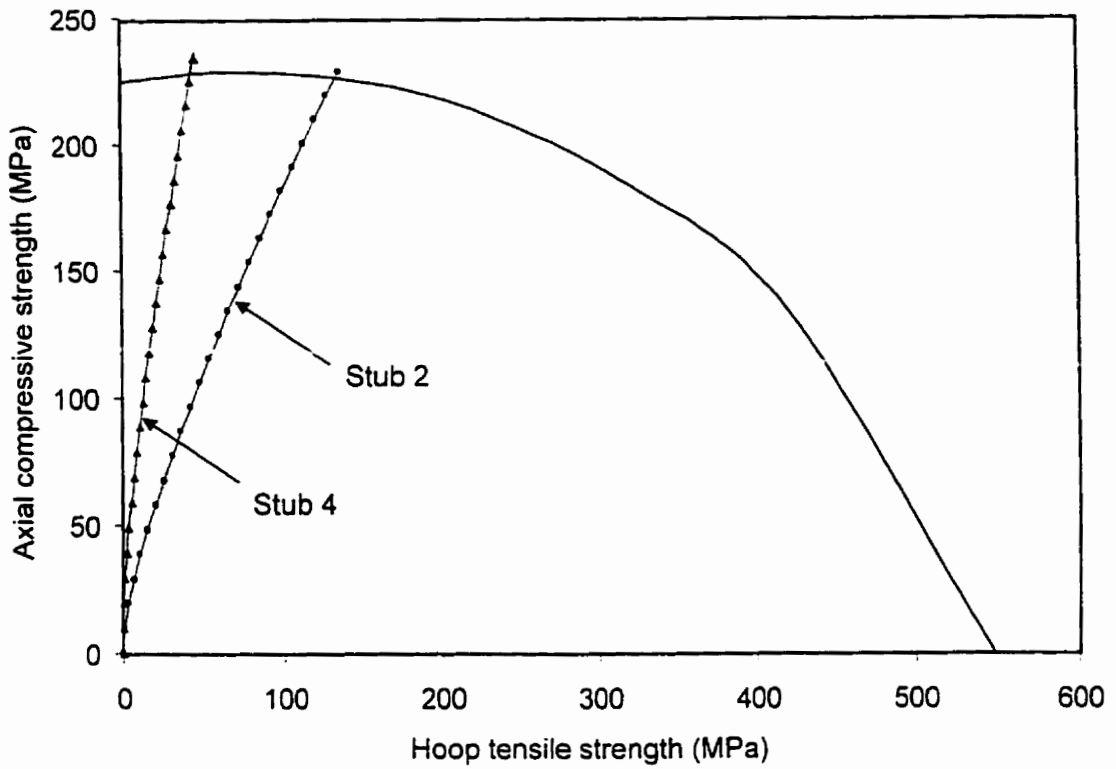
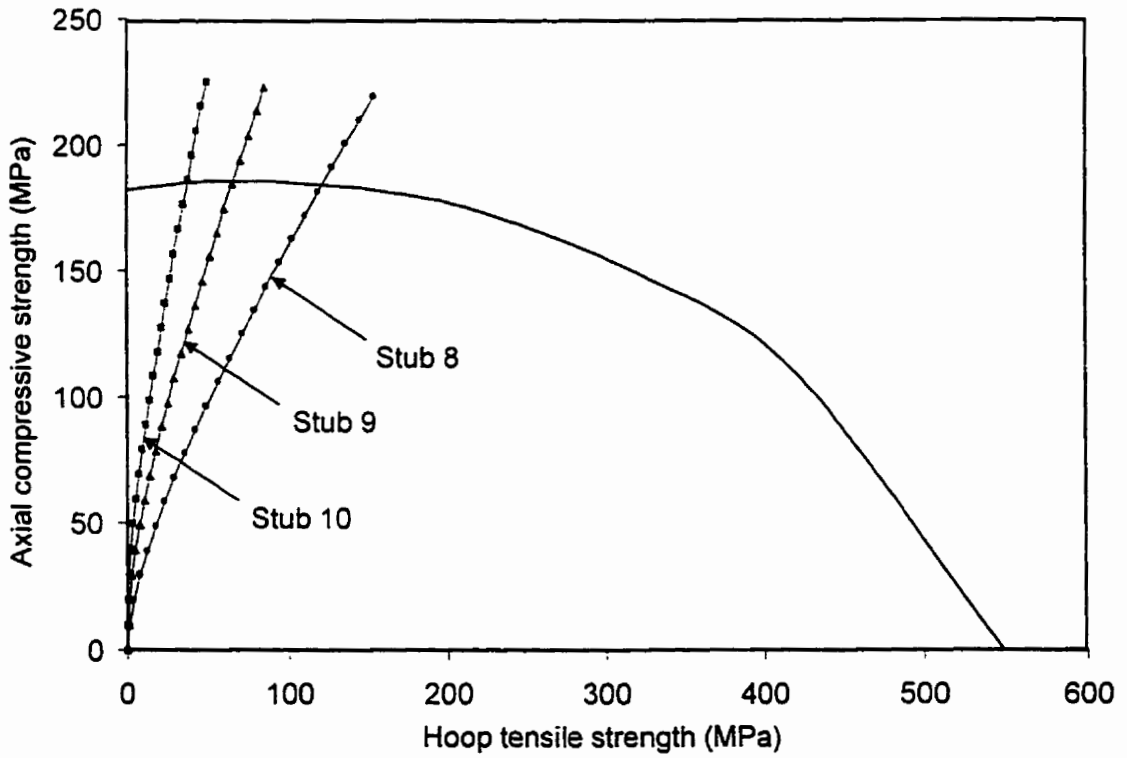


Fig. 5.9 Schematic of Poisson's ratio variation over the history of loading

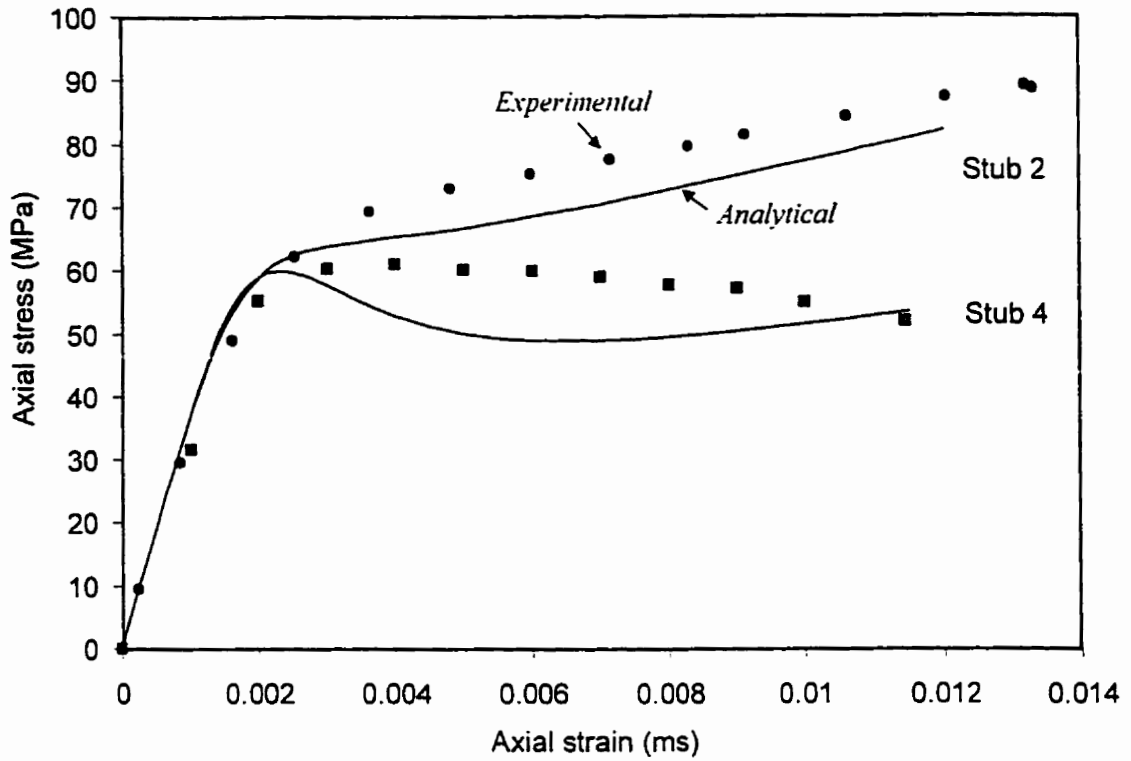


(a) GFRP tube 5 used to fabricate stubs 2 and 4

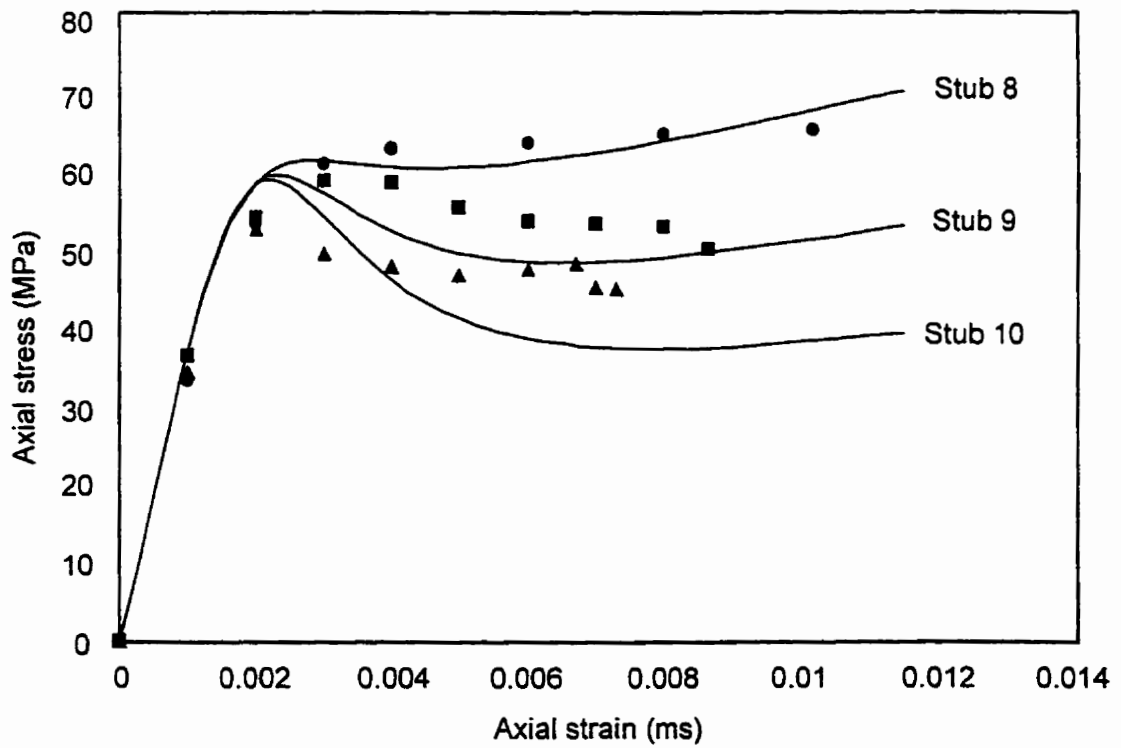


(b) GFRP tube 6 used to fabricate stubs 8, 9 and 10

Fig. 5.10 Bi-axial strength failure envelope and stress path of tubes 5 and 6



(a) Stubs 2 and 4 of the present study



(b) Stubs 8, 9 and 10 of the present study

Fig. 5.11 Experimental versus analytical stress-strain response of stubs tested in this study

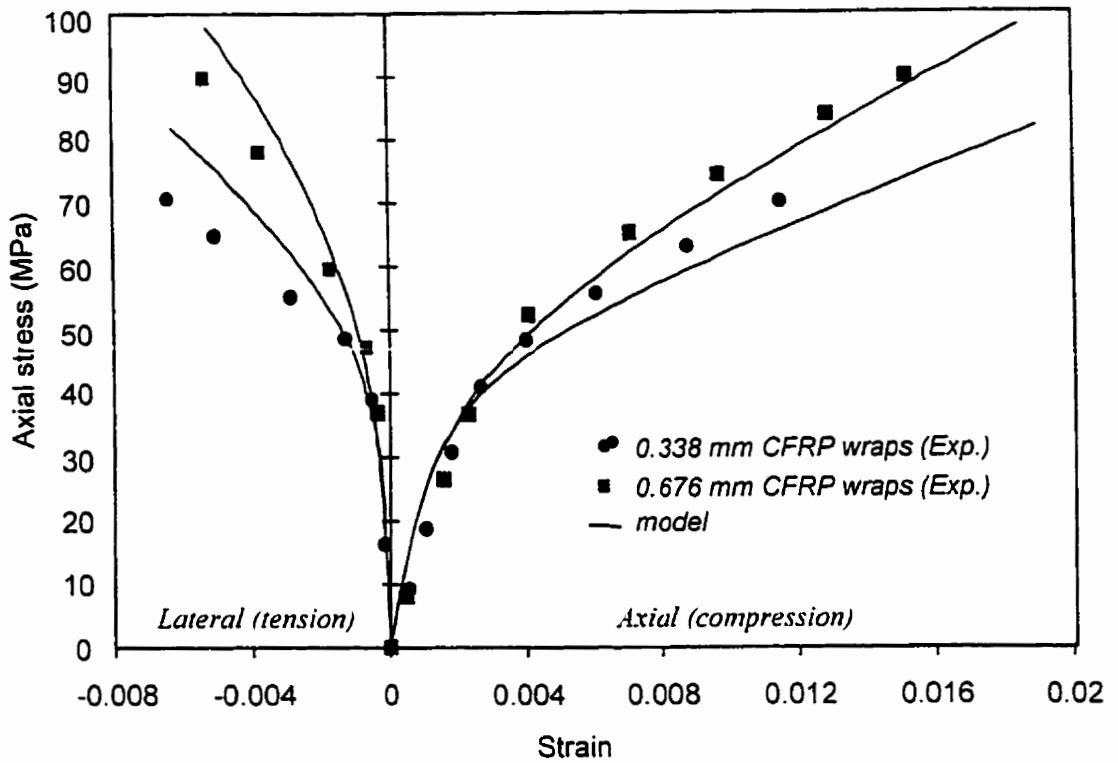


Fig. 5.12 Experimental versus analytical stress-strain response [Kawashima et al 1997]

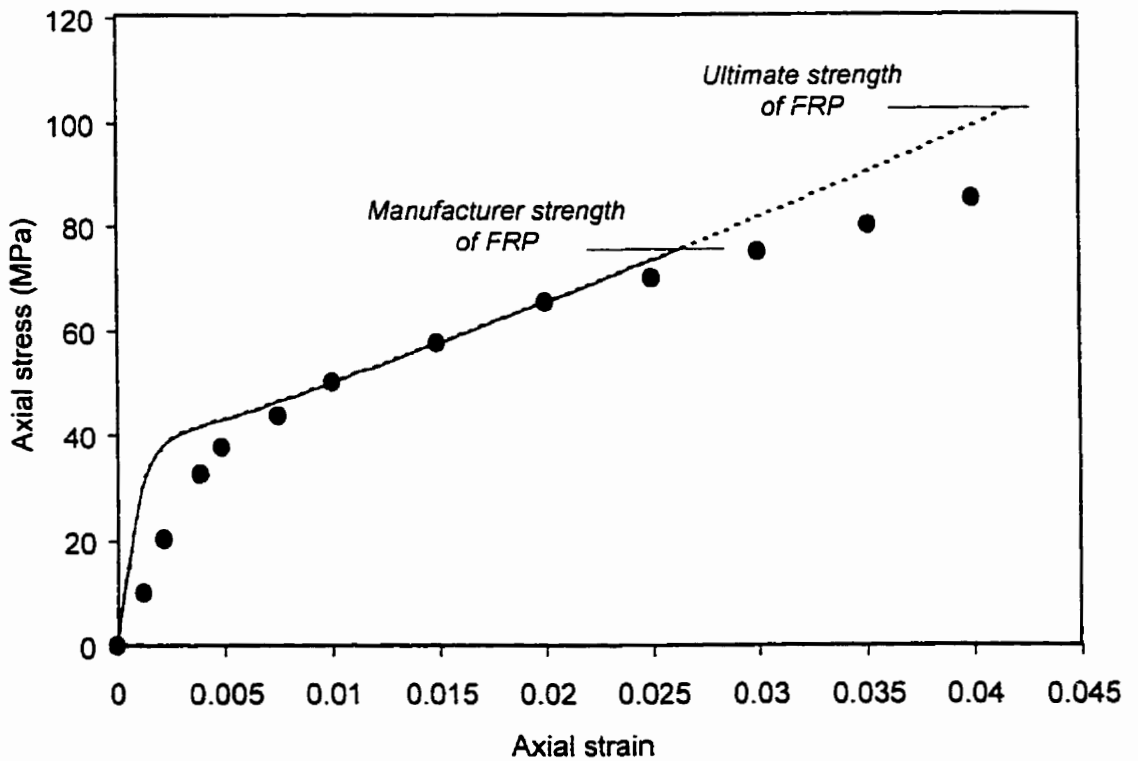


Fig. 5.13 Experimental versus analytical stress-strain response [Nanni and Bradford 1995]

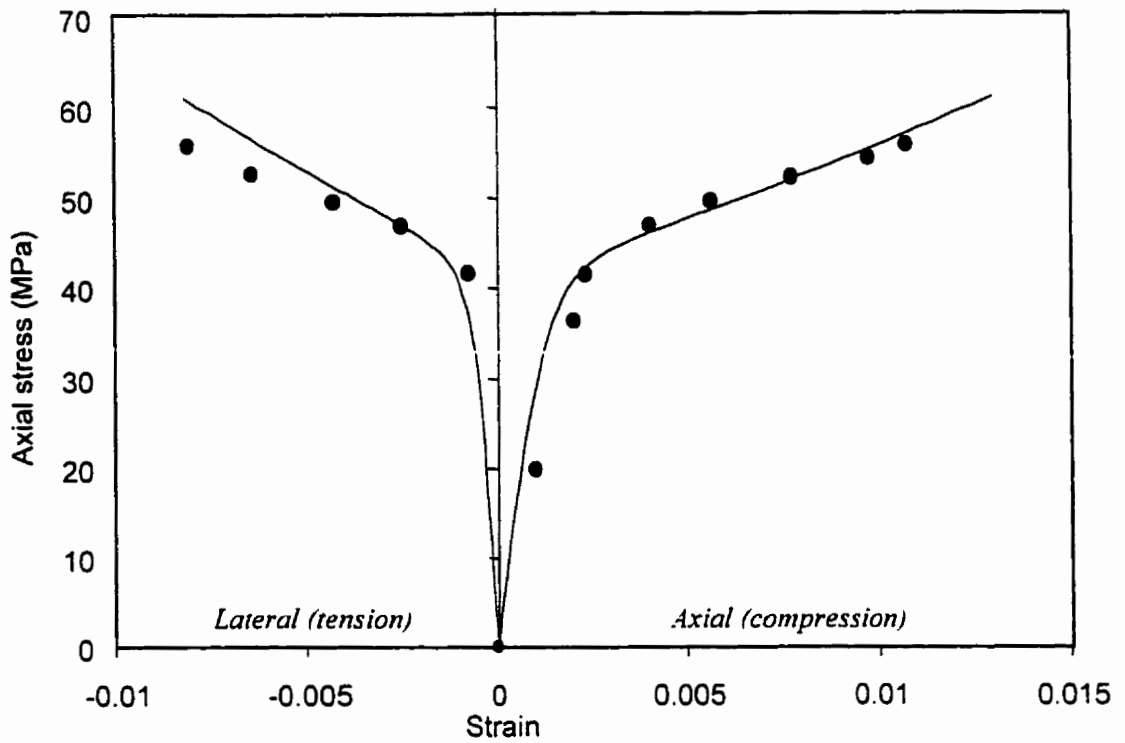


Fig. 5.14 Experimental versus analytical stress-strain response
[Picher and Labossiere 1996]

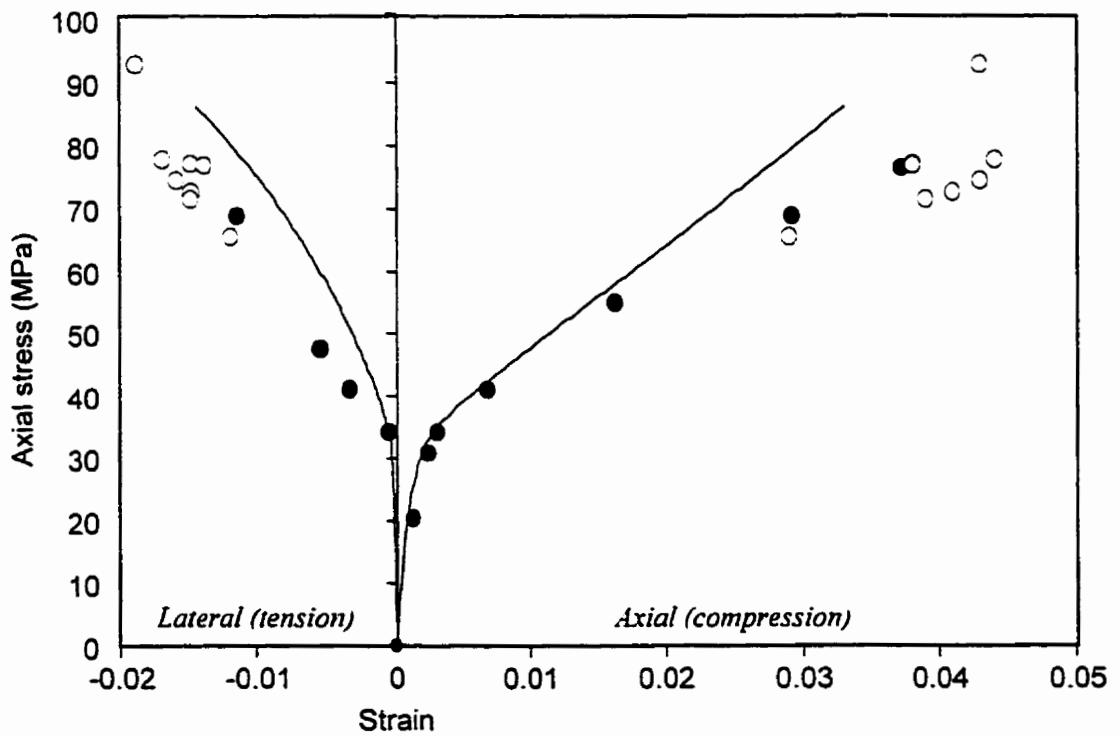
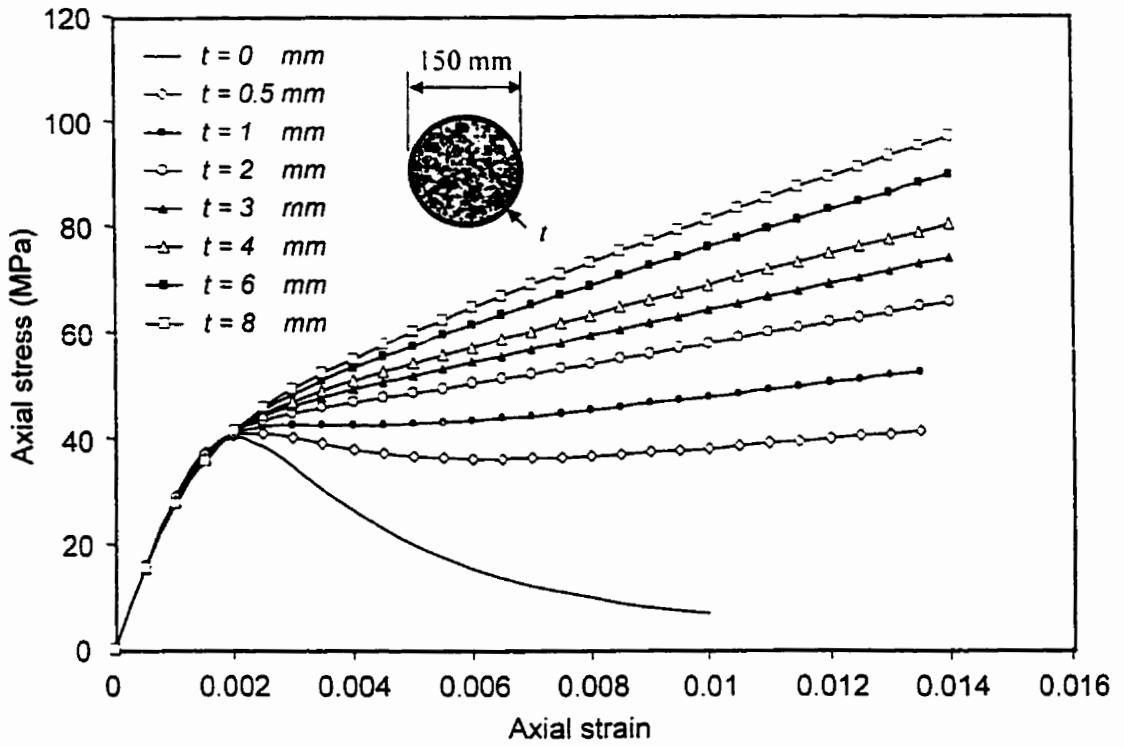
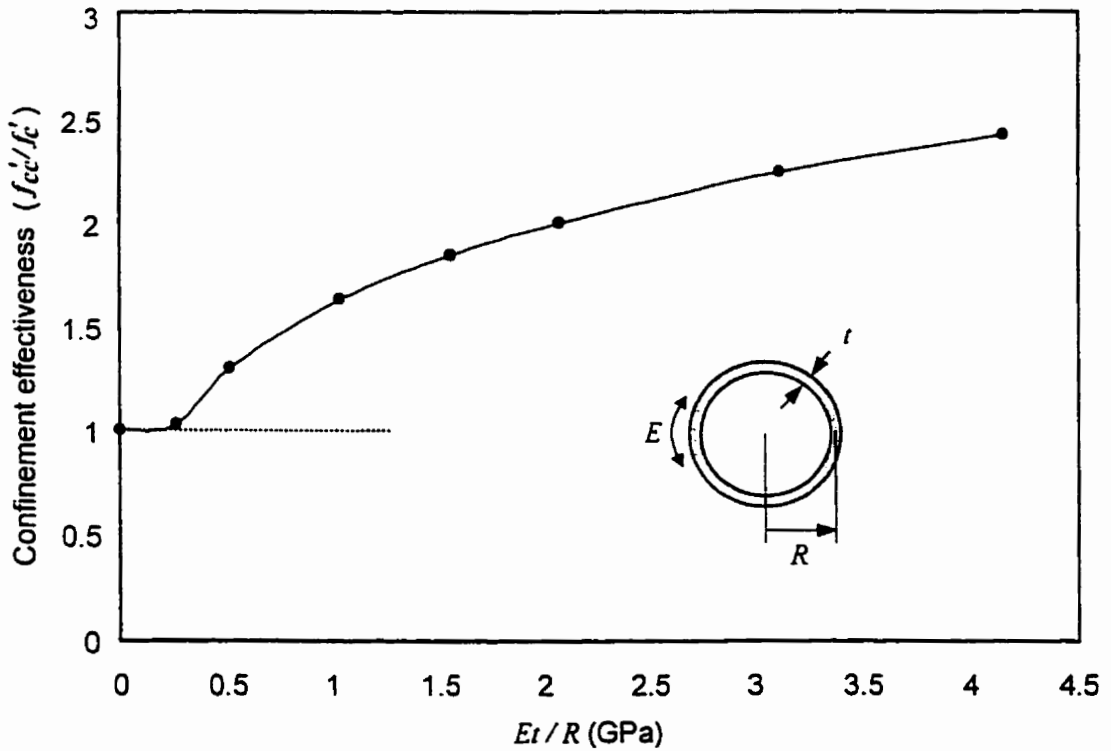


Fig. 5.15 Experimental versus analytical stress-strain response
[Mirmiran and Shahawy 1997]

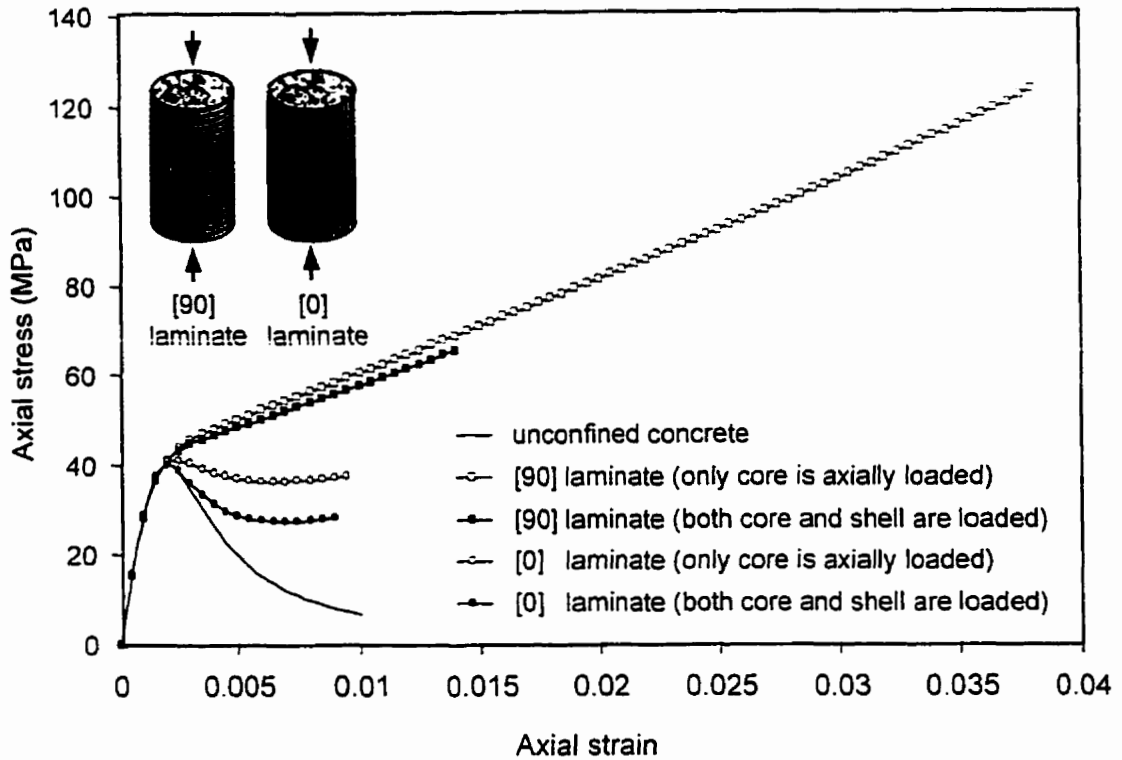


(a) Stress-strain curves of concrete confined using GFRP shells of different thicknesses

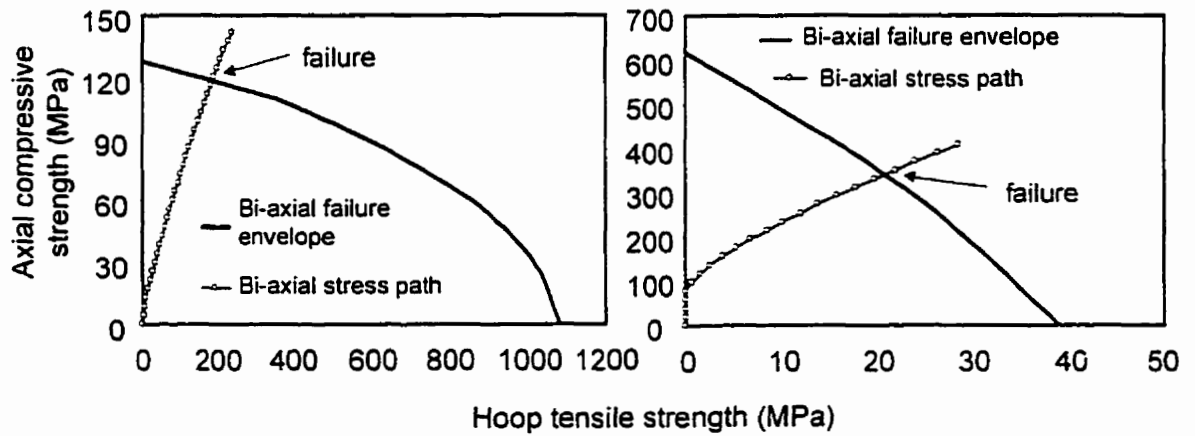


(b) Variation of confinement effectiveness with the stiffness of the shell

Fig. 5.16 Effect of the thickness of GFRP shell on the behaviour of the confined concrete



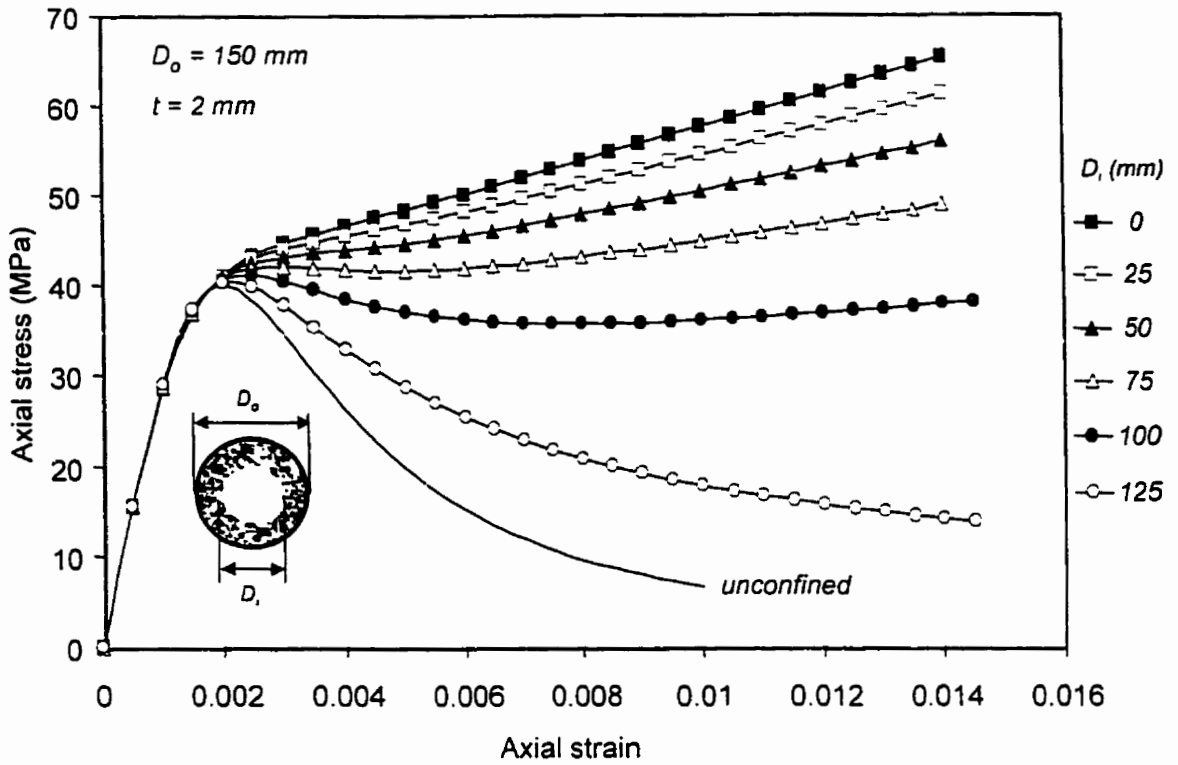
(a) Stress-strain curves of concrete confined using GFRP shells of two different fiber orientations and loading conditions



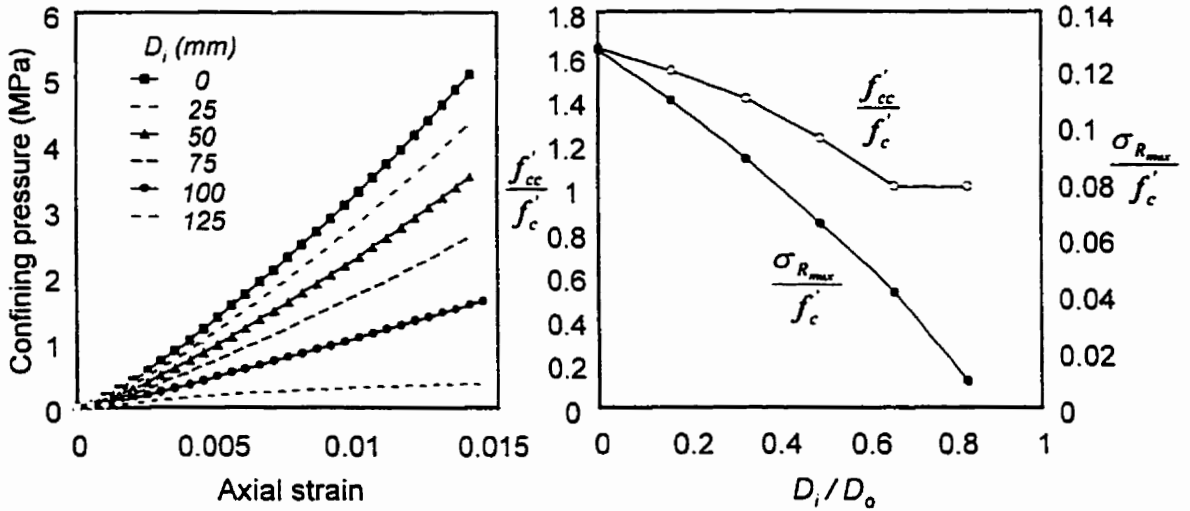
(b) Bi-axial failure envelope for the [90] laminate

(c) Bi-axial failure envelope for the [0] laminate

Fig. 5.17 Effect of fibre orientation within the shell on the behaviour of confined concrete under two different loading conditions



(a) Stress-strain curves of confined concrete with different void sizes



(b) Development of confinement pressure at different axial strain levels

(c) Variation of confinement ratio and confinement effectiveness with void size

Fig. 5.18 Effect of the void size in the concrete core on the confinement level

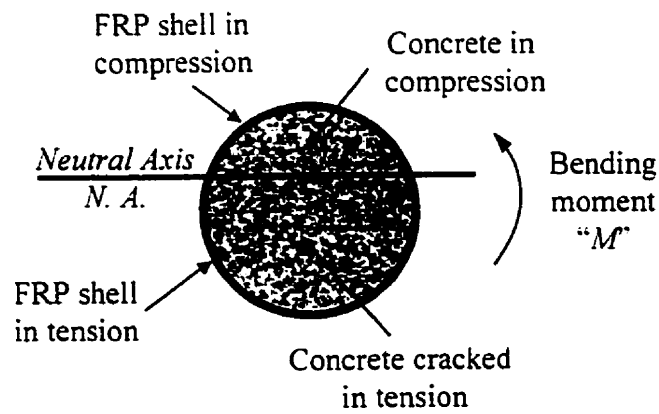
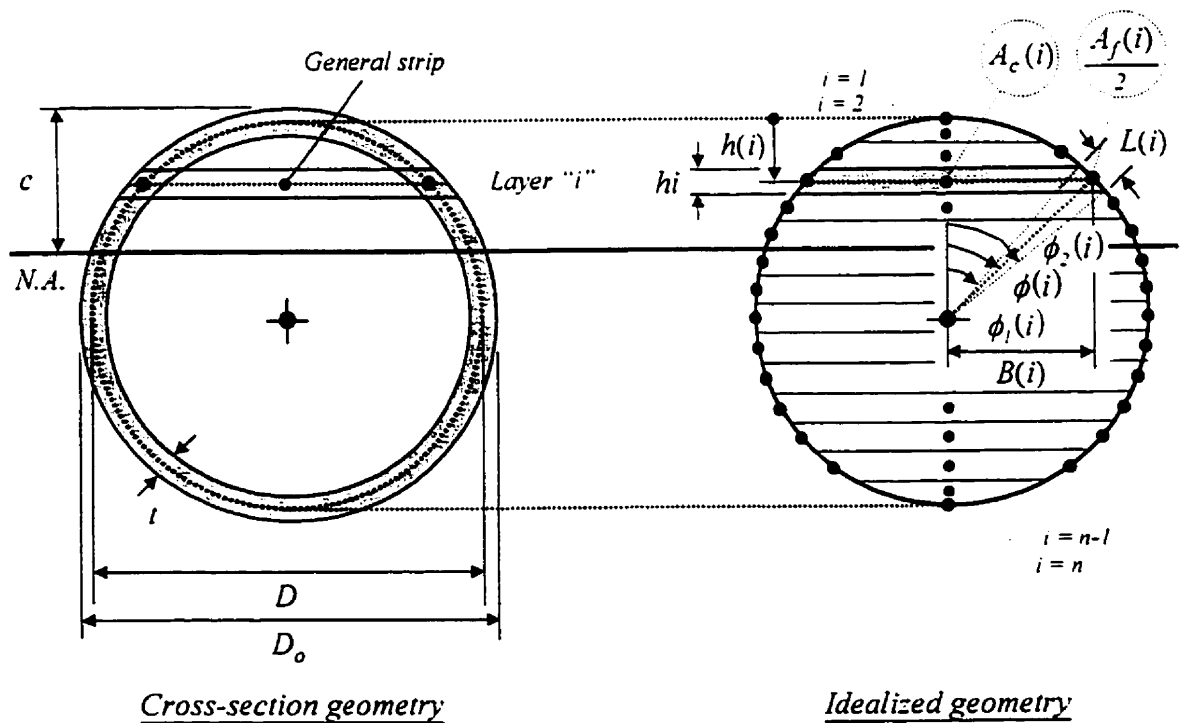


Fig. 5.19 Concrete-filled FRP tube subjected to pure bending



$h_i = \frac{D}{n}$	$D = D_o - t$	$h(i) = h_i (i - 0.5)$	$\phi(i) = \cos^{-1} \left[\frac{0.5D - h(i)}{0.5D} \right]$
$L(i) = 0.5D [\phi_2(i) - \phi_1(i)]$	$B(i) = 0.5D \sin \phi(i)$	$\phi_1(i) = \cos^{-1} \left[\frac{0.5D - h(i) + 0.5h_i}{0.5D} \right]$	
$A_f(i) = 2L(i) t$	$A_c(i) = 2B(i) h_i - 0.5 A_f(i)$	$\phi_2(i) = \cos^{-1} \left[\frac{0.5D - h(i) - 0.5h_i}{0.5D} \right]$	

Fig. 5.20 Geometry of the problem

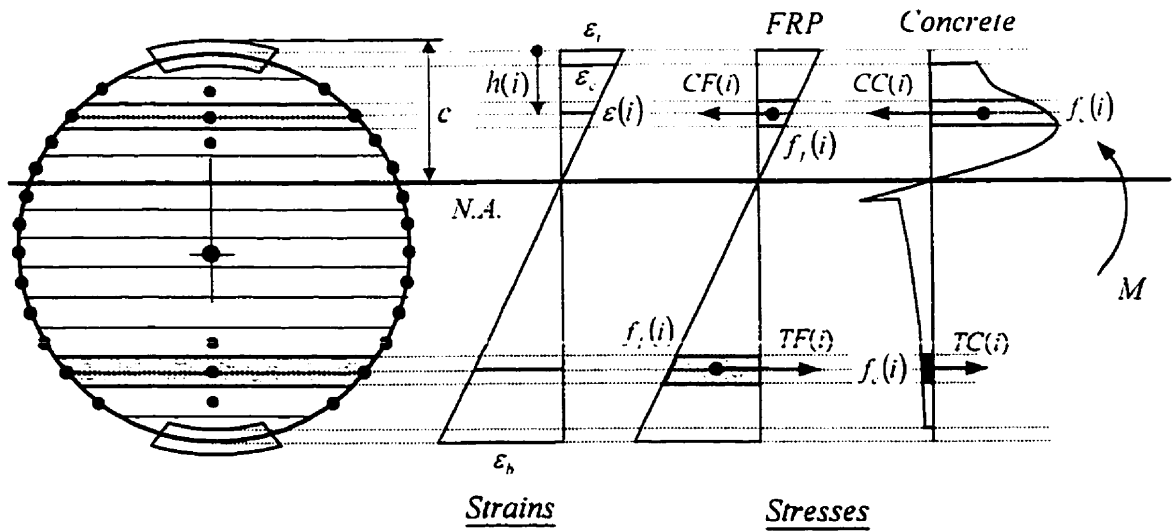


Fig. 5.21 Stress and strain distributions along the depth of the section

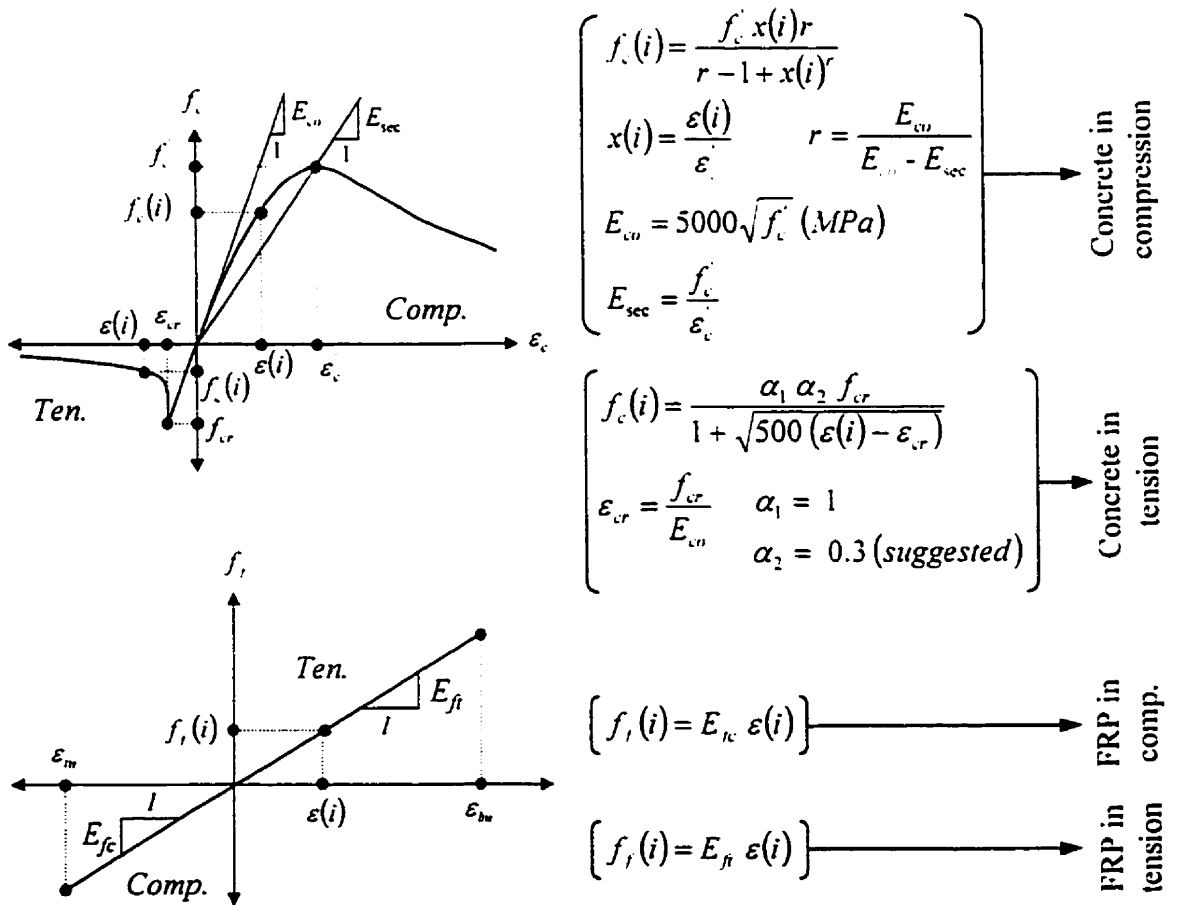


Fig. 5.22 Constitutive relationships for the concrete core and FRP shell

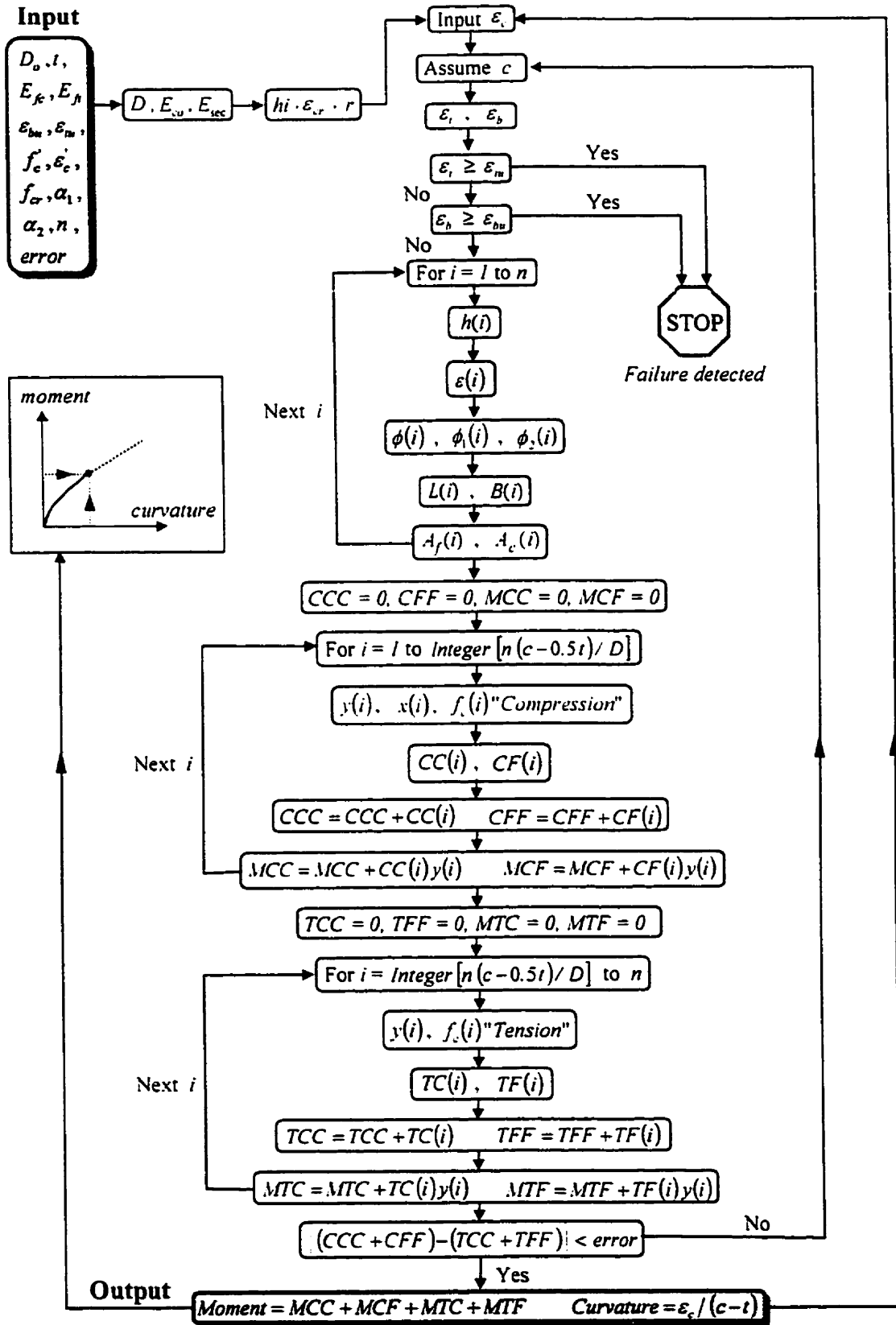


Fig. 5.23 Flowchart of the analytical model used to predict the moment-curvature response of concrete-filled FRP tubes

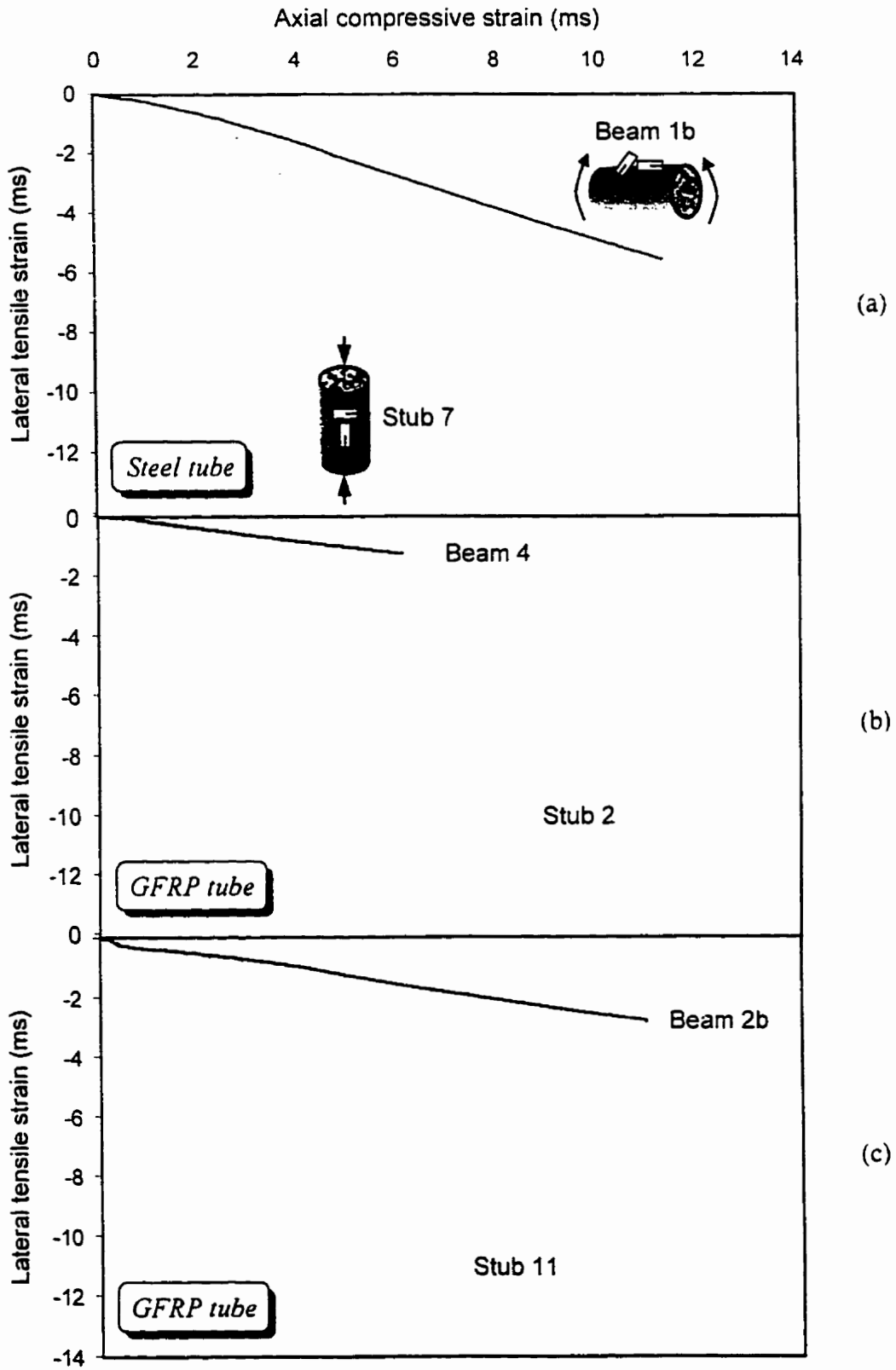


Fig. 5.26 Comparison between axial-lateral strain behaviour in beams and stubs

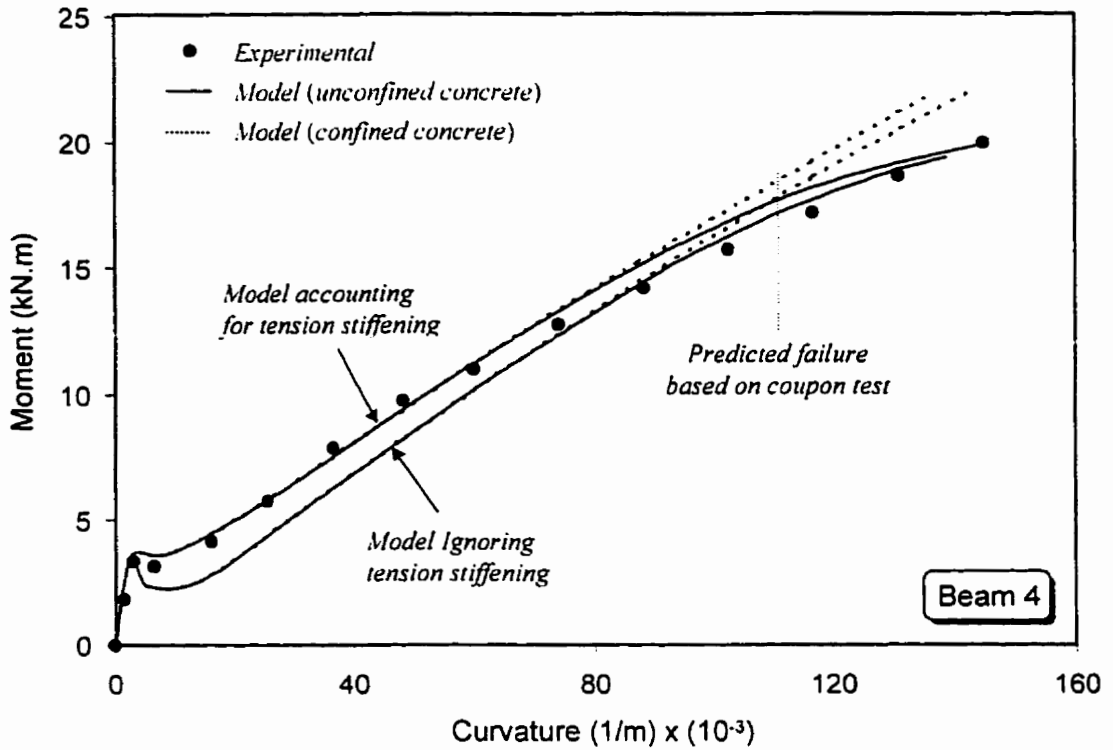


Fig. 5.27 Predicted versus experimental moment-curvature behaviour of beam 4

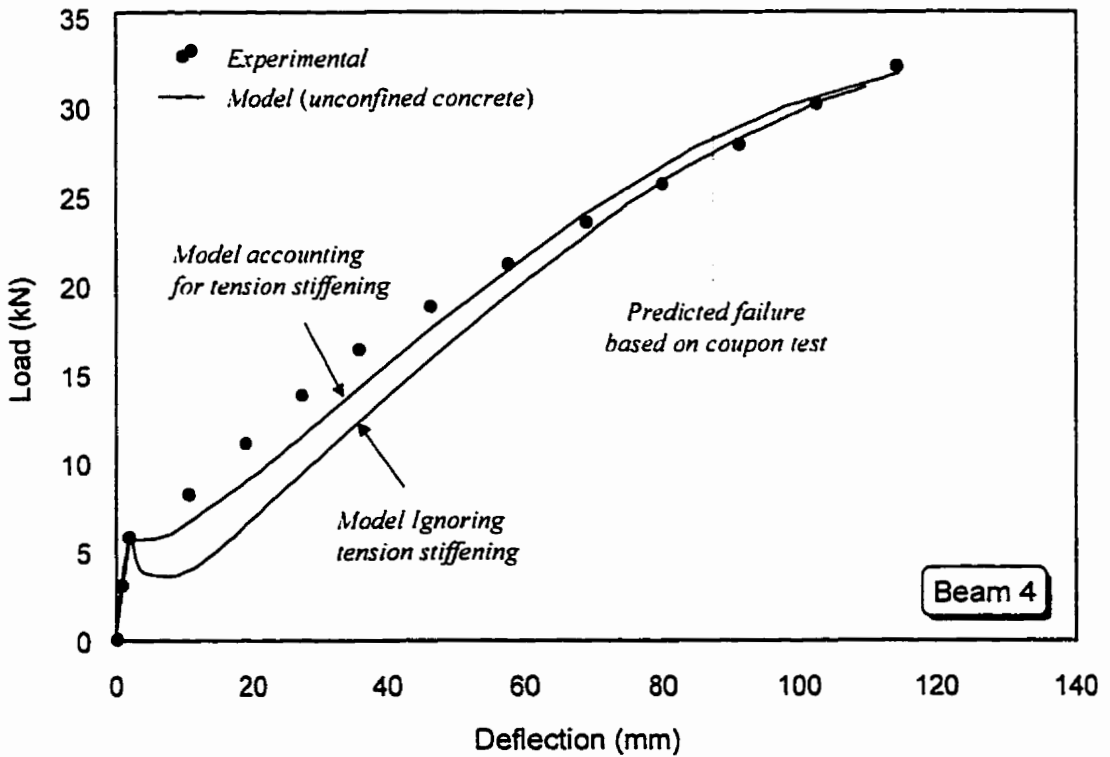


Fig. 5.28 Predicted versus experimental load-deflection behaviour of beam 4

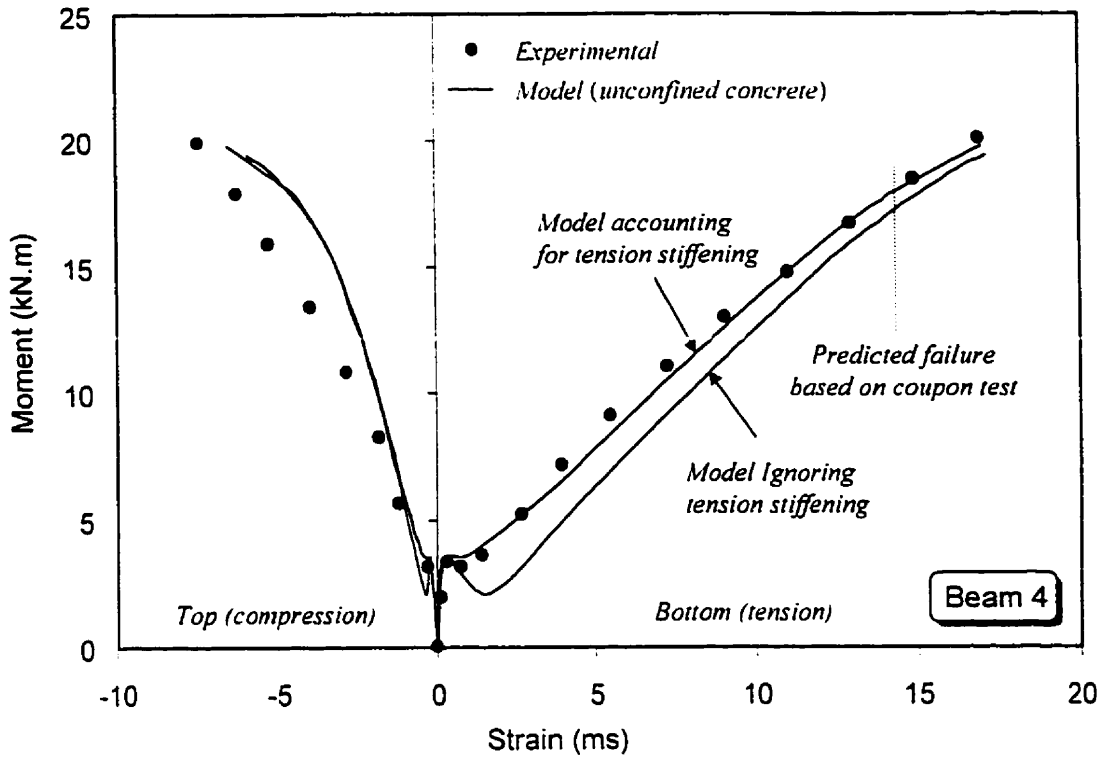


Fig. 5.29 Predicted versus experimental moment-strain behaviour of beam 4

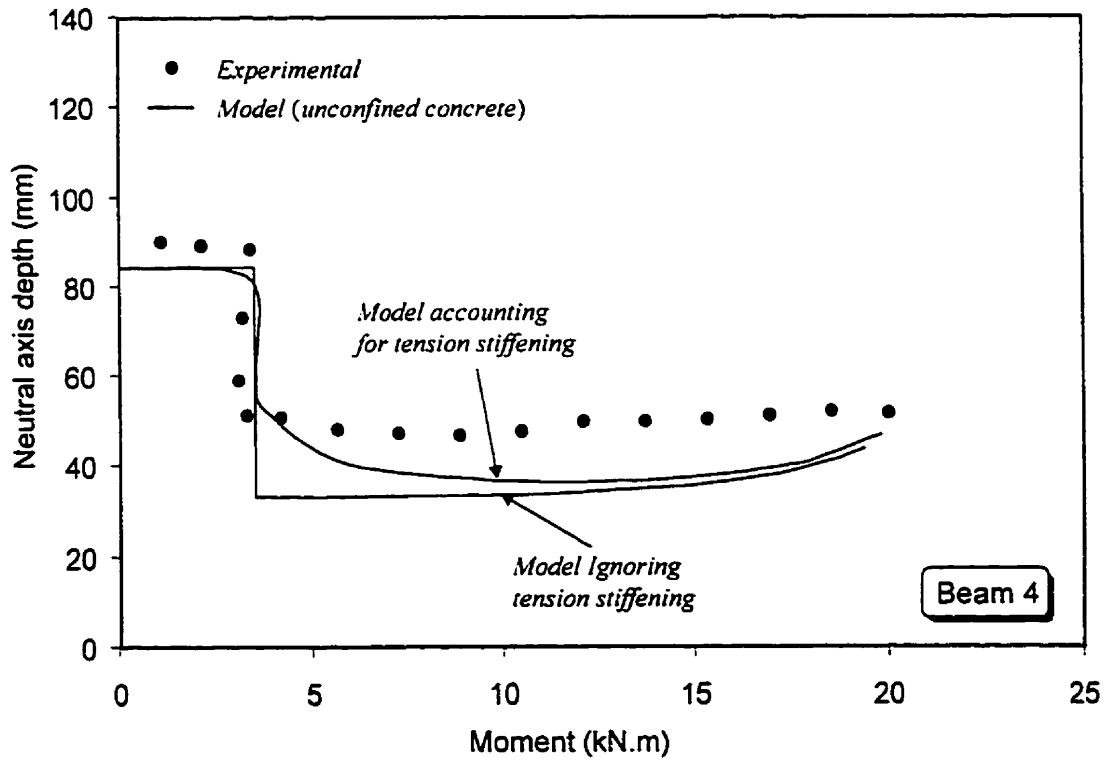


Fig. 5.30 Predicted versus experimental variation of the neutral axis depth of beam 4

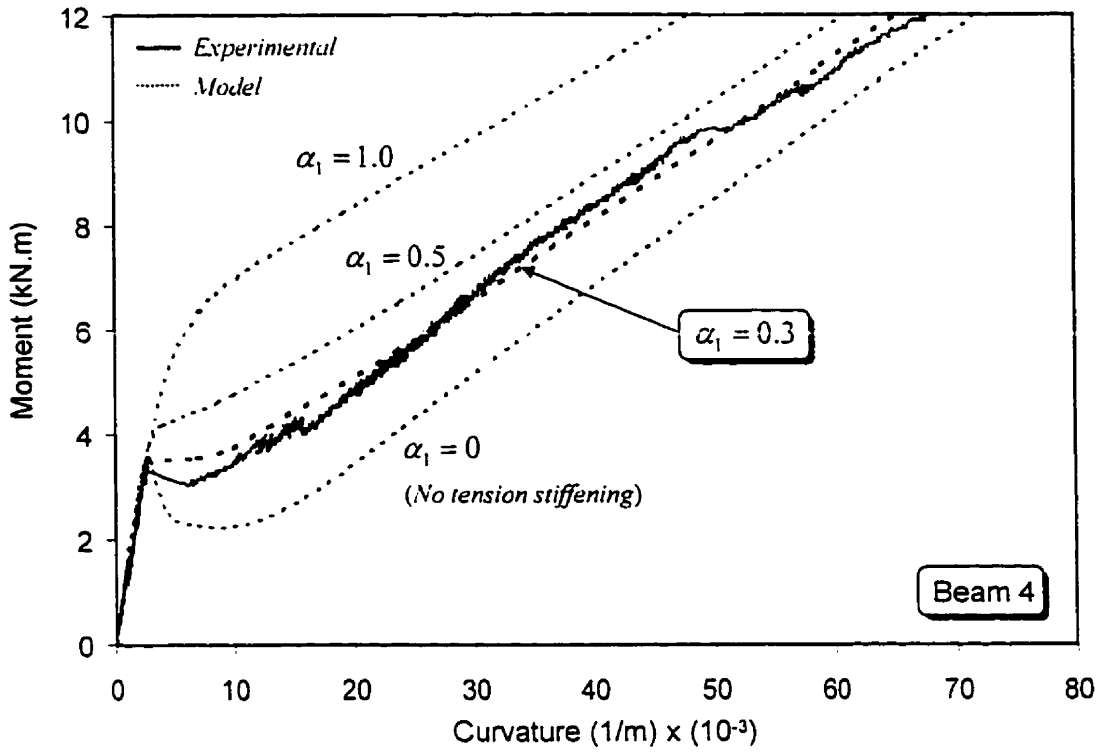


Fig. 5.31 Effect of bond factor α_1 on tension stiffening level

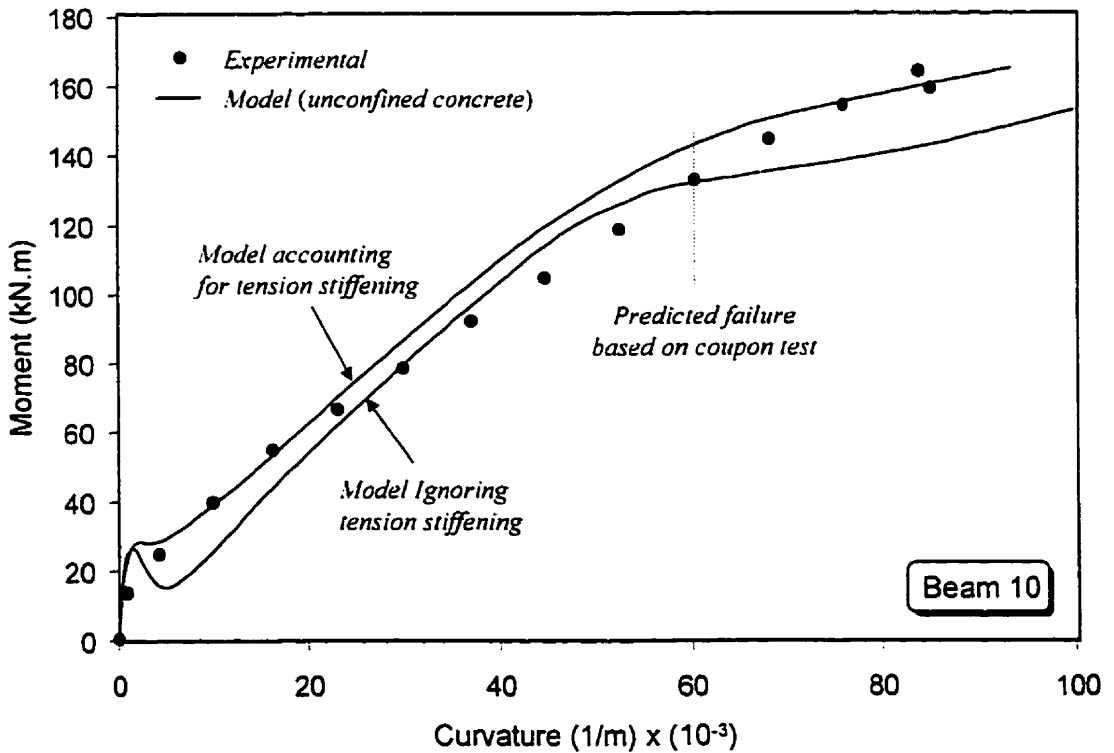


Fig. 5.32 Predicted versus experimental moment-curvature behaviour of beam 10

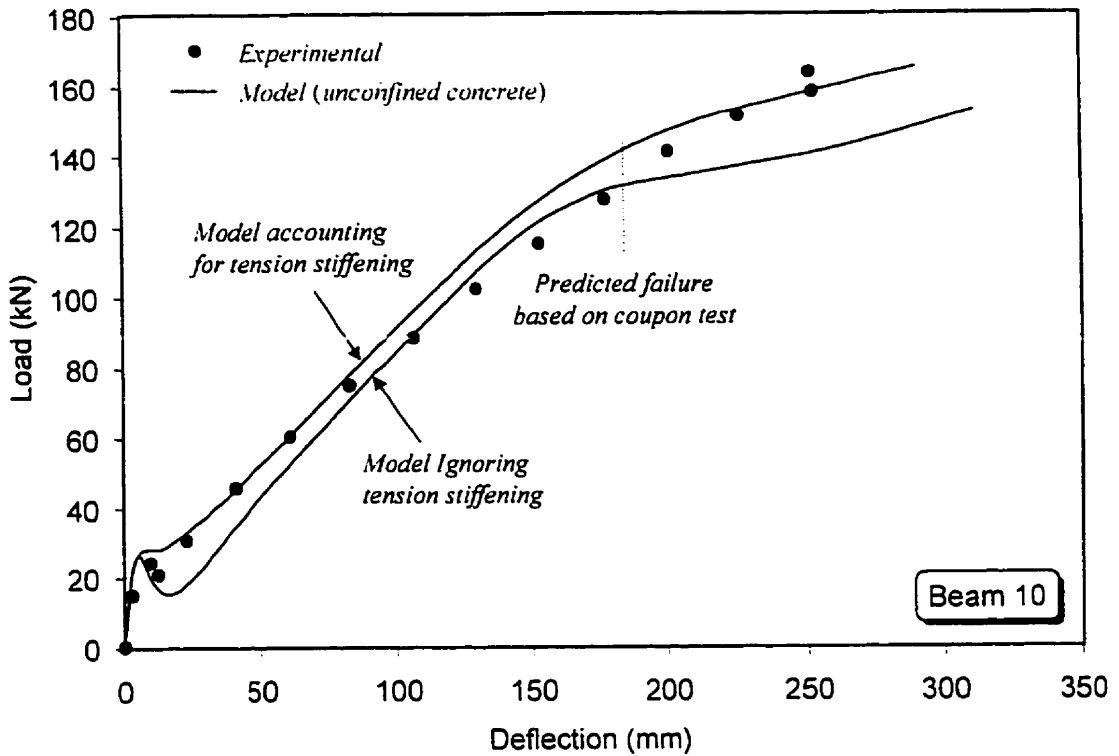


Fig. 5.33 Predicted versus experimental load-deflection behaviour of beam 10

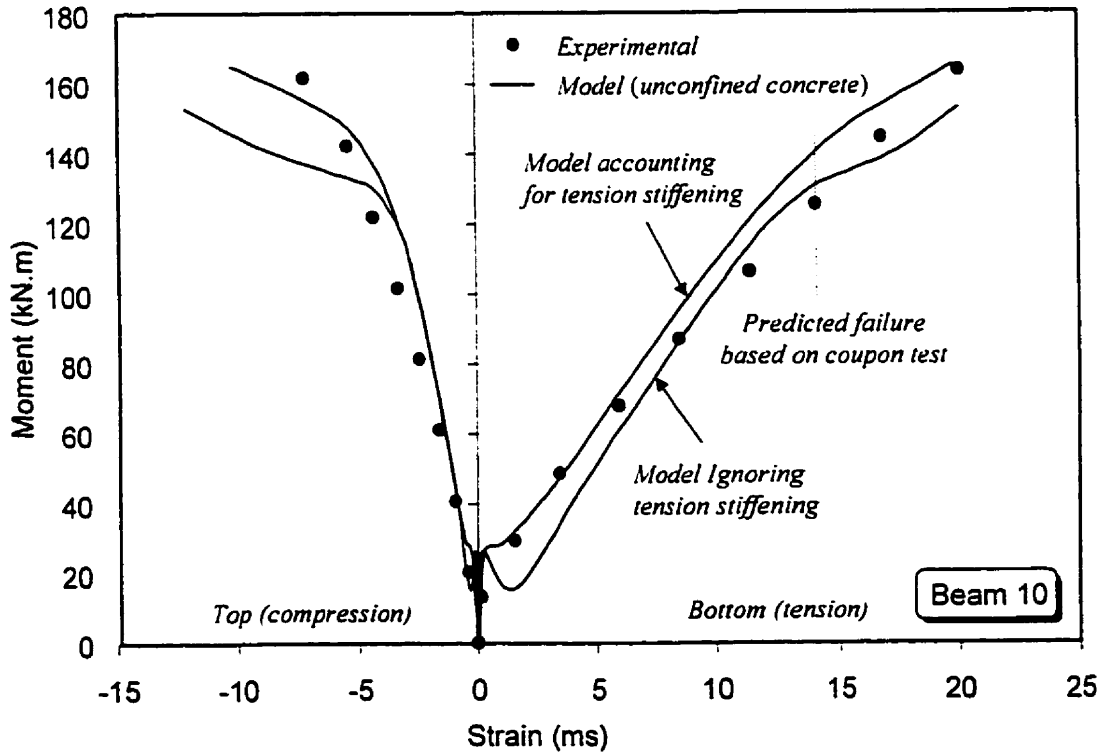


Fig. 5.34 Predicted versus experimental moment-strain behaviour of beam 10

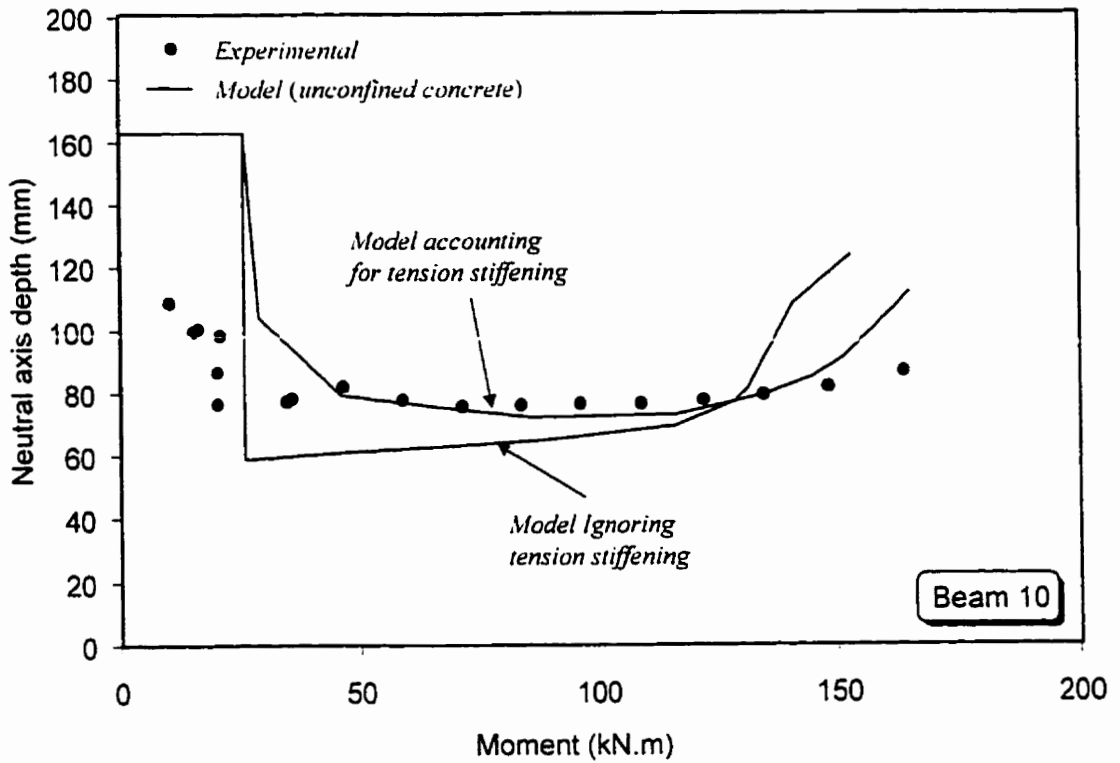


Fig. 5.35 Predicted versus experimental variation of the neutral axis depth for beam 10

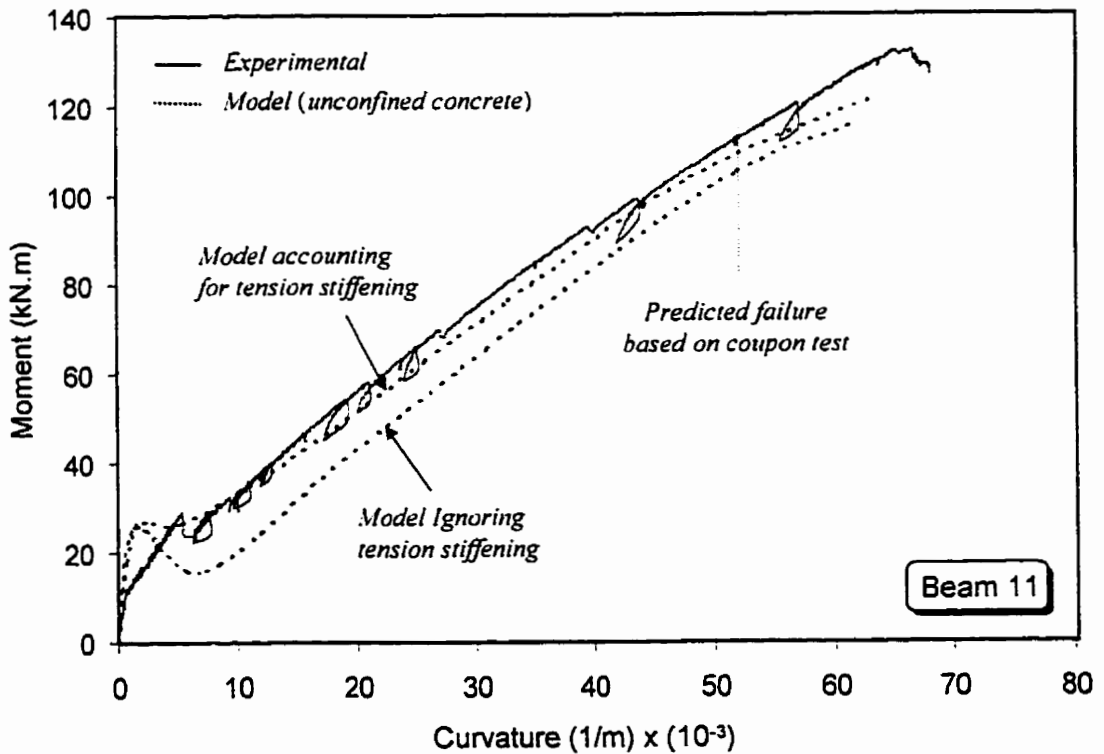


Fig. 5.36 Predicted versus experimental moment-curvature behaviour of beam 11

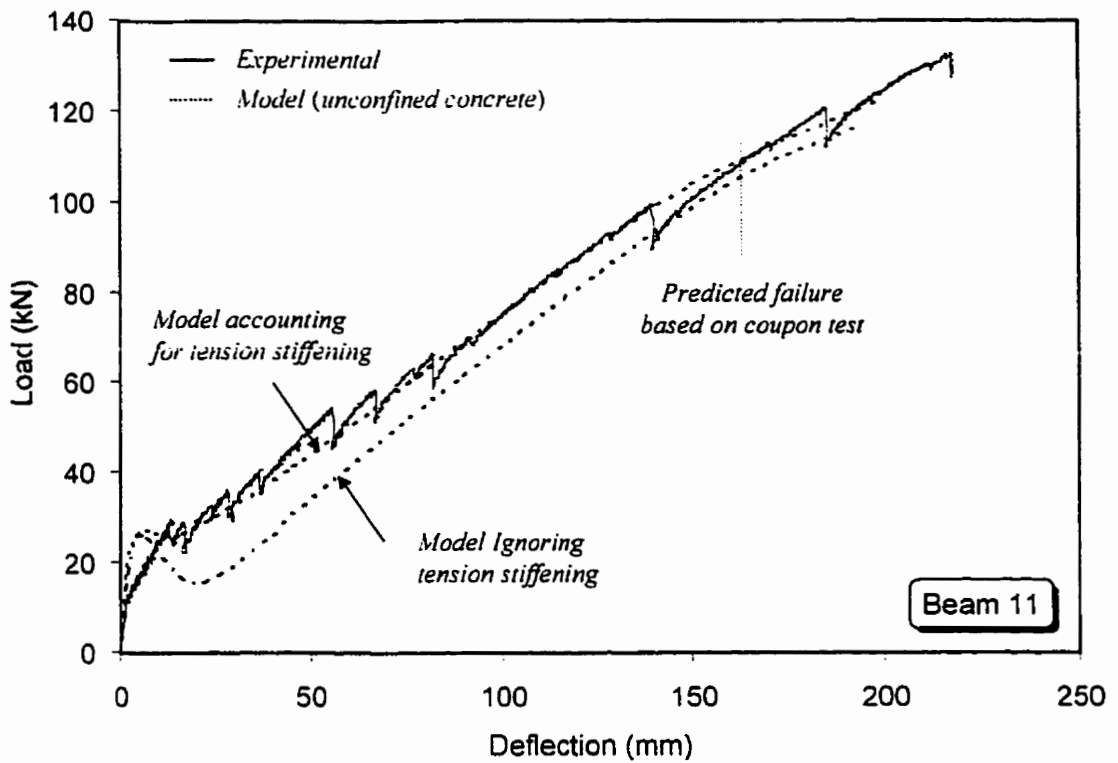


Fig. 5.37 Predicted versus experimental load-deflection behaviour of beam 11

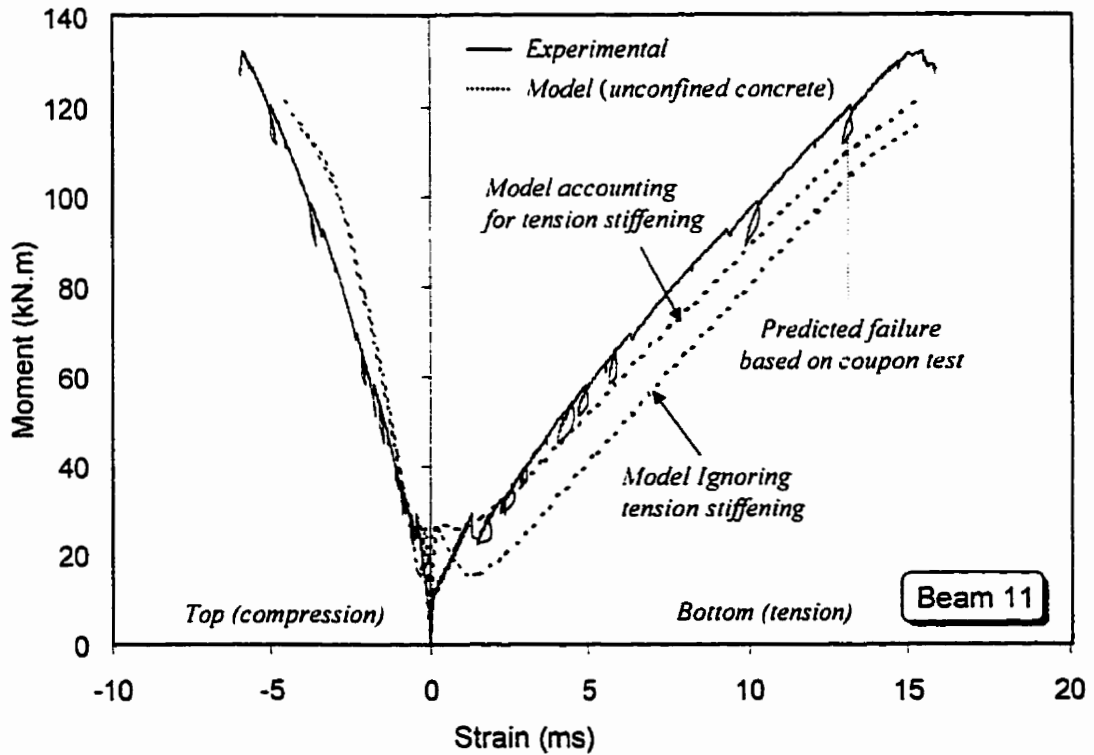


Fig. 5.38 Predicted versus experimental moment-strain behaviour of beam 11

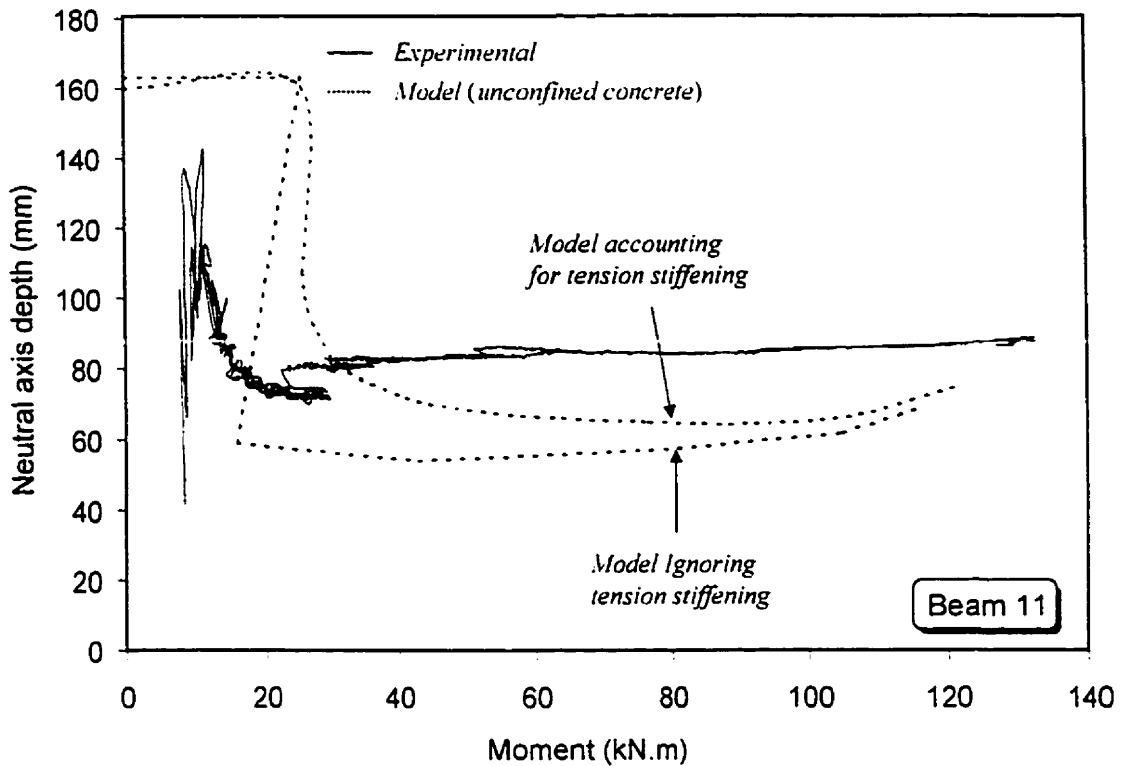


Fig. 5.39 Predicted versus experimental variation of the neutral axis depth for beam 11

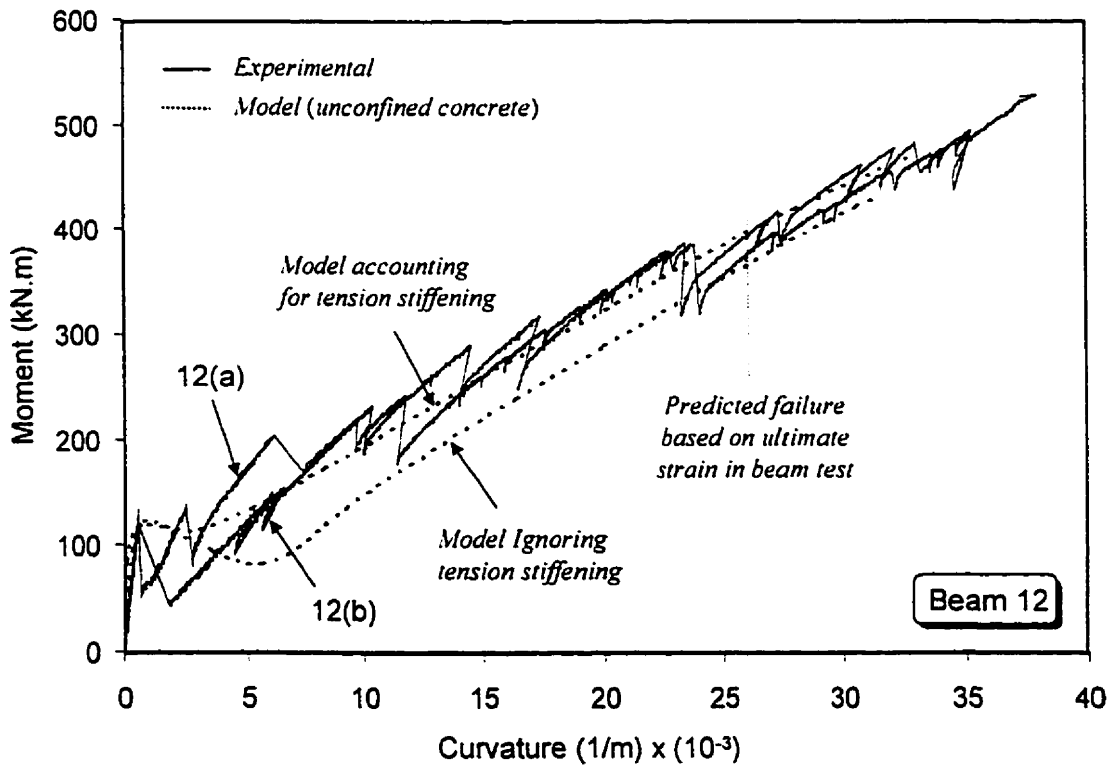


Fig. 5.40 Predicted versus experimental moment-curvature behaviour of beam 12

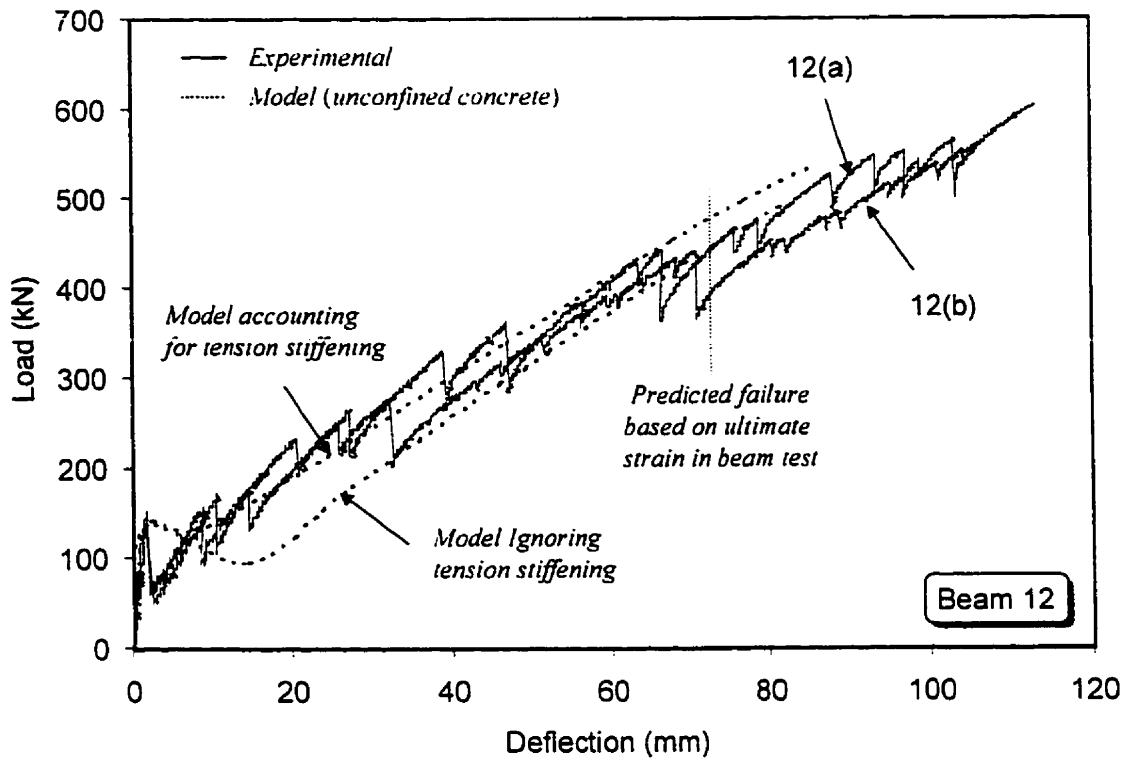


Fig. 5.41 Predicted versus experimental load-deflection behavior of beam 12

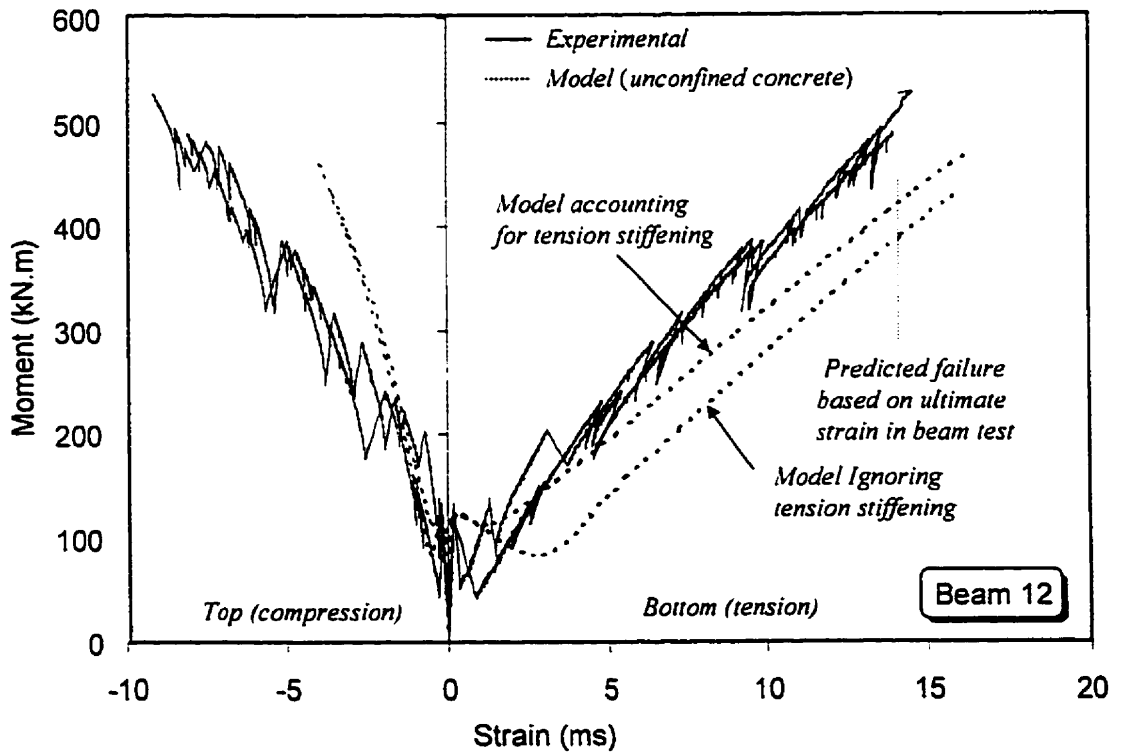


Fig. 5.42 Predicted versus experimental moment-strain behaviour of beam 12

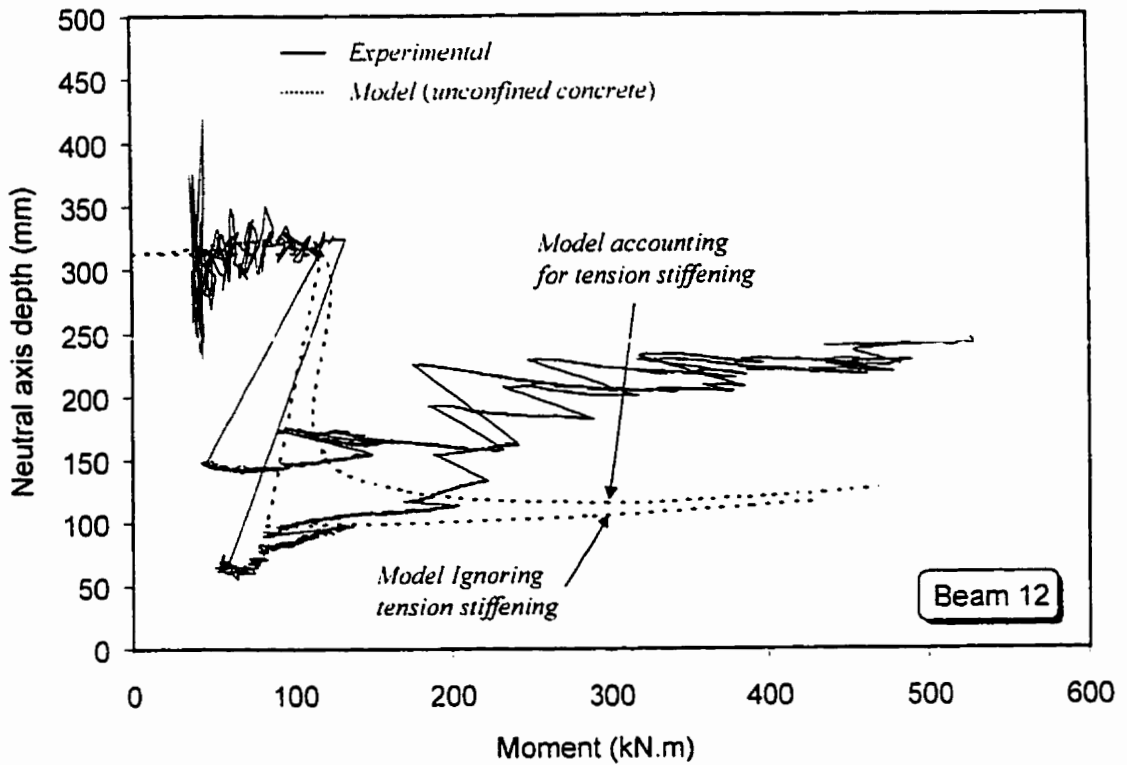


Fig. 5.43 Predicted versus experimental variation of the neutral axis depth for beam 12

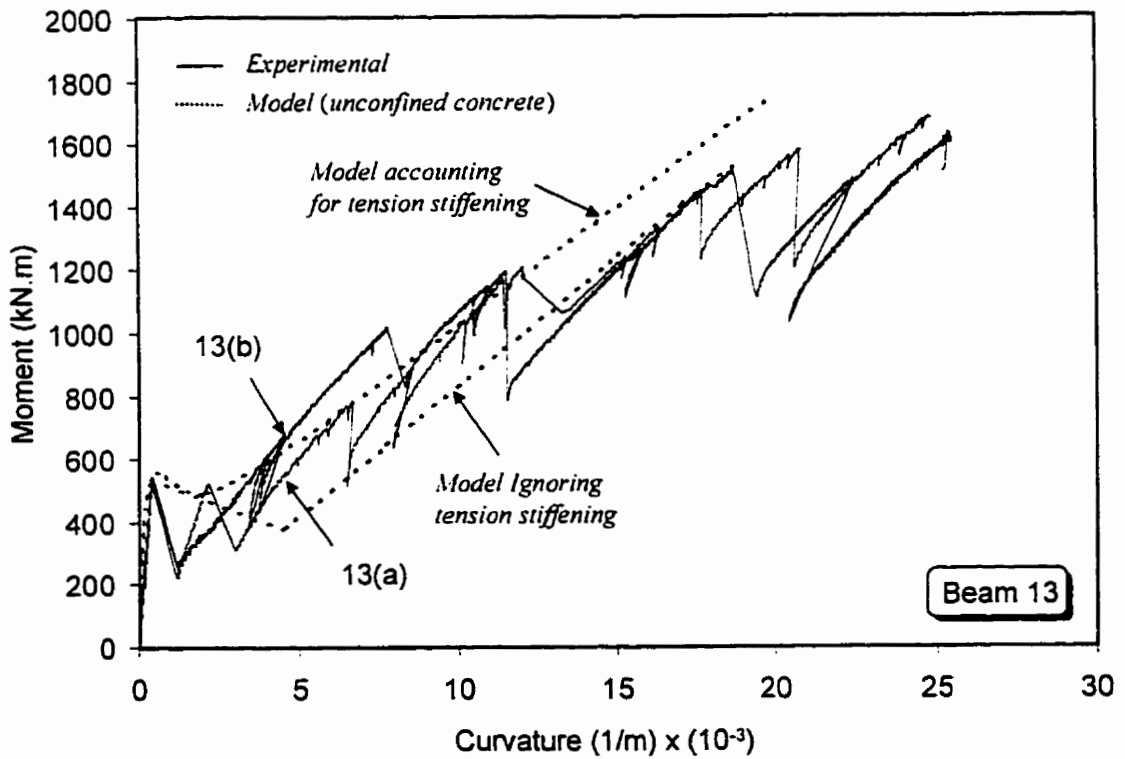


Fig. 5.44 Predicted versus experimental moment-curvature behaviour of beam 13

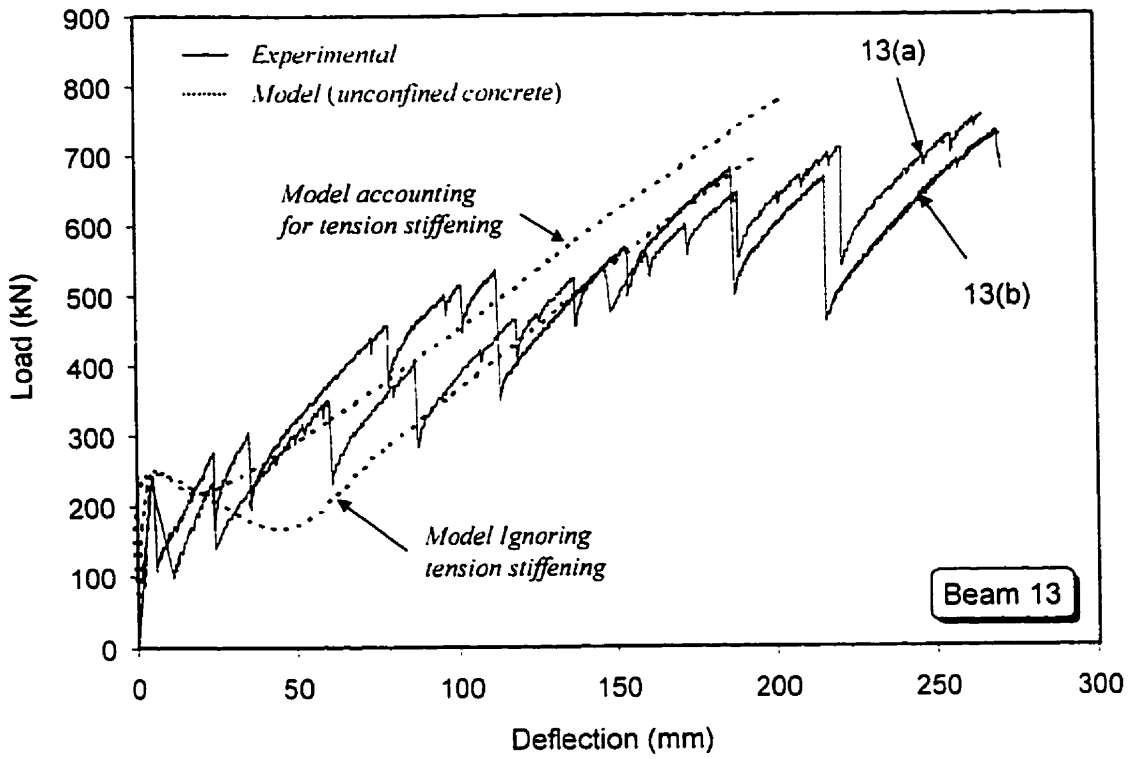


Fig. 5.45 Predicted versus experimental load-deflection behaviour of beam 13

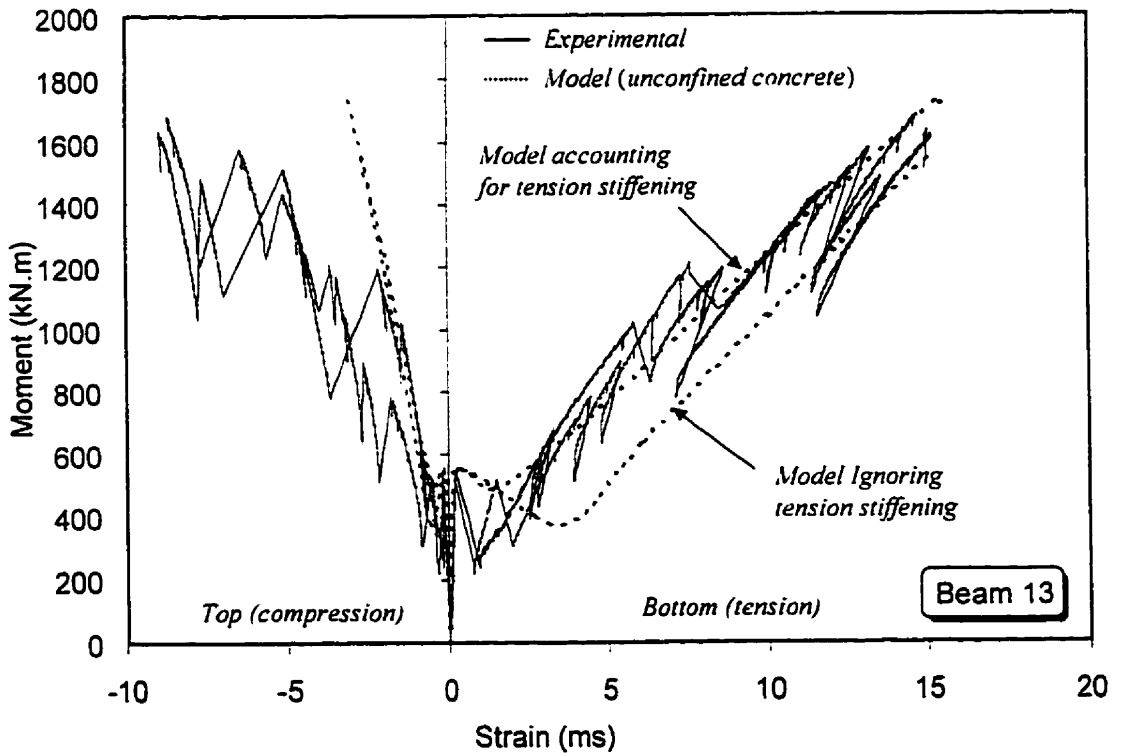


Fig. 5.46 Predicted versus experimental moment-strain behaviour of beam 13

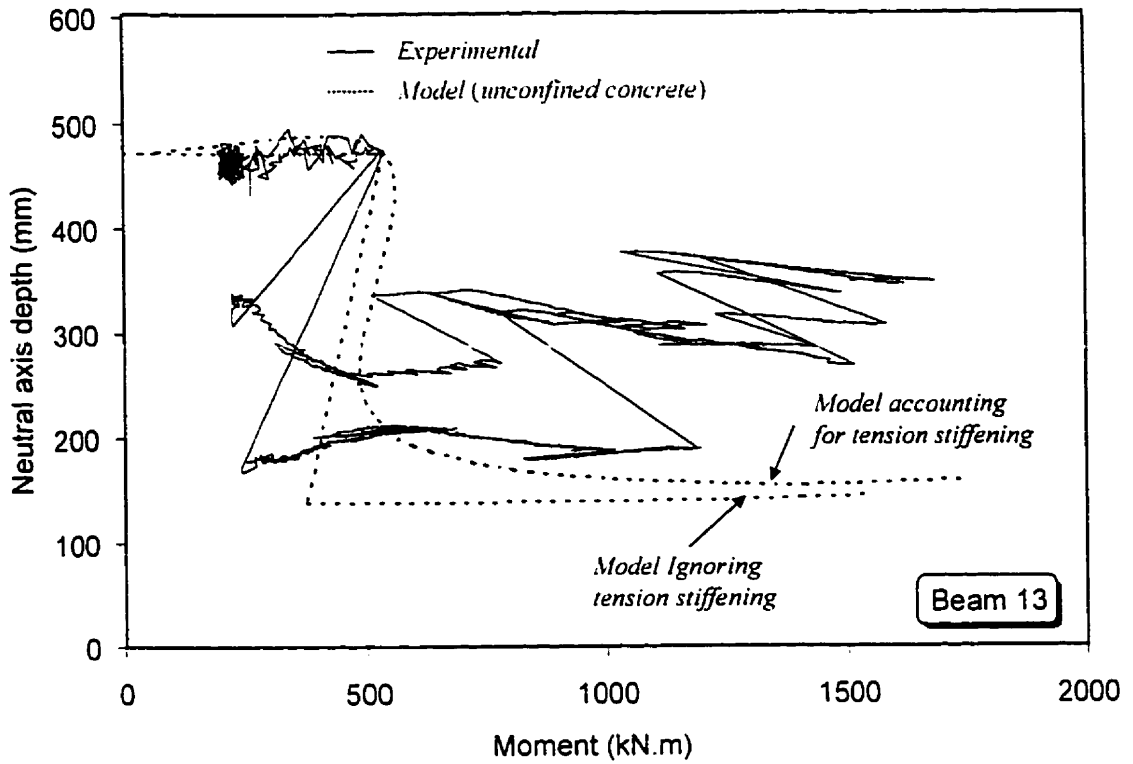


Fig. 5.47 Predicted versus experimental variation of the neutral axis depth for beam 13

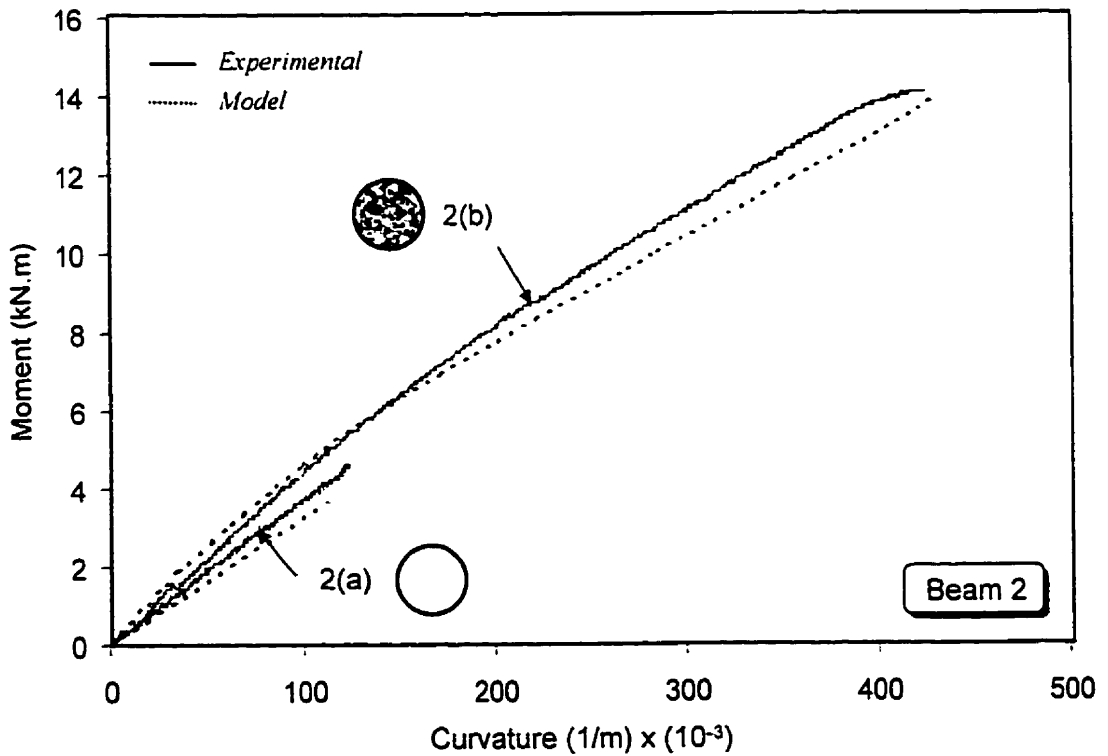
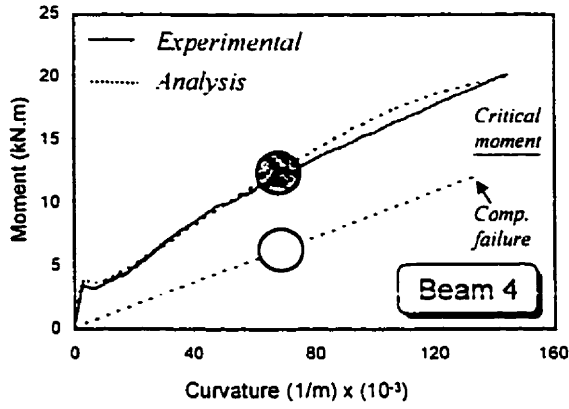
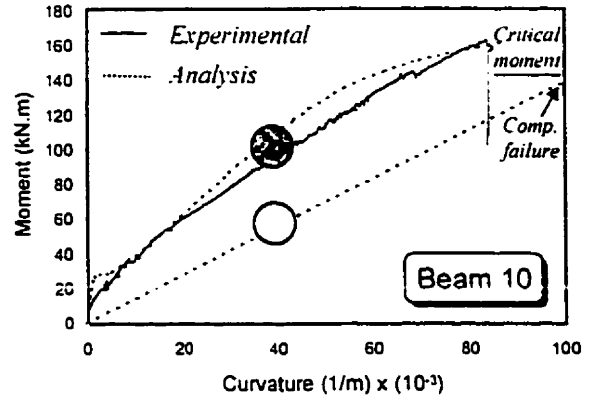


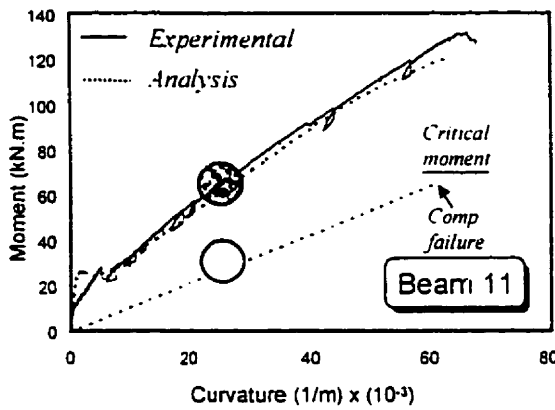
Fig. 5.48 Predicted versus experimental moment-curvature response of beams 2 (a and b)



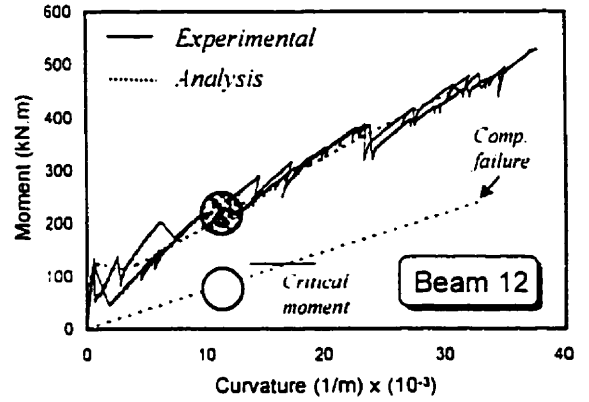
(a)



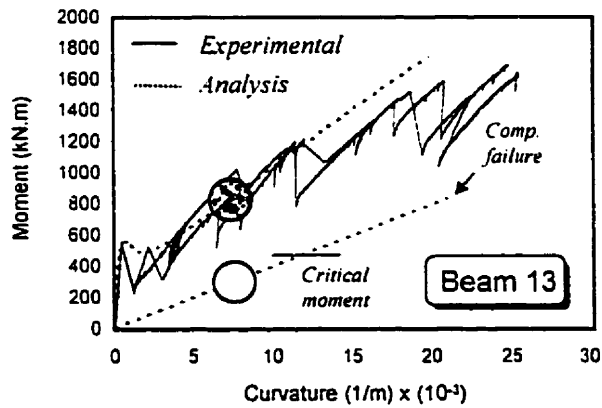
(b)



(c)



(d)



(e)

Fig. 5.49 Moment-curvature response of hollow and concrete-filled tubes for beams 4, 10, 11, 12, and 13

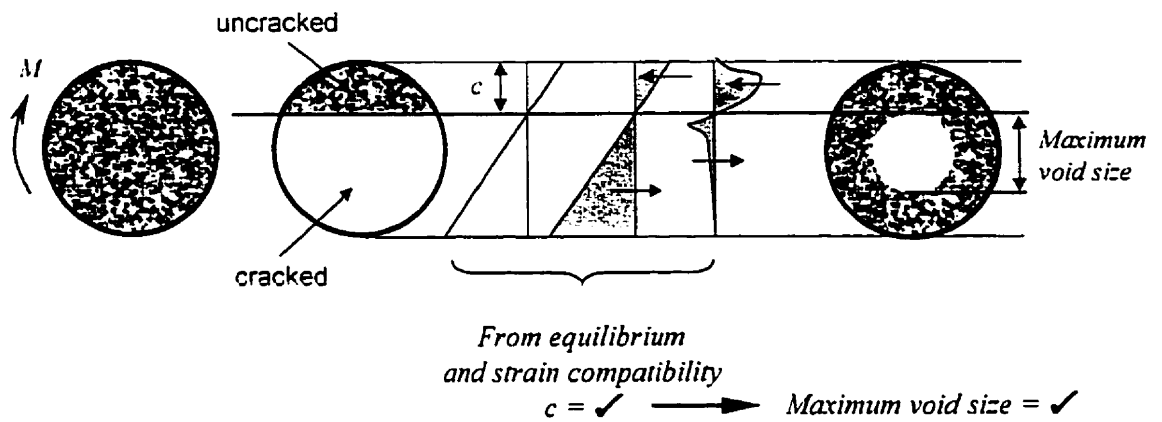


Fig. 5.50 Optimization of void size in flexural members for minimizing the self-weight

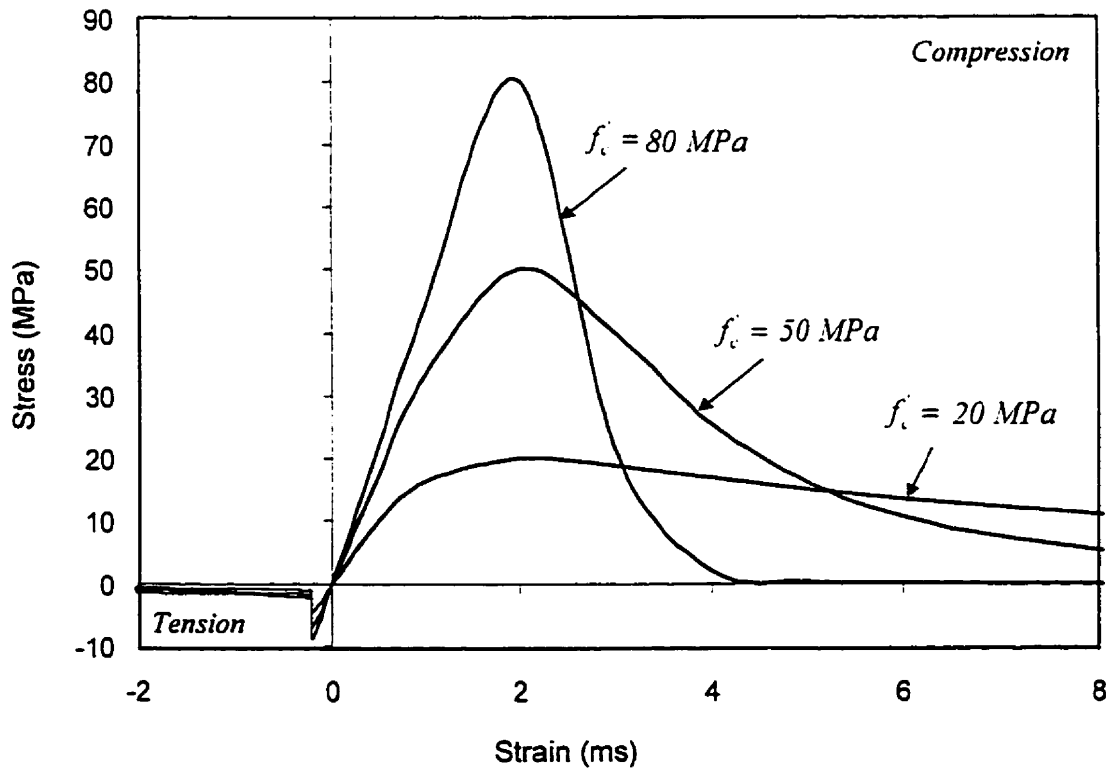


Fig. 5.51 Stress-strain curves of the concrete used in the parametric study

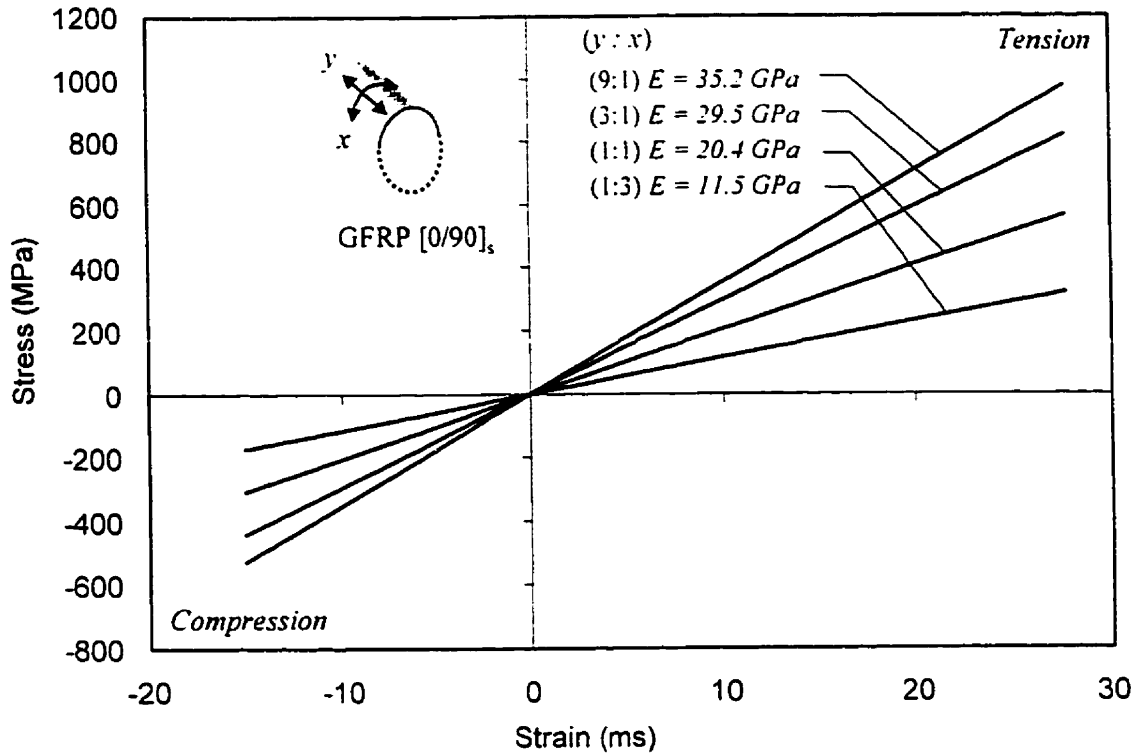


Fig. 5.52 Stress-strain curves for the [0/90] laminates used in the parametric study

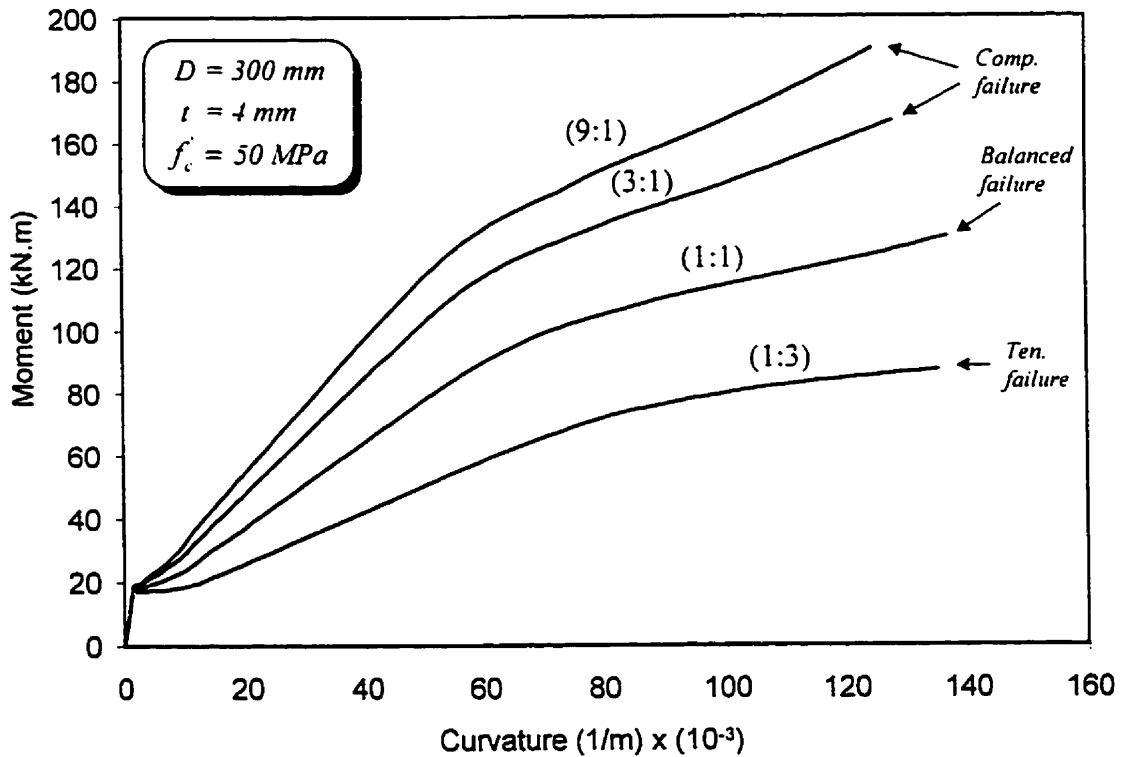


Fig. 5.53 Effect of laminate structure of the tube on the moment-curvature response

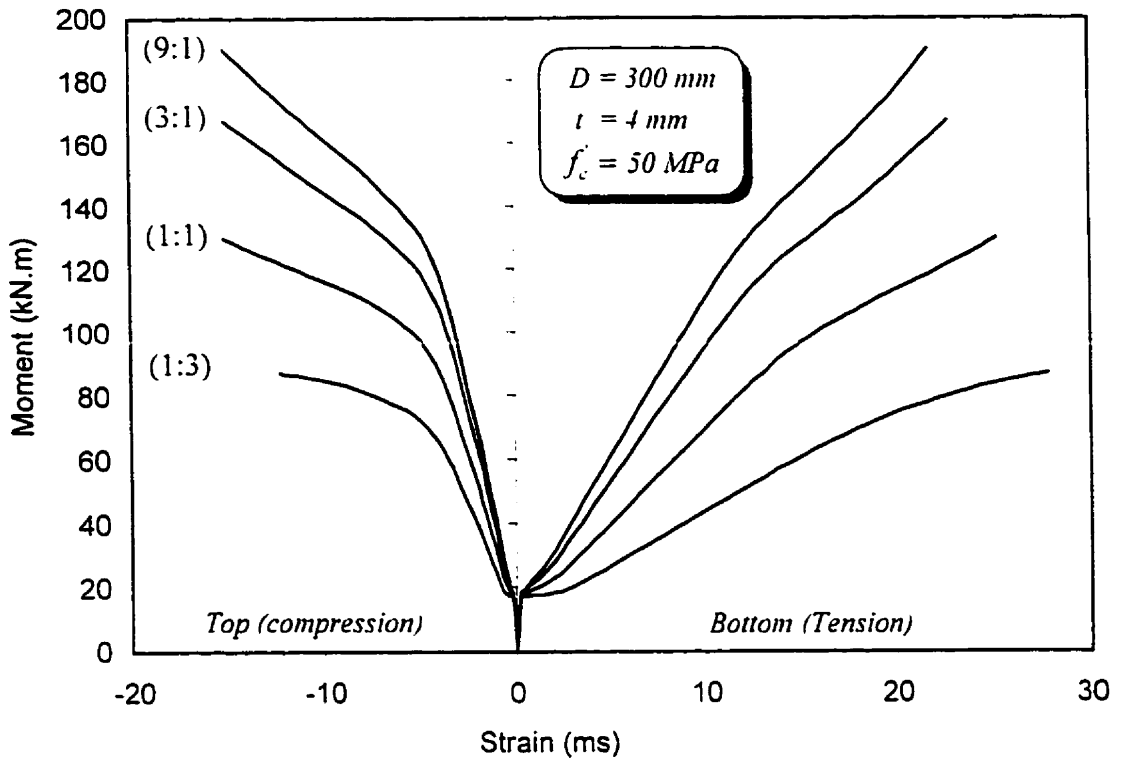


Fig. 5.54 Effect of laminate structure of the tube on the moment-strain behaviour

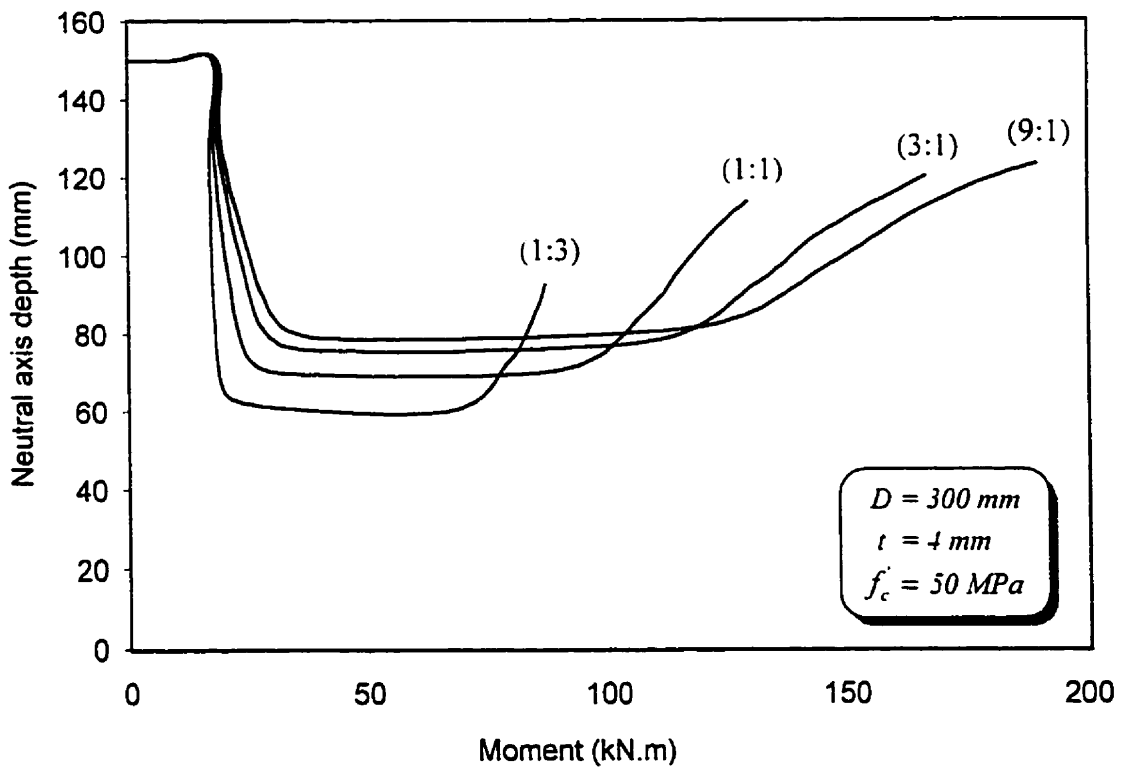


Fig. 5.55 Effect of laminate structure of the tube on the variation of neutral axis depth

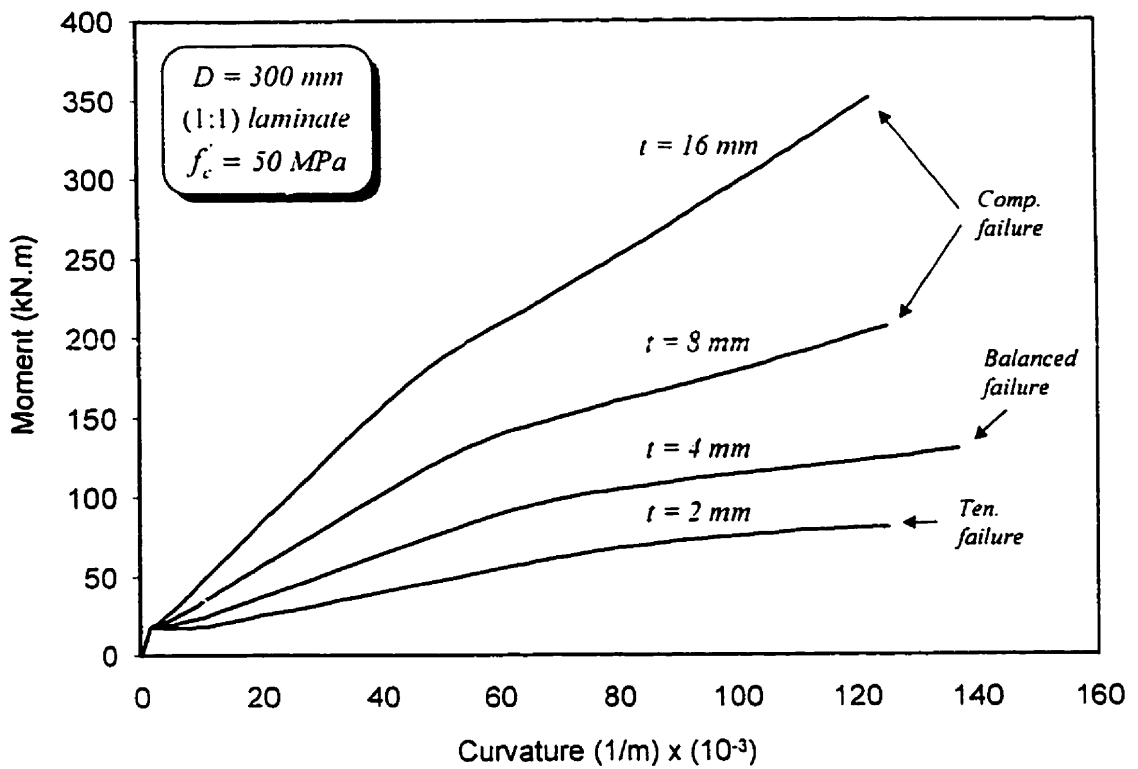


Fig. 5.56 Effect of wall thickness of the tube on moment-curvature response

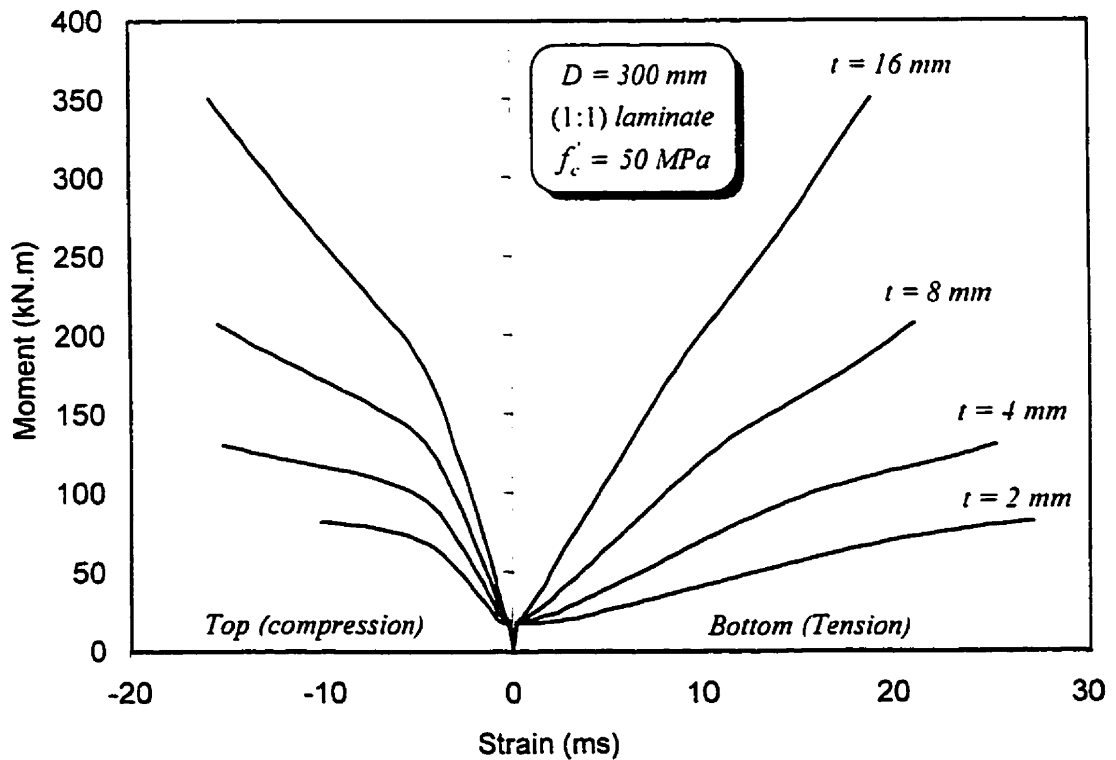


Fig. 5.57 Effect of wall thickness of the tube on moment-strain behaviour

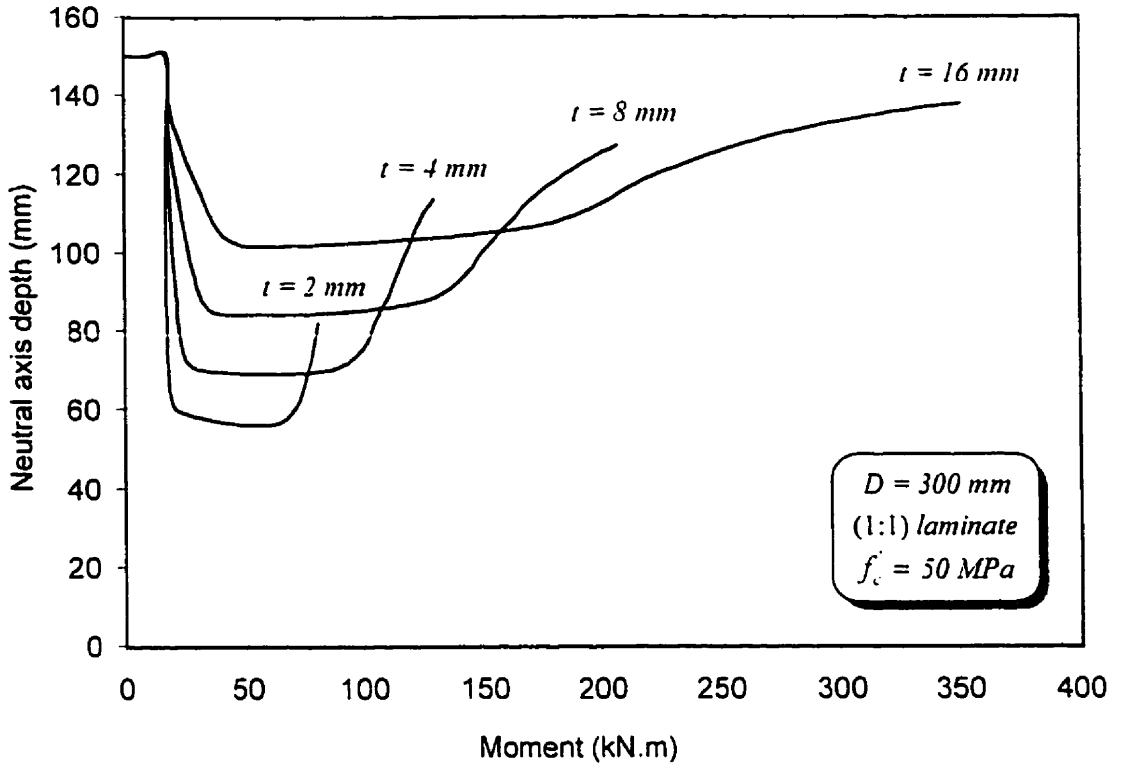


Fig. 5.58 Effect of wall thickness of the tube on variation of the neutral axis depth

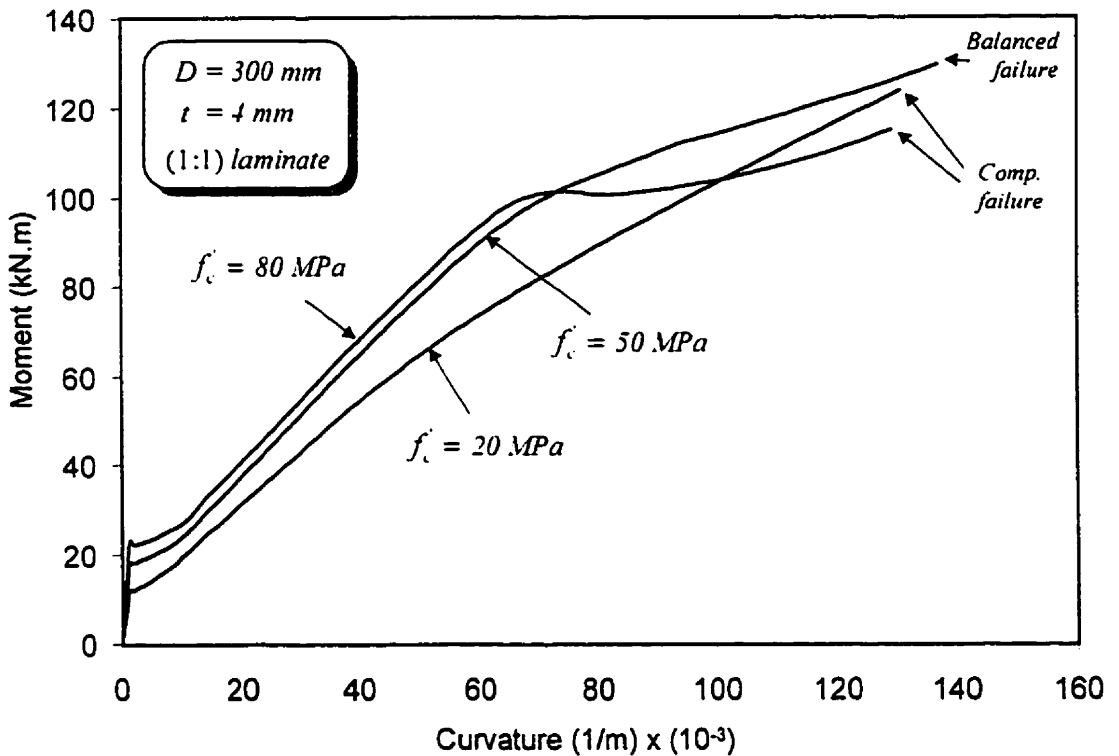


Fig. 5.59 Effect of concrete strength on the moment-curvature response

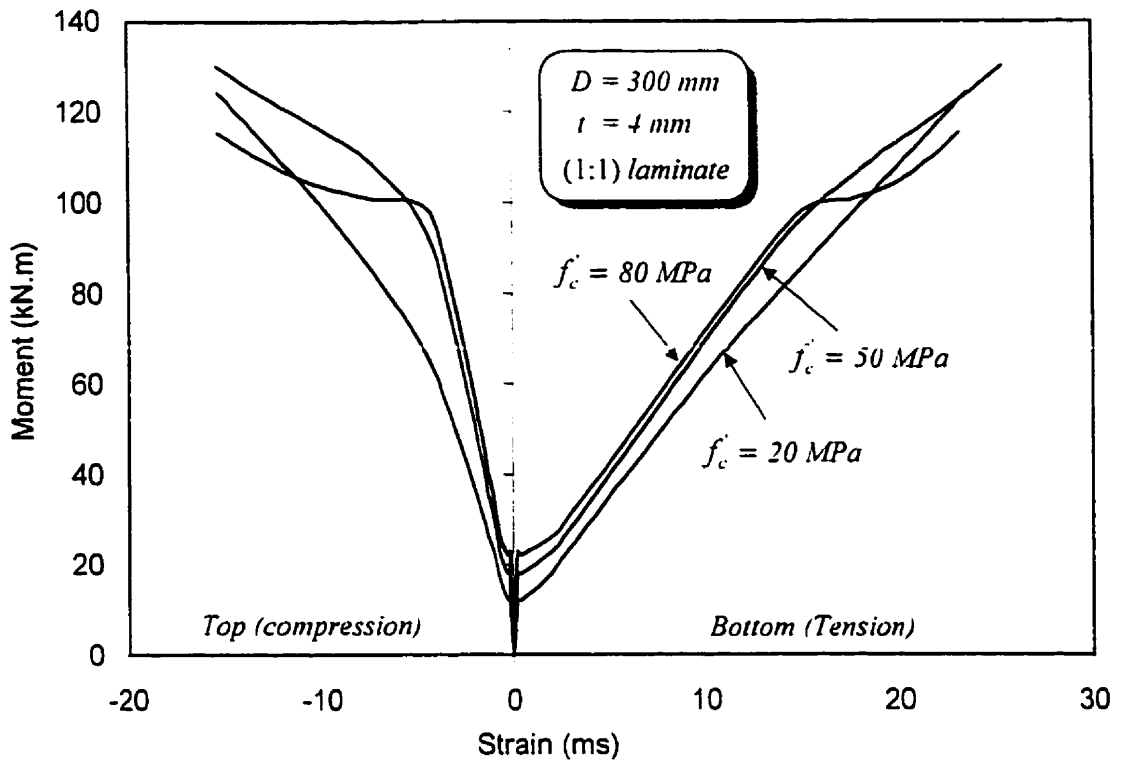


Fig. 5.60 Effect of concrete strength on moment-strain behaviour

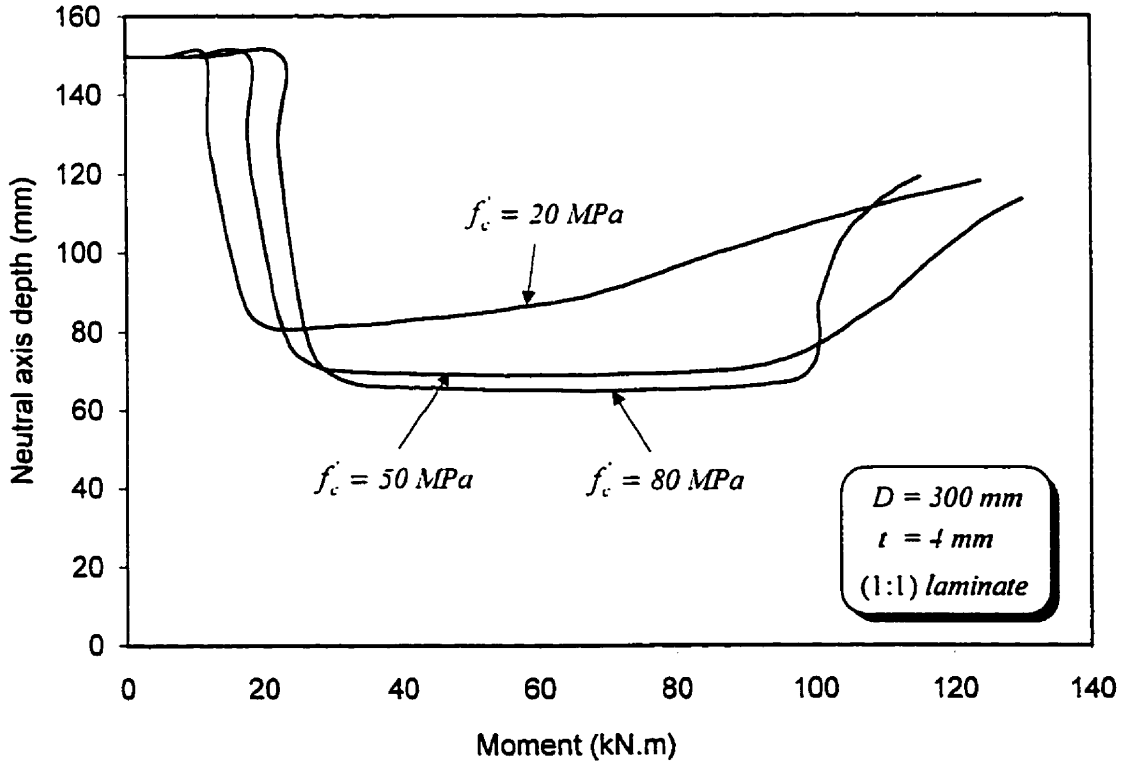


Fig. 5.61 Effect of concrete strength on variation of the neutral axis depth

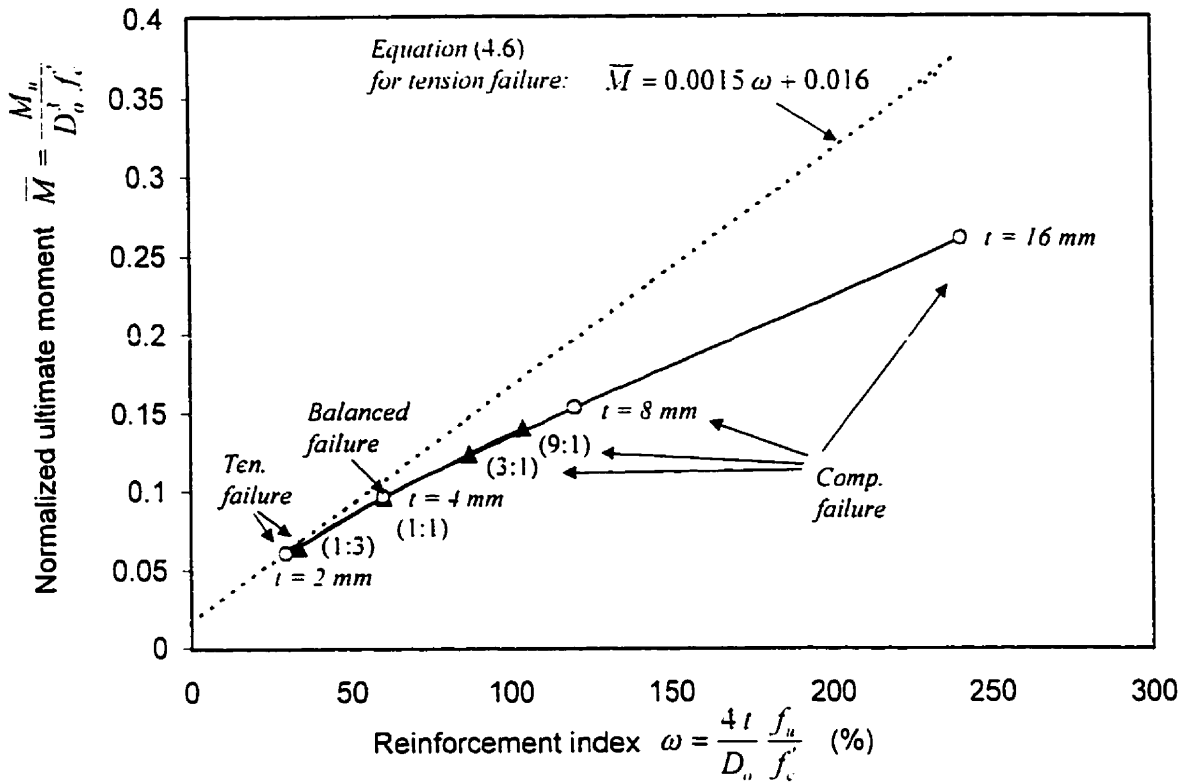


Fig. 5.62 Variation of the flexural strength with the reinforcement index

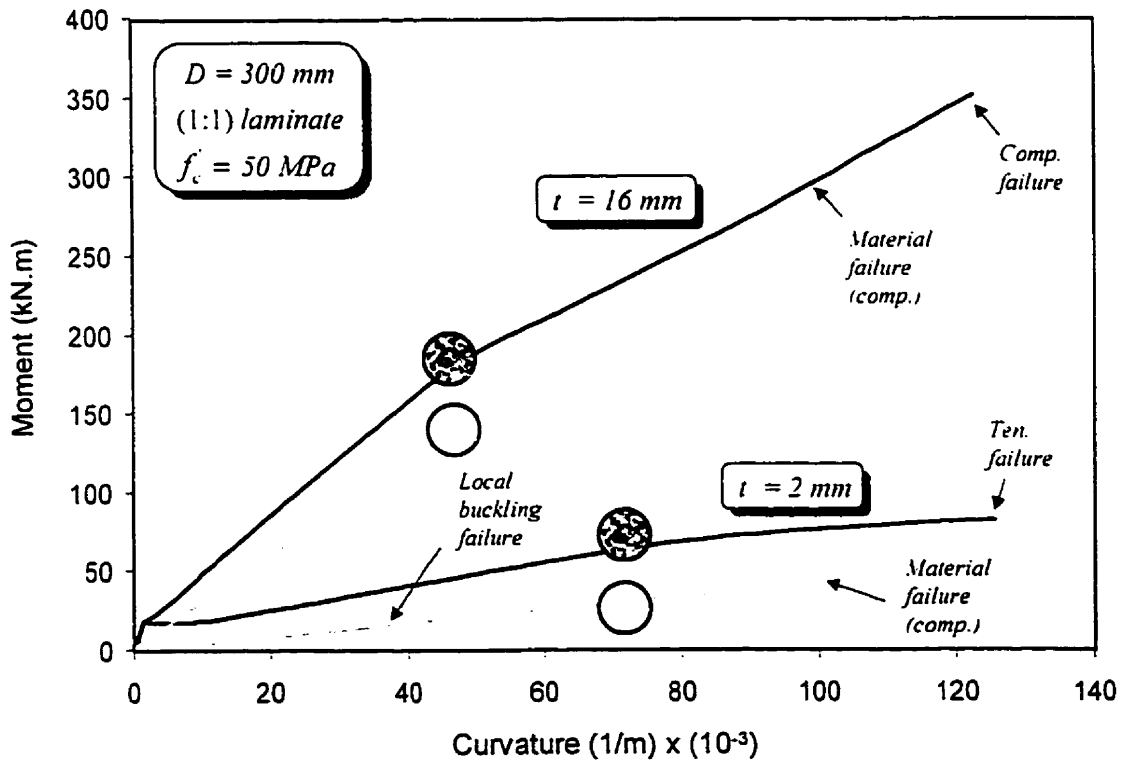


Fig. 5.63 Effect of concrete filling on flexural behaviour of tubes with high and low stiffness

Chapter 6

Summary and Conclusions

6.1 Summary

The main objective of this study was to evaluate the performance of GFRP cylindrical tubes totally and partially filled with concrete under pure bending as beams and under pure axial loads as short columns with emphasis on the confinement effect. Experimental and analytical investigations are conducted. The study showed that the concrete-filled GFRP tubes, with properly designed laminate structure, are excellent candidates for flexural and axial members. In principal, if bending is dominating, more stiffness and strength in the FRP tubes are required in the axial direction, whereas if axial compression is dominating, more strength and stiffness are required in the circumferential direction for confinement. This can be controlled by changing the ratio of the number of layers with longitudinal fibres to the number of layers with circumferential fibres within the wall thickness of the tube.

A two-phase experimental program was carried out. In Phase I, eighteen beams were tested in bending. The beams ranged from 1.07 to 10.4 meters in span and from 89 to 942 mm in diameter. The tests covered various parameters including the effect of concrete filling on flexural behaviour as compared to that of hollow GFRP and steel tubes, different cross-section configurations, and different diameter-to-thickness ratios of

the tubes. Different GFRP laminate structures were included. Phase II included twelve short columns tests used to study the effects of material type of the shell on confinement including steel, pultruded, and filament-wound GFRP tubes. Different cross-section configurations were compared, as well as different surface preparation conditions. Stubs with voided concrete core were also tested to study the effect of the central void size.

Two analytical models have been developed and verified by the experimental results. The first model predicts the full stress-strain response of concrete confined by FRP shells including concrete-filled prefabricated tubes or concrete columns wrapped with FRP sheets. The model considers both totally and partially filled tubes with voided concrete core, as well as columns having the axial load applied to both the concrete core and the tube or applied to the core only. The model is used to investigate the effects of stiffness of the tube in the hoop direction, central void size, and the nature of axial loading. It can also be used to model the concrete in the compression zone for the moment-curvature analyses of a section subjected to a general state of loading including bending moment and axial loads. This can be done by considering the stress-strain response of the confined concrete, which is obtained using this confinement model, as a material constitutive relationship, to be used as an input in the analysis. The second analytical model is intended to predict the full load-deformation response of concrete-filled FRP tubes as flexural members based on equilibrium, strain compatibility and material properties using a layer-by-layer approach and accounting for tension stiffening of concrete. The model is used to investigate the effects of stiffness of the tube.

reinforcement ratio, concrete strength, and the contribution of concrete filling in low and high stiffness tubes.

6.2 Conclusions

6.2.1 Flexural Members

1. Concrete filling has two important functions. It provides internal support for the tube to prevent premature failure due to the excessive ovalization and local buckling. It also contributes to the internal forces in terms of compressive strength, which increases the moment capacity of the section.
2. Strength and ductility of flexural members are greatly improved by filling the tubes with concrete. The gain in strength is slightly higher than double the strength of the hollow filament-wound GFRP tubes used in this investigation and is about 50 percent higher than the strength of the hollow steel tube.
3. The load-deflection behaviour of concrete-filled GFRP tubes is almost bi-linear. The cracking load is small compared to the ultimate load. Flexural stiffness is reduced immediately after cracking and stays almost constant with little reduction till failure.
4. Flexural stiffness after cracking is governed by the laminate structure of the FRP tube in terms of the effective elastic modulus in the axial direction, whereas the flexural strength is governed by the strength of the tube in the axial direction. Concrete-filled GFRP pultruded tubes show higher flexural stiffness compared to concrete-filled filament-wound tubes of the same diameter and thickness due to their higher elastic modulus in the axial direction, yet they fail prematurely in shear.

5. Cracking moment of concrete-filled GFRP tubes is low compared to the ultimate moment, yet the measured values were significantly higher than the predicted values using ACI and CEB-FIP code equations. This is attributed to a state of chemical prestressing developed due to the restrained expansion of concrete in the tubes. A modification for the code equations has been proposed as follows:

For the ACI code: $f_{cr} = \sqrt{f'_c}$

For the CEB-FIP code: $f_{cr} = 0.5 (f'_c)^{2/3}$

6. Hollow GFRP filament-wound tube failed by local crushing in compression near the loading point before the strength of the tube was developed. Hollow GFRP pultruded tube failed by local splitting and crushing at the loading point. Hollow steel tube failed by yielding followed by inward local buckling in compression. All hollow tubes showed excessive ovalization before failure.
7. Concrete-filled tubes develop the full strength of the GFRP tubes before failure. Failure mode is governed by the laminate structure of the tube. All the beams tested in this study had a flexural tension failure by rupture of the fibres, except for two beams, which lack fibres oriented in the hoop direction. One of those two beams failed by splitting of the pultruded tube, while the other failed in compression by cracking of the matrix and buckling of the glass fibres.
8. Concrete-filled steel tube showed a ductile failure with excessive deflection once the tube yielded. The concrete core delayed local buckling and forced it to occur outward, at a higher load level compared to the hollow tube.
9. Higher flexural strength-to-weight ratio can be achieved by providing a central void inside the concrete core. Strength and stiffness of a partially filled GFRP tube with a

- concentric void are similar to those of a totally filled tube if the concrete wall thickness is at least equal to the depth of the compression zone in the totally filled tube.
10. If the voided concrete core is maintained by an inner GFRP tube, the flexural strength and stiffness are increased, especially if the inner tube is eccentric towards the tension side.
 11. Flexural strength and stiffness can be enhanced by either increasing the reinforcement ratio or the effective elastic modulus of the tube in the axial direction. The reinforcement ratio is increased by using thicker tubes, while the elastic modulus is increased by using laminates with higher fibres content in the axial direction.
 12. Slip could reduce the stiffness and strength of the beam. It however does not constitute failure. Using stiffer tubes reduces the effect of the slip.
 13. Slip between the tube and the concrete core can be prevented by using expansive concrete mix as well as a rough layer of silica sand sprayed on a thin layer of adhesive applied to the inner surface of the tube. In this study, this surface preparation was conducted within 10 percent of the length of the tube from each end.
 14. Expansion mechanism of the concrete is more effective for totally filled tubes. Less pressure is built in partially filled tubes since the central void provides an inward radial displacement degree of freedom for the concrete.
 15. Confinement effect of concrete in the compression zone of concrete-filled GFRP tubes under bending is insignificant as evident by comparing the axial-lateral strain behaviour of the part of the tube in the compression zone to that of a similar

concrete-filled tube subjected to pure axial load. This is due to the strain gradient as well as the small size of the compression zone.

16. Although the concrete compressive strength is not increased by confinement in flexural members, the ductility of concrete in compression is improved as evident by the measured axial strain on the compression side of the beams at ultimate, which ranged from 0.007 to 0.017 instead of the typical 0.0035 value provided by the Canadian code.
17. Test results indicate that the size effect is insignificant for the beams tested in this study.
18. Based on the experimental study, simple empirical equations are proposed to predict the ultimate moment and curvature of concrete-filled GFRP tubes failing in tension.
19. For detailed analysis, a strain compatibility/equilibrium analytical model using layer-by-layer approach is developed to predict the full response of concrete-filled FRP tubes in bending using the stress-strain curve of unconfined concrete. The model predicted very well the behaviour of the beams and was used in a parametric study. A 0.3 bond factor is suggested for the tension stiffening equation by Collins and Mitchell (1997).
20. The parametric study indicated that for the same tube thickness, increasing the axial stiffness of the tube by increasing the amount of fibres in the axial direction increases the flexural strength and stiffness of the beam. The failure mode could however change from tension to compression failure of the tube.

21. For the same laminate structure, increasing the wall thickness increases the flexural strength and stiffness of the beam. However, concrete-filled FRP tubes with thicker walls tend to fail in compression.
22. The 28 days compressive strength of concrete has an insignificant effect on the strength and stiffness of concrete-filled FRP tubes in bending in comparison to the effects of the stiffness and wall thickness of the FRP tube as indicated from the parametric study.
23. Effects of concrete filling are more pronounced in FRP tubes with lower stiffness. The stiffer the tube, whether by having a thicker wall or higher axial elastic modulus, the lower the contribution of the concrete filling.

6.2.2 Axial Compression Members

1. The capacity of concrete-filled tubes exceeds the sum of capacities of the concrete and the tube individually. The tube confines the concrete and increases its strength and ductility, while the concrete supports the tube, preventing local buckling failure.
2. Stress-strain response of concrete confined using FRP shells is almost bi-linear. Up to the unconfined peak strength, at about 0.002 strain, the behaviour is similar to that of unconfined concrete. Beyond this stage, a strain hardening, yielding, or softening behaviour is observed depending on the stiffness of the shell and the size of the central void.
3. Below a strain value of 0.002, confinement effect is hardly observed due to the small value of Poisson's ratio of concrete, relative to that of the GFRP tubes, and the relatively low stiffness of GFRP tubes. At an approximate level of 0.002 strain,

concrete expands excessively resulting in activation of the FRP shell in confinement. The confinement pressure is continuously increasing, resulting in a linear stress-strain response of concrete following the linear behaviour of GFRP.

4. Steel-confined concrete shows a plastic behaviour once the steel shell yields due to stabilization of the confining pressure.
5. The ultimate capacity of concrete-filled FRP tubes is governed by the strength of the tube. Once the shell is fractured the column fails. The shell fails due to a bi-axial state of stress including axial compressive and hoop tensile stresses. On the other hand concrete-filled steel tubes sustain large deformations after yielding, which is normally accompanied by bulging of the column.
6. GFRP tubes provide similar confinement effectiveness to that provided by steel tubes using significantly smaller wall thickness of the tube. The concrete-filled GFRP tube in this study had a wall thickness, 37 percent smaller than that of the steel tube, yet they both achieved the same strength.
7. If both the concrete and the shell are axially loaded, the confining pressure is governed by the difference in values of Poisson's ratio of the concrete and the shell. FRP shells are better than the steel since Poisson's ratio can be controlled by the laminate structure design. Most laminates have Poisson's ratio smaller than steel, which provides better confinement.
8. GFRP tubes designed to provide strength in both axial and hoop directions are less effective in confinement compared to tubes with only circumferential fibres. The shell is bi-axially loaded under axial compression and hoop tension, which reduces its

- strength in the hoop direction. It also expands outward, resulting in less contact pressure with concrete.
9. Filament-wound GFRP tubes are superior to pultruded tubes in confinement. The pultruded tubes split immediately once the concrete starts to expand excessively.
 10. Totally filled GFRP tubes provide the most effective confinement. Although a central void offers material saving and reduced self-weight, it reduces the maximum achieved confined strength; however, a high level of ductility can still be achieved.
 11. If the central void is maintained by an inner FRP tube, the confinement effectiveness is improved and could approach that of a totally filled tube, depending on the stiffness of the shell. The outer and inner shells are subjected to hoop tensile and compressive stresses respectively.
 12. Initiation of the confinement mechanism can be detected from the bi-linear axial-lateral strain behaviour of the shell. The slope of the first part represents Poisson's ratio of the shell material. A change of slope occurs when concrete expands, producing more lateral strains in the shell.
 13. The interface condition between the tube and concrete has an insignificant effect on the behaviour when both the concrete core and the tube are axially loaded.
 14. A variable confinement model accounting for the variable confinement pressure and utilizing both the radial displacement compatibility and equilibrium is developed to predict the stress-strain response of concrete confined by FRP shells. The model predicted very well the behaviour of FRP-confined concrete specimens tested in this study and in other different studies and was used in a parametric study.

15. The parametric study showed that increasing the stiffness of the tube in the circumferential direction increases the confinement effectiveness. However, the increase in strength is not linearly proportional to the increase of stiffness. Also increasing the central void size reduces the confinement effectiveness.
16. Ignoring the axial compressive stress developed in the tube in the analysis of axially loaded concrete-filled tubes could highly overestimate the predicted confined strength of concrete.

6.3 Recommendations for Future Work

The research work that has been done in this study for the development of concrete-filled FRP tubes as flexural and axial members is extensive and covered a wide range of parameters. A number of major achievements have been accomplished in terms of full understanding of the flexural behaviour of the system and the confinement mechanism under axial loads as well as the analytical capabilities of the developed models. More work in related areas, however, still needs to be conducted. Areas that need further study to complete the development of concrete-filled FRP tubes as a product ready to be used by the industry and expand the understanding of the behaviour are:

1. Examine the behaviour under combined axial load and bending moment and establish interaction diagrams for the sections.
2. Examine the slenderness effect for long columns.
3. Investigate the shear behaviour and strength of concrete-filled FRP tubes, where the FRP shell acts as the longitudinal and transverse reinforcement simultaneously.

4. Study the effect of cyclic loading on the behaviour of the axial and flexural members.
5. Develop and optimize a unified technique to enhance the bond between the tube and the concrete core in order to eliminate slip in flexural members.
6. Examine the effect of adding rebars and/or prestressing to flexural members.
7. Investigate hybrid laminate structures for the tubes, where carbon fibres are utilized in the axial direction and glass fibres in the hoop direction.
8. Develop joints and connections capable of transferring the moments and/or the shear forces between different members such as beams and columns.
9. Establish practical, standard, and reliable methods of material testing of FRP tubes in order to obtain their effective mechanical properties in the axial and hoop directions.
10. Complete a design guidelines document to be used by engineers for design of concrete-filled FRP tubes in different applications.

REFERENCES

1. ACI Committee 318 "Building Code Requirements for Reinforced Concrete and Commentary," ACI 318M-95/ACI 318RM-95. American Concrete Institute, Detroit, 1995.
2. ASTM C39-96 "Standard Test Method for Compressive Strength of Cylindrical Concrete Specimens," developed by ASTM Subcommittee C09.61, 1996, 5 p.
3. Avram, C., Facaoaru, I., Mirsu, O., Filimon, I., and Terteia, I. "Concrete Strength and Strains." Ed. by Elsevier Scientific Publishing Company, 1981.
4. Barber, E., Kennedy, S., Laurie Kennedy, D., and MacGregor, J. "Flexural Strength of Concrete-Filled Steel Hollow Structural Sections." Proceeding of the 1987 CSCE Centennial Conference, Montreal, May 19-22, 1987, pp. 494-511.
5. Becque, J. "Analytical Modeling of Concrete Columns Confined by FRP." M.Sc. Thesis, University of Manitoba, Winnipeg, Manitoba, Feb. 2000.
6. Beretero, V. and Moustafa, E. "Steel-Encased Expansive Cement Concrete Column." Proceedings of the ASCE, Vol. 96, No. ST11, Nov. 1970, pp. 2267-2282.
7. Burgueno, R., Davol, A., and Seible, F. "The Carbon Shell System for Modular Bridge Components." Proceeding of the Second International Conference on Composites in Infrastructure (ICCI'98), Tucson, Arizona, Jan. 1998, pp. 341-354.
8. Canadian Standard Association (CSA) "Limit State Design of Steel Structures (CAN/CSA-S16.1-94)," Clause 18, 1994, Rexdale, Ontario.
9. Canadian Standard Association (CSA) "Design of Concrete Structures for Buildings (CAN-A23.3-94)," 1994, Rexdale, Ontario.

10. Canning, L., Hollaway, L., and Thorne, A. M. "Manufacture, testing and numerical analysis of an innovative polymer composite/concrete structural unit." Paper 11826 Proc. Instn Civ. Engrs Structs & Bldgs, 1999, 134, Aug. 1999, 231-241.
11. Carrino, L., Moroni, G., and Turchetta, S. "CAD/CAM for Robotic Filament Winding Process Design," Proceeding of European Conference on Composite Materials (ECCM-8), June 1998, pp. 615-622.
12. Collins, M. P. and Mitchell, D. "Prestressed Concrete Structures," Ed. by Response Publications, Canada, 1997.
13. Dallaire, E., Aitcin, P., and Lachemi, M. "High-Performance Powder," *Civil Engineering*, Jan. 1998, pp. 49-51.
14. Daniel, I. M., and Ishai, O. "Engineering Mechanics of Composite Materials," Ed. by Oxford University Press, New York, 1994.
15. Deskovic, N. and Triantafillou, T. C. "Innovative Design of FRP Combined with Concrete: Short-Term Behavior," *Journal of structural Engineering*, Vol. 121, No. 7, July 1995, pp. 1069-1078.
16. Fam, Amir Z. and Rizkalla, Sami H., (a) "Behavior of Axially Loaded Concrete-Filled FRP Tubes." Submitted to *ACI Structural Journal*, March 2000.
17. Fam, Amir Z. and Rizkalla, Sami H., (b) "Confinement Model for Axially Loaded Concrete Confined by FRP Tubes," Submitted to *ACI Structural Journal*, March 2000.
18. Fam, A. and Rizkalla, S., (c) "Hybrid FRP/Concrete Structural Members." proceedings of the ACUN-2 International Conference: Composites in Transportation Industry, UNSW, Sydney, Australia, Feb. 2000.
19. Fam, Amir Z. and Rizkalla, Sami H., (d) "Concrete-Filled FRP Tubes for Flexural and Axial Compression Members," Accepted for publication, Proceeding of the Third International conference on Advanced Composite Materials for bridges and Structures (ACMBS-III), Ottawa, Ontario, Aug. 2000.

20. Fam, A. Z., Rizkalla, S. H., and Tadros, G. "Behavior of CFRP for Prestressing and Shear Reinforcement of Concrete Highway Bridges." *ACI Structural Journal*. Vol. 94, No. 1, Jan.-Feb. 1997, pp. 77-86.
21. Fardis, M. N. and Khalili, H. "Concrete Encased in Fibreglass-Reinforced Plastic." *ACI Structural Journal*, Title No. 78-38, Nov.-Dec. 1981, pp. 440-446.
22. Furlong, R. W. "Strength of Steel-Encased Concrete Beam Columns," Proceeding of the ASCE. Vol. 93, No. ST5, Oct. 1967, pp. 113-124.
23. Gardner, Noel J. "Triaxial Behavior of Concrete." *ACI Structural Journal*, Title No. 66-15, Feb. 1969, pp. 136-146.
24. Gardner, Noel J. and Jacobson, E. Ronald "Structural Behavior of Concrete Filled Steel Tubes." *ACI journal*, Title No. 64-38, July 1967, pp. 404-416.
25. Ghali, A. and Favre, R. "Concrete Structures Stresses and Deformations." Second Edition. Published by E & FN Spon. London, UK, 1993.
26. Ghali, A. and Neville A. M. "Structural Analysis. A Unified Classical and Matrix Approach." Third Edition. Published by E & FN Spon. London, UK, 1989.
27. Gowd, T. N. and Rummel, F. "Effect of Confining Pressure on the Fracture Behavior of Porous Rock." *Int. J. Rock Mech. Min. Sci. & Geomech. Abstr.*, Vol. 17, 1980, pp. 225-229.
28. Hall, J. E. and Mottram, J. T. "Combined FRP Reinforcement and Permanent Formwork for Concrete Members." *Journal of Composites for Construction*. ASCE. Vol. 2, No. 2, May 1998, pp. 78-86.
29. Ibrahim, S. "Performance Evaluation of Fiber-Reinforced Polymer Poles for Transmission Lines," Ph.D. Thesis, University of Manitoba, Winnipeg, Manitoba, April 2000.
30. Kanatharana, J. and Lu, L. "Strength and Ductility of Concrete Columns Reinforced by FRP Tubes," Proceeding of the First International Conference on Composites in Infrastructure (ICCI'96), Tucson, Arizona, Jan. 1998, pp. 370-384.

31. Karbhari, V. M. et al "Structural Characterization of Fiber-Reinforced Composite Short- and Medium-Span Bridge Systems." Proceeding of European Conference on Composite Materials (ECCM-8), June 1998, Vol. 2, June 1998, pp. 35-42.
32. Kennedy, S. J. and MacGregor, J. G. "End Connection Effects on the Strength of Concrete Filled HSS Beam Columns," Structural Engineering Report No. 115, University of Alberta, Edmonton, April 1984.
33. Kibler, John J. "Composite Laminate Analysis Systems," CLASS, Computer Program, Release 3.50, Material Sciences Corporation, Springhouse, PA, 1987.
34. Kilpatrick, A. E. and Rangan B. V. "Tests on High-Strength Composite Concrete Columns." Research Report No. 1/97, School of Civil Engineering, Curtin University of Technology, Perth, Western Australia, March 1997.
35. Kilpatrick, A. E. and Rangan B. V. "Deformation-Control Analysis of Composite Concrete Columns." Research Report No. 3/97, School of Civil Engineering, Curtin University of Technology, Perth, Western Australia, July 1997
36. Kilpatrick, Andrew E. and Rangan, B. Vijaya "Tests on High-Strength Concrete-Filled Steel Tubular Columns," *ACI Structural Journal*, Vol. 96, No. 2, March-April 1999.
37. Knowles, Robert B. and Park, R. "Strength of Concrete Filled Steel Tubular Columns," Proceedings of the ASCE, Vol. 95, No. ST12, Dec. 1969, pp. 2565-2587.
38. Kurt, Carl E. "Concrete Filled Structural Plastic Columns," Proceedings of the ASCE, Vol. 104, No. ST1, Jan. 1978, pp. 55-63.
39. Lancaster Composite, Inc. "COMPOSITE POST 40 Marine Piling & Structural, Sign Support Systems and Fencing Framework Systems," 1000 Houston Street, P.O. Box 247, Columbia, PA 17512-0247.

40. Lu, Yue Qing and Kennedy, D. J. Laurie "The flexural behavior of concrete-filled hollow structural sections." Structural Engineering Report 178. Department of Civil Engineering. University of Alberta. Edmonton. April 1992.
41. Mander, J. B. and Priestley, M. J. N. and Park, R. "Theoretical Stress-Strain Model for Confined Concrete," *Journal of Structural Engineering*, Vol. 114 No. 8, Aug. 1988, pp. 1804-1826.
42. Mirmiran, Amir "Concrete Composite Construction for Durability and Strength." Symposium on Extending Life span of Structures, International Association for Bridge and Structural Engineering (IABSE), San Francisco, CA. Aug. 1995, pp. 1155-1160.
43. Mirmiran, Amir and Shahawy, Mohsen "Comparison of over-and under-reinforced concrete-filled FRP tubes," Proceeding of the 13th ASCE Engineering Mechanics Division Conference, Baltimore, June 13-16, 1999.
44. Mirmiran, Amir and Shahawy, Mohsen "A new concrete-filled hollow FRP composite column." *Composites Part B: Engineering, Special Issue on Infrastructure*, Elsevier Science Ltd., Vol. 27B, No. 3-4, June 1996, pp. 263-268.
45. Mirmiran, Amir and Shahawy, Mohsen "Behavior of Concrete Columns Confined by Fiber Composites." *Journal of Structural Engineering*, May 1997, pp. 583-590.
46. Mirmiran, Amir et al "Effect of Column Parameters on FRP-Confined Concrete." *Journal of Composites for Construction*, ASCE, Vol. 2, No. 4, Nov. 1998, pp. 175-185.
47. Mirmiran, Amir et al "Large Beam-Column Tests on Concrete-Filled Composite Tubes." *ACI Structural Journal*, Title no. 97-S29, March-April 2000, pp. 268-276.
48. Murphy, J. "Reinforced Plastic Handbook," Second Edition, Copyright 1998 Elsevier Science Ltd.
49. Narayanan, R. et al "Double-skin composite construction for submerged tube tunnels," *Steel Construction Today*, 1987, 1, pp. 185-189.

50. Palbøl, L., Jakobsen, U. H., and Thaulow, N. "0 to 60-Year-Old Water Pressure Pipes." *Concrete International*. March 1998, pp. 47-52.
51. Parent, S. and Labossiere P. "Finite Element Analysis of Reinforced Concrete Columns Confined with Composite Materials." Paper, University of Sherbrooke, Sherbrooke, Quebec.
52. Park, R., and Paulay T. "Reinforced Concrete Structures." Ed. by John Wiley & Sons, 1975.
53. Parvathaneni, H. K., Iyer, S., and Greenwood, M. "Design and construction of test mooring pile using superprestressing," Proceeding of Advanced Composite Materials in Bridges and Structures (ACMBS), Montreal, 1996, pp. 313-324.
54. Picher, F., Rochette, P., and Labossiere, P. "Confinement of Concrete Cylinders with CFRP." Proceeding of the First International Conference on Composites in Infrastructure (ICCI'96), Tucson, Arizona, Jan. 1996, pp. 829-841.
55. Prion, Helmut G. L. and Boehme, J. "Beam-Column behavior of Steel Tubes filled with High Strength Concrete," *Canadian Journal of Civil Engineering*, Vol. 21, 1994, pp. 207-218.
56. Rodgers, T. E. "Prestressed Concrete Poles: State-of-the-Art." *PCI Journal*, Sept.-Oct. 1984, pp. 52-103.
57. Samaan, M., Mirmiran, A., and Shahawy, M. "Model of Concrete Confined by Fiber Composites." *Journal of Structural Engineering*, Sept. 1998, pp. 1025-1032.
58. Schneider, Stephen P. "Axially Loaded Concrete-Filled Steel Tubes." *Journal of Structural Engineering*, Oct. 1998, pp. 1125-1138.
59. Seible, Frieder "Advanced composites materials for bridges in the 21st century." Proceeding of the First International Conference on Composites in Infrastructure (ICCI'96), Tucson, Arizona, Jan. 1996, pp. 17-30.

-
60. Seible, Frieder "Innovative designs for pedestrian bridges." Proceeding of Developments in Short and Medium Span Bridge Engineering '98. Calgary, Alberta. 1998.
 61. Seible, Frieder et al "Design issues with carbon fiber composite reinforced concrete structures." Proceeding of the Third International Symposium, Non-Metallic (FRP) Reinforcement for Concrete Structures. Vol. 2. Japan. Oct. 1997. pp. 89-112.
 62. Seible, Frieder et al "Modular advanced composite bridge system for short and medium span bridges." Proceeding of Developments in Short and Medium Span Bridge Engineering '98, Calgary, Alberta. 1998.
 63. Shahawy, Mohsen and Mirmiran, Amir "Hybrid FRP-Concrete Beam-Columns." Proceeding of the Fifth International Conference on Composites Engineering (ICCE/5), Las Vegas. July 1998. pp. 619-620.
 64. Spoelstra, Marijn R. and Monti, Giorgio "FRP-Confined Concrete Model." *Journal of Composites for Construction*. ASCE. Aug. 1999. pp. 143-150.
 65. Stapleman, J. "Pile On The Abuse." *Composite Technology*. Sept./Oct. 1997.
 66. Tomii, Masahide and Sakino, Kenji "Experimental studies on the ultimate moment of concrete filled square steel tubular beam-columns." Translation of A.I.J., No. 275. Jan. 1979. pp. 55-65.
 67. Triantafillou, T. C. "Composite Materials for Civil Engineering Construction." Proceeding of the First Israeli Workshop on Composite Materials for Civil Engineering Construction. Haifa, Israel. May 1995. pp. 17-20.
 68. Triantafillou, T. C. and Meier, U. "Innovative design of FRP combined with concrete." Proceeding of the First International conference on Advanced Composite Materials for bridges and Structures (ACMBS), Sherbrooke, Quebec, 1992. pp. 491-499.

-
69. Wei, S. et al "Performance of New Sandwich Tube under Axial Loading: Experiment." *Journal of structural Engineering*. Vol. 121, No. 12, Dec. 1995, pp. 1806-1814.
 70. Wei, S. et al "Performance of New Sandwich Tube under Axial Loading: Analysis," *Journal of structural Engineering*. Vol. 121, No. 12, Dec. 1995, pp. 1815-1821.
 71. Wernli, M. and Seible, F. "Ductile Connections of Modular Bridge Girders Made of Concrete Filled FRP-Tubes." Proceeding of the First International Conference on Composites in Infrastructure (ICCI'96), Tucson, Arizona, Jan. 1998, pp. 356-367.
 72. Young, Warren C. "Roark's Formulas for Stress and Strain." Sixth Edition, McGraw-Hill Inc., 1989.
 73. Zhao, Lei et al "Experimental investigation of joint response between concrete-filled carbon shell girders and composite decks using "push-out" tests." Report No. TR-97/16. Division of Structural Engineering, School of Engineering, University of California, San Diego, La Jolla, California. Oct. 1997.